ENTRAINMENT, MIXING, AND IGNITION IN SINGLE AND MULTIPLE JETS IN A SUPERSONIC CROSSFLOW

A Dissertation
Presented to
The Academic Faculty

By

Dan Fries

In Partial Fulfillment
of the Requirements for the Degree
Doctor of Philosophy in the
Daniel Guggenheim School of Aerospace Engineering

Georgia Institute of Technology

December 2020

ENTRAINMENT, MIXING, AND IGNITION IN SINGLE AND MULTIPLE JETS IN A SUPERSONIC CROSSFLOW

Approved by:

Prof. Suresh Menon, Advisor
Daniel Guggenheim School of Aerospace Engineering
Georgia Institute of Technology

Prof. Devesh Ranjan, Advisor
George W. Woodruff School of Mechanical Engineering
Georgia Institute of Technology

Prof. Adam Steinberg
Daniel Guggenheim School of Aerospace Engineering
Georgia Institute of Technology

Dr. Timothy Ombrello
Wright-Patterson Air Force Base
U.S. Air Force Research Laboratory

Prof. Jerry Seitzman
Daniel Guggenheim School of Aerospace Engineering
Georgia Institute of Technology

Date Approved: August 19, 2020

"When someone seeks," said Siddhartha, "then it easily happens that his eyes see only the thing that he seeks, and he is able to find nothing, to take in nothing because he always thinks only about the thing he is seeking, because he has one goal, because he is obsessed with his goal. Seeking means: having a goal. But finding means: being free, being open, having no goal."

Herman Hesse, Siddhartha

This thesis is dedicated to my mother, Angelika Fries. Her love and understanding knows no bounds and her sacrifices have made possible my success.

ACKNOWLEDGEMENTS

This thesis and all the associated life experiences would have not been possible without the direct and indirect help of many people that I had the pleasure to meet, work, argue, eat, and drink with.

I am grateful for the support of my advisors, Prof. Suresh Menon and Prof. Devesh Ranjan, throughout my time as a PhD student at Georgia Tech. Both on the research side and for enabling me to visit conferences, seminars and other training opportunities. I would also like to thank my dissertation committee, Prof. Adam Steinberg, Dr. Tim Ombrello, and Prof. Jerry Seitzman, for their time and input to my research. Their commitment to critical review and discussions was instrumental in getting to this point.

During my time as a PhD student I faced numerous challenges going beyond the purely academic nature of things. I owe thanks to the individuals that were willing to engage with me over these issues, to listen and to support. Prof. Jeff Jagoda always has an open ear for students, provides almost unconditional support and does whatever he can to alleviate anxieties. The chair of the school of Aerospace Engineering, Prof. Mark Costello, is genuinely committed to listening to students' grievances and improving the overall experience that we have. Prof. Tim Lieuwen, who gave me the opportunity to push for real improvement in the combustion lab's work environment, also cares deeply about the well-being of students and their success. I would also like to thank the Professors Seitzman, Walker and Ruffin for giving me the opportunity to teach a few graduate level lectures when I showed interest.

On the financial side, I would like to acknowledge the Air Force Office of Scientific Research for supporting me during the first 3-4 years of my PhD.

When I started my PhD journey, I had mostly been working with simulations and had a lot to learn on the experimental end of things. I owe thanks to Bradley Ochs, Sasha Bibik, David Wu, Subodh Adhikari and Chris Ballance who, as research engineers, have taught

me a lot and continuously helped me out with technical questions. Furthermore, Kristopher Manion and Seth Hutchins deserve my gratitude for keeping the lab up and running (the lab is a fickle lover), dealing with my 24/7 messages about missing equipment and non-functional heaters, and handling the THUNDERDOME. Finally, I would like to acknowledge Benjamin Emerson for organizing the lab's equipment schedule and supporting my far fetched ideas for high-speed imaging.

Of course, research could not run without money and equipment. Same as myself, as I still need to eat and drink (a big impediment in being academically successful). I am thankful for Richard Barger and Sadie Marshall for handling financial issues and purchases fast and accurately. Michelle Hall also helped me countless times figuring out last minute orders and shipments.

Without the help of the AE machine shop, a lot of my envisioned experiments would have never become reality. I am very grateful for the help of Scott Moseley, Greg Rogerson and Henry "Red" Russell. Especially Red has shown incredible patience and support in dealing with my escapist engineering designs and zero-tolerance machining requests. And he made them happen while having some of the deepest conversations about life, history and philosophy that I had the pleasure to partake in at Georgia Tech.

My entire family has been incredibly supportive throughout the entirety of my PhD. My mother, Angelika, has always been there for me, listening, understanding and supporting me with anything that came up. My sister, Lea, tolerating me not responding for weeks and forgetting family events and birthdays, yet always supporting me in my decisions and the work I had to do. My father, Matthias, telling me that he is proud of my work and that I am making the right choices. My grandparents, who were always worried about me not having enough friends and food in such a foreign country as the US.

Finally, I am deeply indebted to all my friends. Without them, I could not have gotten to where I am today and it would not have been even half as enjoyable. There are to many names to list individually but I hope that my friends will forgive me this laziness and

recognize themselves in my completely insufficient words of gratitude. In Atlanta, I am thankful for all my friends in the combustion lab and CNES, together we improved the work environment and atmosphere significantly, fought over air slots in the thunderdome as if our life depended on it, and had plenty of good times outside of the lab. This multi-cultural amalgamation of people has taught me a lot about life and the world we live in, and got me started on climbing more seriously. It has also given me hope in times when I thought everything was going to sh*t. I am also grateful for all the friends I made in America along the way outside the lab. A special mention is due for the Spaceport America Cup Rocketry Team at Georgia Tech. Not only was the whole endeavor extremely successful, a wild ride from start to finish, but the people in the club also reminded me how to have fun with engineering. I have the pleasure of knowing a copious amount of beautiful souls. In Germany, I would like to thank my friends from St.Leon-Rot, Walldorf and Stuttgart for staying by my side throughout hundreds of missed calls, ignored messages and late responses. At times, the PhD has made me a bad friend and I cannot express enough my gratefulness for the people that stayed with me, understanding me and making every reunion feel like we only saw each other yesterday. Also, showing me how to prioritize my time to keep such amazing people around that make life worth living.

TABLE OF CONTENTS

LIST OF TABLES

LIST OF FIGURES

NOMENCLATURE

Abbreviations

Ar	Argon
$\mathrm{C_2H_4}$	Ethylene
CVP	Counter-rotating vortex pair
$\mathrm{CO_2}$	Carbon dioxide
DI	Dual injector: system of two streamwise staged jets
FOV	Field of View
$\mathrm{H_2}$	Hydrogen
He	Helium
JICF	Jet in Crossflow
JISCF	Jet in Supersonic Crossflow
LIP	Laser Induced Plasma
MW	Molecular weight
$\mathrm{N_2}$	Nitrogen
$\mathrm{O_2}$	Oxygen
OH	Hydroxyl radical
PDF	Probability Density Function
PIV	Particle Image Velocimetry
PLIF	Planar laser induced fluorescence
RMS	Root Mean Square
$\mathrm{SiO_2}$	Silicone dioxide
SI	Single injector: single jet gas injection

TiO_2	Titanium dioxide
TKE	Turbulent kinetic energy

Latin symbols

A	Area/a constant
a	Speed of sound or a constant
B	A constant
b	A constant
C	Concentration/a constant
C_D	Drag coefficient
C_h	Constant in the developed trajectory scaling connecting crossflow pressure gradient and momentum flux
CH	CH* is the exicted state of the CH radical
C_p	Pressure coefficient
c_p	Specific heat capacity at constant pressure
C_r	Constant in the developed trajectory scaling connecting jet momentum flux ratio and resulting bow shock shape
D	Diffusion coefficient or a constant
d	Diameter
E	Energy or a constant
F	A constant
f	Mixture fraction
$f/\#$	F-number
H	Test section height
h	Height
h_c	Characteristic jet penetration height
I	Image or image intensity
$\rho f/(\rho f)_0$	(normalized) Jet Fluid Signal
J	Momentum flux ratio

k	Turbulent kinetic energy or a rate constant
$\dot{m}$	Mass flux
M	Mach number
N	Number count
n	Number or number density
P	Momentum flux
p	Pressure or a probability density function
R	Specific gas constant
r	Radius/radial coordinate
R^2	Coefficient of determination
r_{CH}	Relative increase in CH* luminous area
s	Arc length $s = \sum_i \sqrt{(\mathrm{d}x_i^2 + \mathrm{d}y_i^2)}$
S_{ij}	Mean strain rate tensor
T	Temperature
t	Time
t	Time
U	Velocity magnitude or uncertainty
u, v, w	Cartesian velocity components
V	Volume
x, y, z	Cartesian coordinates, x : streamwise, y : wall-normal, z : spanwise
Y	Mass fraction

Greek symbols

β	Shock angle/parameter
δ	Boundary layer thickness
δ_s	Spatial extension of boundary layer effects due to shock presence
γ	Specific heat ratio
κ_{ext}	Extinction strain rate

μ	Dynamic viscosity
μ_t	Turbulent eddy viscosity
$\nabla \cdot \vec{\bar{u}}$	Divergence of the mean velocity field
$\nabla \cdot \vec{\bar{u}}$	Divergence of the mean velocity field
$\dot{\omega}$	Source term
ρ	Density
σ	Standard deviation
τ	A time scale
χ	Mole fraction or scalar dissipation rate

Superscripts

$*$	Choked conditions
$\bar{\phi}$	Time or ensemble average of the quantity ϕ
$\hat{.}$	Coordinate normalization of y by h_c and of x by $J_2^{1/2} d_j$
ϕ'	Fluctuating part of the quantity ϕ
$\vec{\phi}$	Vector quantity ϕ

Subscripts

1	Conditions before a shock or initial conditions
2	Conditions after a shock or later conditions
c	Convective property
cf	Crossflow properties
d	Deposited amount
∞	Undisturbed static crossflow conditions
j	Jet properties
p	Particle properties
w	Properties at the wall
0	Stagnation or reference conditions

SUMMARY

Jets in crossflow are a canonical example for three-dimensional turbulent mixing. Here, non-reacting and reacting sonic jets in a supersonic crossflow are studied. The influence of injectant properties on turbulent mixing is investigated. Using pure gases, the molecular weight and specific heat ratio is varied between 4-44 $\mathrm{g/mol}$ and 1.24-1.66, respectively. The jets are injected into a Mach 1.71 crossflow with a stagnation temperature ~ 600 K. Two single jet injectors and two staged jet injectors are designed to characterize potential enhancements in turbulent mixing and combustion processes. Mixture fraction and velocity fields are determined via Mie-scattering off solid particles. Velocity vectors are obtained by processing Mie-scattering image pairs with a correlation technique (particle image velocimetry). To ignite the flow field and enable systematic variation of the ignition location a traversable laser spark system is employed. The reacting flow is probed via CH* chemiluminescence and OH planar laser induced fluorescence visualizing regions containing hot combustion products. A new trajectory scaling improves correlation between all data sets considered, suggesting that the bow shock, boundary layer and momentum flux ratio are the dominant controlling factors. Turbulent mixing rates are highest for injectants with higher molecular weight and lower specific heat ratio. The larger of two jet spacings tested yields the greater enhancement of turbulent mixing rates. Ignition locations on the symmetry plane of the flow field are evaluated for their ability to sustain chemical reactions/heat release. Most favorable ignition locations lie in the windward jet shear layer away from the regions of highest flow strain. The smallest diameter single jet with presumably more boundary layer interaction and moderate strain rates provides the best results with regard to thermal energy release after spark deposition. Trends suggest that moderate compressible strain rates and no flow expansion are advantageous to sustain thermal energy release. Implications for future research directions and opportunities are discussed.

CHAPTER 1
INTRODUCTION

1.1 Jets in a Supersonic Crossflow

The purpose of this thesis it to investigate turbulent mixing and forced ignition of sonic, underexpanded jets in a supersonic crossflow (JISCF). JISCF are an important model problem that is used extensively to perform fundamental studies on turbulent mixing and entrainment in compressible, high-speed flows (Mahesh, 2013; Gruber, Nejad, Chen, *et al.*, 1995; VanLerberghe *et al.*, 2000; Kawai and Lele, 2010). The flow field is highly three-dimensional and exhibits many interesting features that can be studied in the more general context of hydrodynamic instabilities, scalar entrainment and turbulent mixing, and the influence of compressibility on such processes.

JISCF is also a model problem for fuel injection into supersonic crossflows and is used to study the design of related engineering applications. Single jets as well as spanwise jet arrays and streamwise staged jets are of potential interest. The introduction of additional jets can significantly modify turbulent mixing, flow blockage effects and the velocity strain field (McDaniel and Graves, 1988). Such modifications can potentially be exploited to increase mixing efficiency when dealing with the very low flow residence times and the presumed compressible suppression of instability growth in high-speed flows (Papamoschou and Roshko, 1988).

Chemically reacting JISCF are used in scientific studies and engineering applications to enable and investigate burning in compressible flows. For these purposes, the jets usually supply the fuel in the studied systems. While some setups have also used jets to induce deflagration to detonation transition, the majority of the work focuses on deflagration processes consuming the jet fluid (Gamba and Mungal, 2015; Lee, 2006b).

In the following, a short review of relevant literature is given to identify gaps in the current body of knowledge. Based on these gaps, the scope of this dissertation, guiding hypotheses, and related objectives are then established. A more thorough literature review and knowledge gap identification is given in the subsequent Ch. 2.

1.1.1 Turbulent Entrainment and Mixing

Even for one of the simplest JISCF metrics, the mean jet trajectory, no consensus exists regarding the controlling parameters. Most trajectory laws are empirical power-laws and the values of coefficients and exponents vary widely (Mahesh, 2013). This makes comparisons between data sets from different studies difficult and obscures the influence of different flow field parameters on the jet trajectory.

Depending on the velocity and density ratios between the jet and crossflow both Kelvin-Helmholtz and Rayleigh-Taylor instabilities will initiate the large scale turbulent entrainment of crossflow fluid into the jet (Takahashi *et al.*, 2010). As the jet velocity and pressure equilibrate with the crossflow, turbulent mixing further downstream of the injection point will eventually reach an asymptotic state. Since this state is considered to be largely independent of the initial conditions, it is of interest to understand and maximize the growth of instabilities and turbulent mixing regions in the near field of the jet.

While the general process of instability formation and growth is very similar to that of a jet in an incompressible crossflow, the compressible nature of the flow adds a significant additional layer of complexity. Specifically, several studies reported a dependence of certain mixing metrics on the molecular weight and specific heat ratio of the jet fluid (Gruber, Nejad, Chen, *et al.*, 1997a; Ben-Yakar *et al.*, 2006). However, not that much consistent data exists in the form of comprehensive surveys utilizing a wide range of different pure jet fluids and analyzing consistent turbulent entrainment/mixing metrics.

1.1.2 Ignition and Burning

Ignition and burning of a JISCF is challenging. High strain rates and short residence times make it almost impossible to stabilize a flame without employing some type of subsonic cavity or subsonic wake region ahead of the jet. Providing auto-igniting conditions requires high enthalpy flows, restricting research activities mostly to computational efforts or very short testing times (Urzay, 2018). In general, very few studies exist that study combustion in a canonical JISCF setup (Gamba and Mungal, 2015; Brieschenk *et al.*, 2013a).

If auto-ignition is not possible or not fast enough, a forced ignition source is usually provided in the form of wall mounted spark discharges. Thus, spark plug ignition is restricted to regions close to the wall of any test setup. Ignition via temperature increase across shock waves or via shock wave impingement is another possibility (Huete *et al.*, 2017; Rhodes Jr. *et al.*, 1974). However, relatively high freestream Mach numbers are required, the shock waves cause a momentum loss, and the temperature increase mostly serves to locally decrease the auto-ignition delay, not as an actual forced ignition kernel.

A technique that has been gaining more attention for supersonic flows is laser induced plasma ignition (Brieschenk *et al.*, 2013a; An, Wang, *et al.*, 2017). A big advantage of this technique is that the ignition location is flexible, only limited by the positioning of the focusing lens. Since, for a JISCF, different regions are more or less suitable to support sustained burning (Gamba and Mungal, 2015), this flexibility is of great interest to individually probe the effectiveness of different ignition locations in lieu of auto-ignition conditions.

Burning fuels other than hydrogen is challenging because ignition delays increase and flame speeds decrease significantly. It is of interest to enable the burning of liquid hydrocarbon fuels as their energy density per volume is much higher than that of hydrogen and other gaseous fuels. A stepping stone in this development is the conversion of ethylene as an important constituent of heavier cracked hydrocarbons fuels and because it has a relatively low ignition delay (Colket III and Spadaccini, 2001).

Thus, investigating the burning of ethylene in supersonic flows at relatively low stagna-

tion enthalpies could provide additional means to experimentally probe complex compressible burning regimes. This approach could also provide a path from studying fundamental fluid dynamics and combustion processes towards applying lessons learned to current engineering challenges in high-speed propulsion systems.

1.1.3 Staged Jets

In numerical studies, staged jets in supersonic crossflows have been shown to increase turbulent mixing and burning rates in auto-ignited systems (Lee, 2006a; Lee, 2006b; Landsberg *et al.*, 2016). The numerical studies also suggest, that an ideal spacing might exist between jets in terms of mixing and burning efficiency. Some experimental studies have been performed using staged jets, generally confirming the improvement in desirable characteristics (McDaniel and Graves, 1988; Hollo *et al.*, 1994).

So far, experimental studies have not addressed the influence of systematic variations in jet spacing. Moreover, no experimental attempt has been made to utilize staged jets in enhancing forced ignition burning.

1.1.4 Modelling and Engineering Applications

The experimental investigation of flow physics described above can be applied to the validation of computation models and the development of engineering applications utilizing JISCF. The most relevant example of engineering applications probably being the scramjet (supersonic combustion ramjet) propulsion system (Smart, 2007).

The complex nature of the JISCF flow field makes it a well-suited benchmark for computational models to gauge capabilities and identify shortcomings (Kawai and Lele, 2010). However, there is a need for non-intrusive, detailed velocity and concentration field measurements at a wide range of conditions to compare to models and test different aspects of the model's formulation.

On the application side, JISCF-like configurations have the potential to enhance mixing

of injected fuel with minimal pressure loss. Reviews for this particular application are given by Huang (2016) and Lee, Lin, *et al.* (2015). A wide variety of approaches has already been tested in an engineering context. Nonetheless, a physically complete description of the JISCF evolution is missing, making comparisons between different configurations and conditions difficult.

1.2 Scope, Approach, and Objectives

To investigate the physics of turbulent entrainment, mixing and burning in the JISCF flow field, this dissertation focuses on some of the areas of interest outlined above. Specifically, the scope is limited to circular, flush-mounted injectors exhausting under-expanded, sonic jets into a uniform supersonic crossflow. The crossflow itself is "relatively cold", i.e. auto-ignition is unlikely to occur within the length of the test section. Thus, the total temperature of the flow in this dissertation is limited to 600 K with a crossflow Mach number of ~ 1.7 utilizing a blow-down windtunnel.

As mentioned at the beginning, the main goal of this dissertation is to experimentally investigate and characterize turbulent mixing and forced ignition for JISCF, then test a simple strategy (staged jets) to enhance mixing and burning processes. Based on gaps identified in the literature, several research hypotheses are formulated relating to this goal as well as objectives to test them.

The first hypothesis is that "*a flow physics informed scaling can correlate mean jet trajectories better than previous approaches and improve comparability between different studies. Moreover, mean jet trajectories based on jet fluid signal iso-contours will reflect changes in turbulent mixing due to injectant properties, such as molecular weight and specific heat ratio*".

A physics informed scaling for JISCF is developed using the momentum balance approach presented by Muppidi and Mahesh (2005) for incompressible jets in crossflow. This scaling explicitly considers the momentum flux ratio, the presence of the boundary layer,

and the presence of the bow shock in the flow field. To validate the scaling, jet trajectory data is collected for five different gases at four different momentum flux ratios and trajectory results from four other published studies are included for comparison. Most studies in the past have compared two or three gases, most commonly nitrogen, helium, hydrogen and ethylene, e.g. by Gruber, Nejad, Chen, *et al.* (1997a) and Ben-Yakar *et al.* (2006). This dissertation uses argon, ethylene, carbon dioxide, helium and nitrogen covering a range of molecular weights from $4 - 44\ \mathrm{g/mol}$ and specific heat ratios from 1.24-1.66.

To isolate and characterize the influence of gas properties, the scaled jet trajectories, the jet fluid signal fields and the velocity fields are analyzed. The convective Mach number was identified in the past as characterizing the effect of compressibility on turbulent mixing (Papamoschou and Roshko, 1988). This parameter is computed directly from available velocity data in the study, providing a spatially resolved convective Mach number profile over a small region of the flow. A novel measurement that can be compared to point estimates of the JISCF convective Mach number, such as those made by Gruber, Nejad, Chen, *et al.* (1997a) and Ben-Yakar *et al.* (2006).

The second hypothesis is that "*some regions of a JISCF flow field are more favorable than others to sustain an ignition kernel and the release of thermal energy. This will depend on the mean and instantaneous distribution of fuel, strain, and temperature in the flow*".

To test the second hypothesis, a single ethylene jet is used and flow conditions as well as spark locations are selected based on the inert flow results. A traversable laser ignition system is employed to check the efficacy of a grid of flow field positions for their ability to provide sustained chemical reactions/burning. While laser ignition has been used before in a JISCF setup by Brieschenk *et al.* (2013a), this is the first study to systematically deposit energy for ignition at different flow field locations. CH* chemiluminescence imaging and statistical analysis of the inert flow field are combined to evaluate the ignition or quenching process at each spark location. The physical mechanisms determining the outcome of laser spark evolution are discussed in detail.

The third hypothesis is that "*a staged JISCF setup will enhance turbulent mixing and burning initiated by a forced ignition process compared to a single jet setup. The degree of enhancement will depend on the spacing between the jets as the distribution of fuel, low velocity regions, and dilatational strain changes*".

The staged jets used to test the third hypothesis are designed based on the non-reacting single jet studies. Two staged injectors with different spacings are built to probe two different jet interaction regimes. The resulting non-reacting mixture fraction fields are analyzed, as are changes in the velocity field. Based on the initial single jet laser ignition results, a set of promising locations is selected and the evolution of chemically active regions is investigated more closely for both the single jet and dual jet injectors. Planar laser induced fluorescence of the OH radical (OH PLIF) is used to identify regions containing hot combustion products. Statistical information from the non-reacting measurements is used to provide a deeper physical understanding of the results. This is the first type of study attempting to systematically identify jet and ignition configurations that maximize the likelihood of sustained burning for a cold supersonic flow.

The organization of this dissertation is as follows. In Ch. 2 the physics of non-reacting and reacting JISCF are discussed, as are previously published, relevant experimental, theoretical, and numerical studies. In Ch. 3, a detailed description of the experimental setup, the ignition system, flow diagnostics and data acquisition, data processing, and undisturbed flow characteristics is given. The experimental results and analysis for objectives one, two and three are presented in Ch. 4, Ch. 5, and Ch. 6, respectively. Finally, the conclusions and recommendations for future work can be found in Ch. 7.

CHAPTER 2

LITERATURE REVIEW

2.1 Jet Mixing and Entrainment

Jets exhausting into a quiescent environment or into a moving co-flow have long been used as canonical example problems of free shear flows and turbulent mixing (Dimotakis, 2005). For theoretical treatment they can often be considered as statistically two-dimensional or axisymmetric. An important realization is that an incompressible jet emerging into a quiescent environment will have a constant momentum flux across any cross section (White and Corfield, 2006),

$$P = \rho \int_{-\infty}^{+\infty} u^2 \mathrm{d}y = const. \tag{2.1}$$

To potentially enhance mixing processes and introduce three-dimensional effects, wall-normal jets are exposed to a crossflow. This also resembles situations regularly occurring in our environment, such as smoke stack plumes, forest fires and volcanic plumes. Thus, the jet in crossflow (JICF) has become another canonical problem to investigate three-dimensional turbulent mixing processes (Karagozian, 2014; Mahesh, 2013). Additionally, JISCF are used in a wide variety of engineering applications, ranging from fuel injection, cooling, thrust vectoring, to retro-propulsion and reaction control.

An important non-dimensional parameter for JISCF is the ratio of jet momentum flux to crossflow momentum flux as a controlling parameter of the resulting flow field,

$$J = \frac{\left(\rho \bar{u}^2\right)_j}{\left(\rho \bar{u}^2\right)_\infty}. \tag{2.2}$$

In the following, literature pertaining to the study of mixing in incompressible and compressible JISC setups is given a closer look.

2.1.1 Incompressible Flow Conditions

Incompressible JICFs have a long history of being used to study turbulent mixing. Margason (1993) describes a large number of efforts that investigated different JICF configurations to understand the complex flow field better. Among others, notable results are the investigation of jet temperature effects by Kamotani and Greber (1972) and the detailed visualization of vortical structures formed in the flow field by Fric and Roshko (1994). The former found that jet temperature effects are overall weak but a higher jet temperature increases the strength of the jet's vortical motions. The latter describes four dominant vortex structures of the JICF in great detail, see Fig. 2.1.

Fric and Roshko (1994) describe the windward shear layer vortices as being primarily formed by a Kelvin-Helmholtz (KH) instability formed in the annular jet shear layer, see Fig. 2.2. The horseshoe vortices are the result of the near-wall flow seperation and recirculation just ahead of the jet. Wrapping around around the jet column they eventually ineract with the wake vortices. Fric and Roshko (1994) found that the wake vortices are formed not by vortex shedding from the jet itself but from vorticity originating in the boundary later. They also concluded that the streamwise momentum imparted on the jet must be extracted solely from the interaction with the crossflow during the mixing process.

The last type of vortical structure shown is the counter-rotating vortex pair (CVP). The structure is somewhat synonymous with the jet itself after some development and controls many of the global mixing features. Arguably, its formation is one of the reasons that transverse jets have more efficient entrainment properties than free or co-flowing jets, at least in the near field (Smith and Mungal, 1998; Shan and Dimotakis, 2006). The formation of the CVP has been explained by Kelso *et al.* (1996) as being due to the folding of the jet shear layer's cylindrical vortex sheet, see Fig. 2.3.

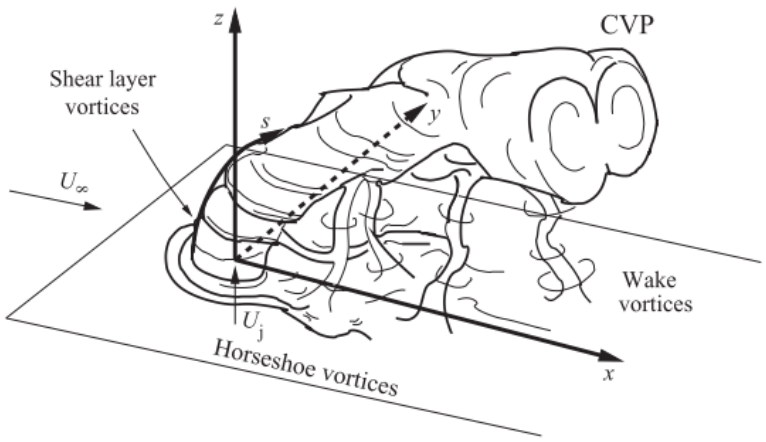

Figure 2.1: Schematic presented in Karagozian (2014) and adapted with permission from Fric and Roshko (1994), copyright 1994 by Cambridge University Press. Shown is a incompressible JICF with a flush wall-mounted jet. Of particular interest are the dominant vortical structures: the counter-rotating vortex pair (CVP), the windward shear layer vortices, the wake vortices, and the horseshoe vortex.

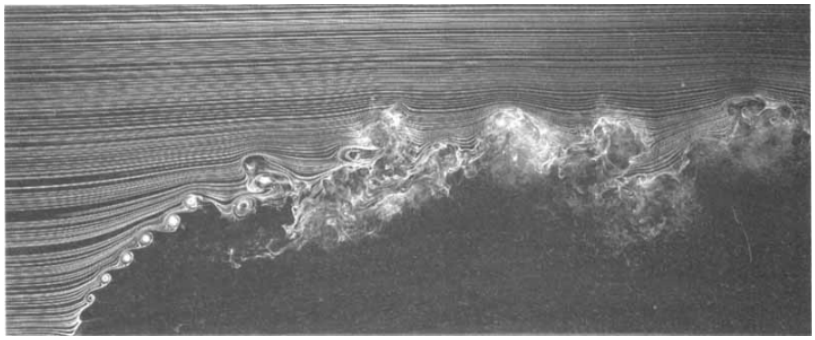

Figure 2.2: Windward jet shear layer vortices visualized using smoke streaklines (Fric and Roshko, 1994).

A metric that is regularly used to assess the JICF is some form of jet trajectory defined on the plane of symmetry. In the incompressible case, this trajectory is often defined as jet center streamline Hasselbrink and Mungal (2001b), the line of maximum concentration (Smith and Mungal, 1998) or as the location of maximum velocity (Kamotani and Greber, 1972). The trajectory is used to measure crossflow penetration and to investigate scalings relevant to said penetration and turbulent mixing.

Using concentration data from acetone PLIF measurements, Smith and Mungal (1998) found that the concentration decay along the centerline trajectory of a JICF for $J = 100 -$

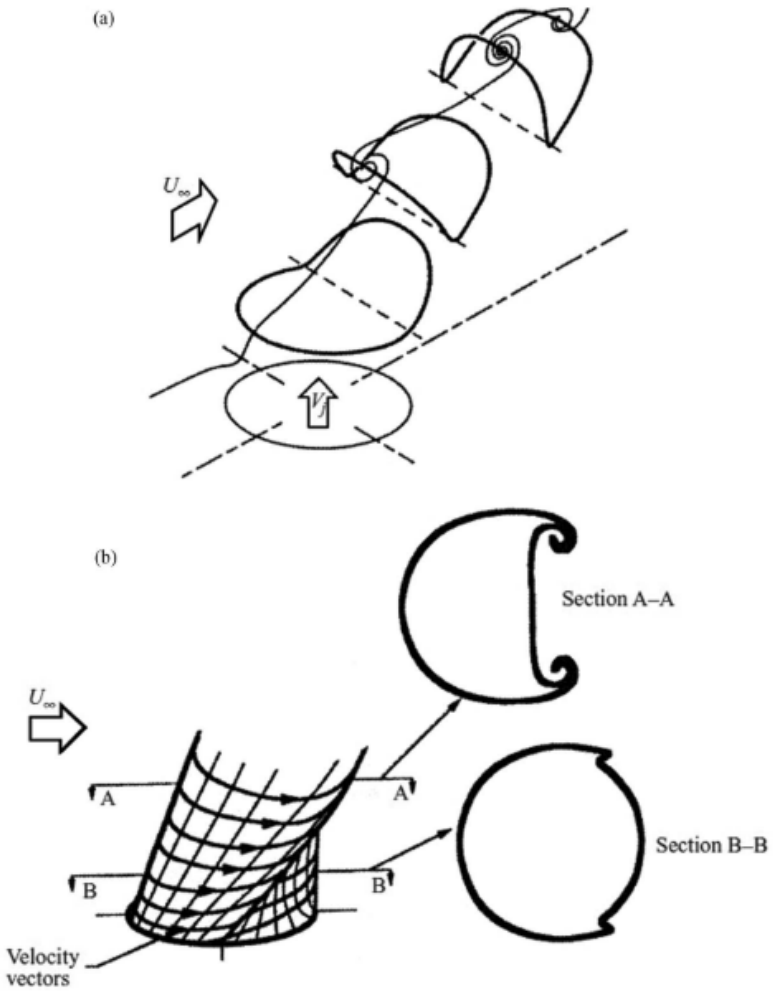

Figure 2.3: Proposed explanation for the CVP formation by Kelso *et al.* (1996): *a* Illustration of vortex ring tilting as they advect with the jet. *b* Associated reorientation of the shear layer vorticity which leads to a folding of the cylindrical vortex sheet and eventually the existence of the CVP.

625 scales inversely with the jet diameter d_j in the vortex interaction/potential core region close to the jet orifice and with $J^{1/2}d_j$ in the near field where the CVP is forming and no self-similarity is possible yet. A scaling of Jd_j did not collapse the concentration decay profiles but aligned the transition points between near and far field, in which the CVP is fully developed and self-similarity is possible. They also concluded that the jet trajectory and other physical dimensions of the jet should scale with $J^{1/2}d_j$.

Hasselbrink and Mungal (2001a) cite the review provided by Margason (1993) in stating that most JICF trajectory data can be collapsed using a power law and a $J^{1/2}d_j$ scaling,

$$\frac{y}{J^{1/2}d_j} = A\left(\frac{x}{J^{1/2}d_j}\right)^B, \tag{2.3}$$

where A and B are fitting parameters. This power-law trajectory had also been derived previously in an analytic fashion by Broadwell and Breidenthal (1984). They considered a characteristic length scale $\mathcal{L} \sim J^{1/2}d_j$ and a self-similar flow with a CVP in the far fiel, yielding $B = 1/3$. Hasselbrink and Mungal (2001a) go on to perform their own self-similarity analysis using a control-volume approach, addressing experimental data that deviates from the power-law in Eq. (2.3). They arrive at a set of equations, one for a jet-like near field region and one for a wake-like far field region, with exponents 1/2 and 1/3, respectively, and multipliers A that depend on the entrainment coefficients of these regions. This again implies that the rate of turning of the jet is directly related to the rate of entrainment of crossflow fluid, i.e. the momentum exchange between jet and crossflow. Hasselbrink and Mungal (2001a) extend their scaling results to provide laws for near and far field centerline velocity components and centerline concentration decay. They also show that the scaling laws they developed should strictly only hold for the case of $J >> 1$.

Muppidi and Mahesh (2005) used DNS simulations of incompressible JICF to investigate the impact of boundary layer thickness on the jet trajectory, varying J from 1.52-5.7 and the boundary layer thickness, $\delta_{80\%}$, from $0.44d_j$ to $6.4d_j$. No meaningful collapse is achieved with either the $J^{1/2}d_j$ or the Jd_j scaling. Considering the evolution of the JICF as a result of the competing inertia between jet and crossflow, they then propose a scaling law based on momentum balance. The key assumptions in their scaling is that the pressure gradient in the crossflow competes with the vertical jet momentum, that this pressure gradient scales with the crossflow momentum flux, and that the jet starts to turn appreciably into the crossflow once the integrated effects of the pressure gradient become comparable to the jet momentum. These assumptions yield the following momentum balance,

$$\rho_{cf}d_j \int_0^h u_{cf}^2 dy = C\rho_j \int_A u_j^2 dA, \tag{2.4}$$

where h is an unknown vertical distance from the wall and C_m is a proportionality constant. Making several further simplifying assumptions, Muppidi and Mahesh (2005) arrive at an analytic expression for a characteristic height, h, at which the jet turns significantly into the crossflow, depending on whether that happens inside or outside the boundary layer. Scaling the x-coordinate with $J^{1/2}d_j$ and the y-coordinate with $\left(J^{1/2}d_j\right)\left(h/d_j\right)^{0.15}$, where 0.15 is an empirically determined constant from considerations regarding the power-law trajectory, they achieve significantly improved collapse of their trajectory measurements.

More recently Gevorkyan *et al.* (2016) investigated an incompressible JICF using acetone PLIF concentration data over a range of $2 \leq J \leq 41$ and jet to crossflow density ratios of 0.35 to 1. Their particular interest were the influence of absolute and convective instability regimes on mixing, as well as the influence of flush mounting versus a raised jet orifice and shaped nozzle versus straight pipe on mixing. For their particular data, a Jd_j scaling collapses the measured jet trajectories from flush mounted jets best. However, they concede that neither $J^{1/2}d_j$ nor Jd_j work particularly well. Compared to some previously mentioned studies their J values are rather low which might be part of the reported scaling results.

Furthermore, the flush mounted jets' maximum mean concentration decay trends seem to scale best with $J^{1/2}d_j$. The decay itself exhibited a range of power-law dependencies from $s^{-1.3}$ and larger to $s^{-2/3}$. The former for higher J in the near field and competitively unstable conditions, the latter for higher J in the far field and lower J, where s is the coordinate along the jet trajectory. The cases with absolutely unstable shear layers being closer to s^{-1}. Similar power-law dependencies had been observed by other researchers, see Smith and Mungal (1998). Gevorkyan *et al.* (2016) emphasize that such measurements on the symmetry plane of the JICF might miss mixing processes going on in the cores of the CVP.

Gevorkyan *et al.* (2016) also investigate the unmixedness and probability density function (PDF) metrics of center plane and cross-sectional measurements to assess mixing

trends. Some of the key conclusions being that there is a strong connection between jet shear layer instabilities and entrainment and mixing, i.e. strong correspondence between center plane and cross-sectional measurements. And that enhanced shear layer instability in the near field of the jet should lead to increased mixing in the parameter space of diffusion limited JICF cases. Finally, they note that different conclusions could be drawn regarding mixing efficiency depending on what metric is being used. Using the actual value of unmixedness, their results show that jets with an absolutely unstable shear layer at lower J achieved greater local mixing, in agreement with increased interface growth due to enhanced hydrodynamic instabilities, i.e. vortex roll-up.

Efforts to analytically model the behavior of an incompressible jet in crossflow have been decently successful by mainly considering the evolution of the CVP. A two-dimensional model that has decent success in predicting vortex trajectory, vortex half-spacing and circulation has been developed by Karagozian (1986). The model accounts for near and far field contributions of vorticity generated by the crossflow and the jet impulse and considers viscous effects. Both for the vortex pair trajectory and half-spacing the model yields power-law dependencies with an exponent close to 1/3, similar to what has been observed and calculated in other studies. Several important insights are provided by this model. One is that the vortex pair separation appears to be a two-dimensional viscous process in the far field, with three-dimensional effects being more important closer to the jet orifice. A second one is that vorticity generated by the jet-crossflow interaction dominates the near field while vorticity generated by the jet impulse itself dominates the far field, i.e. after the jet has started turning significantly into the crossflow.

For the interested reader, more extensive reviews on JICF research are also provided by Karagozian (2014) and Mahesh (2013).

2.1.2 Compressible Flow Conditions

An extension of the previously described incompressible JICF is the jet in a supersonic crossflow (JISCF). Predominantly, this involves the injection of underexpanded, sonic jets into a crossflow that is moving at velocities above the test setup's speed of sound, see Fig. 2.4. In that case, the momentum flux ratio can also be written as,

$$J = \frac{\left(\rho^* \bar{u}^{*2}\right)_j}{\left(\rho \bar{u}^2\right)_\infty} = \frac{\left(\gamma p^*\right)_j}{\left(\gamma p M^2\right)_\infty}, \tag{2.5}$$

The JISCF is of particular interest for engineering applications such as the supersonic combustion ramjet (scramjet), a propulsion system developed to enable hypersonic flight. A continuing issue here is to achieve the maximum rate of mixing within a short time frame and without introducing significant flow obstructions (Smart, 2007). A review of the specific engineering challenges for fuel injection in high-speed propulsion is given by Lee, Lin, *et al.* (2015). However, the present review and study will focus on the fundamental physics that need to be understood to tackle some of these challenges.

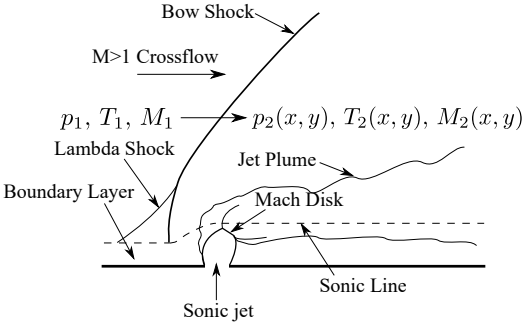

(a) Schematic of the instantaneous JISCF flow field. BL = boundary Layer

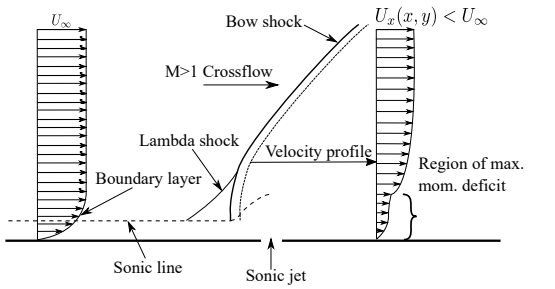

(b) Schematic illustrating the change in flow field velocity profiles due to the presence of the JISCF bow shock.

Figure 2.4: Schematics of JISCF properties on the plane of symmetry.

Incompressible JICF and JISCF share a large amount of dominant features but the high velocities of the latter introduce compressibility effects and associated flow field features such as shocks and expansion fans. Moreover, the very high momentum of the crossflow

makes realizations of $J > 10$ challenging.

The JISCF flowfield is shown schematically in Fig. 2.4. The presence of the jet initially causes the crossflow to turn around it, creating a three-dimensional bow shock ahead of the jet. Close to the wall, this bow shock splits into a lambda shock and causes the boundary layer to separate, creating a recirculation bubble. As shown in Fig. 2.4b, the presence of the bow shock also alters the incoming crossflow velocity profile. The shock and blockage effects by the jet cause a momentum deficit region extending above the boundary layer of the undisturbed crossflow.

A second recirculation region exists right in front of the jet and is part of the horseshoe vortex wrapping around the jet column. Large scale vortical structures, such as Kelvin-Helmholtz instabilities in the windward shear layer and the CVP, initiate entrainment of crossflow fluid into the jet. This is further illustrated in schematics by Ben-Yakar *et al.* (2006) and Gamba and Mungal (2015), see Fig. 2.5.

Underexpanded jet fluid accelerates through a Prandtl-Meyer fan into the crossflow and starts turning due to the entrainment of streamwise directed crossflow momentum, see Fig. 2.4a and Fig. 2.5a. The jet fluid can reach local Mach numbers in excess of the crossflow Mach number and creates a so-called barrel shock which terminates this high velocity jet region. A poignant feature of the barrel shock is the Mach disk, a flat shock that is situated in between two triple points caused by the barrel shock and the subsequent flow evolution. Contrary to the illustration in Fig. 2.5a, most of the jet fluid does not cross through the Mach disk but rather the barrel shock itself as it turns into the crossflow (VanLerberghe *et al.*, 2000).

Crossflow fluid flowing around the jet column close to the wall impinges on itself on the leeward side and accelerates rapidly creating a third recirculation region and a complex reattachment zone (Sun and Hu, 2018a). Further downstream and away from the wall the jet forms the familiar CVP, see Fig. 2.5b. Similar to the incompressible JICF flow field, wake vortices originating from the horseshoe vortex have been observed in the farfield

(Gruber, Nejad, Chen, *et al.*, 2000).

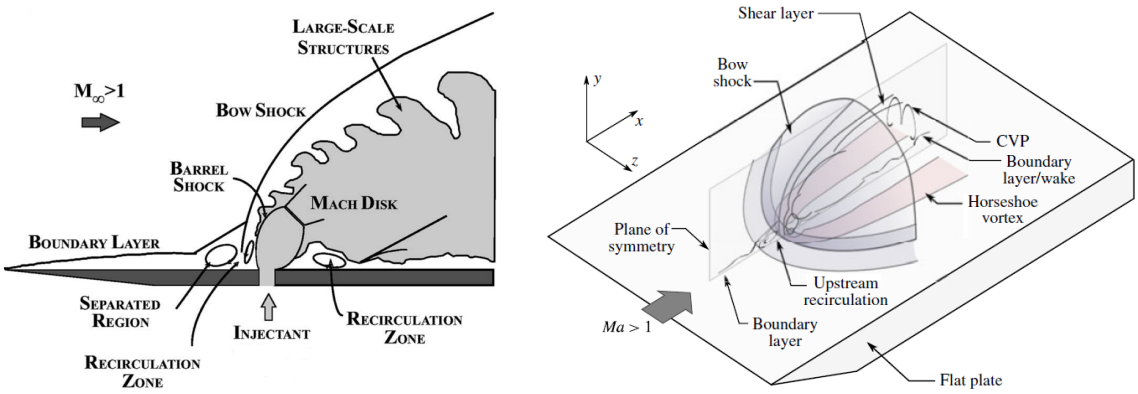

(a) Two-dimensional schematic of the JISCF flow field along the plane of symmetry from Ben-Yakar *et al.* (2006).

(b) Three-dimensional schematic of the JISCF flow field from Gamba and Mungal (2015).

Figure 2.5: Flow field schematics for a flush mounted, single JISCF from other authors.

The height of the Mach disk has been used as a relevant flow length scale in the past. Billig and Schetz (1994) report an empirical power-law for the Mach disk height depending on the jet to crossflow pressure ratio and the jet Mach number, whereas Cohen *et al.* (1971) present an empirical relationship involving J and the angle at which the jets is injected θ_j,

$$\frac{y_{MD}}{d_j} = \frac{1.05}{1 + cos(\theta_j)} \left[\frac{(\rho u^2)_j}{(\rho u^2)_\infty} \right]^{0.5}. \tag{2.6}$$

Another length scale which is on the same order of magnitude as y_{MD} has been defined by Spaid and Zukoski (1968),

$$h = \frac{\dot{m}_j a_j^*}{(1+\beta)(p_p - p_1) + (1+\beta-\alpha)\, p_1}, \tag{2.7}$$

where p_1 is the crossflow pressure, p_p is the plateau pressure in the recirculation region upstream of the jet, α relates to the average base pressure with a range of $0.4 \leq \alpha \leq 1.2$ and,

$$\beta = \beta' \frac{\gamma M_2^2}{1 + \frac{\gamma-1}{2} M_2^2}, \tag{2.8}$$

where M_2 is the Mach number after the bow shock. The plateau pressure is roughly correlated as $p_p/p_1 = 1 + M_1/2$. Spaid and Zukoski (1968) claim that this length scale can be used in simplified estimates of the eddy viscosity in, e.g., the Smagorinsky model,

$$\mu_t = \bar{\rho} C_s L_G^2 \left| S_{ij} \right|, \tag{2.9}$$

where L_G is a locally relevant integral length scale, C_s is a modeling constant, and S_{ij} is the strain rate tensor.

Due to compressibility, the pressure, temperature, and velocity fields are stronger coupled in the case of a JISCF than an incompressible JICF, i.e. viscous dissipation and pressure-dilatation correlation provide additional pathways for energy exchange between mean flow, turbulent fluctuating velocity modes, and internal energy modes (Lele, 1994; Kovasznay, 1953). A conceptual connection between these processes in a compressible flow is shown in Fig. 2.6. At sufficiently high turbulent Mach numbers these processes can influence the turbulent mixing process due to energy moving between internal energy modes instead of equilibrating immediately with the translational mode (Donzis and Maqui, 2016).

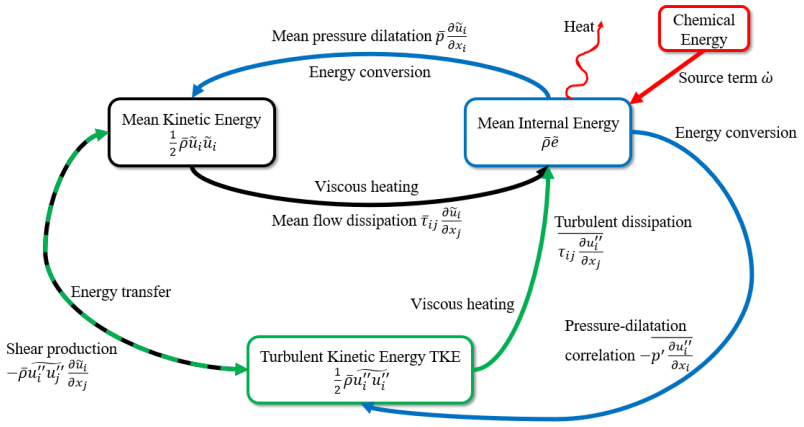

Figure 2.6: Conceptual energy paths in a reacting, compressible turbulent flow. Adapted from Lele (1994).

A prominent example of the influence of compressibility relevant to JISCF has been

reported experimentally for two-dimensional shear layers by Papamoschou and Roshko (1988). Here, the increase of the velocity difference between two streams to transonic or supersonic levels seems to suppress the growth of instabilities. A measure of the suppression of instability growth is related to the convective Mach number, defined as,

$$M_{c,f} = \frac{\bar{u}_1 - U_c}{a_f} \tag{2.10}$$

$$M_{c,s} = \frac{U_c - \bar{u}_2}{a_s}, \tag{2.11}$$

$$\tag{2.12}$$

relative to the faster (f) and slower (s) stream, respectively. $\bar{u}$ is the mean velocity of the respective stream, a the speed of sound, and U_c is the velocity of the advected waves and structures in the shear layer. The larger M_c, the more the growth of the two-dimensional shear layer is suppressed. It can be seen that the properties of the gases used in the two streams enter the problem through the speed of sound as $a = \sqrt{\gamma RT}$.

Karimi and Girimaji (2016) investigated the underlying reason for the suppression using DNS. They come to the conclusion that, in the compressible cases, a dilatational interface forms. Contrary to the incompressible case, this dilatational interface is an oscillatory region, preventing positive feedback between a growing vortex and the shear layer pressure field.

Since JISCF produce a highly three-dimensional flow and vorticity field, they might not be subject to as strong of a suppression of instability growth as two-dimensional shear layers. However, Papamoschou (1992) estimated analytically that for elevated convective Mach numbers three-dimensional disturbances will reduce the growth rate of instabilities even further. An exception being a limited window of convective Mach numbers around $M_c = 1$ and angles at which the disturbance is propagating. Nonetheless, it is possible that vorticity generated along axis other than the one associated with a two-dimensional shear layer might be less susceptible to this suppression mechanism.

The entrainment and mixing characteristics of a JISCF are often investigated in a manner similar to that of an incompressible JICF. However, especially the strongly variable density throughout the flow field make conclusions more difficult and comparisons between experiments challening. Early experimental work has concentrated on basic understanding of the JISCF structure using schlieren and wall pressure measurements (Spaid and Zukoski, 1968; Santiago and Dutton, 1997). Average penetration of the jet is the most common result reported in JISCF studies (Spaid and Zukoski, 1968; Gruber, Nejad, Chen, *et al.*, 2000; Portz and Segal, 2006; Lin *et al.*, 2010; Mahesh, 2013; Gamba and Mungal, 2015).

Zukoski and Spaid (1964) reported a single, analytically estimated scaling factor to collapse characteristic jet penetration heights of sonic jets. Measurements were conducted using a Schlieren diagnostic over two Mach numbers, laminar and turbulent boundary layer, nitrogen and argon as injectants, and pressure ratios from ~ 3 to ~ 17. They consider the force balance between the crossflow and the jet in the streamwise direction, treating the jet as a solid body with the shape of a quarter sphere, calculating the pressure forces on the jet based on modified Newtonian flow, and assuming that the jet expands purely isentropically. This results in,

$$\frac{h_z}{d_j C_d^{1/2}} = \left(\left(\frac{1}{M_\infty} \right) \left(\frac{p_{0,j}}{p_\infty} \frac{\gamma_j}{\gamma_\infty} \frac{2}{C_p^*} \right)^{1/2} \cdot \left\{ \frac{2}{\gamma_j - 1} \left(\frac{2}{\gamma_j + 1} \right)^{(\gamma_j+1)/(\gamma_j-1)} \left[1 - \left(\frac{p_\infty}{p_{0,j}} \right)^{(\gamma_J-1)/\gamma_j} \right] \right\}^{1/4} \right). \quad (2.13)$$

However, the approach does not account for the existence of a boundary layer and state changes across the bow shock or the jet shocks. They also note that there is probably no correspondence between any real measured flow feature and the characteristic penetration height they derived, merely a proportionality. For their data sets, the scaling works decently and is used in the comparison of wall-normal concentration profiles as well.

Table 2.1: Sample of studies reporting JISCF trajectories.

Trajectory data	Exp. or sim.	Parameters	Definition	Fit
Rothstein and Wantuck (1992)	Experiment	$M_\infty = 1.5$, $J = 5.9 - 38.6$	max. intensity of averaged OH-PLIF signal	$A = 2.173$, $C = 0.276$, $B = 0.281$
Lin *et al.* (2010)	Experiment	$M_\infty = 2$, $J = 0.5 - 6$, $d_j =$ 1.6, ,4.8, 7.9 mm, injection angle $30°$ & $90°$	$\chi = 0.01 \approx Y$ of ethylene from Raman scattering	$A = 1.16$, $C = 0.72$, $B = 0.32$
Sun and Hu (2018b)	Simulation	$M_\infty = 2.7$, $J = 1.85,\ 5.5$	$Y = 0.02$ of jet fluid	$A = 2.933$, $C = 0.256$, $B = 0.161$
McClinton (1974)	Experiment	$M_\infty = 4.05$, $J = 1$, $d_j =$ 0.5-1.2 mm	$\chi = 0.005$ of hydrogen via sampling probe	$A = 4.2$, $C = 0.3$, $B = 0.143$
Gruber, Nejad, Chen, *et al.* (2000)	Experiment	$M_\infty = 2$, $J = 2.9$, injector shape round and elliptic, injectant air and helium	10% intensity from Mie-scattering	$A = 1.2$, $C = 0.656$, $B = 0.344$

Rothstein and Wantuck (1992) was one of the first studies to report JISCF trajectories in the form of a power-law similar to that of the incompressible JICF, see Eq. (2.3). In doing so, they used a Jd_j scaling instead of the $J^{1/2}d_j$ derived for the incompressible case,

$$\frac{y}{d_j} = AJ^C \left(\frac{x}{d_j}\right)^B. \tag{2.14}$$

On the other hand, McDaniel and Graves (1988) proposed a logarithmic scaling of the form $y/d_j = A\,J\,ln[B(x/d_j + C)]]$, where A, B and C are fitting parameters, and x and y are the streamwise and wall-normal coordinates, respectively. Both the power-law and the logarithmic scaling are used on a regular basis in JISCF research, e.g. see Karagozian (1986), Lin *et al.* (2010), and Pizzaia and Rossmann (2018).

Examples for the fitting parameters of Eq. (2.14) reported in the literature are shown in Tab. 2.1. There is a rather large scatter in the existing data and a wide variety of methods are used to define and identify the JISCF trajectory. Moreover, contrary to the incompressible case, the trajectory is usually defined as a relatively low concentration iso-contour. This situates the locus of the trajectories further away from variable density (compressibility) effects. It also makes the trajectories a measure of not only the penetration into the cross-fllow but also the mixing characteristics of the flow field. Part of the large scatter can be attributed to the widely varied approach in defining the jet trajectory.

Portz and Segal (2006) attempted to address the large scatter of mean jet trajectory data in JISCF through a literature review and a modified power-law that includes the effects of not only the momentum flux ratio, J, but also of the boundary layer thickness, δ, the freestream Mach number, M_∞, and the jet to freestream molecular weight ratio, MW_j/MW_∞, see Eq. (2.15). While they report an improved collapse of jet trajectories, all of their parameters are curve-fitted as power-laws and multiplied to a trajectory law similar to Eq. (2.14). The parameters are also empirical functions of the freestream Mach number, see Tab. 2.2. They introduce the concept of an effective momentum flux ratio computed after a normal shock for the given crossflow Mach number (M), see Eq. (2.16). As the jet

is preceded by a bow shock, this effective J_2 is more representative of the flow conditions that the jet first encounters upon injection than a global J. In the equation, γ is the specific heat ratio, p is the static pressure, an asterisk denotes sonic conditions, and subscripts 1 and 2 denote quantities computed before and after a normal shock, respectively.

Table 2.2: Coefficients for Eq. (2.15).

A	B	C
$1.049M_\infty - 0.192$	$-0.8M_\infty + 0.615$	$-2.34/M_\infty$
D	**E**	**F**
$-0.069M_\infty + 0.42$	$-0.067M_\infty + 0.325$	-0.025

$$\frac{y}{d_j} = A(J)^B \left(\frac{x}{d_j} + C\right)^D \left(\frac{\delta}{d_j}\right)^E \left(\frac{MW_j}{MW_\infty}\right)^F, \tag{2.15}$$

$$J_2 = J_1 \frac{(\gamma p M^2)_{\infty,1}}{(\gamma p M^2)_{\infty,2}} = \frac{(\gamma+1)_{\infty,1}\, \rho_j^* u_j^{*2}}{(p\gamma\left[(\gamma-1)M^2+2\right])_\infty, 1} \tag{2.16}$$

Although the empirical power-law in Eq. (2.15) suggests that the molecular weight of the injectant has a small influence on jet penetration, several studies have suggested that the combined effects of molecular weight and specific heat ratio have a significant effect on the instantaneous JISCF mixing processes. As described above for the case of a compressible, two-dimensional shear layer, these two parameters enter the picture through the convective Mach number, where the speed of sound $a = \sqrt{\gamma RT}$ depends on them.

Gruber, Nejad, Chen, *et al.* (1997a) provided theoretical and experimental evidence for the influence of MW and γ on JISCF mixing. By making a point estimate of the convective Mach number in the windward jet shear layer, see Fig. 2.7, they support the notion that a helium jet would mix slower with the crossflow than an air jet, due to the higher velocity difference between jet and crossflow. Experimental evidence is provided from Mie-scattering data using silicone dioxide and ice crystals for a Mach 2 crossflow and

$J \approx 2.9$. A faster collapse of the lateral spread of the 10% jet fluid concentration for the air jet is associated with faster mixing, as is the increased broadening of the windward jet shear layer. A two-dimensional correlation analysis suggests that higher shear layer compressibility (lower injectant molecular weight) leads to more coherent shear layer structures with a more elliptical shape downstream of injection.

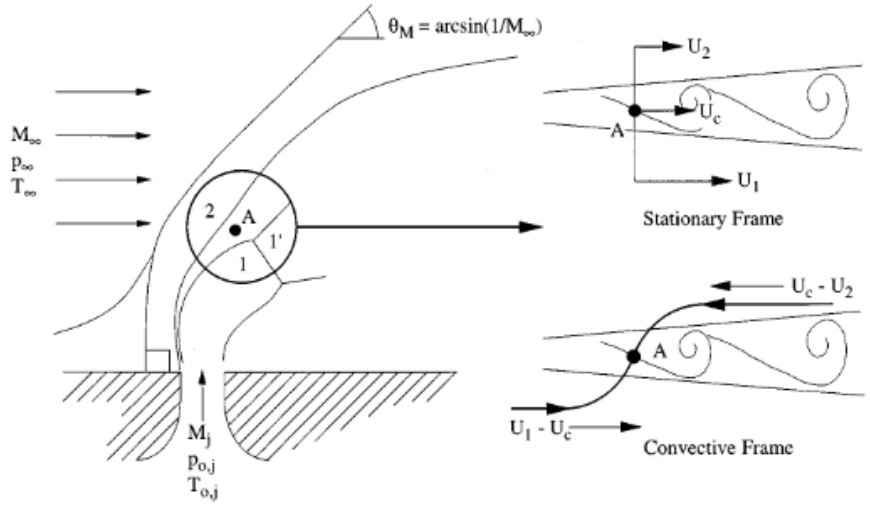

Figure 2.7: Flow filed approximation presented by Gruber, Nejad, Chen, *et al.* (1997a) to make a point estimate of the convective Mach number at point A.

A schlieren system operating at up to 100 MHz has been used experimentally by Ben-Yakar *et al.* (2006) to investigate these compressibility effects further for hydrogen and ethylene jets. Their facility is a shock tube providing a crossflow Mach number of 3.4 and a momentum flux ratio of $J = 1.4$. They observe a faster dissipation of the ethylene structures and deeper, more intermittent penetration of these structures into the crossflow. For an auto-igniting jet they also observe that ethylene provided more distributed regions of OH (indicative of hot combustion products) presence, while the hydrogen jet exhibit only thin flamelets along the instantaneous jet-crossflow interface. They concluded that, instantaneously, the large scale ethylene jet structures penetrate deeper into the crossflow than the hydrogen structures.

Takahashi *et al.* (2010) used acetone PLIF to investigate differences in the structure of

air and helium jets. Their crossflow Mach numbers were 2, 2.5 and 0.9, and the investigated momentum flux ratios are roughly 1.5, 1.7, 1.9, 2.2 and 2.8. They find that the average penetration of the helium jets is slightly higher and attribute this mainly to difference in molecular weight and compressibility effects in the shear layer. Their spatial correlation analysis finds several interesting results: large scale structures appear on the 50% concentration trajectory, irrespective of crossflow Mach number and injectant species. The helium jet produces smaller, more stable elliptical structures that tend to align with the crossflow. The rate of large scale structure production, their inclination angle and their size increased with decreasing shear layer compressibility. They also mention differences in KH and Rayleigh-Taylor instability (RTI) occurrence due to differences in density gradient and acceleration direction between air and helium jet.

Zhang *et al.* (2015) numerically investigate the difference between $J =$ nitrogen and helium jets using a hybrid RANS/LES (Reynolds-averaged Navier-Stokes/Large Eddy Simulation) approach. While they do observe larger instantaneous structures for the nitrogen jet, their results suggest more stable nitrogen shear layer structures and a deeper time averaged penetration of the nitrogen 10% mass fraction contour. The latter two seemingly contradicting the results of previously published experimental studies. The numerical study by Watanabe *et al.* (2012) also comes to the conclusion that there is no effect of the injectant properties on the mean jet trajectory. This indicates possible problems with the numerical models used that should be addressed by further experimental research.

A detailed analysis of jet fluid mixing has been conducted by VanLerberghe *et al.* (2000) using shadowgraphy and acetone planar laser induced fluorescence (PLIF). The PLIF measurements were performed for two conditions with a jet at $J = 1.2$ and 1.7, and a crossflow Mach number of 1.6. The results show the development of structures in the windward shear-layer close to the jet orifice that resemble Kelvin-Helmholtz type roll-ups. Further downstream, large scale structures can still be seen penetrating the crossflow and the topology is likened to that of a planar mixing layer, see Fig. 2.8. Structures rolling

in both counter-clockwise and clockwise directions can be observed, with the dominance of counter-clockwise roll-ups suggesting that, at this boundary, the jet fluid is faster than the crossflow. Mushroom structures are discernible as well, which could indicate jet-like plumes or the growth of a RTI. The ensemble averaged results also show that the majority of the jet fluid flows through windward barrel shock region and some through the Mach disk itself. Very little seems to be flowing through the leeward barrel shock. One of the most important conclusions, based on PDFs of the jet fluid concentration, is that the time-averaged measurements overestimate the actual mixedness of the flowfield. Instantaneously, the boundary between jet and crossflow fluid is much sharper than the average result would suggest. Furthermore, the best instantaneous mixing occurs in the wake of the jet below its centerline.

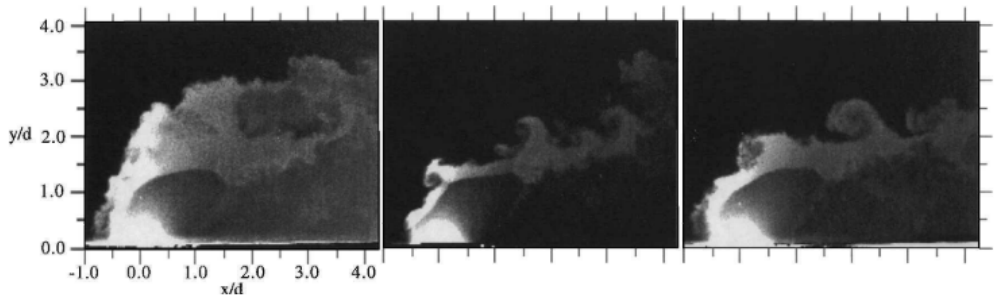

Fig. 4a Representative instantaneous images of the side-view barrel shock region.

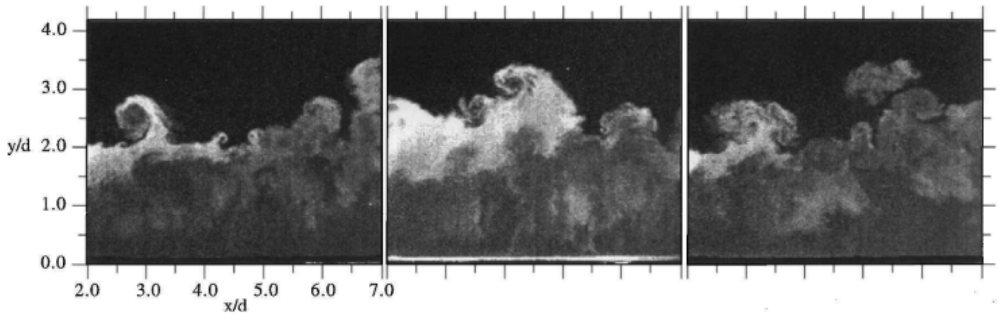

Fig. 4b Representative instantaneous images of the side-view downstream region (x/d = 0.0 is the center of the jet).

Figure 2.8: Instantaneous PLIF images of a JISCF presented by VanLerberghe *et al.* (2000).

RANS models are not particularity accurate in predicting the JISCF flow field numerically. However, useful and more sophisticated results have been obtained using LES sim-

ulations. Kawai and Lele (2010) provide a detailed LES study of the experimental setup presented by Santiago and Dutton (1997) and VanLerberghe *et al.* (2000). Besides identifying the known major vortical structures in the flow field, they emphasize the difference of interaction between jet and laminar or turbulent crossflows. They mention that changes in the boundary layer due to changes in the state of the crossflow could not be resolved with a hybrid RANS/LES approach. Turbulent structures in the boundary layer due to a turbulent crossflow seem to enhance the instability of the windward shear layer and enhances entrainment and mixing.

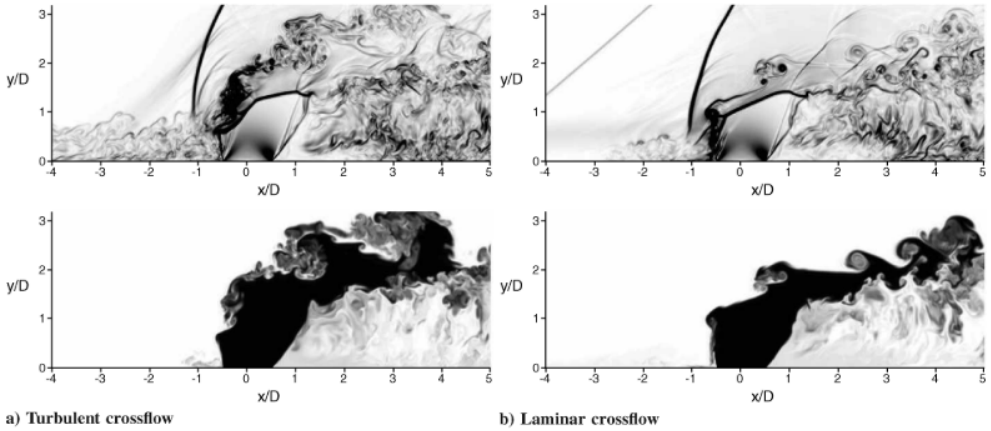

Figure 2.9: Influence of turbulent and laminar crossflow on the JISCF evolution, exemplified by the instantaneous density gradient magnitude on the top and jet fluid concentration on the bottom. Presented by Kawai and Lele (2010).

More results regarding jet penetration and mixing have been reported recently by Pizzaia and Rossmann (2018). Measuring jet fluid concentration via Mie-scattering off of condensed ethanol droplets, they investigate trends in JISCF mixing due to changes in the boundary layer to jet diameter ratio. They use the empirical observation by Papamoschou and Hubbard (1993) that the characteristic penetration of a JISCF seems to scale with the momentum flux ratio according to $h \propto J^{1/3}$, thereby achieving a reasonable collapse of their trajectory data for a given boundary layer thickness to jet diameter ratio δ/d_j. A clear penetration enhancement with increasing boundary layer thickness is reported, as well as an empirical relationship for their observed trends. They also provide detailed analysis of

the mixing processes from cross-sectional images of the jet. For quantification, they compute the effective intensity of segregation and PDFs of the jet fluid concentration. They found that, in general, a thicker boundary layer leads to stronger mixing with the boundary layer vorticity coupling to the vortical structures of the jet.

One of the most detailed experimental velocity data sets for a JISCF has been obtained for the same experimental conditions of VanLerberghe *et al.* (2000) with Laser Doppler Velocimetry (LDV) by Santiago and Dutton (1997). They measured at 4000 discrete locations with measurement volumes on the order of $(0.17\ \mathrm{mm})^3$ to $(0.5\ \mathrm{mm})^3$, seeding the flow with $0.8\ \mu\mathrm{m}$ silicon oil droplets. They identified the dominant vortex structures discussed earlier in their data. The velocity measurements show that jet fluid passing the barrel shock and Mach disk has significantly reduced momentum and turns quickly into the crossflow. Regions of high turbulent kinetic energy (TKE) exist where the bow shock interacts with the boundary layer and in the shear layer of the jet. After turning into the crossflow, regions of high TKE do not penetrate significantly above the transverse position of the jet boundary. Calculating the time averaged vorticity the CVP is also clearly identified by them. They concluded that after about three jet diameters, the jet plume mostly grows in the wall-normal direction, due to the existence of said CVP and the constraints put on it by the bottom wall. They also hypothesized the existence of highly-correlated large scale structures in the windward shear layer and the rapid associated mixing could potentially be exploited for reacting flow fields.

Detailed Particle Image Velocimetry (PIV) results are limited in the literature due to it being a rather challenging diagnostic for a JISCF. Seeding material that can follow the high frequency content of a supersonic flowfield, which can easily approach hundreds of kilohertz, is required (Ragni *et al.*, 2011). In inert JISCF flowfields, solid particles, such as titanium dioxide and silicon dioxide, silicon oil or fog fluid have been used to seed the flow and vector resolutions in the range of $(0.5\ \mathrm{mm})^2$ - $(2.4\ \mathrm{mm})^2$ have been achieved (Ali and Alvi, 2015; Ragni *et al.*, 2011). Due to the high flow and shear velocities involved, very

small laser pulse spacing is necessary, on the order of hundreds of nanoseconds (Koike *et al.*, 2007).

Additionally, compressibility features, such as shocks, represent rapid changes in density and, thus, rapid changes in the index of refraction which can lead to aero-optical effects affecting image acquisition. These effect have been discussed by Elsinga *et al.* (2005a). Two forms of related errors are identified, position error and velocity error. Image blur due to changes in the index refraction mainly affects the signal-to-noise ratio and can be counteracted to some degree by increasing the f-number of the camera lens used for image acquisition. Using experimental data from PIV and background oriented Schlieren (BOS) as well as simulations show that the errors are small for compressible shear layers. For a velocity change of 520 to -50 $\mathrm{m/s}$ a maximum absolute velocity error of 5.8 $\mathrm{m/s}$ is measured and the aero-optical effects lead to an over-estimation of the velocities in the shear layer. On the other hand, for the velocity change through an expansion fan from 232-335 $\mathrm{m/s}$ the maximum absolute error is larger with 6.5 $\mathrm{m/s}$ and the uncorrected measurement is both under- and over-estimating the true velocity at different stations throughout the expansion. A correction based on BOS measurements is proposed.

At shocks, the methods used in the previous study no longer hold and velocity errors up to 10% relative to the real values have to be expected, as measured by Elsinga *et al.* (2005b). For planar shocks, this study also found that increasing interrogation window size, decreasing $f/\#$ and a positive viewing angle relative to the shock decrease errors due to aero-optical distortion. In all cases, the error due to additional displacement dominated over errors due to particle blur.

Koike *et al.* (2007) presented a correction method for supersonic PIV measurements based on Stokes drag law and applied it to a JISCF flow field. For incompressible flow fields particles usually have an easier time actually following the instantaneous streamlines, while in supersonic flows a myriad of reasons exist for the particles to significantly lag behind changes in the flow field, such as very large velocity changes, low densities and

high frequency oscillations. The correction considers the equation,

$$\vec{u}_f = \vec{u}_p + \alpha\vec{\beta}_p, \tag{2.17}$$

where $\vec{u}_f$ is the real flow velocity, $\vec{u}_p$ is the PIV measured particle velocity, and α and $\vec{\beta}_p$ are parameters that depend on the particle drag (Stokes drag in the viscous limit) and the advective effects of the measured particle velocity, respectively. It is necessary to make an estimate of α to perform the correction. This estimate requires the relative Reynolds number, the relative Mach number and the Knudsen number to be low. Moreover, the solution of the equation describing α yields several solutions and the authors have to use a numerical validation to choose the correct one, i.e. in their case the solution they label as the "weak correction".

The experimental validation by Koike *et al.* (2007) is done for a Mach 1.8 crossflow and a $J = 1.8$ jet. They find that near the flow shock waves some of the assumptions made for the correction might be violated. Moreover, the flow field has to be smooth enough to find a solution for α. While the corrected velocity fields appear slightly more noisy, the velocity contours are grouped closer together at presumable shock positions, appearing to be more well-defined. The maximum velocity correction occurs in the shock regions very close to the jet orifice. It is much smaller in all other regions, see Fig. 2.10. An interesting conclusion is that their corrected, time averaged jet streamlines penetrate less into the crossflow and seem to be more comparable with maximum concentration trajectories from acetone PLIF. It is unclear as to how this correction relates to aero-optical effects, if it does at all.

Attempts to circumvent the tracer particle issues have been made in supersonic flows by using molecular tagging techniques. For example Donohue and McDaniel Jr. (1996) developed and deployed an iodine PLIF technique to obtain time averaged pressure, temperature and velocity fields. for a rearward facing step. Hollo *et al.* (1994) applied the

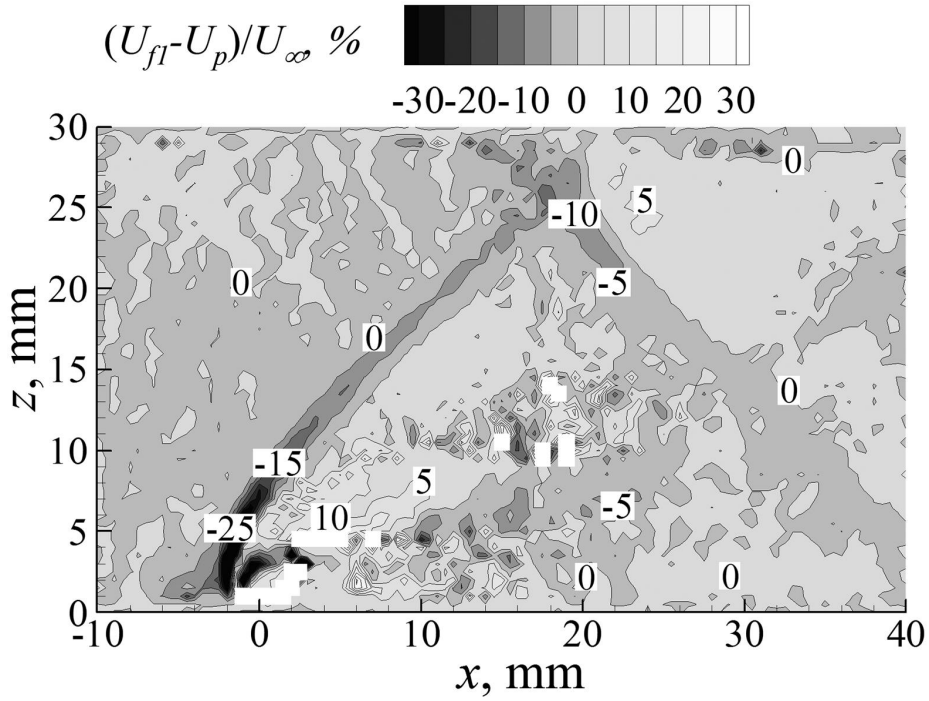

Figure 2.10: Difference between the original PIV velocity field and the field corrected with the weak α-solution, normalized by the undisturbed crossflow velocity. Presented by VanLerberghe *et al.* (2000).

same technique to a JISCF flow field obtaining mean velocity and concentration fields. Another technique developed by Hsu *et al.* (2009) uses vibrationally excited NO molecules for velocimetry measurements on underexpanded jets. However, the molecular tagging techniques come with their own difficulties and have rarely been applied to complex flow fields. The measurements require high precision equipment and are sometimes challenging to extend from line to planar measurements. Substances like iodine can be corrosive to test equipment, and effects such as line shift/broadening, molecular quenching and reflections from test section surfaces can present a challenge in obtaining reliable results. Moreover, the spatial resolutions are often lower than for PIV and in some cases only time-averaged data can be obtained.

Several analytical models exist for the JISCF. One being the JETPEN model, developed in Schetz and Billig (1966) and Billig and Schetz (1994). The model is based on a differential force balance considering the jet trajectory as segments of a cylindrical solid body. The

position of the Mach disk plays an important role in this model as do the drag coefficient on the cylindrial segments and the effective back pressure on the jet, all of which are modeled using Newtonian flow or empirical relationships. Entrainment relationships are adapted from incompressible JICF results. Finally, momentum, species and energy conservation equations have to be solved to obtain jet trajectory, jet fluid concentration and jet plume growth. From the study of Lin *et al.* (2010) the agreement of the JETPEN predictions with experimental data is acceptable in the far field of the jet for $J = 0.5 - 1$. However, the model completely neglects the existence of the CVP, the mixing interaction of the jet with the boundary layer and results deteriorate for higher J values

Another model was developed by Heister and Karagozian (1990). It is an extension of the CVP based model of Karagozian (1986) to a compressible flow field and perfectly expanded or slightly underexpanded jets, i.e. no or only weak jet shock structures. This model is purely analytical and uses no empirical relationships. However, it requires the numerical solution of the flow field around a compressible vortex pair in crossflow. The model agrees reasonably well with a collection of experimental results but differences grow with $J > 1$.

2.1.3 Staged Jets

McDaniel and Graves (1988) mention that in previous studies the "the optimum fuel-injection configuration (i.e., the configuration giving auto-ignition and flame holding at the lowest total temperature) uses in-line, or staged, fuel-injection orifices located behind a rearward-facing step". A schematic of the staged JISCF flow field is shown in Fig. 2.11. Thus, they attempt to provide a quantitative measure of the penetration/mixing improvements possible with this kind of setup. They vary J from 0.35 to 1 in a crossflow with $M = 2$ and the two jets have a separation distance of $6.35d_j$. Iodine PLIF is used to visualize the jet fluid distribution. In their work, significantly enhanced penetration of the flow is achieved for the second jet while the lateral spread is influenced only slightly.

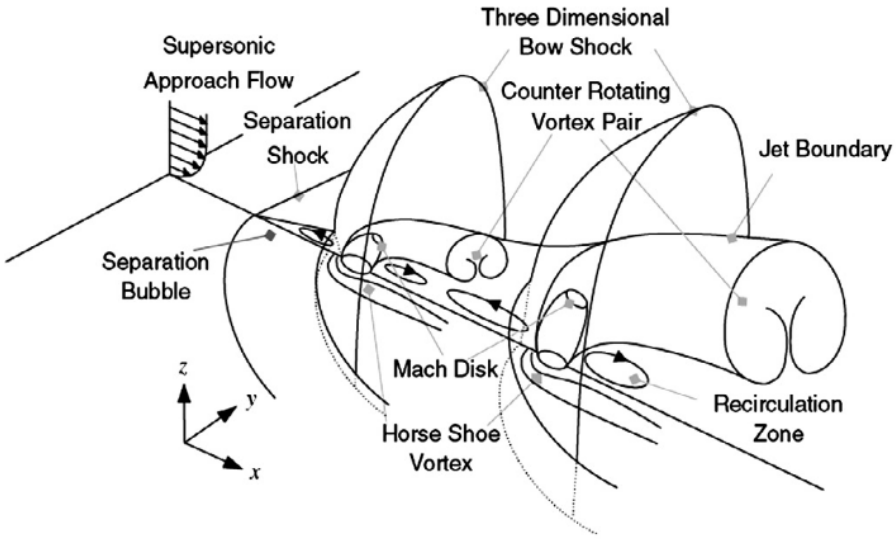

Figure 2.11: Schematic of the mean flow field around two staged injectors in a supersonic crossflow, from Lee (2006a).

Hollo *et al.* (1994) investigate the flow field of flush-mounted staged injectors without any steps on the test section walls also using iodine PLIF for concentration and velocity measurements. Their jets are $6.16d_j$ apart and exhaust into a Mach 2 crossflow. Their results clearly show the enhanced penetration of the second jet due to the blockage of the crossflow momentum by the first jet. The effects of the CVP downstream of the second jet appear to be weaker than after the first one. The data shows that the far field rate of mixing seems to be largely independent of the existence of the second jet, while the near field mixing rate can be significantly enhanced due to it. The near field is dominated by large scale mixing due to vortical structures while the far field mixing is largely diffusive. Thus, in the far field the mixing process becomes independent of the details of the injection strategy. Comparing their air injection results with hydrogen data published by Rogers (1971), they concluded that mixing rates in the far field are independent of both crossflow Mach number and injectant molecular weight. The velocity data of Hollo *et al.* (1994) shows an extended low velocity region between the first and the second jet which is potentially subsonic and would allow for both jets to significantly influence mixing in this region.

Lee (2006a) used RANS simulations to investigate a wider range of staged injector

spacings and multiple momentum flux ratios. While RANS has been shown to not provide high fidelity results for JISCF, the trends identified are still useful. The boundary layer thickness is about $0.3d_j$ for the staged jets. Jet spacings considered are 1.41, 2.82, 4.23, 5.64, 7.05, and $9.87d_j$. Momentum flux ratios investigated are $J = 1$ and 2. A single jet with the same total mass flow rate as the two staged jets is considered as a baseline. The simulations show that for the smallest spacings, the bow shock of the two jets merge while at the largest spacings the two jets each behave more and more like the single jet. All penetration and mixing metrics computed show that the staged jets enhance both penetration and mixing in the near field while trends converge again in the far field. For large enough spacings, almost no difference between the single and staged jet Mach disk height is detectable. The second jet does not profit of the blockage and low pressure effects caused by the first jet anymore. The trends also suggest that for a given momentum flux ratio there exists an optimal spacing between the jets that maximizes penetration, mixing rates and mixing efficiency with the crossflow. Larger and smaller spacings than the optimal one will lead to reductions in those two metrics. Stagnation pressure losses are generally higher for staged injector setups and the smallest spacings between the jets.

The trends observed by Lee (2006a) were largely confirmed by another RANS study performed by Landsberg *et al.* (2016). Even though they used an upstream injector with half the diameter of the downstream jet orifice, the second jet benefited clearly from the flow obstruction effects of the first jet. The study used seven staged jet configurations with spacings from 2-10d_j and crossflow Mach numbers ranging from 2.6-5.3. The single jet baseline has a larger diameter to keep the total mass flow rate constant. The momentum flux ratio was kept constant at $J = 1$ and no clear optimum jet spacing was found for varying crossflow Mach number. Nonetheless, performance enhancements in terms of mixing rates and pressure losses are reported for jet spacings on the order of 4-6 times the single jet diameter.

2.2 Ignition and Burning in High-Speed Flows

Introducing chemical reactions into a compressible, turbulent flow field adds another layer of complexity. In contrast to passive scalars, chemically reacting fluids add heat release, density changes, and pressure waves which alter the surrounding flow while at the same time depending on the state of said flow Dimotakis (2005). However, recent DNS studies of two-dimensional mixing layers have found that the largest changes in the compressible reacting flow field, compared to the incompressible case, occur due to the compressibility itself, not due to the introduction of chemical reactions. The particular case studied by O'Brien *et al.* (2014) coming to this conclusion was a highly compressible, reactive hydrogen-air mixing layer.

While scramjets are one of the most relevant engineering applications for JISCF, burning at supersonic flow velocities is challenging. The speed of laminar deflagration waves for hydrogen is on the order of 1-10 $\mathrm{m/s}$ (one of the fastest burning substances we know of), while supersonic flow speeds in a scramjet are $> 600\ \mathrm{m/s}$. Even for turbulent cases the enhancement is only on the order 10-30 times the laminar flame speed (Kobayashi, Tamura, *et al.*, 1996), still well below the flow velocities in a scramjet combustors. Thus, making it virtually impossible to stabilize combustion directly in a supersonic flow. Instead, subsonic recirculation regions (such as bluff bodies, cavities and steps), continuous auto-ignition or continuous forced ignition are required to achieve a decent combustion efficiency (Urzay, 2018). An alternative would be the transition to burning via continuous detonation waves, but the high pressures and transient nature of the resulting flow field present their own challenges (Kailasanath, 2000).

Approaches to provide a forced ignition source for combustion in supersonic flows include spark ignition in cavities (Ma *et al.*, 2016), as well as torches (Kobayashi, Bowersox, *et al.*, 2007; Matsubara *et al.*, 2013) and laser induced plasma (LIP) ignition (Brieschenk *et al.*, 2013a; An, Wang, *et al.*, 2017).

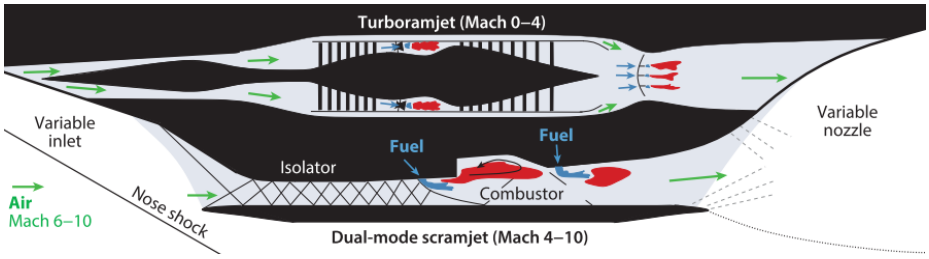

Figure 2.12: Typical design of a hypersonic air-breathing aircraft from Urzay (2018). The combination of a turbo ramjet and a dual-mode scramjet is also called a "combined-cycle propulsion system". To operate in the intermediate Mach number regime ($M = 4 - 6$), the scramjet is sometimes designed to act as a ramjet with subsonic combustion at these conditions, switching to supersonic combustion at $M > 6$. Hence the name, dual-mode scramjet. The injection of fuel via some form of JISCF configuration is hinted at in this sketch

Ma *et al.* (2016) studied a spark plug ignition process in a Mach 2 cavity configuration using three-dimensional, high-speed chemiluminescence measurements. The spark plugs are installed in the cavity wall, creating ignition kernel slightly above them and achieving a stabilized combustion process within the ethylene fueled cavity, a subsonic region. Ethylene has a high reactivity making the ignition and flame stabilization easier than in the case of other gases or liquid fuels, such as methane or JP-7. At a crossflow static temperature and cavity pressures of 340 K and 63-69 kPa, respectively, the ignition kernel appears about 0.5-3.05 ms after spark initiation. Shorter times are observed for the lower fueling rate investigated. The two spark plugs used can each deliver up to 100 mJ of energy over time period of 3-4 ms. A transition from ignition kernel to a stable flame was observed within 3.5-5.5 ms.

Kobayashi, Bowersox, *et al.* (2007) used an ethylene torch ahead of flush mounted JISCF. The torch provides a certain mass flow rate of gases with elevated temperatures, $\sim 1750\ \mathrm{K}$, and high concentrations of radicals, which can help shorten the ignition delay at the actual fuel injector jet. At a crossflow temperature and pressure of $\sim 357\ \mathrm{K}$ and 26.5 kPa they did not observed sustained combustion using their torch configurations as igniters. Moreoever, the influence of the torch gases on the jet structure itself was deemed to be small.

Matsubara *et al.* (2013) combined an equilibrium plasma torch with a dielectric-barrier-discharge device producing non-equilibrium plasma upstream of the torch. Ignition was attempted behind a rearward-facing step with a Mach 2 flow and hydrogen injection from a 1 mm jet at different locations. Static temperature and pressure of the flow were 167 K and 13 kPa, respectively. The plasma torch used nitrogen as the working gas and ionized it via electrical discharge before injection into the main flow. Operating both plasma system simultaneously required several kW of power. Wall pressure measurements indicate the presence of significant hydrogen combustion processes for cases operating the plasma torch at higher powers, i.e. $\sim 2-4$ kW. An influence of the non-equilibrium plasma was detected mostly for weaker combustion cases. In these cases, $\mathrm{O_3}$ was identified as the main contributor to the enhancements in combustion inferred from pressure measurements.

Non-resonant laser induced plasma ignition in a flush mounted JISCF flow field was demonstrated by Brieschenk *et al.* (2013a). They place the laser focal point in the jet shear layer, 1.7 mm downstream of the injector. The laser enters the test section through a port hole in bottom of the test section and is focused by a 100 mm focal length lens in this port. Their measurements showed that at a laser wavelength of 694.3 nm, about 54% of the 750 mJ laser pulse energy are actually deposited in their flow. The flow having a Mach number of 9.4 and a static temperature and pressure of 424 K and 0.7 kPa, respectively. With a 500 ns exposure time, > 7 µs after energy deposition their OH-PLIF diagnostic setup did not detect any appreciable amounts of plasma broadband luminescence anymore. Their OH-PLIF recordings start at 12 µs after laser sparking and show strongly transverse elongated OH-PLIF active regions advecting with the crossflow downstream, see Fig. 2.13. The PLIF signal weakens significantly until it encounters a secondary oblique shock system in their setup, around 27-32 µs, at which point the signal strengthens again downstream of the shock lines. The authors conclude that a laser pulse frequency of 100 kHz would be sufficient to create a continuous stream of hydroxyl (OH) radicals. Results in subsonic flows by Lefkowitz and Ombrello (2017) seem to indicate that such an ignition scheme

might indeed be viable.

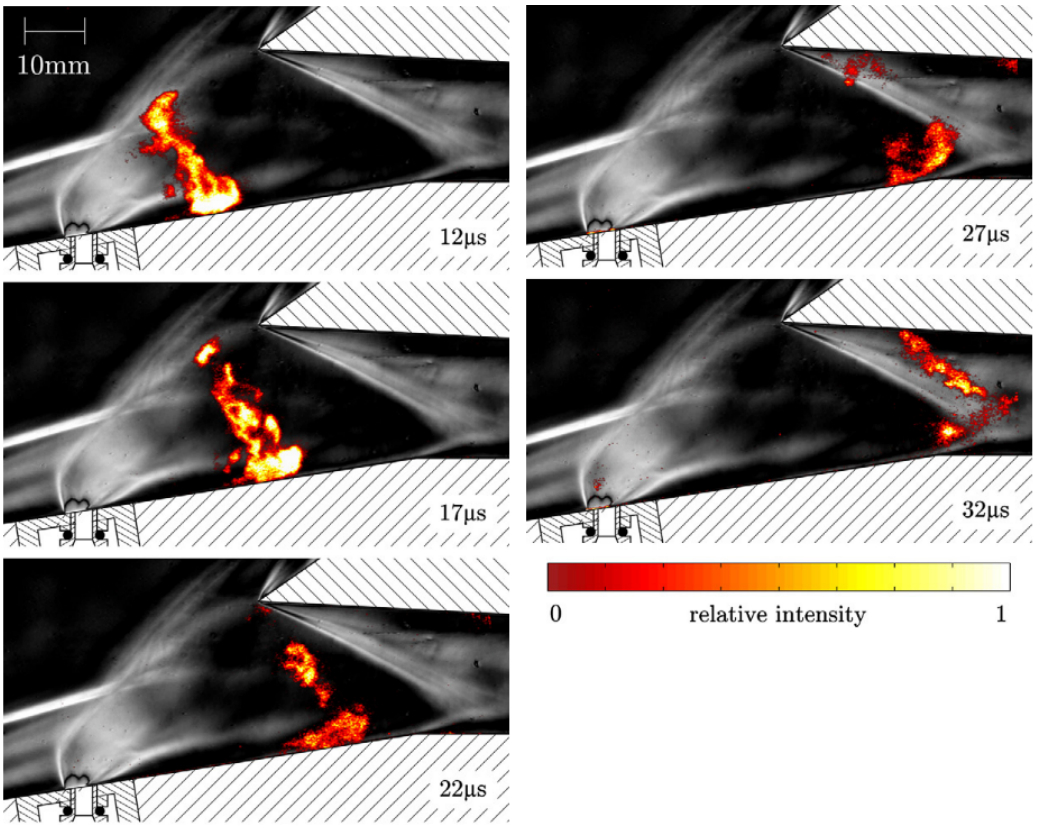

Figure 2.13: Visualization of the OH radical using PLIF in a LIP experiment, from Brieschenk *et al.* (2013a).

In follow up experiments, Brieschenk *et al.* (2014) investigated the focusing of the laser at or just above the exit plane of the jet orifice itself. Among other things they found that energy deposition at a certain height above the jet orifice is advantageous for JISCF ignition applications because it reduces the available time for recombination of the laser generated plasma, irrespective of confinement and refocusing effects for ignition at the jet throat. Investigating different injection gases (air, argon, hydrogen), they found that the LIP shock wave speed is faster for lighter gases. More over, temperatures behind the shock wave are in the range of 1000-10,000 K and the shock heated volume is larger for the heavier injectants. Due to these effects, diluting hydrogen with argon led to greatly enhanced OH-PLIF signals, even with a LIP energy about 50% lower than in the pure hydrogen case.

LIP ignition has also been used in cavity configurations. An, Wang, *et al.* (2017) ex-

ploited the flexibility of this technique to introduce laser sparks at three different locations in a cavity with a Mach 2.92 flow. The static temperature and pressure are 610 K and 79.8 kPa. They then investigated the evolution of resulting ignition kernels using CH* and OH* chemiluminescence. With a nominal ignition energy of $\sim$ 304 mJ the results showed a significant dependence of ignition probability, propagation speed and signal intensity on ignition location, due to differences in local flow conditions. Their results also noted a dependence of the initial flame kernel size on the laser energy, i.e. lower energies resulted in initially smaller kernels and lower initial signal intensities.

Bradley *et al.* (2004) has provided a detailed study regarding the fundamentals of non-resonant LIP ignition in premixed flammable gases using a Q-switched 1064 nm Nd:YAG laser. A number of insights important for the non-premixed case are given in the following. Absorption of the the laser energy occurs mainly through electronic breakdown due to multi-photon ionization and electron-ion inverse bremsstrahlung. The energy required to achieve breakdown depends strongly on the ambient pressure. Immediately after spark initiation, blast-wave calculations suggest temperatures above 100,000 K in spark region for an ignition energy of 224 mJ in propane-air. The spark plasma is an elongated ellipsoid with its semi-major axis oriented along the laser beam path. The hot plasma region and blast wave initiate a toroidal vortex structure with a third lobe in the center, which has a tendency to propagate towards the laser beam, see the example in Fig. 2.14. Finally, the non-resonant LIP process can impart an over-drive on the start of a combustion process, i.e. in the early stages of burning the burning rate and other processes might not be independent of the laser energy deposition details.

To use continuous auto-ignition requires flow temperatures and pressure that lower the auto-ignition time of a given fuel-oxidizer mixture well below the characteristic flow time of a scramjet, i.e. < 1 ms. This usually involves static flow temperatures > 1300 K. For a scramjet flying at Mach 6-10, such temperatures in the combustor are not unreasonable (Urzay, 2018). However, at intermediate supersonic Mach numbers and in the laboratory it

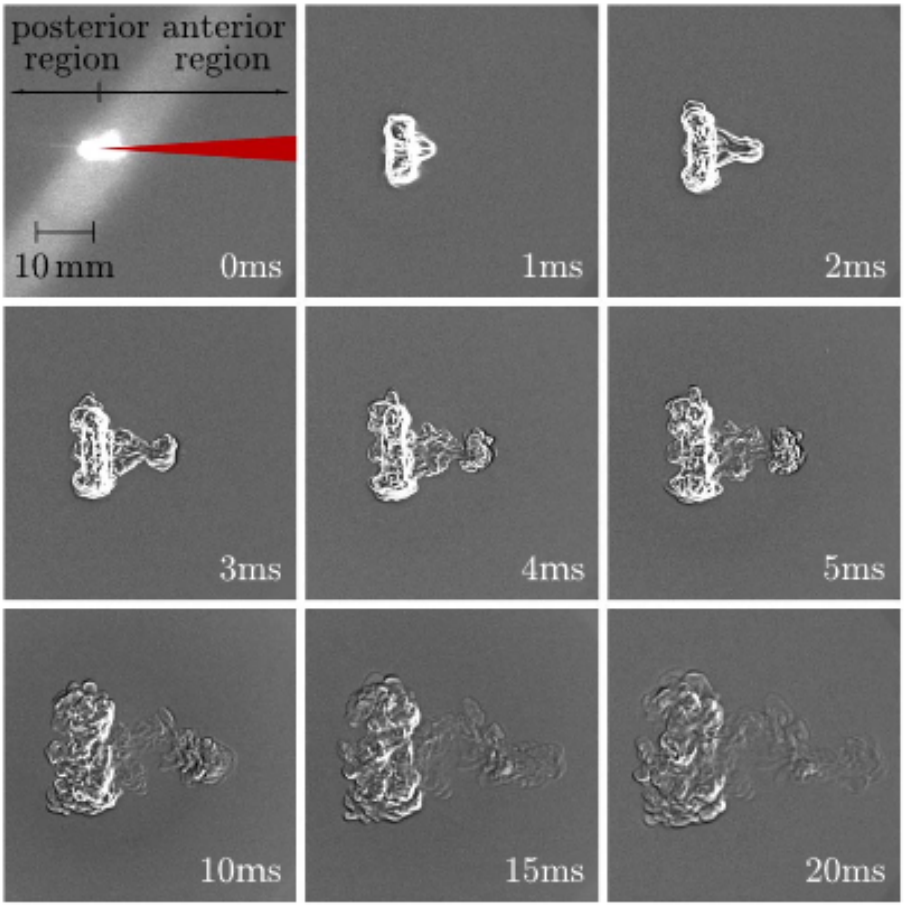

Figure 2.14: Example of the later time toroidal vortex structure and third lobe evolution for a LIP, from Brieschenk *et al.* (2013b). The laser beam is coming into the picture from the right.

is challenging to achieve such conditions.

An example for a study performed in the hydrogen auto-ignition regime is the work of Gamba and Mungal (2015). They used an expansion tube setup with Mach number 2.4, a static temperature of 1400 K and a static pressure of 40 kPa. A single, flush mounted jet injects hydrogen fuel into the crossflow. Using OH-PLIF as a combustion indicator, at low J they observed ignition and broad reacting regions only in the wake of the jet near the wall. At higher J, the flame stabilization point moves to the upstream recirculation region of the JISCF and ignites the windward shear layer.

Other concepts that rely on auto-ignition processes but could function at lower static temperature are shock induced ignition and radical farming techniques. Mai *et al.* (2011)

have reported experimental evidence of a flame holding region behind a flush mounted JISCF, if an oblique shock was impinging on the wake region of the jet. Their crossflow static temperature was 355 K while their jet was significantly hotter due to being preburned. In this case the sustained heat release was mostly attributed to mixing and recirculation enhancement due to the presence of the shock. Analytical considerations to achieve ignition via impingement of an oblique shock on a compressible mixing layer have been presented by Huete *et al.* (2017). Their study showing that relatively specific requirements have to be met to achieve ignition at lower temperatures and pressures.

Finally, a radical farming scramjet makes use of the hot pockets created in the isolator of a scramjet combustor inlet due to the existence of oblique shocks compressing the incoming air and fuel. These hot pockets generate radicals which cause chain branching reaction to be sustained and, at a critical concentration, will cause a thermal explosion, or combustion process, without requiring the entire flow to be above the normally required auto-ignition temperature. Boyce *et al.* (2012) studied an example of such a setup. They tested the radical farming efficacy in the Mach number range 5.9-6.54 with static temperatures and pressures in the range of 763-340 K and 6.71-5.14 kPa, respectively. These conditions are well below the temperatures and pressures normally required for auto-ignition to occur over a reasonable length at such high flow velocities. Wall pressure measurements and OH-PLIF visualization seemed to indicate that this technique could yield sustained combustion processes but only in very localized regions.

2.2.1 Burning Jets in Crossflow

There are relatively few published experimental studies of detailed combustion processes and burning dynamics in single, flush-mounted jets in a supersonic crossflow. Part of that is the difficulty to ignite and sustain a deflagration under such conditions, without any structurally imposed subsonic or recirculation region. Therefore, the majority of experiments also deals with gaseous fuels such as hydrogen, which is highly reactive.

As mentioned above, Brieschenk *et al.* (2014) studied forced LIP ignition in the flow field of a JISCF located on the intake ramp of a model scramjet intake. Importantly, their OH-PLIF data found that the LIP spark seemed to result in chemical reactions between the main air flow and the hydrogen jet that were sustained for a limited amount of time before blowing out. Important also because the static temperature and pressure of 424 K and 0.7 kPa in the experiment are far too low to allow for auto-ignition within the dimensions of their setup. Moreover, laser energy deposition in the shear layer of the jet resulted in about five time higher OH-PLIF signals than deposition close to the jet orifice, for all pure hydrogen jet cases.

Yoshida and Tsuji (1977) reported Schlieren results and temperature profiles for auto-ignition of a hydrogen jet in a vitiated Mach 1.81 flow at static temperatures in the range of 600-1020 K and varying jet supply pressure. They found indicators for sustained chemical reactions at the higher end of their temperature ranges. Ignition appeared to be easier for higher jet supply pressures and chemical reactions were mostly present in the upstream recirculation region of the jet. The peak temperatures measured indicate that combustion is probably slow, as they were well below the temperatures observed in regular hydrogen flames.

Later on Rothstein and Wantuck (1992) used OH-PLIF to investigate a auto-igniting hydrogen jet in a Mach 1.5 crossflow with a static temperature of 1200 K. The flow was heated using radio frequency driven discharges. They mostly focused on deriving jet penetration curves from the PLIF signals over a large range of momentum flux ratios, $5.9 \leq J \leq 38.6$. An interesting observation was the onset of OH active regions close to the injection point of the jet in the windward shear layer, subsequent disappearance of that signal and re-appearance of the signal further downstream. They associated the inactive region with the existence of weak expansion waves.

One of the most detailed experimental investigations focused on the combustion physics of an auto-igniting hydrogen JISCF has been conducted by Gamba and Mungal (2015).

Their shock tube setup provides stable conditions with a Mach number of 2.4, a static temperature of 1400 K and a static pressure of 40 kPa over a test time of ~ 500 µs. The main goal of the study is to investigate the influence of the global momentum flux ratio J on the burning processes; it is varied from 0.3-5. Schlieren, OH* chemiluminescence and OH-PLIF diagnostics are used to investigate the flow field physics. For this setup, burning of the shear layer only became relevant at $J > 3$, but for all cases the near wall region in the wake of the jet contains the most intense combustion reactions. For the highest J value they identified a region between the near jet burning zone and the downstream shear layer burning zone that exhibits very little OH activity. They associate this with quenching in the shear layer due to a rapid expansion process in the jet. While especially the shear layer seems to burn predominantly in a non-premixed mode, the stabilization regions for the entire J range tend to be in locations where at least some premixing has occurred, i.e. the near wall wake and recirculation regions around the jet. A non-linear dependence of the OH* signal was observed for $J < 1$ while linear trends are identified at $J > 1$.

Based on the average OH* chemiluminescence recordings Gamba and Mungal (2015) also extracted jet trajectories, defined as the points where the signal intensity is 10% of the maximum in a region downstream of $x/d_j = 30$. Assuming a particular form of Eq. (2.14) with $B = 1 - C$, they reported an empirical dependence of A and C on the value of J as follows,

$$A = 1.05\left(1 - \mathrm{e}^{-J}\right) \tag{2.18}$$

$$C = 0.5J^{-1/4}. \tag{2.19}$$

Possible reasons for the observed dependency in the exponent are mentioned to be the relatively low momentum flux ratio and the widely varying trajectory definitions and measurement conditions.

An example instantaneous OH-PLIF results on the symmetry plane of the flow field is shown in Fig. 2.15. The OH layer thickness is on average between 0.3 mm in the near field and 0.5 mm in the far field. Due to the thin, layer-like structure Gamba and Mungal (2015) approximate them as strained laminar diffusion layers with a characteristic thickness of,

$$\lambda \sim \sqrt{\frac{\mathcal{D}}{S}}, \tag{2.20}$$

where S is the strain rate and $\mathcal{D}$ is a scalar diffusivity. Thus postulating that the OH layers

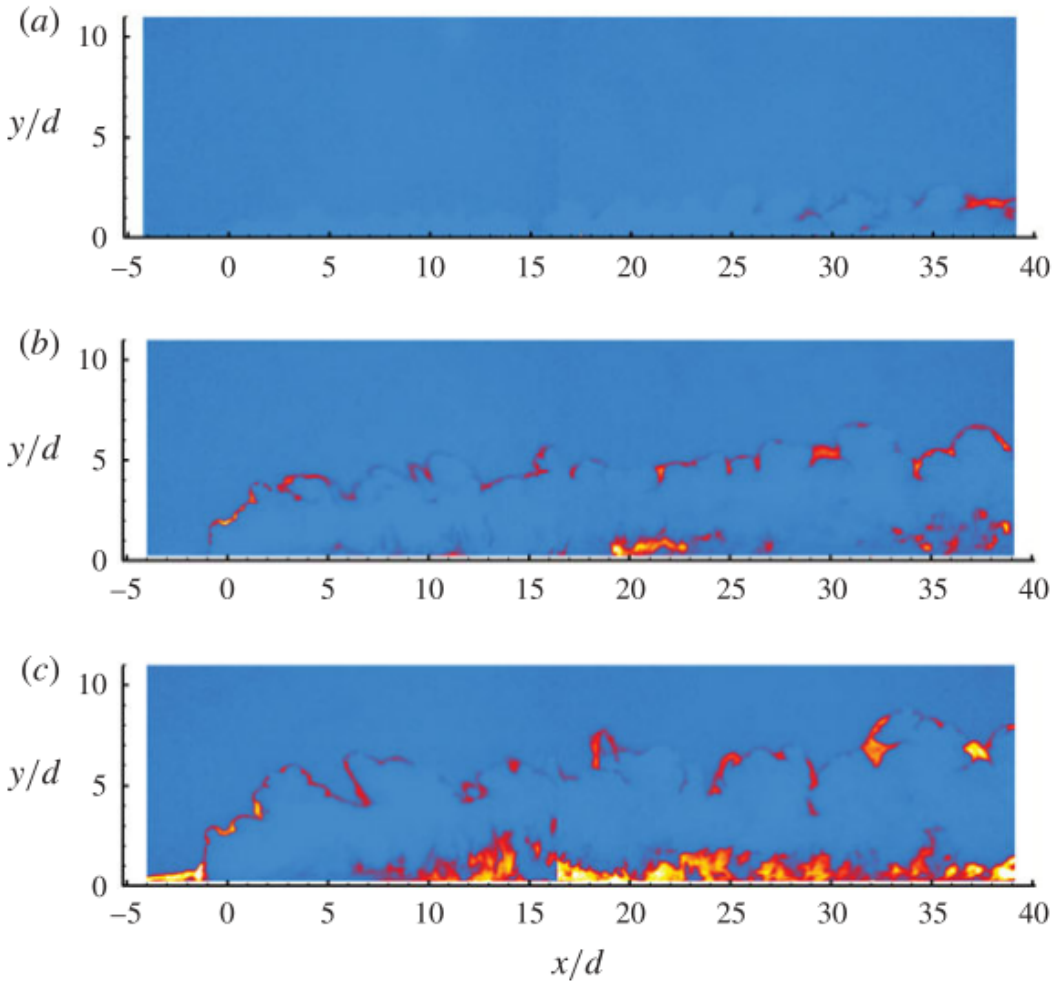

Figure 2.15: OH-PLIF results from Gamba and Mungal (2015) on the symmetry plane for *a* $J = 0.3$, *b* $J = 2.7$, and *c* $J = 5$.

can be treated as flamelets. With these assumptions they arrive at the conclusion that both

the characteristic velocity and length scale are constant in the far field or varying at the same rate. Together with the fact that the OH layer orientation in the far field is mostly parallel to the crossflow, they further conclude that shear is small and chemical reactions are probably entirely diffusion controlled to due to the lack of large scale entrainment structures. Making the far field an inefficient combustion environment for the setup studied.

Top-down OH-PLIF data presented by Gamba and Mungal (2015) also provided a wealth of information on the near jet and near wall burning structures. An example set of images is shown in 2.16. Flame stabilization upstream of the jet orifice is visible, as well as unburned regions and structures corresponding to specific vortex systems. The thickness of the near wall burning regions appeared to be controlled by the boundary later thickness. The authors also speculate that the structure of the OH active regions hints at a complex mixture of premixed, non-premixed and potentially distributed-reaction-zone burning modes.

Finally, Gamba and Mungal (2015) provided a schematic map of the main fuel entrainment pathways in the JISCF flow field which is reproduced in Fig. 2.17 for reference.

The usefulness of such detailed results for a canonical configuration is exemplified by the study of Saghafian *et al.* (2015). They presented a flamelet model for compressible flows and tested it numerically using RANS and LES on the configuration reported by Gamba and Mungal (2015). The incompressible, steady flamelet equations can be written as,

$$\rho \frac{\chi_f}{2} \frac{\partial^2 Y_\alpha}{\partial f^2} = \dot{\omega}_\alpha \quad \alpha = 1, 2, \ldots, N. \tag{2.21}$$

Here χ_f is the scalar dissipation rate of the mixture fraction f ($\chi_f = -2\mathcal{D}_f \left|\nabla f\right|^2$), Y_i is the species mass fraction of species i, and $\dot{\omega}$ is the corresponding source term. Especially the last term is sensible to fluctuations in thermodynamic properties due compressibility. A correction based on reference densities and temperatures was introduced using the Arrhe-

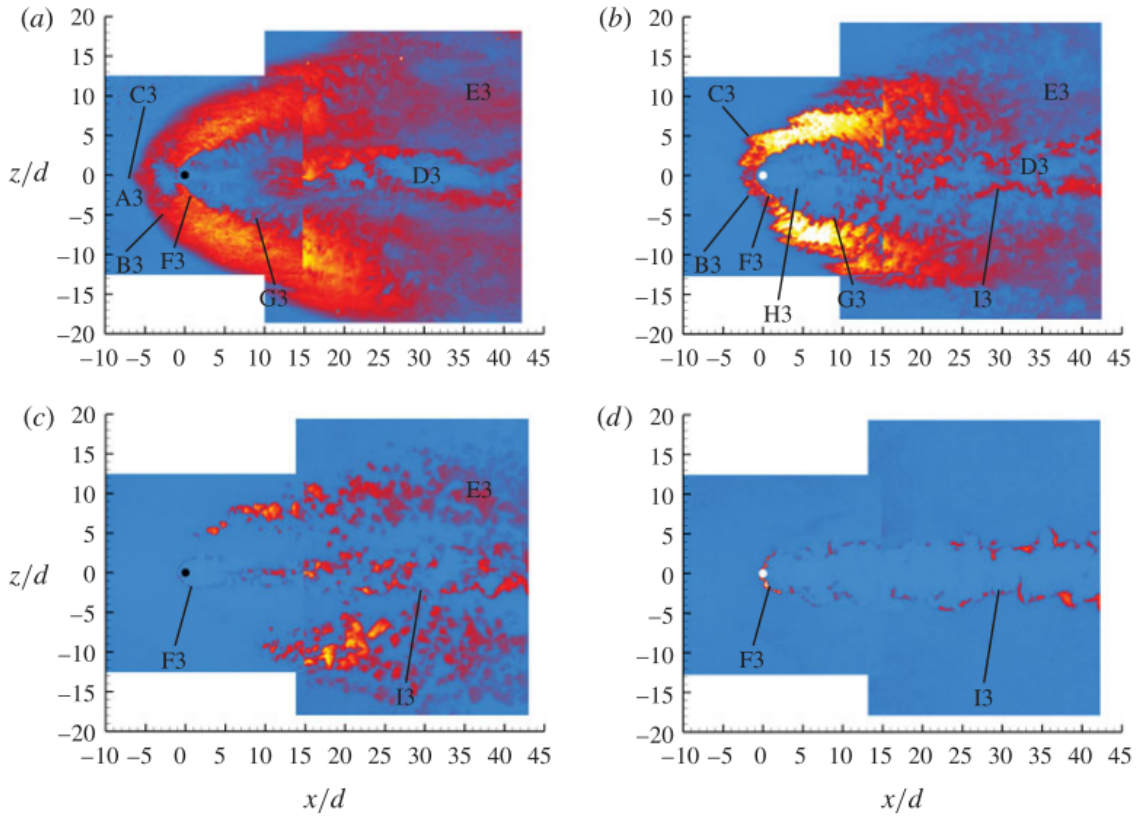

Figure 2.16: OH-PLIF results from Gamba and Mungal (2015) for $J = 5$ of top down views at different planes parallel to the bottom of the test section. Imaging plane heights are *a* $y/d_j = 0.25$, *b* $y/d_j = 0.5$, *c* $y/d_j = 1$, and *d* $y/d_j = 3$.

nius behavior of reactions involved in combustion processes,

$$\frac{\bar{\dot{\omega}}}{\bar{\dot{\omega}}_0} = \left(\frac{\bar{\rho}}{\bar{\rho}_0}\right)^{a_\rho} \exp\left[-T_a\left(\frac{1}{\tilde{T}} - \frac{1}{T_0}\right)\right]. \tag{2.22}$$

Here subscript 0 denotes the reference case, a_ρ and T_a are precomputed values, $\bar{\cdot}$ denotes direct averaging and $\tilde{\cdot}$ Favre averaging/filtering. Agreement of their model with experiments was good for the case of LES simulations but less so for the RANS approach. The latter probably is less accurate due to deficiencies in the mixing model. The compressibility correction apparently improved the fidelty of the results significantly.

Ben-Yakar *et al.* (2006) also performed auto-igniting JISCF experiments in an expansion-tube with hydrogen and ethylene jets. Since their jets were relatively cold in comparison to

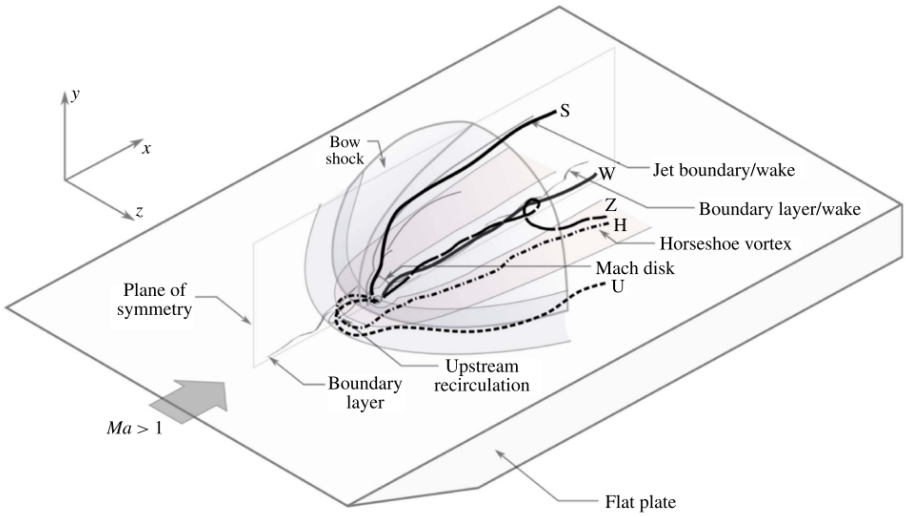

Figure 2.17: Schematic of fuel entrainment pathways identified and presented by Gamba and Mungal (2015). The possible pathways were inferred from observations made in the OH* chemiluminescence and OH-PLIF measurements.

the crossflow, they found that lean regions favored ignition. Moreover, due to differences in the mixing characteristics of ethylene and hydrogen jets, the former exhibited much more distributed OH active regions. As opposed to the hydrogen jet for which burning seemed to be confined to the thin jet-crossflow interface. However, the ethylene was harder to ignite.

2.2.2 Burning Staged Jets in Crossflow

Reacting staged jets, even though they are promising with regards to mixing enhancements and flame stabilization, have rarely been discussed in the literature outside of their direct application to scramjet combustor development.

Abbitt III *et al.* (1993) presented a reacting flow follow-up study to the work by McDaniel and Graves (1988). The staged jets were located behind a rearward-facing step and ignition was achieved using a spark plug and a hydrogen pilot feed in the subsonic region close to the base of the step. At momentum flux ratios of 1.5 and below they achieved continuous burning with this setup even though the total temperature was as low as 315 K and the ignition source was shut-off after the start-up. Broadband chemiluminescence and OH-PLIF revealed that the burning occurred mostly in the low speed regions close to the

wall, not in the shear layer of the jets. The study also claimed a large effect of heat release on the mixing dynamics of the jets, due to a pressure rise in the test section. This effect seems to depend on the size of the test section itself.

Lee (2006b) also presented an extension of the computational non-reacting study in Lee (2006a). Here the two jets are mounted flush to the wall without any steps. The combustion process considered is auto-igniting hydrogen jets in an air crossflow. A schematic of the reacting flow field is shown in Fig. 2.18. This computational study found that, similar to the non-reacting case, an optimal distance exists between injectors with regard to burning rate and flame height. The optimal distance increased with increasing J and is larger than in the non-reacting case due to preheating effects at the first jet.

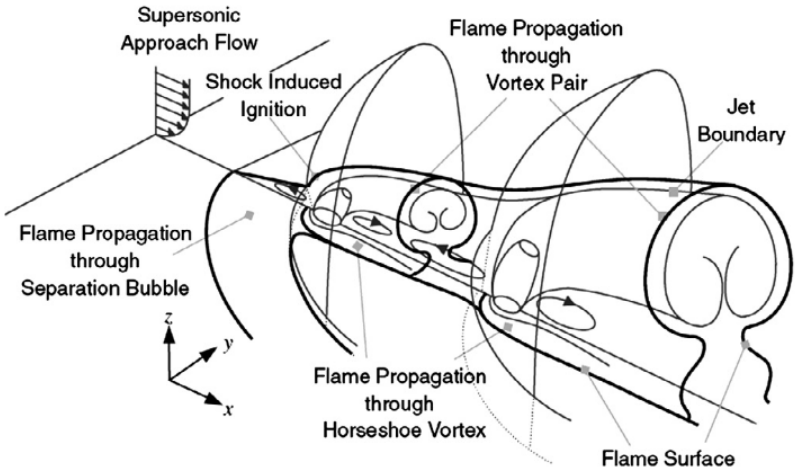

Figure 2.18: Ignition and flame propagation in a staged JISCF flow field as presented by Lee (2006b)

.

2.3 Experimental Setups

For a better impression of the facilities and methods (and their capabilities) used to perform different studies on JISCF, a few representative examples are described below.

Gruber and Nejad (1995) described a regularly used continuous flow windtunnel at Wright-Patterson Air Force Base. The maximum stagnation temperature and pressure were

922 K and 2,758 kPa, respectively. Heating of the air flow is achieved with a series of gas-fired heat exchangers and a maximum continuous flow rate of 15.4 $\mathrm{kg/s}$ is possible. The test section has a nominal cross section of 12.7×15.2 cm. Mach numbers of the main flow can be varied by exchanging the converging-diverging nozzle, but the presented characterization was for a rectangular Mach 2 nozzle producing a relatively uniform flow.

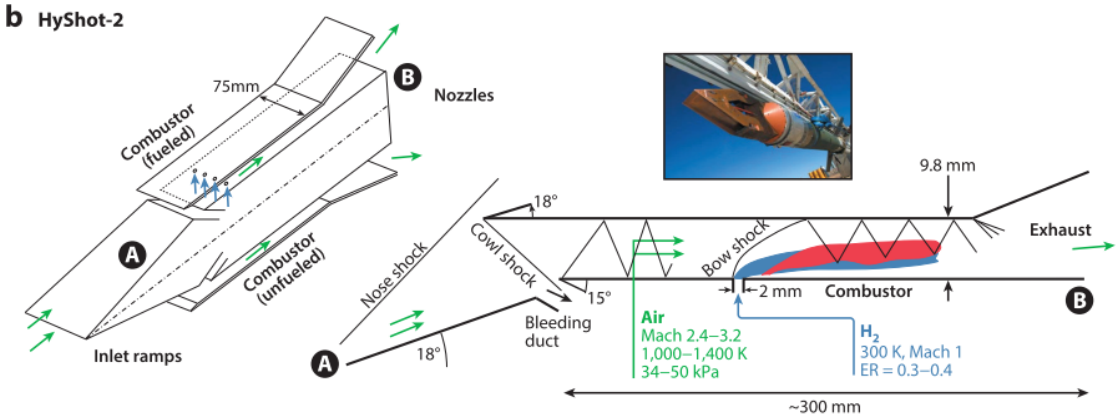

Figure 2.19: Sketch of the HyShot-2 flight experiment from Urzay (2018). The fuel injection scheme is a single flush mounted JISCF.

.

An alternative setup at Los Alamos National Lab is described by Wantuck and Watanabe (1990). Heating of the main flow is achieved using an inductively coupled plasma tube which causes Ohmic heating and electric breakdown in the air flowing through it. While relatively high stagnation temperatures are possible using this approach, it is desirable to not flow pure air because molecular species require additional energy to ionize. Thus, among other mixtures, a main flow composition of 80% Ar and 20% $\mathrm{O_2}$ has been reported. Maximum achieved total temperature and pressure were 3000 K and 203 kPa, respectively, and a Mach 2 nozzle is installed upstream of the test section. This resulted in mass flow rates of 50.4 $\mathrm{g/s}$. The test section was connected to a vacuum/expansion tank. The latter was used to achieve pressure ratios necessary for choke flow in the Mach 2 nozzle.

Gamba and Mungal (2015) and Ben-Yakar *et al.* (2006) used an expansion tube setup situated in the High Temperature Gas Dynamics Laboratory at Stanford University. This

facility can achieve flow conditions similar to what the combustor of a hypersonic air-breathing aircraft would experience. Mach numbers between 2.4-3.4, stagnation temperatures between 3000-4300 K, and stagnation pressures between 585-2077 kPa. However, the test times are relatively short, on the order of 500 $\mu\mathrm{s}$. An expansion tube can be thought of as a modified shock tube. It consists of a driver section, a driven section and, additionally, an expansion section. Driver and driven section are separated by one diaphragm, driven section and expansion section by another one. Precise pressure ratios between the different sections have to be managed to achieve the desired final flow conditions. Rupturing the first diaphragm by exceeding a critical pressure in the driver section will create a shock traveling into the driven section. The shock causes the second diaphragm to rupture initiating another shock traveling through the expansion section. Simultaneously, the gas from the driven section starts accelerating into the expansion section to match the lower pressure and higher velocity. Testing is possible between the arrival of the contact surface between expansion and driven gas at the end of the expansion section, and arrival of subsequent rarefaction waves.

An alternative to laboratory experiments are small scale flight tests. While they are expensive and complex they can provide valuable real-world data for the engineering applications of JISCF. Of particular interest for the motivation of this study is the HyShot-2 experiment run by the University of Queensland, see Smart *et al.* (2006). Using a single, flush mounted hydrogen jet in crossflow configuration, the combustor seemed to provide sustained supersonic combustion over three seconds. A sketch of the test article configuration is shown in Fig. 2.19. The combustor inlet Mach number varied between 2.4-3.4, the combustor inlet total temperature and pressure between 3040-3100 K and 640-1830 kPa. After three seconds of experimental data the test article seemed to experience mechanical failure. One could interpret this as encouraging for the use of JISCF in scramjet applications. However, it also emphasizes the need to understand the resulting flow and combustion regimes better to provide reliable engineering guidelines.

CHAPTER 3
EXPERIMENTAL DESIGN AND METHODOLOGY

In this chapter the experimental facility, flow conditions, data acquisition, diagnostics, data processing techniques and basic crossflow and jet flow characterizations are presented. Where appropriate, details are added in the subsequent results chapters themselves.

3.1 Experimental Setup

The experimental setup is a blow down windtunnel situated in one of the high-pressure cells at the Ben T. Zinn Combustion Laboratory. Air is supplied to the setup from the lab's high-pressure system. The system is fed by a Norwalk Compressor and multiple 2500 psig storage tanks with a maximum pressure inside the lab of 720 psig. The air is filtered and dried in an Ultra Filter refrigerating dryer before being pumped up to storage pressure. In addition, the storage tanks have a manifold and relief valve installed at the bottom allowing one to manually vent any residual moisture in the tanks. Details on selected experimental conditions and flow properties are presented in the following sections.

An isometric schematic of the full test facility is shown in Fig. 3.1. The main flow is preheated to stay at elevated temperatures during experiments because the air flow will cool down during expansion through the converging-diverging nozzle. At a design Mach number of 1.7, the approximate change in temperature for air ($\gamma = 1.4$) is $T_\infty = 0.63T_0$. For all presented experiments the crossflow is preheated to $\sim 600\ \mathrm{K}$ yielding an approximate static temperature in the test section of $\sim 378\ \mathrm{K}$. At a targeted stagnation pressure of 379 kPa the system delivers a mass flow rate of about 2.95 $\mathrm{kg/s}$. Part of the experimental setup is built on rails to allow for thermal expansion.

In the homogenizer, the flow is conditioned by a series of stainless steel honeycomb and wire screens. The honeycomb characteristic opening diameter is 5 mm with wall thick-

nesses of 0.5 mm. It is followed by two wire screens with an opening size of 6.9 mm and 66% open area, as well as two wire screens with an opening size of 3.2 mm and 57% open area.

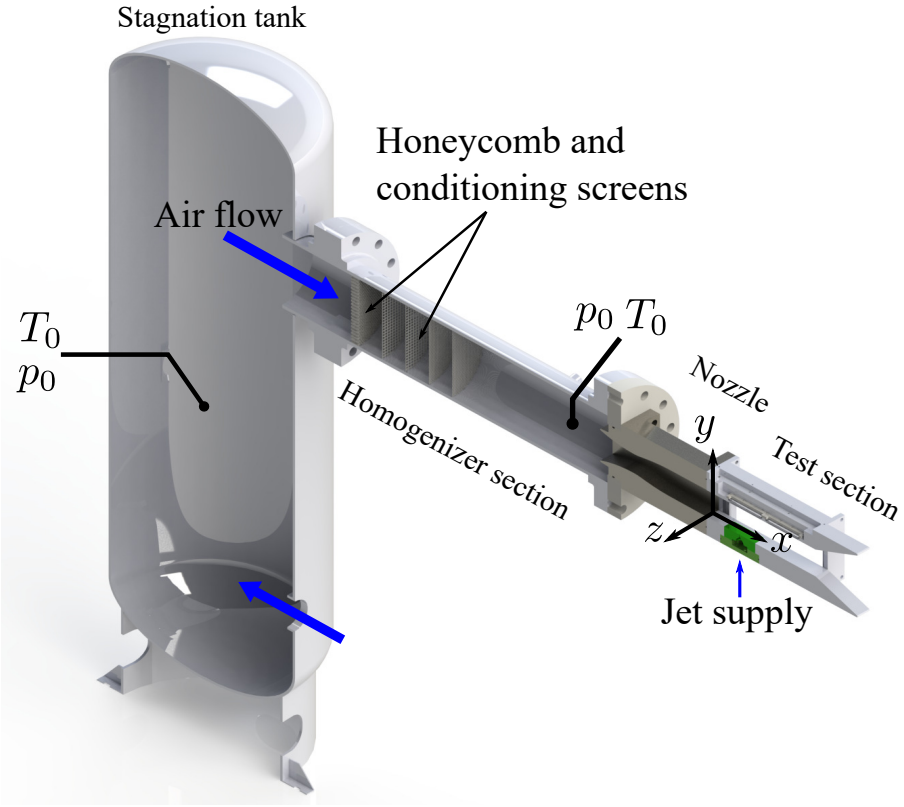

Figure 3.1: Isometric schematic of the experimental facility used in the present study.

Thermocouples are installed in multiple locations to monitor crossflow and jet fluid temperature. The most important ones are located in the stagnation chamber and the homogenizer of the windtunnel and at the injector. All thermocouples installed agree to within 1.0 K and have an accuracy of ± 1.0 K, measured via the boiling and freezing point of water.

The three most important pressure transducers measure in the stagnation chamber and the homogenizer (Omega PX309-500GI) of the windtunnel and at the injector (Omega PX309-500A5V). All of them were tested with an analog precision pressure gauge, which has a reading accuracy of ± 1.0 psi. The resulting relationships for linearity and other errors are given here:

- Stagnation pressure in the flow conditioning section.: $0.002 \cdot p_{meas} + \frac{0.25\%}{100} \cdot FS(500\text{psi})$
- Jet stagnation pressure: $0.002 \cdot p_{meas} + \frac{0.25\%}{100} \cdot FS(500\text{psi})$

Static wall pressure measurements are made with a Scanivalve DSA 3217 16-channel pressure scanner with $\pm 0.05\%$ full scale long term accuracy.

The pressure transducers and thermocouples measure the pressures and temperatures in Tab. 3.1 for the different parts of the presented study. Given ranges in the table represent the statistical uncertainty of measured quantities (95% confidence intervals) computed from all experimental runs performed in that part of the study. That is 35 runs for Ch. 4, 60 for Ch. 5, and 45 for Ch. 6. The static conditions are computed assuming isentropic expansion, see Eq. (3.4). Reference velocities are calculated with the relationship $U_0 = M_\infty \sqrt{\gamma R T_\infty}$, where $\gamma = 1.4$ and $R = 287\ \text{J/kg K}$ are assumed for the crossflow air and the Mach number is 1.71 as determined in Sec. 3.5. The small variations between different parts of the study are mostly due to changes in seasons as the outside storage tanks and the positive displacement exhaust system leave the lab influenced by ambient conditions. With the calculated Reynolds numbers, a turbulent boundary layer is expected (White and Corfield, 2006, chap. 5).

Table 3.1: Measured stagnation conditions in the homogenizer section and static crossflow conditions computed assuming isentropic expansion to Mach 1.71 for the different parts of this study. Corresponding reference crossflow velocities are used throughout this study. The given ranges are based on 95% confidence intervals of normally distributed variables.

	p_0 [kPa]	T_0 [K]	p_∞ [kPa]	T_∞ [K]	U_0 [m/s]	Re_x 1/m
Ch. 4	379.2 ± 4	595 ± 10	75.7 ± 0.8	375 ± 6	664 ± 5	$21.36 \cdot 10^6$
Ch. 5	377.8 ± 3	596 ± 7	75.4 ± 0.6	376 ± 4	665 ± 4	$21.24 \cdot 10^6$
Ch. 6	378.7 ± 4	594 ± 7	75.6 ± 0.8	375 ± 4	664 ± 4	$21.38 \cdot 10^6$

Computations using Chemkin Pro 19.1 and the GRI 3 mechanism (Smith, Golden, *et al.*, 2020) are used to confirm that auto-ignition is extremely unlikely under the present flow conditions. Iterating through temperature and pressure from static to stagnation conditions in a perfectly stirred reactor with ethylene air mixtures at an equivalence ratio of one yields

essentially infinite ignition delays. Thus, no auto-ignition is to be expected in the presented experiments.

The maximum available run time is $\sim$10 min. It takes one to two minutes to reach the desired stagnation temperatures, after which another one to three minutes are required to equilibrate the tunnel, leaving about five to seven minutes for experimentation and data acquisition. An example of a typical experimental run to collect Mie-scattering data is shown in Fig. 3.2. In this figure, the reference pressure for the jet is the theoretically required stagnation pressure to achieve the desired momentum flux ratio. The conditions are relatively stable with small drifts in the test section pressure and temperature, as well as the jet temperature. During data acquisition, the tunnel conditions generally do not change more than 2%.

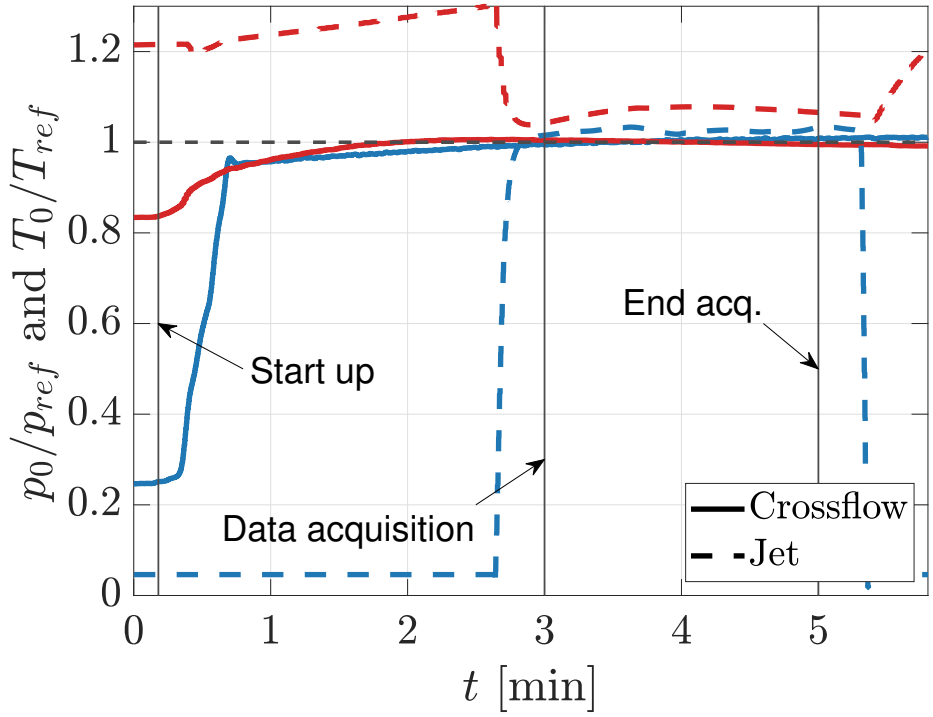

Figure 3.2: Example of typical facility conditions during an experiment as recorded with the LabView interface. Blue lines: pressure, red lines: temperature. The specific experiment here is for an ethylene jet at a momentum flux ratio of $J = 4$. Reference pressure and temperature are 379 kPa and 600 K for the crossflow, and 1,795 kPa and 300 K for the jet, respectively.

3.1.1 Nozzle Design

To achieve supersonic flow conditions, a converging-diverging nozzle was designed using the two-dimensional Method of Characteristics. The design Mach number is 1.7 and a minimum length nozzle contour was constructed based on the method outlined by Anderson (1990) with a rounded expansion region. While this kind of nozzle does not provide the most uniform outflow, it is a space saving and economic option for windtunnel experiments. Boundary layer growth was accounted for using empirical corrections reported by Sibulkin (1957) and Rogers and Davis (1957).

304 stainless steel was selected as the nozzle material to withstand elevated temperatures. Eleven 0.08 mm diameter holes are added along the centerline of one side of the nozzle to allow for static pressure measurements as the flow accelerates. These measurements are part of the flow quality assessment presented in Sec. 3.5.

The final nozzle is shown in Fig. 3.3. For the computation of theoretical flow properties at the exit plane of the nozzle and further analysis later, the isentropic nozzle expansion equations for temperature, density, pressure and the mass flow rate are used:

$$\frac{T_0}{T} = 1 + \frac{\gamma - 1}{2} M^2 \tag{3.1}$$

$$\frac{p_0}{p} = \left(1 + \frac{\gamma - 1}{2} M^2\right)^{(\gamma/\gamma - 1)} \tag{3.2}$$

$$\frac{\rho_0}{\rho} = \left(1 + {}^{\gamma - 1}\!/_{2} M^2\right)^{\left(\frac{1}{\gamma - 1}\right)} \tag{3.3}$$

$$\dot{m} = p_0 A^* \sqrt{\frac{\gamma}{R T_0}} \left(1 + \frac{\gamma - 1}{2} M^2\right)^{({}^{\gamma + 1}\!/_{-2(\gamma - 1)})} . \tag{3.4}$$

3.1.2 Test Section

The test section, shown in 3.3 has a square interior of $80 \times 80\ \mathrm{mm}^2$ and is made out of 303 stainless steel. Its height is denoted as H throughout the study. Steps in the transition

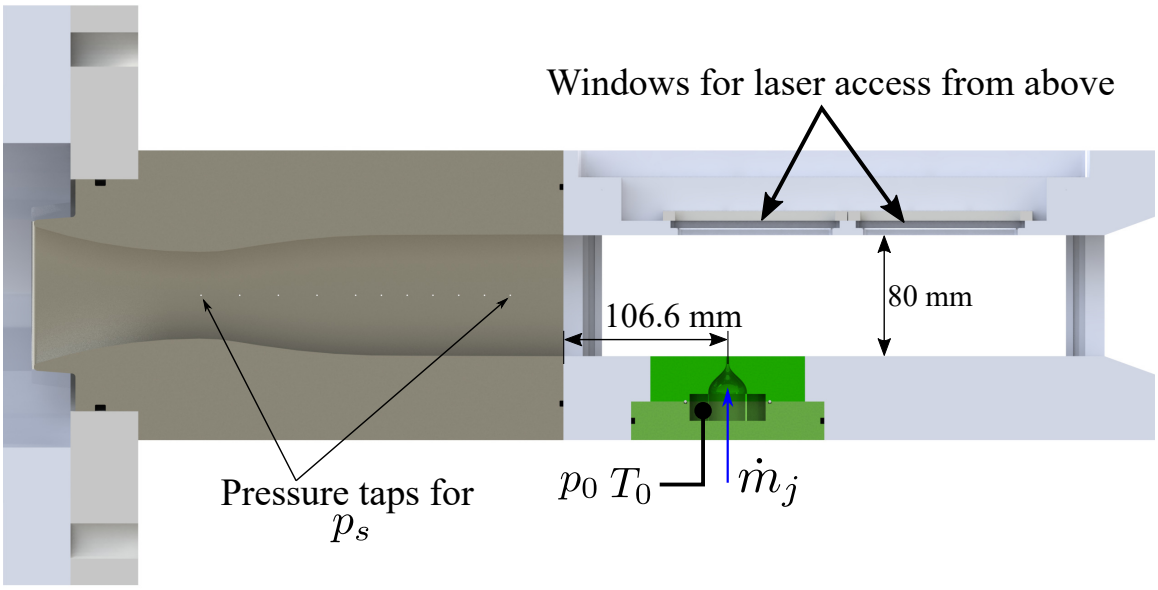

Figure 3.3: Side-view of the nozzle and test section with single jet injector installed.

from nozzle to test section are barely perceptible and in all cases smaller than 0.3 mm. Reliable positioning is achieved with a set of four dowel pins. Tight tolerances, on the order of 0.1 mm, ensure that the test section interior is smooth and that any gaps (e.g. at the windows) are minimized. This is important as for supersonic flows any such feature can cause a significant flow disturbance in the form of an expansion/compression or shock wave. Any still remaining gaps are sealed with red high-temperature RTV silicone gasket maker as much as possible.

The test section can withstand intermittent temperature rises due to ignition and combustion processes but not prolonged exposure to heat sources such as stabilized flames. The 305×80 mm windows provide access for a range of optical diagnostics. The top of the test section can be switched out, providing space for either static pressure measurements or optical access for lasers and cameras.

The bottom section has a 101.5×61.0 mm cutout in which different injector blocks or other test articles of interest can be inserted. The centerline of the injector jet orifice is 106.6 mm away from the nozzle exit. In the case of multiple staged jets, the first jet is at this position.

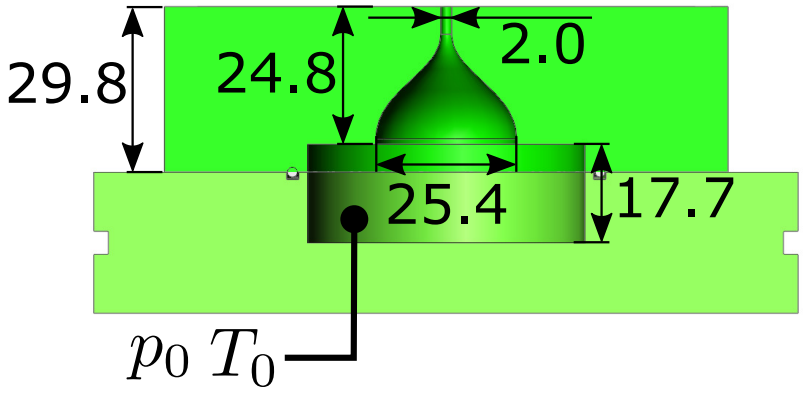

Figure 3.4: Single injector design with reservoir base. Jet Stagnation temperature and pressure are measured in the base. All dimensions in [mm].

3.1.3 Injector Design

The presented study uses both single jet and staged dual jet injectors. The design of both is described below. The dimensions of the staged injectors are justified in part with results from Ch. 4.

The single jet injector block shown in Fig. 3.4 is designed to provide a well-defined top-hat velocity profile upon injection. It is also denoted as SI. The exit diameter is $d_j = 2.0$ mm with a preceding flow contraction defined by a fifth order polynomial. Similar contractions have been used by other researchers to achieve well defined exit velocity profiles (Lin *et al.*, 2010). The jet exit is positioned such that it lies on the centerline of the test section.

To maximize modularity and measure the jet properties during each experiment, the injector blocks are mounted to a stainless steel base. This base acts as a quasi-reservoir that the injectant enters before encountering the flow contraction into the test section. In the reservoir section, supply stagnation pressure and temperature of the jet are measured. These measurements are then also used in the data processing to obtain the momentum flux ratio, J. The injectant gas supply comes from a manifold of four pressurized gas bottles.

Two staged injector configurations are chosen that should result in two different interaction regimes. One where the second jet impinges on the first one before it has turned completely into the crossflow and one where the interaction occurs further downstream af-

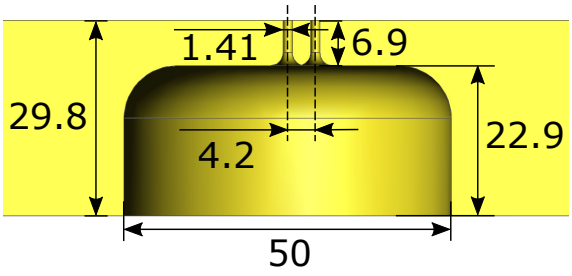

(a) Staged injector with two jets at a normalized distance of $x/J_2^{1/2}d_j = 1$ for $J_1 = 4$.

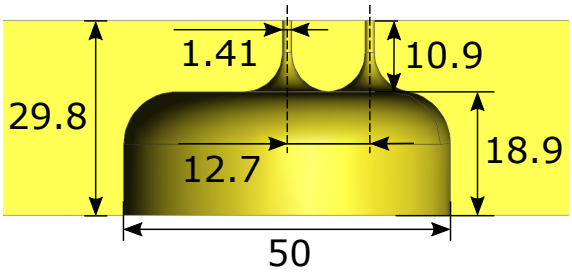

(b) Staged injector with two jets at a normalized distance of $x/J_2^{1/2}d_j = 3$ for $J_1 = 4$.

Figure 3.5: Staged injector designs without the reservoir base. All dimensions in [mm].

ter completely turning the first jet. This results in a jet spacing of $x/J_2^{1/2} = 1$ (near-field interaction) and $x/J_2^{1/2}d_j = 3$ (far-field interaction), with physical spacings of $\Delta x = 4.2$ mm and 12.6 mm, respectively. The staged injector with closer spacing is also denoted as DI1, while the one with the larger spacing is also denoted as DI2.

The diameter of the dual jets is reduced to $\sqrt{2} \approx 1.41$ mm to keep the total mass flow roughly constant, an approach that has been followed in past staged injection studies (Lee, 2006a). The designs of the two dual injectors are shown in Fig. 3.5. The contraction has an initial diameter equal to the separation between the jets and is tangential to both the interior of the injector and the direction of injection.

While the total length of the contractions is different for the three injectors, the length of the minimum diameter is kept the same at 5.0 mm. Since this study is only investigating choked sonic jets, the history of the jet before the throat is secondary for its evolution downstream. Thus, comparable conditions for all jets upon injection into the crossflow should be achieved.

3.1.4 Jet Supply System

A schematic of the jet supply system with PIV seeder is shown in Fig. 3.6. After opening the main pneumatic valve (Valworx 522504A), it takes less than 10 s for the jet supply pressure to stabilize. The valve is normally closed, actuated with 552-827 kPa pilot air, and rated for up to 6895 kPa working pressure at temperatures 255-355 K. The working

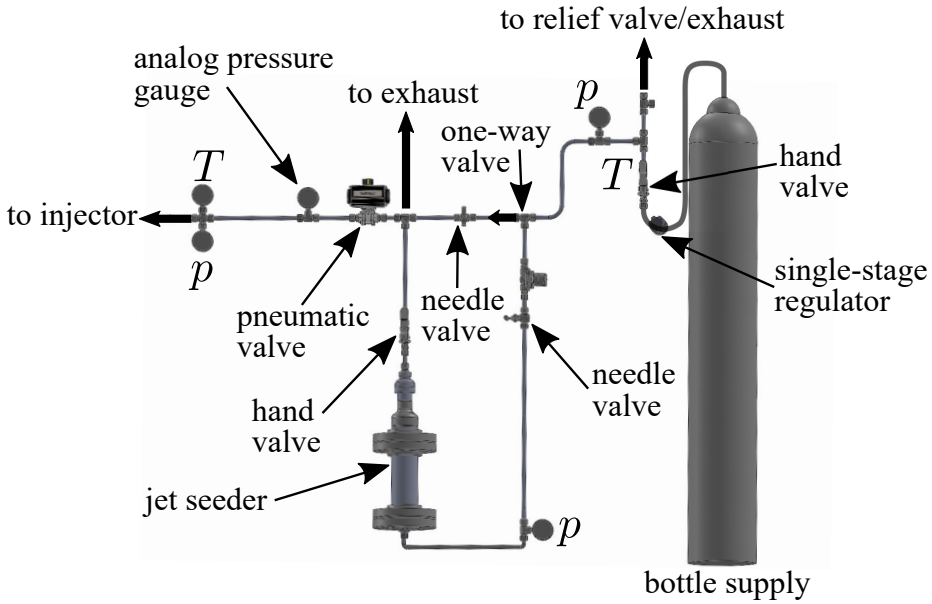

Figure 3.6: Schematic of the jet supply system. Single letters p and T, denote approximate locations of digital pressure and temperature measurements, respectively, via LabView.

fluid can be air, oil, water, helium, argon, ethylene etc., as long as it is compatible with the stainless steel material. The pilot air is controlled by a normally-closed 3-way solenoid valve (Parker 71315). The injectant gas supply comes from a manifold of four pressurized gas bottles. In the case of flammable injectants one of the bottles is a nitrogen bottle to flush the system before and after every run.

The injectant pressure is controlled manually with a single-stage regulator (Tescom 44-1300 series). The regulator pressure and the jet supply pressure have a linear relationship which was confirmed experimentally. The momentum flux ratio is set nominally to 1, 2, 4 and 6 for all gases used in this study, with jet stagnation pressures in the range of 414 - 2,758 kPa. Gases used in this study, their main properties of interest and the the resulting nominal jet conditions are summarized in Tab. 3.2.

Due to the Joule-Thompson effect, the jet manifold has to be heated to keep the injectant stagnation temperature at acceptable levels during an experiment. This effect limits the mass flow rate of real gases as the injectant starts cooling and eventually liquefies during expansion from the pressurized storage bottle. In general, the greater the specific heat of a

gas, the more significant the effect. Around room temperature this is relevant for all gases except the most simple or mono-atomic gases, e.g. H_2 or He (which can still warm up instead of cooling down during expansion).

The Joule-Thompson effect can be quantified with the Joule-Thompson coefficient,

$$\mu_{JT} = \frac{\partial T}{\partial p} \mid_h = \frac{V}{c_p} \left(\alpha T - 1 \right), \tag{3.5}$$

where α is the coefficient of thermal expansion and h, for this one equation, is the specific enthalpy. Or it can be quantified via a constant enthalpy calculation, i.e. $h_1 = h_2$ where state 1 is before the expansion and state 2 after the expansion, roughly corresponding to flow states right before and after the regulator.

With the planned experiments the worst case scenarios are injection of carbon-dioxide and ethylene. Using the software "Engineering Equation Solver" (EES, F-Chart Software (2018)) the change in temperature due to the Joule-Thompson effect can be estimated accounting for temperature dependent gas properties. For the highest expected mass flow rates in the presented work, EES predicts $T_{CO_2} = 264.6$ K and $T_{C_2H_4} = 256.6$ K after the regulator for pressure changes of $835\,\mathrm{psig} \rightarrow 400\,\mathrm{psig}$ and $1200\,\mathrm{psig} \rightarrow 400\,\mathrm{psig}$, respectively. At these conditions, ethylene would partly liquefy. Thus, to keep the ethylene at room temperature, roughly 1.18 kW of heating are required. This additional power input is realized by wrapping the jet manifold tubing with heat tape capable of $1.4\,\mathrm{kW}$ power output and adding insulation around the heated tubing parts. In addition, heat transfer through the wall of the metal tubing compensates a small part of the Joule-Thompson effect.

With the aforementioned measures, the stagnation jet temperature upon injection is always at $T_{0,j} = 311.4 \pm 12$ K and never drops low enough to damage upstream components, see also the example run conditions in Fig. 3.2. The variations in $T_{0,j}$ are due to the expansion properties of the different gases and changes in ambient conditions as discussed in Sec. 3.1.

Table 3.2: Properties of gases used for injection and design ranges of nominal mass flow rates and jet Reynolds numbers. Entries marked with * depend strongly on temperature, the values reported here are representative at room temperature. Molecular weight MW in $[\mathrm{g/mol}]$. SI refers to the single jet injector, DI to the staged dual jet injectors.

Gas	Argon Ar	Carbon dioxide $\mathrm{CO_2}$	Ethylene $\mathrm{C_2H_4}$
MW $[\mathrm{g/mol}]$	40.00	44.01	28.05
γ	1.66	1.28*	1.237*
J	1-6	1-6	1-6
$\dot{m}$ $[\mathrm{g/s}]$	$3.5 - 21.0$	$3.9 - 23.3$	$3.1 - 18.7$
$Re_d \cdot 10^3$ SI	$151.8 - 910.7$	$148.1 - 888.6$	$117.4 - 704.1$
$Re_d \cdot 10^3$ DI	$107.0 - 642.0$	$104.4 - 626.5$	$82.7 - 496.4$
Gas	Helium He	Nitrogen $\mathrm{N_2}$	
MW $[\mathrm{g/mol}]$	4.00	28.00	
γ	1.66	1.40	
J	1-6	1-6	
$\dot{m}$ $[\mathrm{g/s}]$	$1.1 - 6.7$	$3.0 - 18.2$	
$Re_d \cdot 10^3$ SI	$48.0 - 288.0$	$120.8 - 724.5$	
$Re_d \cdot 10^3$ DI	$33.8 - 203.0$	$85.2 - 510.8$	

The standard deviation of the momentum flux ratio, J, during data acquisition is on average $\sigma_{J,run} = 0.08$ for all cases presented, with a maximum value of 0.22. The variations are due to jet supply temperature and pressure changes. The temperature can vary during data acquisition due to transient heating effects along the jet manifold. The pressure varies slightly as the bottles are emptying due to the characteristics of the single stage regulator. Bottles are exchanged before these supply pressure effects become significant.

Run-to-run, the desired set point for J can be attained with an absolute standard deviation in the range $\sigma_J = 0.05 - 0.23$ (with larger absolute deviation for higher J). This range corresponds to a relative run-to-run variation of $\sigma_J/J \approx 0.03 - 0.05$.

3.2 Laser Induced Plasma Ignition

To initiate chemical reactions in the JISCF flow field, laser induced plasma (LIP) ignition is utilized. In this technique a laser beam is focused and the pulse energy increased until the

gas in a small volume at the focal point is ionized and dissociated. This is a non-resonant process, i.e. no particular transition is targeted and the absorption process depends on multiphoton ionization leading to electrical breakdown and subsequent inverse bremsstrahlung. Temperatures in excess of 100,000 K in the LIP region have been measured (Bradley *et al.*, 2004).

Throughout this study, the term "spark" refers to the initial plasma region created by the laser energy deposition. This spark evolves into an "ignition kernel" if it is in contact with a potentially reactive mixture and not immediately quenched. The ignition kernel can then grow or quench, depending on flow conditions. Burning and non-stationary flame growth can occur as the ignition kernel evolves. A fully developed flame, however, would only be reached if the kernel evolves into some asymptotic, stable state and does not quench or blow out eventually.

Bradley *et al.* (2004) describes the evolution of a LIP spark in great detail. In their mesurements, most of the laser energy is transferred to the gas in about 10 ns. The laser energy deposition leads to the existence of a high temperature, high pressure region, resulting in an outward traveling spherical shock wave. Preferential absorption leads to an elliptical shape of the plasma region and a displacement of the shock wave center relative to the plasma ellipse centroid. A rarefaction wave following the shock wave, together with the specific spatial temperature distribution, leads to the formation of two ring vortices and contra-rotating toroidal gas motion. The toroids have their symmetry axis aligned with the laser beam direction. At later times (> 50 µs), a strength imbalance between the two vortices leads to preferential gas flow towards the incoming laser beam and the formation of a third lobe, see the example in Fig. 2.14.

In reacting mixtures, Bradley *et al.* (2004) and Ochs and Menon (2020) observe an overdrive effect due to the laser spark, i.e. during a certain time after LIP initiation, the particular gas dynamics and the amount of energy deposited can enhance and definitely influence the flame development.

A schematic of the LIP setup for this study is shown in Fig. 3.8. The driving laser beam comes from a fundamental frequency (1064 nm) Nd:YAG laser. The focusing lens for this beam is a 25.4 mm diameter, 80 mm focal length aspheric lens with a 1064 nm V-coating.

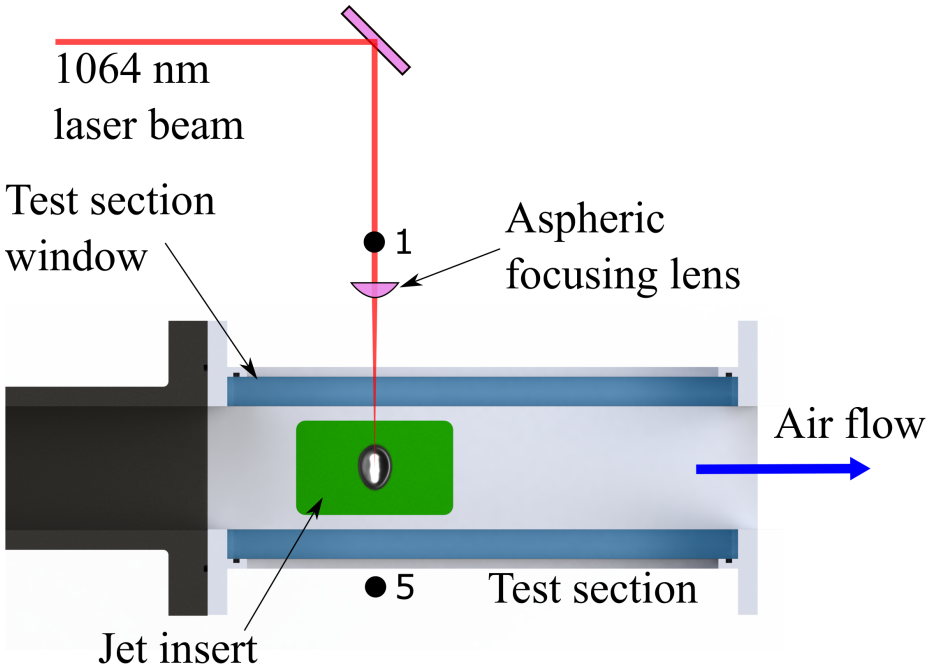

Figure 3.7: Top view of the LIP setup used in the reacting JISCF experiments presented in this study.

Based on a study by Ochs and Menon (2020) for premixed flames in a supersonic flow it is desirable to deposit > 10 mJ of energy into the laser spark to ensure that breakdown and ignition probability are close to 100%. Their results were reported for an equivalence ratio of one (methane-air) and a flow static density of ~ 0.79 $\mathrm{kg\,m^{-3}}$. Since, for this study, the static crossflow density is expected to be slightly lower (~ 0.7 $\mathrm{kg\,m^{-3}}$), it is desirable to deposit more energy. Moreover the study by Bradley *et al.* (2004) used a 532 nm laser while the present study utilizes 1064 nm. Phuoc (2000) found that for the latter wavelength, the breakdown threshold energy increases by a factor of $\sim 1.7 - 2$. The flow through times are too short to achieve complete independence from the initial laser energy deposition, but Ochs and Menon (2020) recommend higher laser energies to minimize variability. Considering all these different factors, a minimum deposited ignition energy of

35 mJ is chosen for this study and all reported data sets.

To ensure the desired amount of energy is deposited, the transmission coefficients of optical components in the beam path need to be known. Moreover, the size of the initial ignition kernel size depends weakly on the deposited energy (Mulla *et al.*, 2016), as does the rate of growth of the kernel in a reactive mixture (Ochs and Menon, 2020). To address both the transmission coefficients and the dependency of the initial ignition kernel on the amount of deposited energy, additional experiments at ambient conditions are conducted.

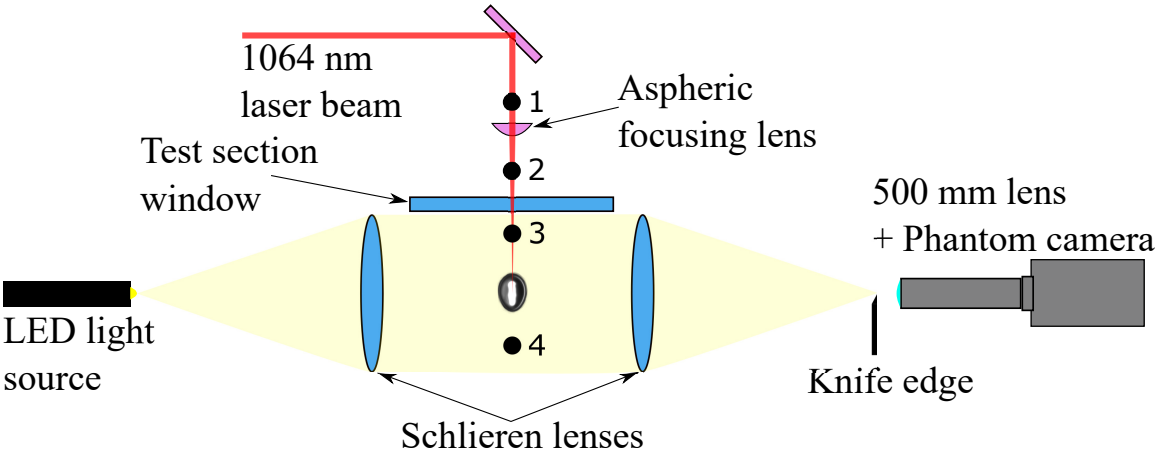

Figure 3.8: Schlieren and laser induced plasma setup used for characterization of the resulting plasma kernel.

For the required characterization the schlieren and LIP setup in Fig. 3.8 is utilized. More details about the schlieren diagnostic are given in Sec. 3.3.1. Laser energies and transmission through optical components is measured with a Coherent LabMax-TOP laser power meter and a J-50MG-YAG sensor. Schlieren recordings of the ignition kernel are accomplished using a Phantom v2640 camera and a horizontal knife-edge cut-off.

Laser energies are measured at positions 1, 2, 3 and 4. Tested energy levels are nominally $E_1 = 85$, 110, 135 and 150 mJ. The focusing lens transmission was determined to be $\sim 90\%$ while the window transmission is $\sim 87\%$ for all energy levels tested. The energies measured at 4 are interpreted as the energy not absorbed by the plasma kernel, however, due to the refractive effects in the vicinity of the hot plasma, it is likely that this somewhat underestimates the actual amount of energy not absorbed.

The resulting deposited energy is $E_d \approx 33$, 51, 65, 76 mJ for $E_1 = 85$, 110, 135 and 150 mJ, respectively. Because the amount of actual energy not absorbed could be higher than measured at position 4, a nominal laser pulse energy of $E_1 = 135$ mJ ($E_d \approx 65$ mJ) is chosen for the experiments in this study.

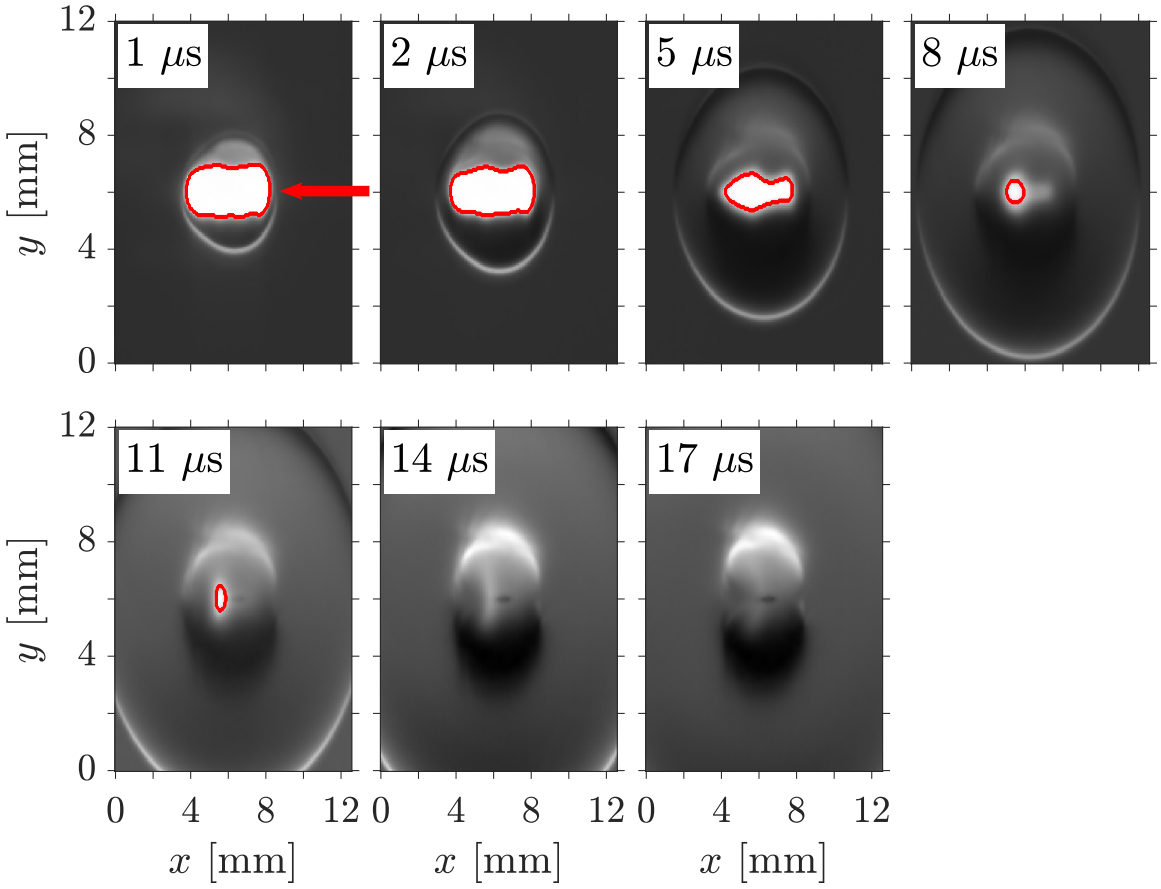

Figure 3.9: Evolution of the $E_1 = 135$ mJ spark in air at ambient conditions. The laser beam comes into the image from the right and is indicated in the first image by the red arrow. The contour used for ellipse fitting is denoted red lines around the plasma region.

Fig. 3.9 shows the evolution of the $E_1 = 135$ mJ spark in air at ambient conditions. The bright region in the center of the images is the plasma. It decays over time and exhibits the expected elliptical shape. At 14 µs after laser energy deposition, no plasma is visible anymore. Around 5 µs, the formation of a region of hot gas can be discerned close to the the plasma kernel. This region grows very slowly compared to the shock wave, is nearly circular, and does not radiate at visible wavelengths. At 14 µs and 17 µs it can be seen

that the hot gas region starts fold in on itself along the axis of the incoming laser beam due to the toroidal vortex motion discussed earlier. The observed times are too early for the formation of the third lobe to occur.

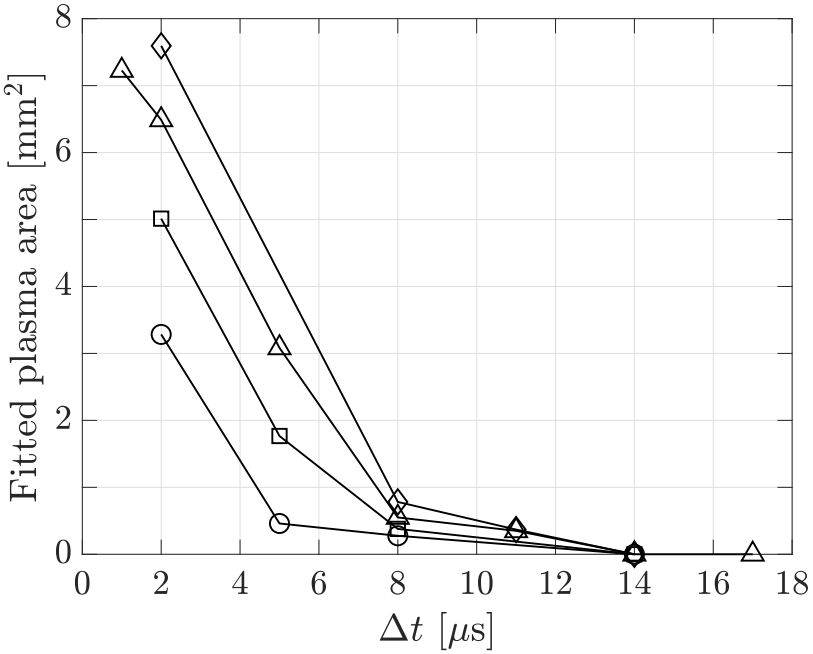

Figure 3.10: Time evolution of the visible light emitting plasma area. ◯ : $E_1 = 85$ mJ, □ : $E_1 = 110$ mJ, △ : $E_1 = 135$ mJ, ◊ : $E_1 = 150$ mJ.

To quantify sensitivites of the laser spark on the deposited energy, the edge of the plasma region is found in the schlieren images using a thresholding technique. Then, an ellipse is fitted (Fitzgibbon *et al.*, n.d.) to the plasma contour to get the semi-major and -minor axis and the plasma area. The plasma area evolution with time is presented in Fig. 3.10. Clearly, the volume of gas ionized and heated by the laser increases with increasing spark energy. Moreover, no visibly active plasma seems to exists after 14 µs for all cases. The plasma is probably going to be visibly active for a longer time at the actual experimental conditions of this study because the density is lower, i.e. collisional energy transfer and recombination take longer.

The nominal laser energy used in this study is $E_1 = 135$ mJ. One microsecond after laser energy deposition, the semi-major axis of the resulting spark is 2.4 mm and the semi-

minor axis is 0.9 mm. Furthermore, a linear estimate of the spark size dependence on deposited ignition energy is made. This yields the following sensitivities for the major axis, minor axis, and fitting ellipse area,

$$\frac{\partial r_{maj}}{\partial E_d} = 0.023\,\mathrm{m/J}, \tag{3.6}$$

$$\frac{\partial r_{min}}{\partial E_d} = 0.008\,\mathrm{m/J}, \tag{3.7}$$

$$\frac{\partial A_{ell}}{\partial E_d} = 1.070 \cdot 10^{-4}\,\mathrm{m^2/J}. \tag{3.8}$$

Interestingly, the semi-major axis, the axis aligned with the incoming laser beam, is more sensitive to the ignition energy than the minor axis. Thus, an increase in deposited laser energy will increase the plasma volume mostly in one direction. These sensitivities are also used in the uncertainty estimates described in Appendix C.

As can be seen in Fig. 3.10, the light emissions from the plasma kernel region saturate the camera chip. This can lead to blooming and a subsequent overestimation of the plasma kernel size. However, the calculation of the derivatives described above shows no significant sensitivity to the time delay at which it is performed. Thus, it is concluded that blooming has no impact on these quantities of interest.

During each LIP experiment presented in this study, the laser energy ahead of the focusing lens at position 1 and after the second test section window at position 5 in Fig. 3.7 is measured before and after data acquisition. In combination with the characterization above, this is used to calculate the actual deposited energy in each experimental run. Some deterioration on the windows and the focusing lens between experiments in Ch. 5 and Ch. 6 changed the mean deposited energy from $E_d = 70 \pm 4\,\mathrm{mJ}$ to $E_d = 55 \pm 10\,\mathrm{mJ}$, respectively. The $\pm$-values reported are one standard deviation computed from all data sets collected. In all reported cases the ignition energy is above the selected threshold of 35 mJ.

3.3 Diagnostics

The test facility is monitored using a National Instruments LabView setup. Data from pressure transducers and thermocouples is read out and recorded through the LabView interface at 10 Hz, as well.

The jet flow field has to be fully established and light sources, cameras and simultaneous diagnostics have to be synchronized to obtain meaningful results. This is achieved using Berkeley Nucleonics Corp. 575 Pulse Generators.

For accurate results, all optical diagnostics are calibrated with a LaVision 058-5 calibration target or a two-dimensional version of said target.

Due to preheating of the test air the facility experiences thermal expansion during experimental runs. Before data acquisition, some time is allocated to achieve thermal equilibrium. However, the field of view (FOV) of the installed cameras still experiences a shift of 0.18-0.83 mm during data acquisition. An additional camera is used to track a target on the test section and this thermal shift is corrected during data processing.

All images obtained via optical diagnostics have to be dewarped and transformed from pixel to physical lab coordinates. The LaVision DaVis 8.4 software is used for this step, in combination with calibration images from standard 58-5 calibration plates. The calibration images are taken at least once a day and before every first run of a given experimental set. In all cases the calibration yields a standard deviation of the polynomial mapping function $<$1 px. Additional processing steps depend on the diagnostic used and will be described in the following sections.

3.3.1 Schlieren

Two Toepler-type schlieren setups are used in this study to visualize line-of-sight averaged density gradients. One is a linear lens setup discussed in Sec. 3.2 and used for laser spark imaging. The other is a Z-type two-mirror schlieren arrangement (Settles, 2001) used for

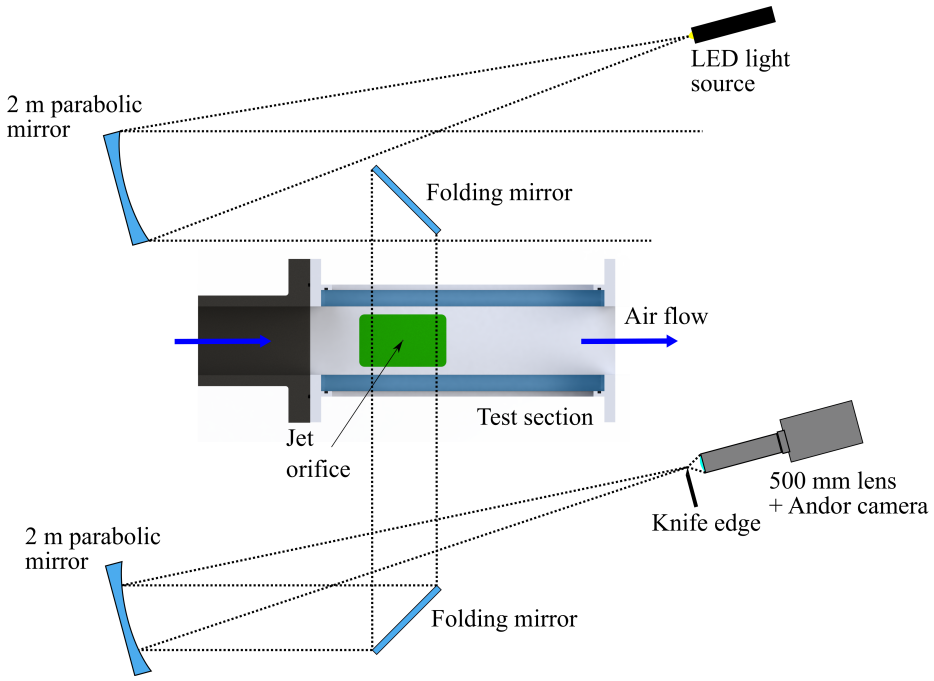

Figure 3.11: Schematic of the Z-type schlieren setup in its arrangement around the JISCF experiment. Distances and angles are not to scale. In the experiment the angles of the parabolic mirrors relative to the flow direction are $\sim 5°$.

imaging in the actual test section.

The Toepler setup around the test facility is shown schematically in Fig. 3.11. The main components are the LightSpeed HPLS-36 Dragon Series LED light source, two 0.20 m parabolic mirrors with a surface accuracy of $\lambda/8$ and a focal length of 2.032 m, a straight knife edge on a Thorlabs precision height-adjustable mounting post and a Sigma 50-500 mm, $f/\# = 4.5 - 6.3$ Telephoto zoom lens before the camera. The light source can be run continuous or in a pulsed mode with a maximum duty cycle of 1% and is used in both schlieren setups.

For all line-of-sight averaged schlieren data presented in this study, the light source pulse length is 300 ns. A Phantom v2640 camera and magnification of 0.24 is used to image the laser spark. An Andor Zyla 5.5 camera is used for imaging with the Z-schlieren setup and a magnification factor of roughly 0.258.

3.3.1.1 Data Processing

The schlieren records are median filtered, flat-field and background corrected, before any further evaluation or computation of statistics. The dark-field and light-field images required for the flat-field correction are obtained as follows. For the dark-field image, the camera is turned on but the lens cap is not taken off. 20-40 images are taken in this state to get a measure of the average dark current recorded by the camera. For the light-field image, a uniform LED source of illumination is used and adjusted such that all pixels of the camera are at approximately 60-70% saturation. Again, 20-40 images are taken in this state to get a measure of the pixel response. All records used to form the background-correction image are also flat-field corrected.

The flat-field correction of an image is performed as follows,

$$I_f = \frac{(I - D)\, m}{L - D}, \tag{3.9}$$

where I_f is the flat-field corrected image, I is the image to be corrected, D is the dark-field image, L is the light-field image, and m is the average value of the difference between light- and dark-field.

Subsequently, the background correction is performed based on,

$$I_b = I_f - \bar{B_f}', \tag{3.10}$$

where $\bar{B_f}$ is the flat-field corrected, average background image. The background correction images are recorded at the end of each data acquisition.

For schlieren specifically, the background image is taken as the difference to the average illumination in the field of view,

$$\bar{B}'_f = \bar{B}_f - \langle \bar{B}_f \rangle. \tag{3.11}$$

The flat-field and background corrected images are used for further evaluation.

3.3.2 Mie-Scattering and PIV

Visualization of the jet fluid is achieved using Mie-scattering off of small particles. For PIV measurements, not only the jet but also the crossflow is seeded. The diagnostic setup is shown schematically in Fig. 3.12.

A 532 nm Big Sky laser is used for particle illumination with a pulse length of 8 ns, 30-40 mJ/pulse of energy, and running at 5-10 Hz. Three cylindrical lenses are used to shape the laser beam into a sheet with a collimated width of $\sim 50\ \mathrm{mm}$. The lenses are a 1500 mm concave and a 750 mm convex lens for the sheet width and a 500 or 750 mm convex lens for the thickness. The thinnest part of the laser sheet is positioned 2-3 mm above the test section floor.

Andor Zyla 5.5 cameras record the Mie-scattering with a 5.5 Megapixel sCMOS chip. Tokina 100 mm macro lenses are used for light collection and focusing. Apertures are set to $f/\# = 8$ for all Mie-scattering concentration measurements, and $f/\# = 11$ and $f/\# = 16$ for zoomed-in and zoomed-out PIV data sets, respectively.

Utilized resolutions and laser sheet thicknesses for the different Mie-scattering data sets in the presented work are summarized in Tab. 3.3. It is clear that the limiting resolution in all cases is the out-of-plane laser sheet thickness.

To improve the fidelity of Mie-scattering concentration measurements, a part of the laser sheet is split off the main beam, using a quartz-glass plate, and directed into a rhodamine dye-cell. The fluorescence in the cell is imaged with an additional camera to provide an instantaneous laser profile for image correction. No attempt was made at measuring the laser energy itself during the experiment for shot-to-shot image corrections. However, the laser is relatively stable with RMS energy fluctuations below 1 mJ.

Aero-optical effects as described by (Elsinga *et al.*, 2005a) are only mitigated in so far as negative viewing angles relative to the symmetry plane bow shock position are avoided.

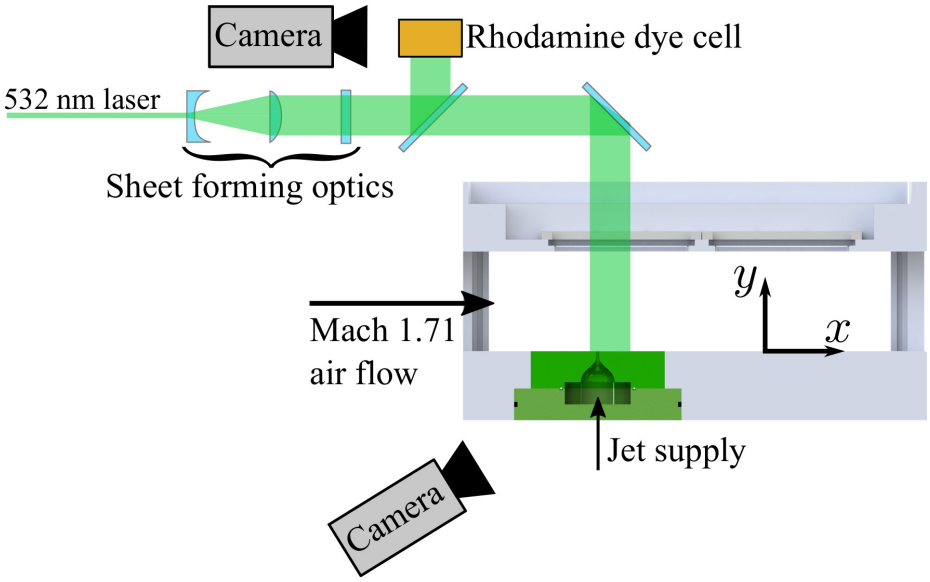

Figure 3.12: Optical setup for Mie-scattering experiments. For PIV measurements the rhodamine dye cell is not used.

Table 3.3: Summary of imaging properties for the Mie-scattering based diagnostics in different parts of this study. The first and second part have the same properties because the same data sets are being used. w_{ls} is the laser sheet width and d_{ls} the thickness. Due to the method used in calculating the mixture fraction field (Sec. 3.3.2.2) the effective resolution is lower than the pixel resolution.

	w_{ls} [mm]	d_{ls} [mm]	pixel res./eff. res.	vector res. [mm/vec]
Ch. 4	~ 50	0.64	~ 9.8 µm/px/108 µm	~ 0.16
Ch. 5	~ 50	0.64	~ 9.8 µm/px/108 µm	~ 0.16
Ch. 6	~ 50	0.64/0.82	~ 15.2 µm/px/137 µm	~ 0.24

Additional corrections are not implemented due to the lack of background-oriented schlieren data (Elsinga *et al.*, 2005a) and the relatively complicated shock geometries in the JISCF flow field. This can lead to unquantified errors remaining in both concentration and PIV measurements. It is expected that the error is only significant in the presence of shocks (around 5% deviation from the real value for PIV data (Elsinga *et al.*, 2005b)) and that regions of interest such as the jet shear layer are less affected.

That the current experiments are indeed affected by aero-optical effects is exemplified in Fig. 3.13. In the vicinity of the jet orifice, both the strong expansion and the subsequent barrel shock and Mach disk introduce changes in the index of refraction. The blurring effect

both in the core of the jet and close to the shock structures is clearly visible in Fig. 3.13a. Blurring is also evident in the vicinity of the stronger parts of the bow shock, see Fig. 3.13b. The aero-optical effects cause the formation of streak-like structures in the images.

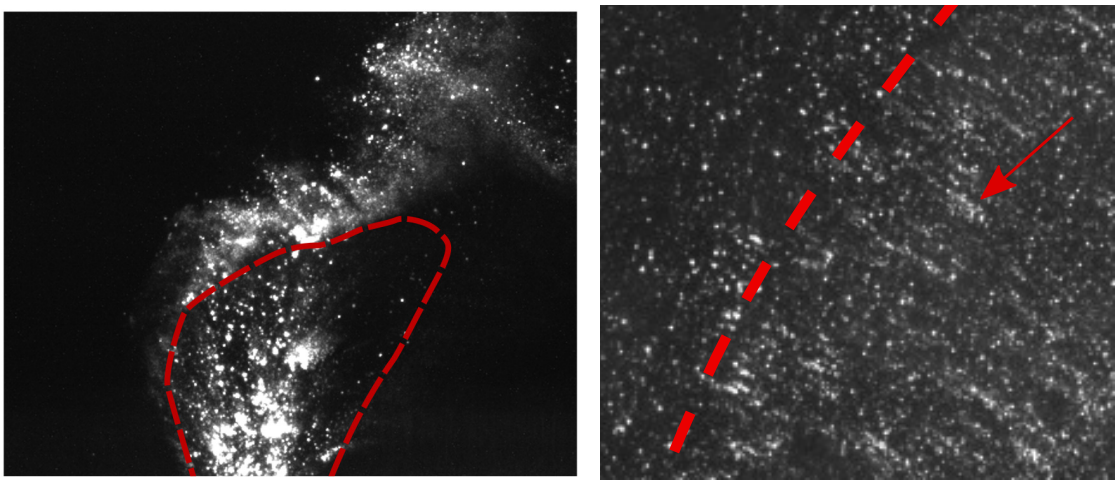

(a) Close to the jet orifice particle blur is clearly visible in the strong expansion region and close to the barrel shock structure. The approximate position of the shock is indicated by the dashed line.

(b) Close to the stronger parts of the bow shock, the particle blurring manifests itself in streak-like structures. The approximate position of the shock is given by the dashed line.

Figure 3.13: Examples of aero-optical effects in this study's flow fields.

For concentration data from Mie-scattering, potential errors are likely further mitigated by filtering and averaging in the post-processing. However, they could lead to an overestimation of concentration values in the vicinity of strong shock and expansion structures. In the case of PIV data, the largest source of error is likely the additional optical displacement of particle images introduced by beam-steering in regions with large density gradients.

3.3.2.1 Tracer Particle Fidelity

Measurements using tracer particles in supersonic flows are a complex matter due to the high velocities and resulting short time scales. To address this difficulty, it is of paramount importance to select particles with sufficiently small response times to changes in the flow field, e.g. across shocks and expansion fans. In the following, the characteristic

response/relaxation time τ_p of different seed particles and seeding strategies is evaluated using the approach of Ragni *et al.* (2011).

In their study, τ_p is measured across a well-defined planar oblique shock. In the present experiments, an initial evaluation is performed across the Mach disk of a free, sonic jet with $p_j/p_\infty = 9.5$. The most promising seed particles are then evaluated again across a planar oblique shock generated by a 10° ramp in the current experiments supersonic crossflow, for more reliable estimates of the response times.

The equation to compute τ_p from velocity data in these flow fields is,

$$\tau_p = \xi_p \left[u_{n1} - (u_{n1} - u_{n2})\, e^{-1} \right] - 1, \tag{3.12}$$

where subscripts 1 and 2 refer to states before and after the shock and n is the shock normal direction. The quantity ξ_p is the shock-normal distance from the leading edge of the shock to the point where the pre-shock velocity has been reduced to,

$$u_n = u_{n2} + (u_{n1} - u_{n2})\, e^{-1}. \tag{3.13}$$

The required velocity data is obtained from Mie-scattering image pairs with a laser pulse separation of 300 ns. The image pairs are processed with the PIV software LaVision DaVis 8.4. The resulting vector resolutions are in the range of 150-210 μm.

The seed particle options considered for this study consist of solid titanium dioxide, solid silicone dioxide, and a white mineral oil based liquid. While tracers based on oil or smoke can potentially yield lower relaxation times, solid particles are desirable for a possible extension of the presented work to other applications. Specifically, to employ Mie-scattering diagnostics in hot, reacting supersonic flows. Titanium dioxide and silicone dioxide have both been used in supersonic flows in the past (Ragni *et al.*, 2011; Howison and Goyne, 2010).

A wide range of concepts exist to actually introduce tracer particles into the flow of in-

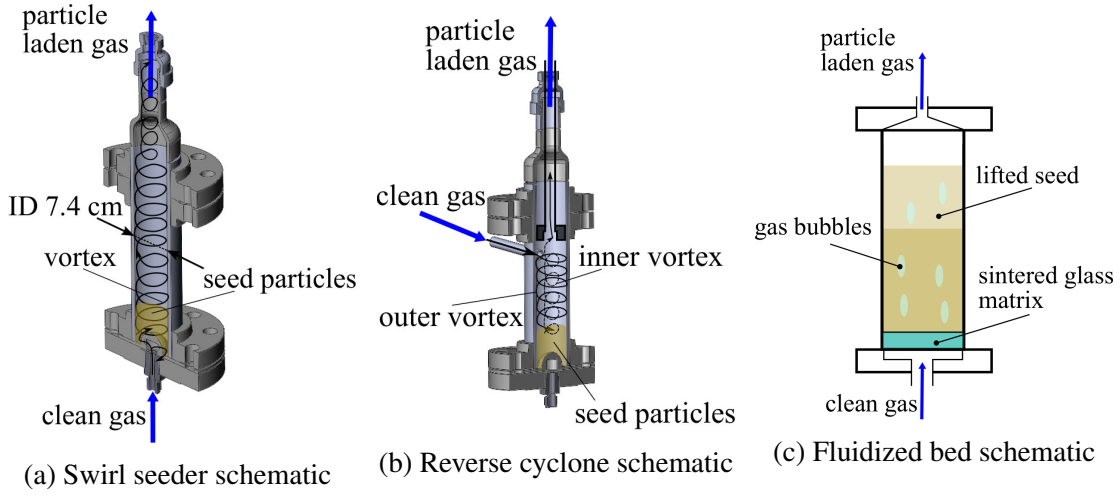

(a) Swirl seeder schematic (b) Reverse cyclone schematic (c) Fluidized bed schematic

Figure 3.14: Schematics of the different seeding devices evaluated in this study for the seeding of an underexpanded, sonic jet.

terest. For high velocity jet flows, high-shear concepts appear to be advantageous (Howison and Goyne, 2010). The high-shear is required to uniformly seed the flow and effectively separate the very small particles, which can exhibit strong attractive forces due to electrostatic charges, van der Waals interaction, and capillary bridges (Rhodes, 2008). In this study, the three concepts evaluated are a swirl seeder, a fluidized bed seeder, and a reverse cyclone seeder. The ratio of jet fluid flowing through the seeder to jet fluid bypassing it is controlled by adjusting the pressure drop across two needle valves, as shown in Fig. 3.6.

The swirl seeder generates a vortex at the bottom of the device by directing incoming gas through multiple, similarly oriented orifices, which are arranged in an axisymmetric fashion. In the process, tracer particles are entrained and transported towards the outlet and the particle bed is partly fluidized. Out of the three concepts investigated, this one probably generates the largest amount of shear acting on the seed particles, as the orifices can choke. Fig. 3.14a shows a schematic of the device used in this study, it has two orifices in the small central dome at the bottom.

The reverse cyclone is a technique that is based on a device commonly used in particle processing, called the gas cyclone. However, instead of its original purpose of separating particles from a gas, the reverse cyclone obviously has the purpose to seed the gas with

tracer particles. It has been proposed for usage in Laser Doppler Velocimetry (LDV) by Glass and Kennedy (1977), who found the device produced a very steady seeding density with alumina particles. To evaluate the performance of a reverse cyclone, the swirl seeder is modified based on guidelines found in Rhodes (2008, chap. 9) for a high efficiency Stairmand cyclone. A schematic of the device is shown in Fig. 3.14b.

Finally, the fluidized bed is a commonly used type of seeder and also a common processing technique in the field of particle technology. At a sufficiently high gas flow rate through a particle bed, the gas drag force will equal the apparent weight of the bed and particles will lift and move around. Ideally, one wants to achieve non-bubbling fluidization which yields an evenly seeded working fluid or gas. However, whether this is achievable depends on the desired gas velocities, particle properties, and the seeder geometry. For a range of very small particle sizes, proper fluidization becomes difficult (Rhodes, 2008, chap. 7). The fluidized bed device used for this study is presented in Fig. 3.14c.

For the mineral oil based tracers, a pressure and heat driven system is used to atomize the oil. The system has to be installed close to the injection system and a heat trace has to be used in the device's nozzle to avoid excessive agglomeration of the liquid droplets before injection into the main flow. The main flow itself cannot be too hot or the droplets will completely evaporate. Thus, the white mineral oil approach limits the test section operating temperature to $\sim 450\ \mathrm{K}$.

With the solid particle seeding approaches, in-house designed and built seeders are used. The mineral oil liquid seed is injected using a commercially available Pea Soup Phantom Hazer.

The data used to determine relaxation times of solid particle tracers across the jet Mach disk are shown in Fig. 3.15a. The actual relaxation times measured are summarized in Tab. 3.4. Results for the mineral oil based approach are discussed later in this section. During the trials it became evident that after a storage time of two to three weeks, heating the seed particles significantly improved their performance. Therefore, only relaxation

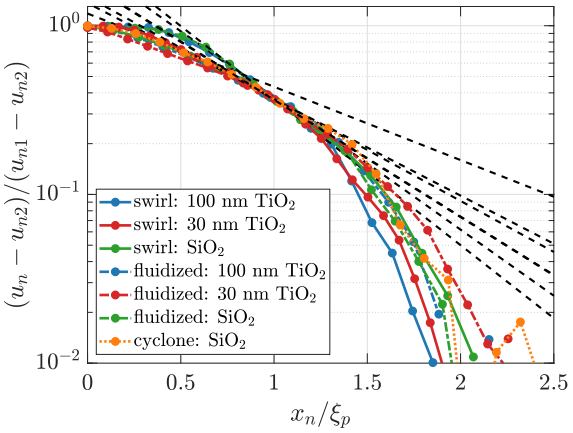

(a) Free jet velocity data and curve fits for a preliminary estimate of τ_p and corresponding trends for solid particles.

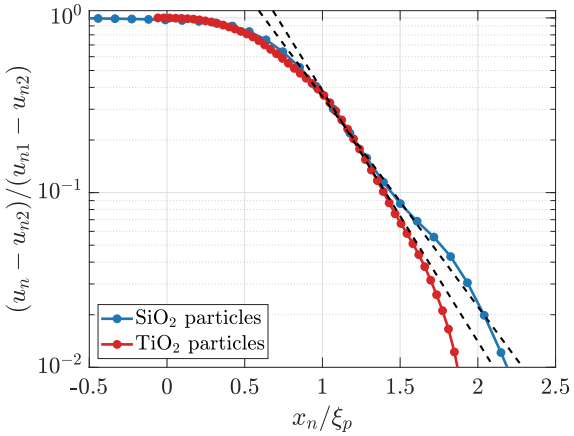

(b) Planar oblique shock velocity data for the more reliable determination of 100 nm TiO_2 and SiO_2 relaxation times.

Figure 3.15: Velocity data used to determine solid particle relaxation times. As described by Ragni *et al.* (2011) only the velocity component normal to the shock wave is considered and τ_p is determind from a curve-fit to $\ln(u_n^*) = -t/\tau_p = -x_n/\xi_p$, where $*$ denotes the normalized velocity given on the y-axis of these figures. Dashed lines are the curve-fits used for τ_p. x_n is the coordinate normal to the shock wave. Position 0 corresponds to the shock position.

Table 3.4: Particle relaxation times measured across the Mach disk of an underexpanded sonic nitrogen jet. The symbol $\times$ denotes cases in which the seeding density was too low to obtain reliable velocity measurements.

Particles	Nom. d_p [nm]	Swirl	Fluidized Bed	Reverse Cyclone
TiO_2	100	1.04 µs	1.25 µs	$\times$
TiO_2	30	1.77 µs	1.68 µs	$\times$
SiO_2	15	0.87 µs	0.75 µs	0.98 µs

times for seed particles that have been heated to > 480 K for more than 24 hours are reported.

It is important to note that the results from the Mach disk tests are not as well-defined as the relaxation times measured across an oblique shock. This is due to the lack of well-defined pre- and post-shock flow states.

Nonetheless, the trends of the measurements in Tab. 3.4 can be used to make a preliminary assessment of the seeding strategies. Overall, the SiO_2 particles perform best out of the three types of solid particles investigated. Interestingly, the 30 nm TiO_2 particles

perform the worst, which is probably due to the growing influence of attractive forces between the particles over inertial forces trying to separate them. The relaxation times of the $100\ \mathrm{nm}\ \mathrm{TiO_2}$ particles are slightly worse than those of the $\mathrm{SiO_2}$ particles and they seem to work better with a swirl technique than a fluidized bed, for the case of jet seeding.

Comparing the qualitative seeding uniformity of the jet using $\mathrm{SiO_2}$, the best results were achieved using the swirl seeder, see Fig. 3.14a. Presumably, the swirl approach imparts larger shear forces on the seed which leads to a more uniform tracer distribution. Since Mie-scattering diagnostics are also to be used for jet fluid concentration measurements and not only for PIV, and because the measured relaxation times are only about $15 - 20\%$ different, it was decided to use the swirl approach for jet seeding purposes.

To summarize, out of the techniques and particles evaluated, the preliminary particle relaxation time measurements together with a qualitative assessment of the seeding quality show that Aerosil R974 silica ($\mathrm{SiO_2}$) particles in a swirl seeder work best for the purpose of seeding a sonic, underexpanded jet.

The measurements for the $\mathrm{SiO_2}$ particles were repeated using free nitrogen, helium and argon jets with pressure ratios corresponding to momentum flux ratios of one, two, four and six: $p_j/p_\infty = 4.1$, 8.5, 16.3 and 22.8. In all cases relaxation times between $0.7\,\mu\mathrm{s}$ and $1.5\,\mu\mathrm{s}$ were measured, confirming the previous trials and the adequacy of the $\mathrm{SiO_2}$ particles. Lower relaxation times are measured for injectants with higher sonic speeds, i.e. likely higher shear generation.

To compute the $\mathrm{SiO_2}$ particle Stokes number the LDV data provided by Santiago and Dutton (1997) is used, which yields a maximum fluctuating velocity component of $\sqrt{\overline{u'^2}} = 178$ m/s. Together with a jet diameter of $2\ \mathrm{mm}$ the large-scale characteristic time-scale is estimated as $\tau = \sqrt{\overline{u'^2}}/d_j \approx 11.2\,\mu\mathrm{s}$, yielding a Stokes number of $St_{\mathrm{SiO_2}} = 0.08$. Ragni *et al.* (2011) also quote properties of a similar Silica product, Aerosil R972, with a response time of $\tau_p \approx 2.3\ \mu\mathrm{s}$, which is close to the presented result and still yields a sufficiently low Stokes number. Thus, it is concluded using the swirl seeder the $\mathrm{SiO_2}$ particles are able to

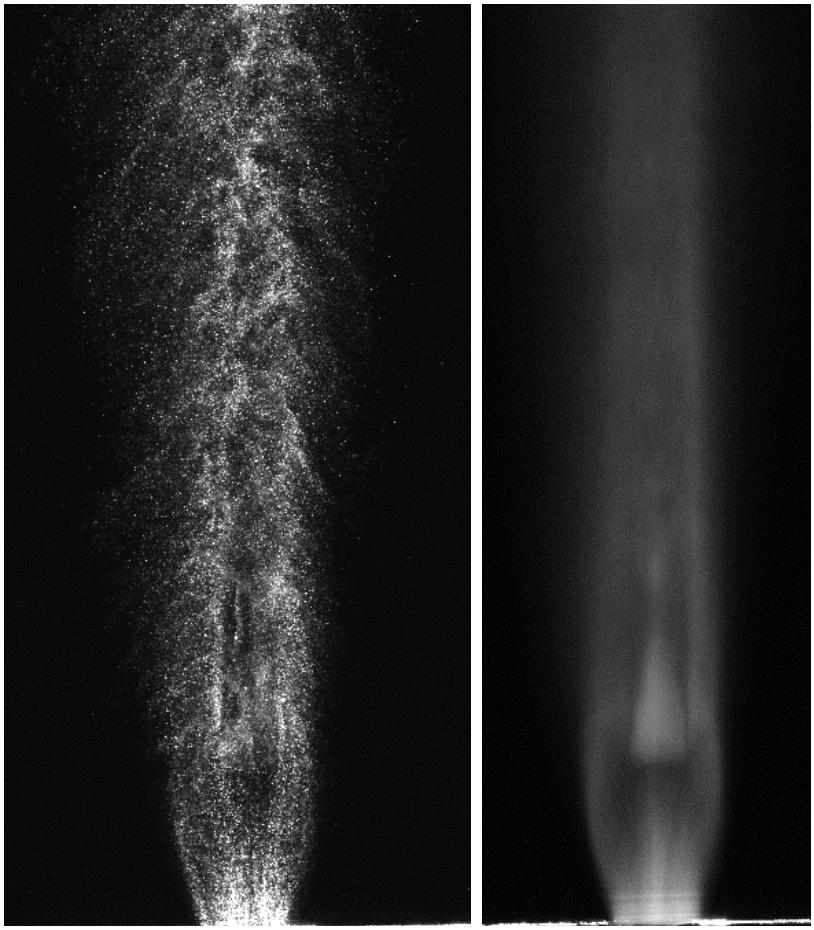

Figure 3.16: Example of free jet seeding results using $\mathrm{SiO_2}$ particles with the swirl seeder. Left: instantenous image, right: mean Mie-scattering image. The shear layer is discernible in the instantaneous image. The averaged image shows the expansion region near the jet orifice, the subsequent Mach disk shock region and re-expansion downstream.

follow large scale motions of the jet fluid reliably.

To obtain more reliable relaxation time measurements, a 10° oblique shock generator is installed in the test section. Then, the response time of the 100 nm $\mathrm{TiO_2}$ and $\mathrm{SiO_2}$ particles is measured across the resulting planar shock. Characterizing the particle relaxation time in this fashion yields the following results: $\tau_{\mathrm{SiO_2}} \approx 1.6$µs and $\tau_{\mathrm{TiO_2}} \approx 1.9$µs. Thus, a more reliable estimate of the particle Stokes numbers are $St_{\mathrm{SiO_2}} = 0.14$ and $St_{\mathrm{TiO_2}} = 0.17$, respectively. This agrees with trends from the jet measurements and confirms that the selected particles are suitable for the proposed experiments. Ideally, the Stokes number is below 0.1, but values below 0.3 should be sufficient to have tracer particles follow large

scale structures reliably.

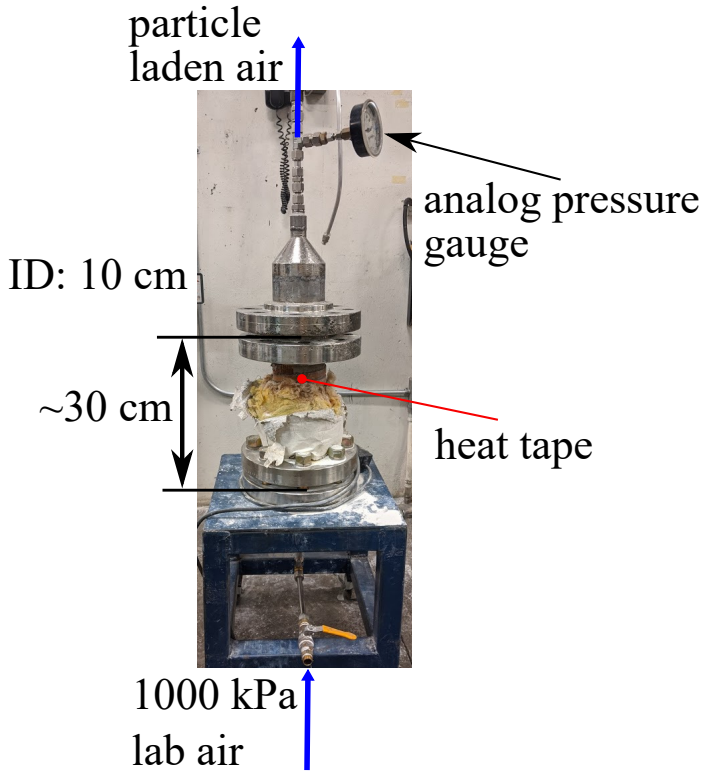

Figure 3.17: Annotated image of the fluidized bed seeder used for seeding of the supersonic crossflow with TiO_2 particles.

With a nominal diameter of 200 nm, the mineral oil based approach provided lower relaxation times than any of the solid particle tracers, consistently $\tau_p < 1$ µs. However, in further tests it was not possible to achieve continuous operation with high enough seeding densities and without significant deposition of liquid oil on the test section windows. This is likely due to the insufficient pressure head on the particular Phantom Hazer unit used and the relatively high crossflow stagnation temperature. The unit is rated for a maximum supply pressure of ~ 862 kPa, while the crossflow pressure is ~ 379 kPa. At lower flow temperatures or if the unit could be retrofitted to provide a larger pressure head, it might be possible to overcome this limitation.

In contrast to the jet flow, the crossflow is seeded with a fluidized bed setup. The crossflow is not directed through the seeder directly, instead an additional 862 kPa air line in the laboratory is used that runs through the seeder and is then directed into the crossflow

through an array of counterflowing jets. The decision to use the fluidized bed for crossflow seeding is based on two factors. One, this setup seems to provide sufficient shear and time for a relatively uniform distribution of seed particles in the test section flow. Two, a large fluidized bed seeder is available that is compatible with the mass flow rates and pressures required to seed the crossflow. A picture of the fluidized bed seeder used is shown Fig. 3.17.

For experimental data presented in the rest of this study, the crossflow is seeded with US Research Nanomaterials 100 nm $\mathrm{TiO_2}$ particles and the jet with the Aerosil $\mathrm{SiO_2}$ particles. $\mathrm{SiO_2}$ does not work well in the crossflow due to the low bulk density and the high air mass flow rates. The 100 nm $\mathrm{TiO_2}$ particles performed very well with regard to qualitative crossflow seeding density and their relaxation time is only $\sim$19% higher than that of the $\mathrm{SiO_2}$ particles.

3.3.2.2 Mixture Fraction Measurements

In an isobaric and isothermal flow, the Mie-scattering signal averaged over a finite area is directly proportional to the jet fluid concentration, if the jet fluid is the seeded stream. This also assumes that the Mie-scattering recordings are fully corrected for background and laser sheet non-uniformities, multiple scattering of light is negligible and the particle image size is diffraction limited. For a binary mixing process of two pure fluids the mass concentration, or density, of one component can be directly related to the mixture fraction, f, in that fluid element as $\rho_j = \rho f$. Here, subscript j refers to the fluid that originates in the jet.

The recorded Mie-scattering signal, S, can be described by the equation,

$$S = C E_I \alpha_j \frac{d\sigma}{d\Omega} d\Omega \rho f. \tag{3.14}$$

Here, C is a calibration constant, E_I is the incident laser energy, α_j is the jet seeding rate and Ω is the solid angle. Furthermore, the differential scattering cross section $d\sigma/d\Omega$

describes the strength of the scattered signal as a function of incident light wavelength and particle size. The expression assumes that the lineshape of the scattered light is within the transmission window of any filters and lenses in front of the camera chip.

Due to dilatation caused by the compressible nature of the JISCF flow field, variations in temperature and density are decoupled from the jet fluid concentration. Thus, in regions where such effects are strong, the signal S in Eq. (3.14) cannot be unique related to ρ_j but only to the product ρf (Sautet and Stepowski, 1994). The latter now also reflecting changes in density that are not associated with changes in local composition.

Dilatation effects are especially strong close to the injection point of the jet, where strong flow expansion and compression occur (e.g. the Mach disk, barrel shocks and jet bow shock). Further away from the injection point and the jet centerline, it is more likely that the scattering signal actually represents the local jet fluid mass concentration only. Nonetheless, without a separate density measurement, no definitive statement can be made regarding this issue in any region of the flow.

Furthermore, the differential scattering cross section varies strongly and non-linearly with particle size, i.e. $d\sigma/d\Omega = f(r_p^n)$. Where n varies from roughly six, in the Rayleigh scattering regime, to two, in the high-frequency optical limit. This represents a problem if the distribution of particle sizes is not uniform, e.g. due to agglomeration.

To account for these effects, a technique proposed by Pernpeintner *et al.* (2011) is utilized. They treat the Mie-scattering image recorded by the camera as a convolution of the actual mixture fraction, f, and the seeding density, ω. Here, the latter includes effects due to variable α_j and $d\sigma/d\Omega$. By solving this ill-posed inverse problem the seeding density probability density function (PDF), p_ω, and the Mie-scattering signal PDF, p_S, can be deconvolved and one can recover the PDF of $(\rho \cdot f)$, for dilatational flows. While this is still not the pure mixture fraction, it improves the fidelity of the results and simplifies interpretation.

The formulation of Pernpeintner *et al.* (2011) is modified to a 2^{nd} order regularization

as it should yield more physically reliable results, i.e. the Tikhonov matrix is not a constant multiplied to the identity matrix, but rather a finite difference operator yielding the 2^{nd} derivative of p_S. To find the ideal value of the Tikhonov regularization parameter, the L-curve method is used in conjunction with the triangle method to find the L-curve corner (Castellanos *et al.*, 2002). Furthermore, a bin size of 11×11 pixels is chosen, yielding at least 121,000 samples for each p_S across the domain. For p_ω, a slightly larger domain very close to the jet exit is chosen, with a bin size of 50×50 pixels yielding 2.25 million samples for p_ω. The dynamic range of the Mie-scattering recordings is reduced from 2^{12} to 2^8 to limit the number of PDF bins.

Using this technique, the dependence of the Mie-scattering signal on the calibration constant and E_I in Eq. (3.14) is also removed. The Mie-scattering signal is normalized using a reference, p_ω, from a region where it is known that $f \approx 1$. Thus, the statistics reported in this study are the normalized average $\overline{\rho f}/\overline{\rho f}_0$ and the normalized root-mean-square (RMS) $\sqrt{\overline{(\rho f)'^2}}/\overline{\rho f}_0$ of the density-mixture fraction product. In the following, the normalized product of density and mixture fraction will also be referred to as the (normalized) jet fluid signal.

To some degree, this technique is equivalent to normalizing each recorded Mie-scattering image by an instantaneous reference signal taken in the potential core close to the jet orifice, see Sautet and Stepowski (1994). The Tikhonov regularization provides one additional parameter to relate the reference signal to the recorded scattering signal and the true tracer particle concentration. Moreover, the binning yields a more meaningful average Mie-scattering signal per bin.

To test how sensitive the presented results are to the technique used in computing jet fluid signal statistics, two other, simpler techniques are compared to the PDF method in Sec. 3.3.2.4. One being a direct average of the Mie-scattering records, the other based on a thresholding and binarization of particle images.

Uncertainties reported directly for the mean and rms jet fluid signal are computed as

described in Appendix C. This uncertainty only represents the statistical uncertainty but not the true data uncertainty. For the latter, since an ill-posed inverse problem is solved to obtain the jet fluid signal statistics, a Bayesian inference approach is required. The quantification of the corresponding uncertainty has not been attempted for this study.

A possible factor deteriorating jet fluid measurements is excessive re-scattering or absorption of photons in the case of an optically thick medium. A medium is no longer optically thin, if the following inequality is violated,

$$x\sigma_{ext}[C]_{avg} = x/\ell \leq 0.1, \tag{3.15}$$

where x is the characteristic distance over which photons will travel through the absorptive medium to the imaging system and ℓ is the optical depth. For the present case of Mie-scattering, σ is taken to be the extinction coefficient, which is the measure of energy attenuation as light interacts with a Mie-scattering seed particle. This will lead to a more conservative estimate as it neglects forward scattering. The extinction coefficient is estimated as $\sigma_{ext} = 2.69 \cdot 10^{-12}\,\mathrm{m}^2$ using MiePlot v4614 (Laven, Philip, 2016).

Assumptions for this calculation include a refractive index of air $n_{air} = 1.0001539$, computed via the modified Edlén equation, and a worst case particle (SiO_2) diameter in the range $d_p = 0.8 - 1.6\,\mu\mathrm{m}$. Rearranging Eq. (3.15) and setting $x = 40\ \mathrm{mm}$ (half-width of the test section), thus, yields a maximum permissible seeding density of $C_{avg} \sim 10^{12}\ \mathrm{m}^{-3}$. With seeding densities that should be on the order of $\mathcal{O}\left(10^8 - 10^10\,\mathrm{m}^{-3}\right)$ (Melling, 1997), there should be no significant absorption or re-scattering affecting the presented data.

3.3.2.3 PIV

To obtain velocity fields from Mie-scattering records both the jet and the crossflow are seeded. Image pairs with a laser pulse spacing of 300 ns are collected and the pairs are processed using LaVision's DaVis 8.4 software to find correlation peaks and displacements.

A 50% overlap between interrogation windows is used to obtain smoother velocity fields.

Vector spacings for the different parts of this study are summarized in Tab. 3.3 and the data processing is described further in Sec. 3.3.2.4. For a more detailed description of PIV as a technique see the book by Adrian *et al.* (2011).

While the particle response has been characterized thoroughly in Sec. 3.3.2.1, the results show seeding in the jet wake near the wall is insufficient to obtain reliable vectors, see the example velocity vector field in Fig. 3.18. In fact, it seems the dynamics of the flow field are such that achieving sufficient seeding density in this region is even more challenging than in the rest of the flow field. Thus, vectors with an insufficient amount of samples or too high uncertainty were masked out completely.

Three mechanisms have been identified which, by themselves or working in collaboration, can cause the seedings density in the jet wake to drop significantly. One is the generally low density in the jet wake due to expansion effects. The strong expansion of jet and crossflow fluid in this region lowers the density of seedings particles in this region. Moreover, very little jet fluid flows into this region to begin with as most moves through the windward barrel shock and the Mach disk. A second possible mechanisms is tied to the strong streamline curvature that the crossflow fluid has to follow around the jet column, close to the wall. If this curvature is large enough, the centrifugal forces can push seeding particles away from the corresponding streamlines. The pushed out particles will eventually follow a different, less curved streamline that might lead back into the wake region further downstream. However, close to the jet column, a seed depleted region is created by this mechanism. The first and second mechanisms can be aggravated by a third one, where the three-dimensional nature of the bow shock preceding the jet generally lowers the available seeding density on the plane of symmetry. The deflection of the flow around the bow shock is such that fluid, and seed particles, will partly flow around it, away from the symmetry plane.

For the analysis presented in this study, only the mean velocity field, its derivatives,

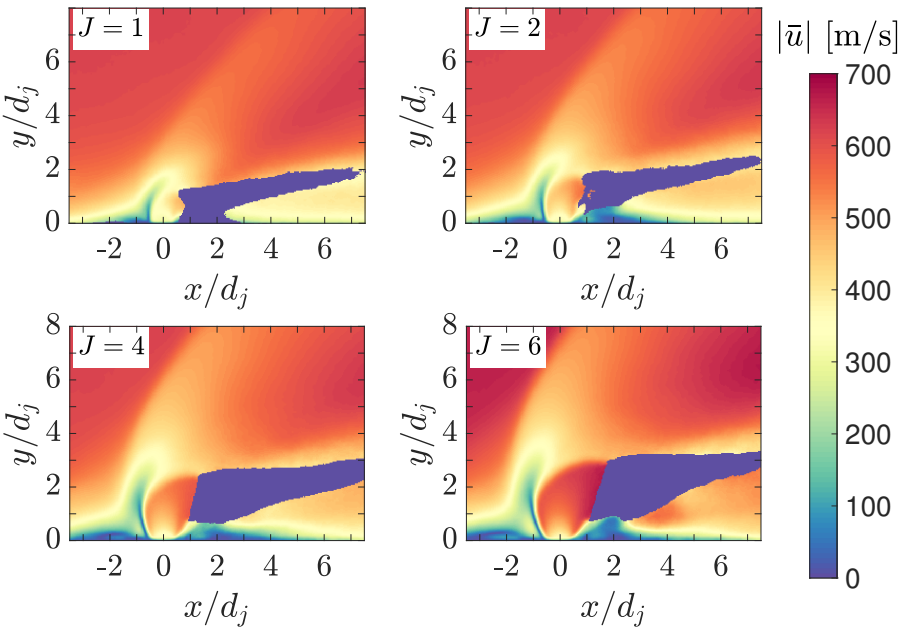

Figure 3.18: Example of PIV mean velocity fields for the nitrogen jet illustrating the missing vectors in the jet wake.

the bow shock position, and trends in the fluctuating velocity components are used. With a measured Stokes number of 0.14-0.17, trends in first and second order statistics should be reliable. An exception being regions directly downstream of shocks. The leading edge position of shocks, however, should be identifiable with reasonable accuracy. Furthemore, second order statistics will experience significant filtering due to smaller scale dynamics not being followed.

For further validation of the velocity quantities of interest, two steps are taken. One is a comparison between bow shock shapes that can be extracted from PIV results and bow shock shapes observed in schlieren data. The other step is to compare the presented results to published literature at similar experimental conditions, assuming these are correct. Results of these validation attempts are described in Sec. 3.6.

3.3.2.4 Data Processing

The jet fluid signal Mie-scattering images are median filtered, intensity normalized, background and flatfield corrected, as well as laser sheet profile corrected. Finally they are

dewarped and cropped as required. The background images are recorded at the end of data acquisition with the lasers running but the seed particle and jet supply turned off. For some data sets, regions near the wall had to be cropped to exclude wall reflections from further evaluation.

As described in Sec. 3.3.2.2, the jet fluid signal fields are determined via a PDF method that attempts to separate effects of seeding density fluctuations and seed size from the effects of changing jet fluid concentration and flow density. Two other methods are compared to this one to assess the influence of the data processing on results. One will be termed the "direct method", computing statistics directly from the corrected Mie-scattering images and normalizing the intensity by the average value of a region close to the jet orifice, see Sautet and Stepowski (1994). The other one will be termed the "area method", thresholding and binarizing the instantaneous corrected Mie-scattering images and then calculating normalized statistics to directly relate the average number of particles in an image region to the concentration of jet fluid.

Fig. 3.19 shows an example comparison of average results determined via the PDF method, the direct method, and the area method. For higher jet fluid signal values (> 0.1) the differences between the methods are negligible. At lower values, the area method clearly suggests a significantly faster drop in the jet fluid signal. This is probably due to the thresholding excluding information from low intensity regions and regions with a large amount of very small particles. It is difficult to select the right threshold to isolate seed particles in the images, and it is even more difficult in the present situation where the seed particle size is not perfectly uniform and a more continuous distribution of tracers is desired for accurate jet fluid signal measurements. Thus, for this study, the area method probably underestimates the spatial distribution of jet fluid.

The differences between the PDF and the direct method are overall small. For the 0.05 and 0.02 jet fluid signal contours, the PDF method yields a slightly lower centerline signal decay, less jet fluid penetration towards the wall on the leeward side, and more penetration

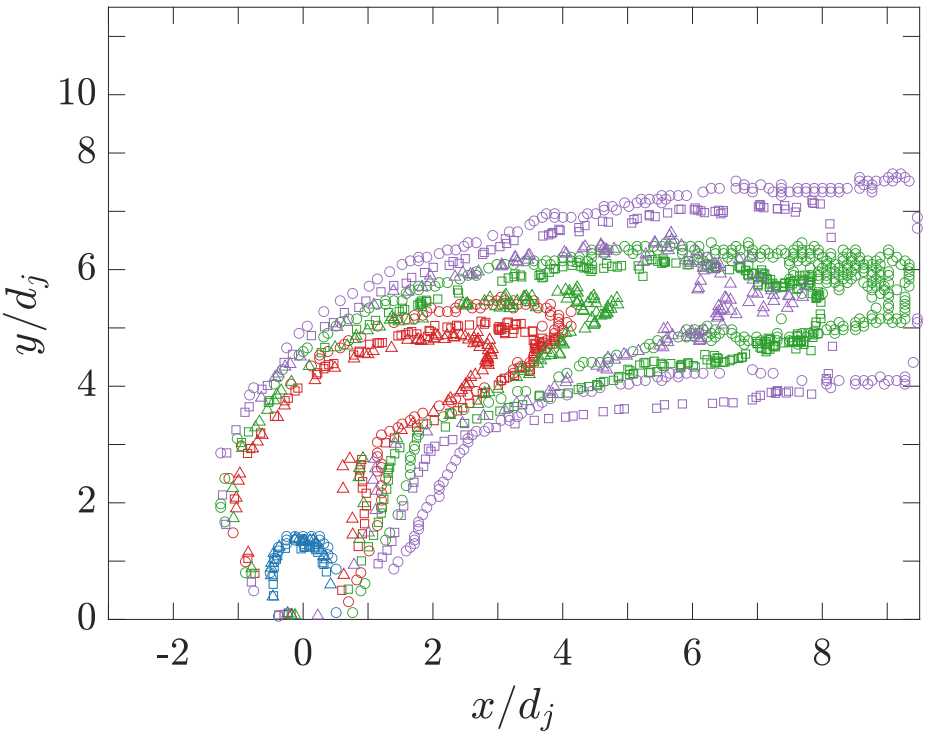

Figure 3.19: Comparison of average jet fluid signal contours resulting from three different processing methods. ◯−PDF method, □−direct method, △−area method. Blue: $\overline{\rho f} = 0.5$, red: $\overline{\rho f} = 0.1$, green: $\overline{\rho f} = 0.05$, purple: $\overline{\rho f} = 0.02$. In all cases the quantity $\overline{\rho f}$ is normalized by the signal close to the jet orifice.

into the crossflow on the windward side. Upstream of $x/d_j = 3$ on the leeward side of the jet, the PDF method predicts slightly deeper penetration of jet fluid into the wake region than the direct method. It is not too surprising that the PDF method agrees largely with the direct method. The deconvolution of the PDFs and subsequent computation of statistics is not too different from a direct normalization of the Mie-scattering signal with a reference followed by averaging. The main source of the differences might actually be the binning used for the PDF method.

Given that the area method appears to underestimate jet fluid signal iso-contour spread and the differences between the PDF and direct method are relatively small, it is concluded that usage of the PDF method is reasonable for the remainder of this study.

The determination of jet trajectories is based on a technique described by Gevorkyan *et al.* (2016). An additional step is added to find trajectories defined by a desired arbitrary

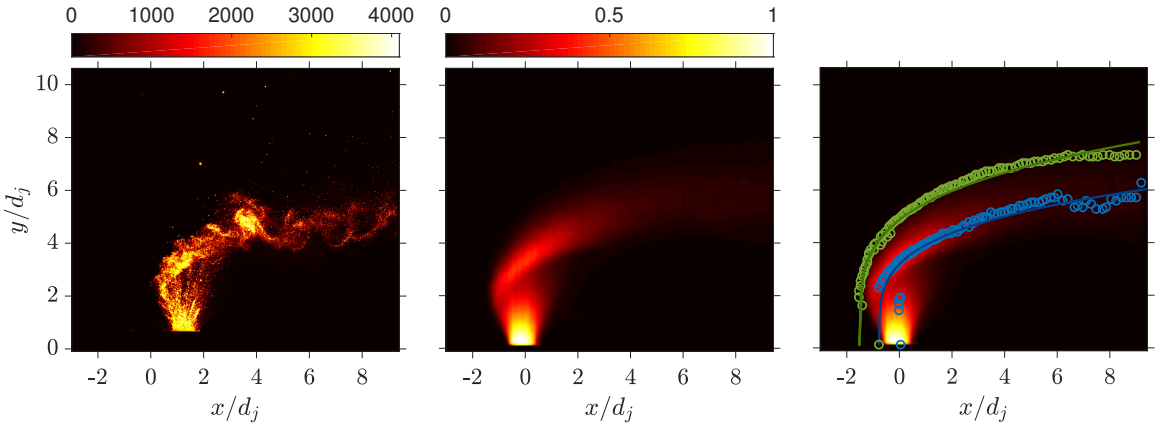

Figure 3.20: Example of the jet trajectory determination with a 2 mm nitrogen jet at $J = 6$. Left: instantaneous Mie-scattering image (after flatfield correction, median filtering and Gaussian filtering) with arbitrary intensity count. Middle: mean jet fluid signal image after the numerical PDF inversion procedure with a range from zero to one. Right: mean image overlayed with two relevant trajectories determined via the iterative procedure: the maximum jet fluid signal (blue) and the 2% jet fluid signal trajectory (green). For the trajectories both the actual data (circles) as well as power-law curve-fits (solid lines) are shown.

jet fluid signal, i.e. $\overline{\rho f}/\overline{\rho f}_0$. In this additional step the desired jet fluid signal is found on the windward side of the jet along normals defined relative to the maximum jet fluid signal trajectory. An example of the required processing steps and results is shown in Fig. 3.20.

For PIV, the initial steps are similar to the Mie-scattering processing, however, no laser sheet profile correction, background or flatfield correction are necessary. Instead a cross-correlation technique implemented in the Lavision's DaVis 8.4 software is used to compute the two-dimensional velocity vector field Willert and Gharib (1991).

At least 850 image pairs are used to compute statistics for all presented PIV data sets. The Mie-scattering images are dewarped and particle-correlations are found in regions of a certain size to determine the instantaneous velocity vectors for each interrogation window (Willert and Gharib, 1991). A multi-pass approach is used for successively smaller interrogation windows (Soria, 1996). To increase accuracy, sub-pixel interpolation is applied finding correlation peaks in the interrogation window (Willert and Gharib, 1991). Interrogation windows are overlapped by 50% to increase the spatial vector sampling rate. During

multi-pass processing outliers are removed based on a median filter universal outlier detection (Nogueira *et al.*, 1997). Details of the processing settings are given in Tab. 3.5.

The choice of interrogation window size results in $\sim 4-9$ particle images per window, which is slightly less than ideal (Melling, 1997), but yields better results in all presented cases, especially in the high shear regions of the flow. Better results here meaning higher correlation values and lower instantaneous uncertainties, as measured by the DaVis built-in correlation statistics method (Wieneke, 2015).

Additional post-processing of the vector fields is performed before evaluating them. Outlier vectors are removed based on a scatter threshold which, on average, deletes $< 0.5\%$ of the field's vectors and does not interpolate or re-insert them. Furthemore, as explained in Sec. 4.3, seeding density issues in the wake of the jet required complete masking of some areas. The masking is based on the total number of vectors available at a given point in the flow field and the corresponding instantaneous uncertainty magnitude. The latter is computed with the methods described by Sciacchitano and Wieneke (2016). If the number of vectors is less than 10% of the number of vector fields available or the uncertainty magnitude is more than 2.5 standard deviations above the average the vector is removed from further processing.

3.3.3 CH*-Chemiluminescence

High-speed CH*-chemiluminescence is used as a line-of-sight technique to visualize the evolution of chemical reactions initiated in the flow via laser induced plasma ignition. The measurement of CH* radicals is chosen as it is regularly used in literature to probe the evolution of ethylene combustion in supersonic flows (Ombrello *et al.*, 2015; An, Yang, *et al.*, 2020) and it does not require specialized UV-transmitting lenses. The chemiluminescence signal is related to the combustion heat release. However, strong turbulent fluctuations, high strain rates and non-premixed burning also influence the signal (Lee and Santavicca, 2003). Thus, it is only used as a qualitative indicator of burning processes in the flow field.

Table 3.5: PIV processing settings used in the DaVis PIV software for this study. Ch. 4 and Ch. 5 use the same data sets.

	Pre-Processing	Correlation	Multi-pass	Post-processing
Ch. 4	3×3 Gaussian smoothing, time filter min. intensity, mask regions with low seeding density	$2\times$ (64×64) window: 50% overlap Gaussian weighted, $3\times$ (16×16) window: 50% overlap adaptively weighted	$3\times$ median filter universal outlier detection: remove if residual > 2, re-insert if residual < 3, filter region 5×5, min. number of vectors: 4	$3\times$ median filter, strongly remove and iteratively replace: remove if difference to average > 1.5 std. dev. of neighbours, re-insert if diff to average < 1.7 std. dev. of neighbours. Interpolate if not re-inserted.
Ch. 6	3×3 Gaussian smoothing, mask regions with low seeding density, time filter min. intensity,	$2\times$ (64×64) window: 50% overlap Gaussian weighted, $3\times$ (16×16) window: 50% overlap adaptively weighted	$3\times$ median filter universal outlier detection: remove if residual > 2, re-insert if residual < 3, filter region 5×5, min. number of vectors: 4	$3\times$ median filter, strongly remove and iteratively replace: remove if difference to average > 2 std. dev. of neighbours, re-insert if diff to average < 2.3 std. dev. of neighbours. Interpolate if not re-inserted.

The setup utilizes a Photron SA-Z camera running at a frame rate of 120 kHz, resulting in a temporal image spacing of 8.33 µs. The camera is coupled to a HiCATT intensifier with a gating time of 3 µs. Light is focused into the intensifier with a 50 mm Nikon objective that has a 425 ± 25 nm band-pass filter mounted to it. The latter primarily transmits emissions from CH^*, but also some from CO_2^*, C_2^* (Lauer and Sattelmayer, 2011), and part of the initial broadband emissions caused by the laser induced plasma. The first image is recorded 2 µs after the laser spark. To allow for comparison, all time-series are recorded with the same camera and intensifier settings.

An example time series is shown in Fig. 3.21 excluding the very first image, as that is strongly over-exposed due to the plama emissions. Nine time series could be collected per experiment. A meaningful average would ideally include more samples. Thus, to gauge the variability between time series the RMS is formed. Comparing the mean and the RMS in Fig. 3.21a and Fig. 3.21b, respectively, the RMS signal is, for the most part, significantly below the mean. However, in some regions the variability is comparable to the strength of the mean signal. Nonetheless, the general shape and orientation of the average CH* recordings should be reliable. The intensity and spread of the RMS signal is representative of all collected CH* data.

The camera images the flow in the test section at a 90 ° angle to the symmetry plane using 348×288 pixels. During the inter-image delay and the gating time, the crossflow moves approximately 5.5 mm and 2 mm downstream, respectively. After the bow shock and closer to the jet orifice, it is a smaller distance, as the x-component of the crossflow is reduced. Together with a pixel resolution of 130 µm/px, this leads to a shift of approximately 15 pixel on the camera chip during exposure at nominal crossflow velocities.

Due to optical imperfections, the usage of an intensifier, and line-of-sight averaging, the pixel resolution of 130 µm/px does not correspond to the effective resolution of the system, i.e. the maximum spatial frequency that can be resolved by the imaging system is lower than the corresponding pixel resolution. The effective resolution is measured with a 1951

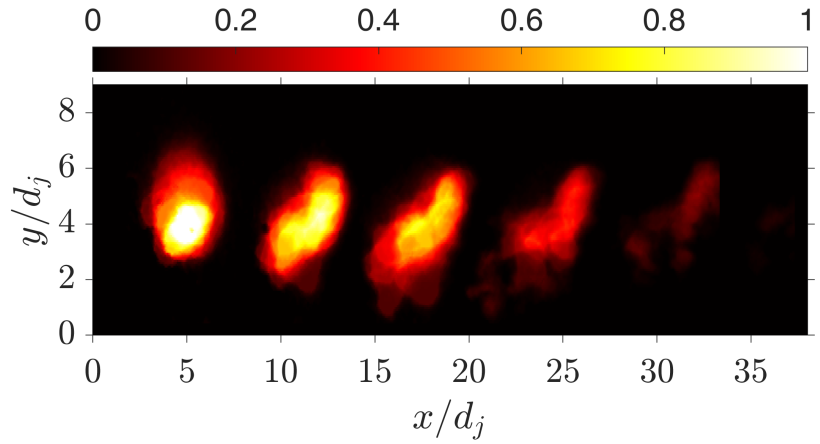

(a) Example of a mean CH* time series.

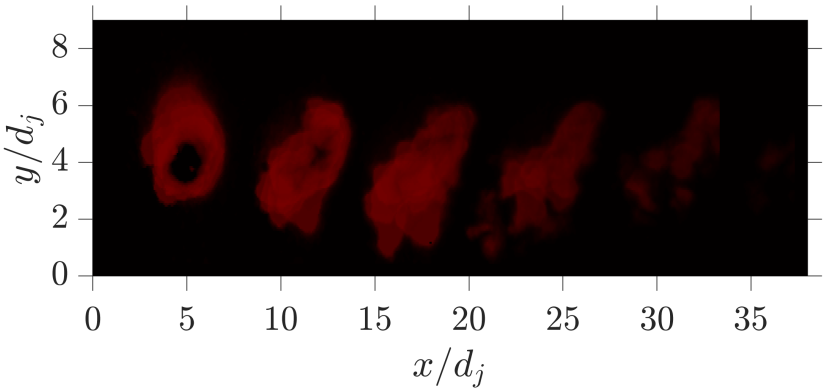

(b) Example of a root-mean-square CH* time series.

Figure 3.21: Example of a CH* time series. The signal is normalized to the camera's 12-bit intensity count.

USAF resolution test chart. Based on the resolution chart the system can resolve 2-2.24 line pairs per millimeter. In other words, features and objects as small as 0.45-0.5 mm can be distinguished, which is smaller than the maximum image shift of 2 mm during exposure. In any case, due to the line of sight averaged nature of chemiluminescence images, any discernible feature can still not be uniquely attributed to a spanwise position in the flow.

Using the 1951 USAF bar patterns to determine effective resolution corresponds to an estimate of the contrast transfer function (CTF). Wang and Clemens (2004) have shown that an estimate of the CTF is inferior to an estimate of the modulation transfer function (MTF). This is because the CTF measurement is more noisy (due to aliasing) and overestimates the responsiveness of the optical setup slightly. However, the agreement is still fairly good and,

keeping in mind the limitations, deemed sufficient for the interpretation of first and second order statistical moments in this study.

3.3.3.1 Data Processing

Nine time series are collected for each CH*-chemiluminescence data set, i.e. each spark location. The recordings are median filtered, background and flatfield corrected, dewarped and cropped as required. The background images are recorded at the end of an experiment with the jet supply and ignition system turned off.

To find the area of the CH* signal, the images are binarized using a Matlab routine. The routine first finds the edges of the luminous regions by searching for zero crossings in an image after applying a Gaussian filter. The found edges are then filled in to obtain the binarized image. An example of this process is shown in Fig. 3.22.

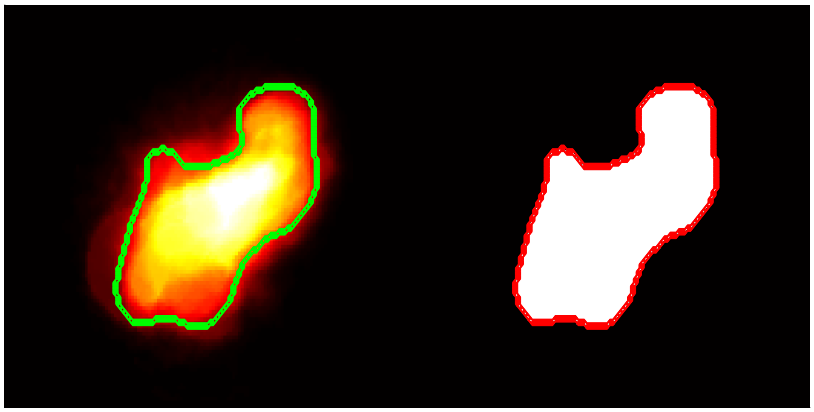

Figure 3.22: Example of the binarization process used for CH* data. Left: average CH* signal at a certain time delay. The detected contour is overlayed in green. Right: binarized image with contour outlined in red.

3.3.4 OH-Planar Laser Induced Fluorescence

OH-PLIF is used to provide a visualization of the C_2H_4 flame evolution that is not line-of-sight averaged or time averaged and can be correlated directly with mixture fraction measurements from Mie-scattering and velocity field data from PIV. The hydroxyl (OH)

radical primarily exists in the reaction or primary heat release zone of a flame and in regions containing hot products. Therefore, it is indicative of regions in which combustion processes are taking place or where hot products exist.

To probe the desired OH florescence band an Nd:YAG laser, emitting 532 nm light at 10 Hz, pumps a Lambda Physik dye laser operating on Rhodamine 6G. With a frequency-doubling crystal, the dye laser is tuned to provide an ultra-violet laser beam at ~ 283.2 nm with ~ 8 mJ/pulse. This UV laser beam excites the $Q_1(7)$ line of the OH $A^2\sum^+(\nu' = 1) \leftarrow X^2\Pi(\nu'' = 0)$ transition. The life time of the excited states is below ~ 10 ns. This makes it almost instantaneous in the context of this study, with an estimated large scale turn-over time of 11.2 µs (see Sec. 3.3.2.1) and flow through times > 450 µs.

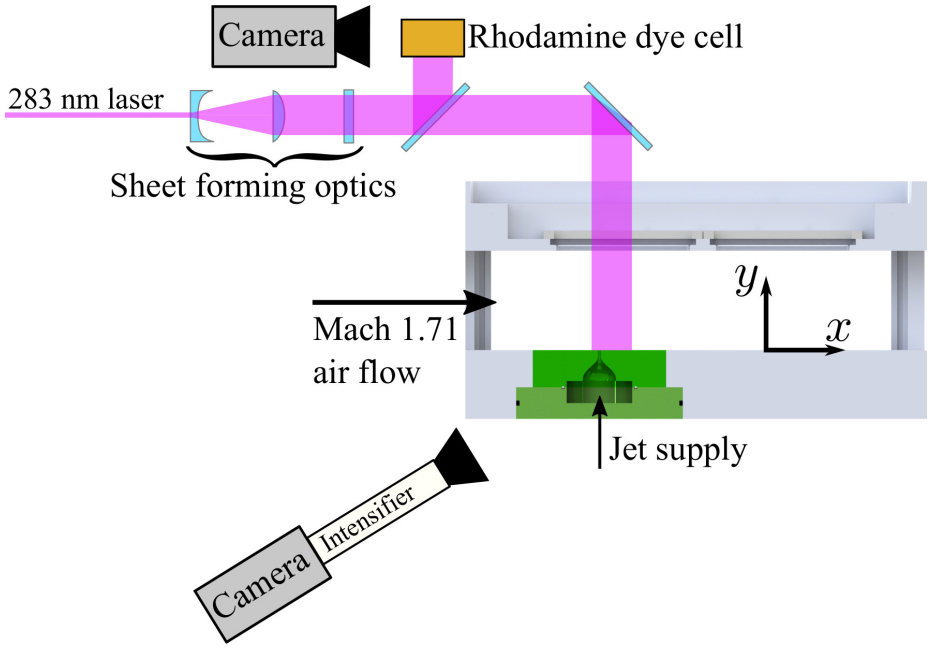

Figure 3.23: Optical setup for OH-PLIF experiments.

Using three cylindrical lenses, the laser beam is formed into a sheet with a collimated width of ~ 50 mm and a thickness of 63 µm (FWHM measured with the knife-edge method). The latter also represents the out-of-plane resolution. The lenses are a 1500 mm concave and a 750 mm convex lens for the sheet width and a 500 mm convex lens for the thickness. The thinnest part of the laser sheet is positioned 3-4 mm above the test

section floor. A part of the laser sheet is split off and imaged with a rhodamine dye cell for instantaneous correction of laser sheet non-uniformities. No attempt was made to measure instantaneous laser energy itself for shot-to-shot corrections. A sketch of the PLIF setup is shown in Fig. 3.23.

The fluorescence signal collected by a camera can be written as (Hanson *et al.*, 1990),

$$S \propto E_I f_B(T) \frac{n_{OH}}{Q_{21}(T)} \tag{3.16}$$

where f_B is the Boltzmann population fraction of the lower laser-coupled state, n_{OH} is the number density of the absorbing species, and Q_{21} is the quenching rate. The expression has been simplified by considering two things. One, around atmospheric pressures, it is reasonable to assume that quenching dominates over spontaneous emission. Two, spontaneous emission coefficients are independent of temperature, thus scaling the signal but not changing its trends. The OH fluorescence signal is weakly dependent on temperature (Lee, McMillin, *et al.*, 1992) but strongly on quenching processes. In the current setup, the quenching rates could not be determined. Thus, the signal recorded can be related to the OH concentration only in a qualitative sense.

The OH-PLIF fluorescence signal is recorded by an Andor Zyla 5.5 camera coupled to a HiCATT intensifier and a band-pass filter centered at 310 ± 20 nm, providing an in-plane pixel resolution of 19.3 µm/px. The gating time on the intensifier is 150 ns, i.e. flow features moving with the nominal crossflow velocity would move ~ 100 µm during exposure or 5 pixels on the camera chip. While the shorter gating time will reduce the exposure to broadband LIP emissions, the PLIF records can still be affected by it. To allow for comparison, all data sets are recorded with the same camera and intensifier settings.

The effective resolution of the camera-intensifier system is measured with a 1951 USAF resolution test chart. According to the resolution target, the system can resolve 1.12 line pairs per millimeter or spatial frequencies with a wavelength of 0.9 mm. This is $\sim 50\%$ of

the single injector diameter and $\sim 64\%$ of the dual injector diameter. Thus, the effective resolution is the limiting factor in imaging OH-PLIF emissions and large scale burning structures influenced by the jet shear layer should be resolved sufficiently.

3.3.4.1 Data Processing

1100 PLIF images are recorded during one continuous run of the test facility. After outlier removal, based on the standard deviation of the integrated intensity, $> 90\%$ of the samples collected for any given data set are used in further evaluation, i.e. > 1000 samples for each data set.

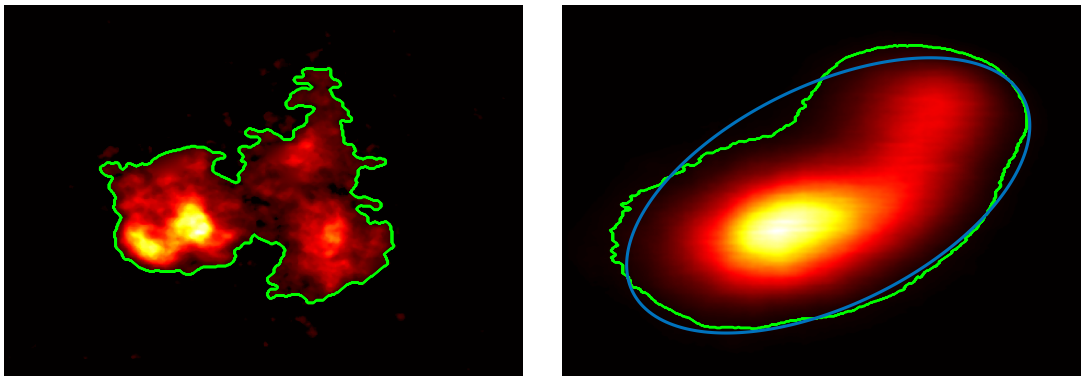

(a) Instantaneous PLIF signal with detected edge (green).

(b) Mean PLIF signal with detected edge (green) and ellipse fit (blue).

Figure 3.24: Examples of instantaneous and mean OH-PLIF signals collected in this study. Associated detected edges and an ellipse fit are shown, too.

For the computation of certain statistics, OH fluorescing regions have to be identified. The associated edge finding and binarization are performed using the SUSAN algorithm (Smith and Brady, 1997) together with a histogram based threshold. The same technique has been used before in Fries *et al.* (2019). An example of an instantenous PLIF realization and the corresponding edge is shown in Fig. 3.24a.

The average OH-PLIF signal is normalized to a range from zero to one and interpreted as the likelihood for chemical reactions to take place in a certain region of the flow. For further analysis the edge of the average signal is found using the SUSAN algorithm described

above (Smith and Brady, 1997). Then, an ellipse is fitted to the detected edge based on the general, implicit equation for a conic section Fitzgibbon *et al.* (n.d.),

$$Ax^2 + Bxy + Cy^2 + Dx + Ey + F = 0. \tag{3.17}$$

Properties and trends of the averaged signal and the fitted ellipses are described further in the results, see Ch. 6. An example for an average PLIF signal, the corresponding edge and the ellipse fit are shown in Fig. 3.24b.

3.4 Error Analysis

Established guidelines for turbulent statistics are used throughout this study as outlined by Benedict and Gould (1996) and Bendat and Piersol (2010). Unless otherwise stated, variance estimators for the mean and higher order statistics are assumed to be normally distributed random variables. The corresponding estimators for N independent samples are listed in Tab. 3.6. These variances are used to compute confidence interval for Gaussian distributions, $\pm z_\alpha (s^2/N)^{1/2}$, where z is the number of standard deviations, α is the probability/confidence level, and s^2 is the estimated sample variance. All statistics converge with $N^{-1/2}$.

Table 3.6: Estimator variances for velocity statistics (Benedict and Gould, 1996; Bendat and Piersol, 2010).

Statistic	$\overline{u}$	$\overline{u'^2}$	$\sqrt{\overline{u'^2}}$
$s^2 \times N$	$\overline{u'^2}$	$2\overline{u'^2}^2$	$\overline{u'^2}/2$

If less than 20 samples are available for a random variable the student's t-distribution is used to estimate confidence intervals of single variables and the chi-square distribution is used for products of random variables (Bendat and Piersol, 2010). More detailed uncertainty estimates for different reported quantities of interest are described in Appendix C.

3.5 Flow Characterization

3.5.1 Crossflow Properties

The conditions of the characterization presented below correspond to the study part in Ch. 4. The corresponding static flow properties are summarized in Tab. 3.1. Static wall pressure ratios, PIV and schlieren measurements are consistent and indicate a Mach number of 1.71 at the jet injection point.

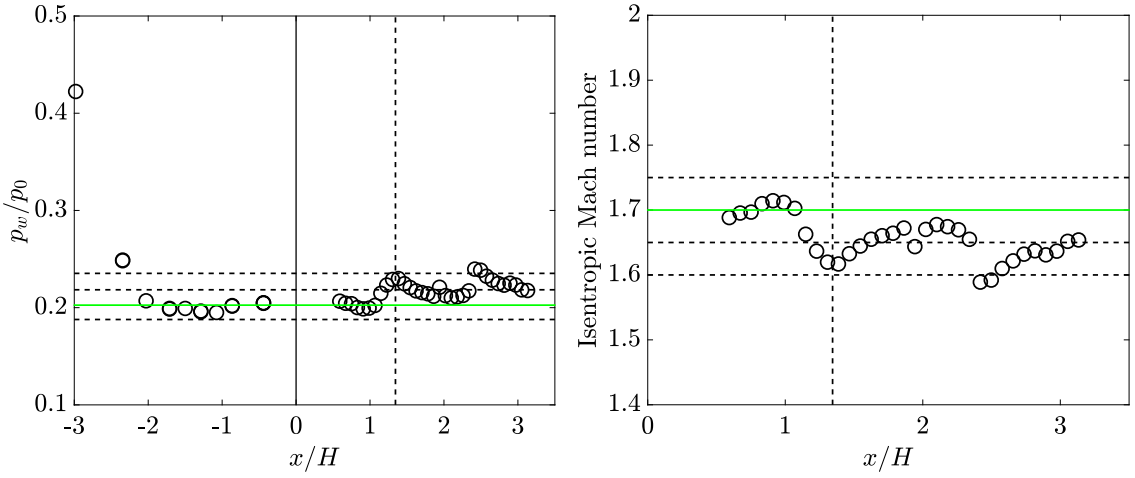

(a) Static wall pressure measurements.

(b) Mach number in the test section.

Figure 3.25: Static wall pressure derived flow conditions. The Mach 1.7 condition (nozzle design Mach number) is indicated by the green dashed line in both the wall pressure and Mach number plot.

The measurements also reveal several weak shocks remaining in the test section flow. In the worst case, these shocks correspond to oblique shocks generated by a turning angle of $\sim 2.7°$, with the Mach number changing from 1.71 to 1.62 and the pressure, density, and temperature increasing by 14.4%, 11%, and 4% compared to the pre-shock static values, respectively. The pressure increase of 14.4% is consistent with wall static pressure measurements, see Fig. 3.25a. For this kind of oblique shock the stagnation pressure loss across a wave is $< 0.1\%$, i.e. an approximately constant stagnation pressure should be given along the test section even after multiple wave crossings. This has been confirmed by Pitot probe measurements showing that the stagnation pressure in the test section is

within 3% of the total pressure measured upstream in the homogenizer section. The percentage change is smaller than the total uncertainty of the pressure transducers used in the homogenizer section and the pressure probe.

Nonetheless, the remaining shock waves cause a change in flow properties across the test section. For example, see the change in Mach number in Fig. 3.25b, calculated from wall pressure measurements using an isentropic expansion relation, Eq. (3.4). PIV and schlieren measurements show that the weak shock wave closest to the jet orifice impinges on the wall $\sim$27 mm behind the jet injection point, see Fig. 3.26a. Thus, if there is any direct influence on the jet it would manifest itself in its downstream wake. On average, the angle of the weak waves in the schlieren images (not shown) is $\sim 36.01^\circ$ corresponding to Mach numbers around 1.7, which is consistent with the static wall pressure measurements, as mentioned above.

Horizontal velocity profiles above the bottom wall are shown in Fig. 3.26b. They indicate that the crossflow velocity is fairly constant within 3% of the reference velocity, $U_0 = M_\infty \sqrt{\gamma_\infty R_\infty T_\infty} = 664$ m/s. It decreases slightly over the field of view due to the remaining weak shocks. The maximum deflection of velocity vectors from the streamwise direction is 1.4° upwards with a maximum transverse velocity component of ~ 16 m/s or 2.5% of the crossflow reference velocity.

To characterize the boundary layer in the present facility it is compared to measurements made by Pizzaia and Rossmann (2018) and the analytical log-law after applying the van Driest transformation (White and Corfield, 2006). It is also curve fitted to the generalized outer-region turbulent equilibrium boundary layer profile defined by Chauhan *et al.* (2009). The results are shown in Fig. 3.27a. While the structure of the velocity data roughly resembles a turbulent boundary layer it deviates from the utilized references. This is probably due to the pressure gradients induced by the remaining weak shock waves in the test section. The velocities in the near-wall region are lower than predicted by theory, which would correspond to an adverse pressure gradient caused by a compression wave

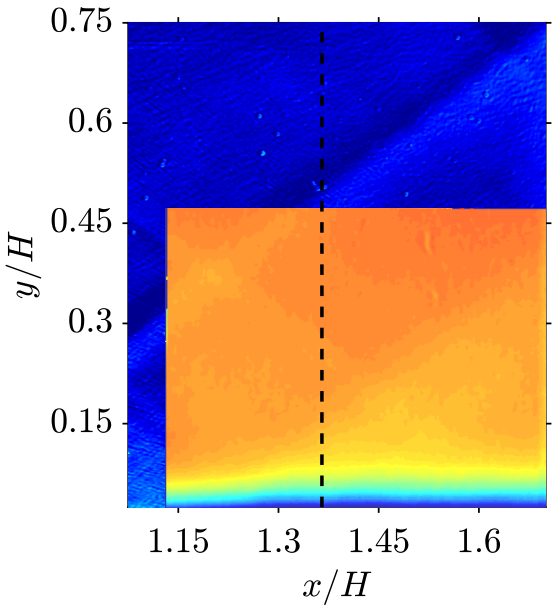

(a) Qualitative overlay of schlieren and PIV measurements in the test section. The schlieren image is in the background. Remaining waves are visible in both types of measurements manifesting themselves in sudden density and velocity changes.

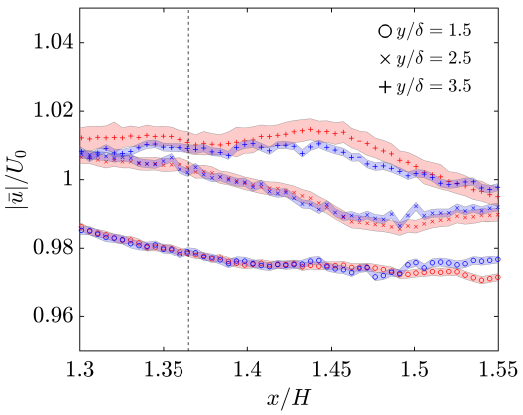

(b) Horizontal velocity profiles taken at different heights above the bottom wall. Red color corresponds to a measurement magnification of 0.66, blue color to a magnification of 0.36. The dashed vertical line is the injector location on the bottom wall. Uncertainty bands correspond to a 95% confidence level and account for instantaneous (Scicchitano and Wieneke, 2016) and statistical uncertainty.

Figure 3.26: Schlieren and PIV characterization of the current facility's main flow. The dashed vertical line is the location of the injector on the bottom of the test section. H is the test section height.

impinging on the boundary layer downstream. That this impingement indeed occurs was shown in Fig. 3.26a.

In addition, the computed crossflow Reynolds numbers in Tab. 3.1 suggest it is likely that the experiments are conducted with a turbulent boundary layer. However, not a well defined turbulent boundary layer in the classical sense, i.e. it is a non-equilibrium boundary layer subject to local pressure gradients. In the presented results, the best fit parameters for the boundary layer equation given by Chauhan *et al.* (2009) are the friction velocity $u_\tau = 24.84$ m/s, the wake parameter $\Pi = -0.13$ and the real boundary layer thickness $\delta = 17.25$ mm. The streamwise development of the 95% boundary layer thickness is shown in Fig. 3.27b.

To summarize, the flow conditions in the test section are not perfectly uniform, due to weak shocks generated in the nozzle that are not completely canceled out in the turning

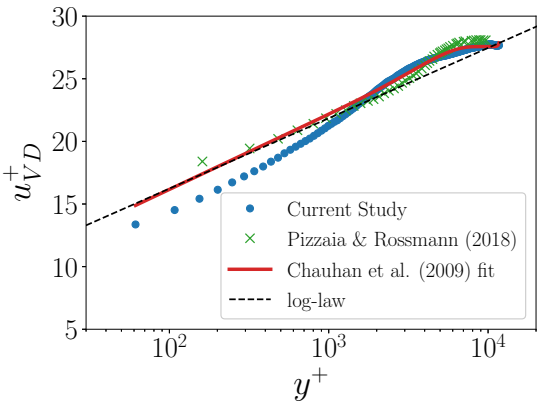

(a) Comparison of the supersonic boundary layer profile in this study to theory and experimental results by Pizzaia and Rossmann (2018). The presented data is extracted on the symmetry plane at the jet centreline location.

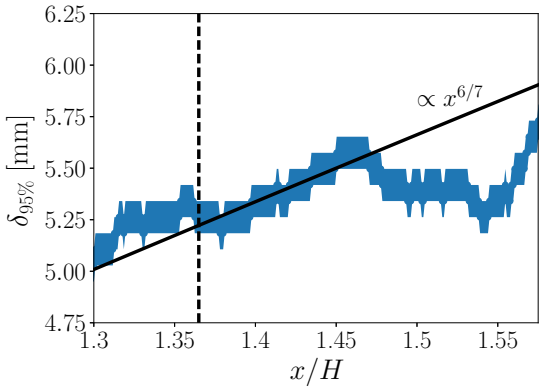

(b) Streamwise development of the 95% boundary layer thickness. Also shown is the expected turbulent boundary layer growth assuming a turbulent $1/7$ power-law velocity profile (White and Corfield, 2006). Shaded areas indicate the confidence interval. H is the test section height.

Figure 3.27: Velocity data relating to the analysis of the boundary layer state in the current study. The dashed vertical line denotes the location of the jet orifice. Velocity uncertainty is below 3% at a 95% confidence level for the entire boundary layer profile.

section. The Mach number of the flow in the region of interest close to the jet is $M_\infty = 1.71$ and the boundary layer thickness is $\delta_{95\%}$ =5.3 mm at the jet injection point. These values will be used as reference values in the remainder of this study. For all experiments the stagnation conditions are recorded during data acquisition and static flow values are computed with the aforementioned Mach number.

3.5.2 Injector flow properties

The discharge coefficient of the SI (2 mm single jet) injector is determined by comparing measurements from a MicroMotion Coriolis flow meter with choked nozzle mass flow calculations. For all injected gases, the discharge coefficient is between 0.9 and 0.97 in the range of pressures used, i.e. 414.0 - 2,758 kPa. The discharge coefficient remains in the same range for the smaller diameter SI*, DI1 and DI2 injectors.

To validate that the jet setup is behaving as expected, the properties of "free" jets generated with the presented experimental setup are investigated. The jets are not entirely free as

they exhaust into the confined space of the test section. Thus, general, but not exact, agreement with free jet experiments is expected. In Fig. 3.28, Mach disk heights determined via schlieren visualization are shown. The agreement with empirical correlations reported in the literature improves with increasing pressure ratios. The Mach disk height of the lowest pressure helium jet was difficult to determine accurately because of the strong turbulence present close to the jet orifice.

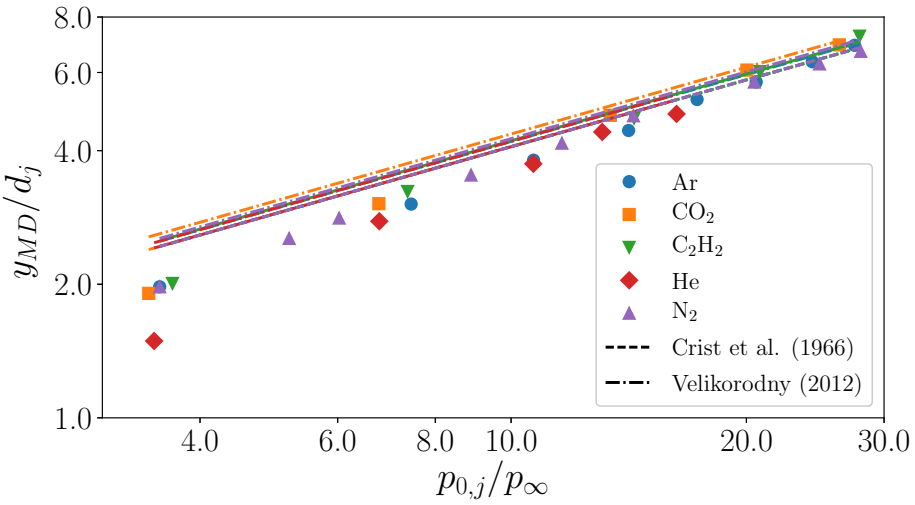

Figure 3.28: Comparison of measured Mach disk heights to correlations of Crist *et al.* (1966) and Velikorodny and Kudriakov (2012). The agreement is very good at higher pressure ratios. At lower pressures larger deviations are visible, possibly due to the jet not actually being unconfined in the test section and experiencing a back pressure higher than the ambient pressure. Line colors correspond to the gases tested.

Centerline and horizontal velocity profiles from PIV measurements are presented in Fig. 3.29a and Fig. 3.29b, respectively. The centreline velocities in Fig. 3.29a show the characteristic acceleration an underexpanded sonic jet experiences as it expands downstream of its choke point, followed by an abrupt deceleration at the Mach disk and re-acceleration.

An exception is the helium jet at a low pressure ratio corresponding to $J = 1$. Upon injection, the helium jet is at approximately two times ambient pressure. Thus, while the resulting Mach disk after expansion is barely detectable in schlieren images it is likely too weak or too close to the wall to be picked up properly by the PIV setup. Hence the velocity

profile exhibits a seemingly continuous acceleration initially.

The horizontal velocity profiles in Fig. 3.29b are slightly asymmetric due to the draft created by the exhaust system that is running during experiments. The profiles extracted closest to the jet orifice resemble more of a top-hat than a parabolic profile.

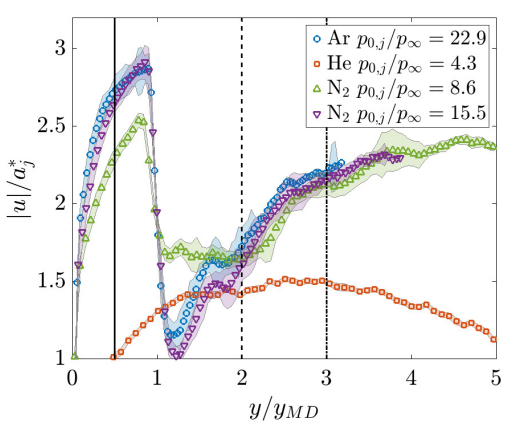

(a) Wall-normal centreline velocity profiles. Shaded uncertainty bands correspond to a 95% confidence level. Vertical lines correspond to the locations at which the horizontal velocity profiles are taken.

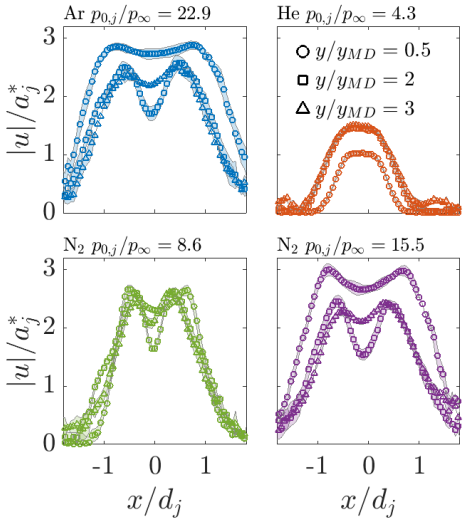

(b) Wall-parallel velocity profiles cutting through the jets.

Figure 3.29: Velocity profiles of free jets in the current setup normalized with the sonic velocity at the choke point. The pressure ratios of the free jets $p_{0,j} = 22.9, 4.3, 8.6$ and 15.5 correspond to $J = 6, 1, 2$ and 4, respectively, in the case of a supersonic crossflow at the targeted operating conditions.

3.6 PIV Validation

Two measures are taken to validate the presented PIV velocity fields. The first one is a comparison between bow shock shapes that can be extracted from PIV results and bow shock shapes observed in schlieren data. The latter being a line-of-sight gas-phase measurement that does not suffer from the drawback of relying on tracer particles. The second one is to compare the presented results to published literature.

3.6.1 Bow Shock Geometry

First, the bow shock shape extracted from schlieren data (see Fig. 3.30a) is compared to the bow shock shape determined via PIV results (see Fig. 3.30b). The results of this bow shock extraction are also used in further analysis in Ch. 4. At a given height above the wall, the bow shock position is found in schlieren images as the first peak of the second streamwise derivative of the image intensity. For PIV data, it is found as the center point between the two peaks of the second streamwise derivative of the streamwise velocity. The small difference in definition is due to the line-of-sight averaging in schlieren data and the different behavior of density gradient and PIV records around shocks.

To make the shock finding technique more robust, the detected discrete shock positions are fitted with a curve proposed by Billig (1967) for bow shocks ahead of three-dimensional blunt bodies. The curve has the following form,

$$x = R + \Delta - R_h \cot^2(\beta_h) \left[\left(1 + y^2 \frac{\tan^2(\beta_h)}{R_h^2} \right)^{1/2} - 1 \right], \tag{3.18}$$

where R is the body radius, Δ is the shock stand-off distance, R_c is the equivalent radius of a hyperbola, and β_h is the shock angle at infinity, which should approach the Mach angle of the given flow field. All presented bow shock positions are curve fits of this form.

Qualitatively, the agreement between bow-shock shapes in Fig. 3.30 is good. Quantitatively, at higher momentum flux ratios the difference between the schlieren and PIV derived bow shock locations starts to grow. The relative difference in J to the schlieren data is 0%, -3.8%, -4%, and -3%. Thus, the PIV momentum flux ratios are slightly lower at $J = 2,\ 4$ and $J = 6$. However, the main reasons for the difference in bow shock position is probably the growing shock strength and the finite response time of PIV tracer particles.

The bow shock angle β is an important quantity as it relates directly to the flow state behind the shock. Schlieren and PIV results for β are compared in Fig. 3.31. The largest

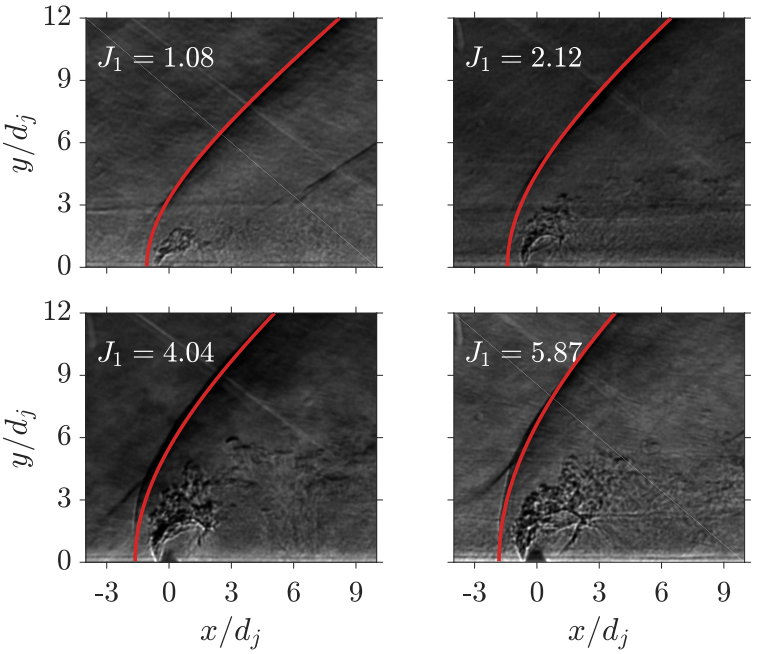

(a) Schlieren data used as the bow shock detection baseline. Red lines are the curve-fitted edges of the detected bow-shock front. The shock shape is determined from averaged schlieren images but representative instantaneous images are shown because the shock structures are better visible.

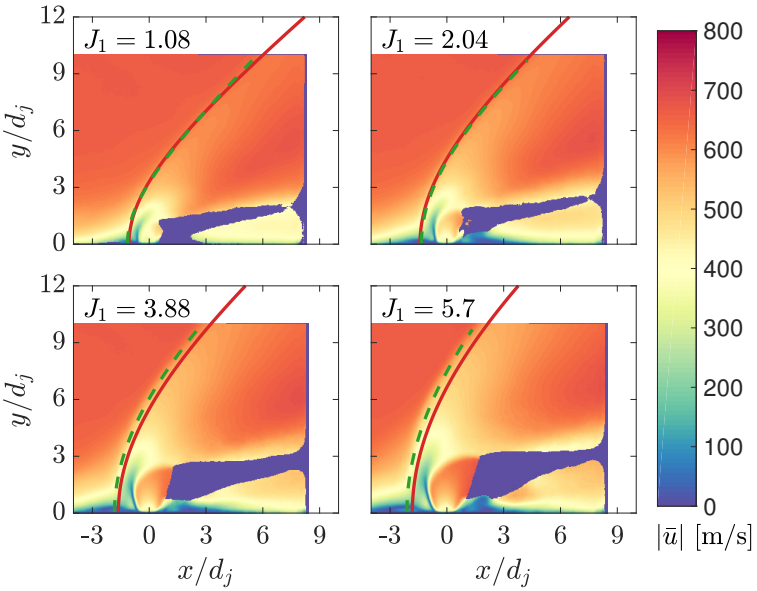

(b) Comparison between bow shock edges detected in PIV data and their respective schlieren baselines. Shown is the velocity magnitude. — schlieren results, - - - curve-fitted bow shock edges derived from PIV results.

Figure 3.30: Testing and validation of the bow shock edge detection implemented for this study. The test cases are for N_2 jets at momentum flux ratios of nominally 1, 2, 4 and 6. Schlieren and PIV data are acquired during separate experimental runs.

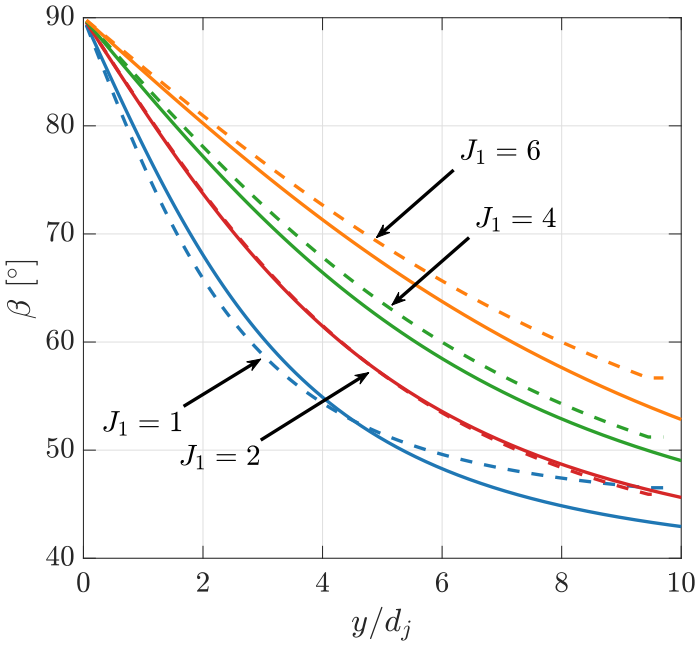

Figure 3.31: Comparison between bow-shock angles detected in schlieren and PIV data at approximately the same momentum flux ratios.

discrepancies occur above $y/d_j = 4.5$ for the $J = 1$ cases, and in general at higher J. The absolute difference at a given y/d_j is always smaller than $5°$.

Together with the consistent results between PIV, schlieren and static pressure measurements in Sec. 3.5, the analysis of the bow shock geometry suggests that PIV derived mean flow velocities in this study are reliable. The position of the shock velocity gradient is correct and the undisturbed mean crossflow velocity agrees well between the different diagnostics. The velocity data apperas to be more reliable at lower momentum flux ratios, whereas larger deviations to the real flow properties seem to occur for momentum flux ratios > 4. The mean flow velocities and bow shock geometry are going to be used in further computations of the convective Mach number and to analyze the behavior of ignition kernels with regard to the velocity field.

3.6.2 Comparison to Literature

Fig. 3.32 shows a qualitative comparison of the region near the jet orifice between this study and Santiago and Dutton (1997). For the current study the presented data corresponds to a

nitrogen jet at $J = 2.04$ and $\delta/d_j = 2.63$. The LDV data of Santiago and Dutton (1997) was acquired with an air jet at $J = 1.7$ and $\delta/d_j = 0.775$. Due to the slightly higher momentum flux ratio and the much thicker boundary layer in the present study, the expansion region and the barrel shock system do not turn into the crossflow as strongly as in the results of Santiago and Dutton (1997). Nonetheless, the newly presented PIV data does exhibit the same salient features of the mean JISCF flow field. Ahead of the jet in Fig. 3.32, the near-wall flow separation is identifiable by a recirculation region. The barrel shock structure is clearly delineating the jet expansion region as a sudden change in flow direction and reduction in velocity. While the results of Santiago and Dutton (1997) show a low velocity region directly downstream of the jet, they do not exhibit as clear a second recirculation near the wall as the present data. This is probably due to the difference in δ/d_j. The jet has an easier time overcoming the crossflow momentum in the thicker boundary layer, creating a larger recirculation region downstream of injection. The qualitative agreement between salient flow field features further supports the claim that mean velocity trends are captured correctly in the current study.

A qualitative comparison to the turbulent kinetic energy (TKE) and shear stress fields of Kawai and Lele (2010) is shown in Fig. 3.33 and Fig. 3.35, respectively. While their LES simulations can resolve all three velocity components, the two-dimensional PIV data in this study is used to approximate the filtered TKE as,

$$k = \frac{1}{2}\left(\overline{u'^2} + 2\overline{v'^2}\right). \tag{3.19}$$

The TKE is filtered because limited spatial resolution and tracer response time reduce the spectral content that is actually resolved by the experiment.

Peak values of the TKE magnitude in Fig. 3.33 are lower for the PIV data, although J is higher. This is due to the limited spatial resolution and flow tracer response time. The third velocity component $\overline{w'^2}$ not being measured also contributes to the values being

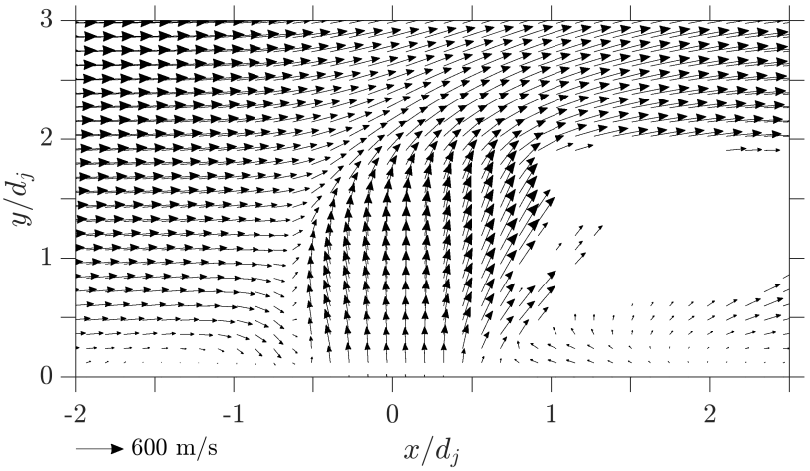

(a) Nitrogen jet, $J = 2.04$ and $\delta/d_j = 2.63$. Only every third vector is shown.

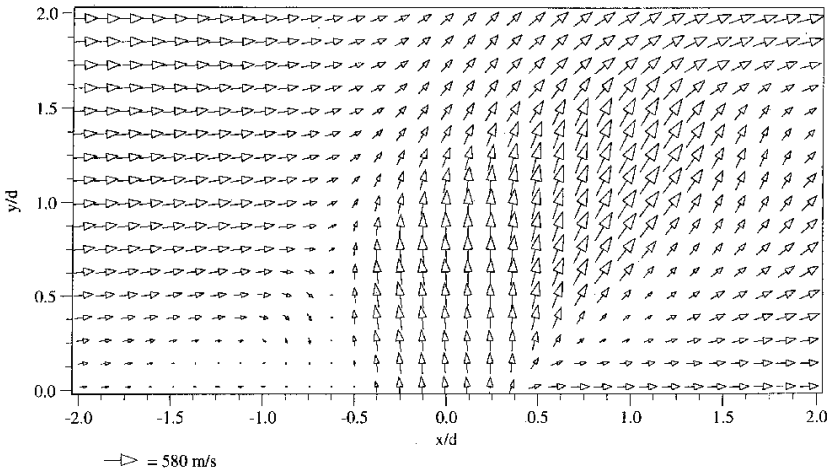

(b) Air jet, $J = 1.7$ and $\delta/d_j = 0.775$ from Santiago and Dutton (1997).

Figure 3.32: Comparison of mean JISCF vector fields on the flow symmetry plane near the jet orifice.

lower. However, given that the lateral component should be small on the symmetry plane it is more likely a resolution and tracer particle effect.

That the finite response time of the tracer particles influences the results can also be seen in the significant smearing of the unsteady bow shock component. Penetration of the expansion region into the crossflow is higher for the experimental data as expected from the momentum flux ratio and δ/d_j. Locations of peak TKE can be found on the windward side of the barrel shock in both data sets. The TKE peaks in the wake of the jet cannot be resolved due to the missing data in the present study.

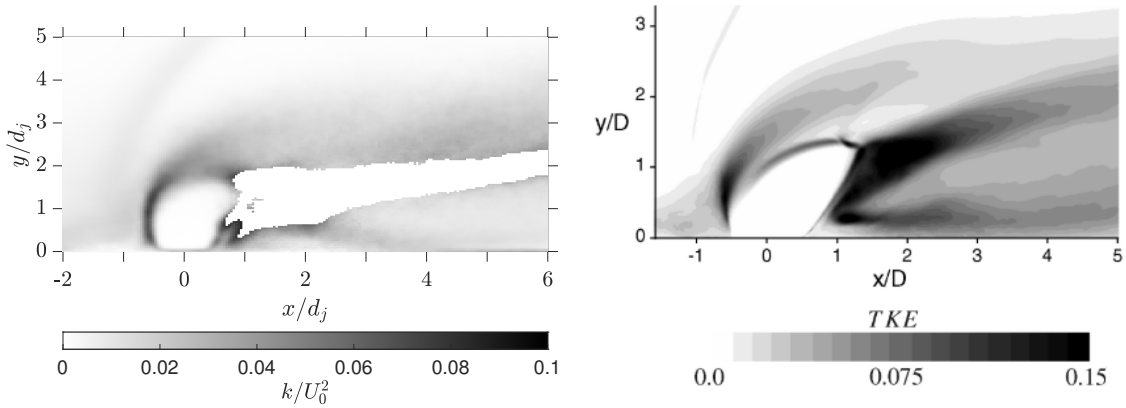

(a) Turbulent kinetic energy of a nitrogen jet at $J = 2.04$ and $\delta/d_j = 2.63$.

(b) Turbulent kinetic energy of an air jet at $J = 1.7$ and $\delta/d_j = 0.775$ from Kawai and Lele (2010).

Figure 3.33: Comparison of the TKE field on the symmetry plane of a JISCF. The simulation results by Kawai and Lele (2010) specifically consider a turbulent boundary layer.

A direct comparison of a TKE profile at $x/d_j = 4$ is shown in Fig. 3.34. The general trends captured by the experimental data agree with the simulation. A small peak is visible close to the wall, followed by a decrease in TKE and another peak. However, while the trends agree, the present PIV data significantly underestimate the peak magnitude of turbulent kinetic energy.

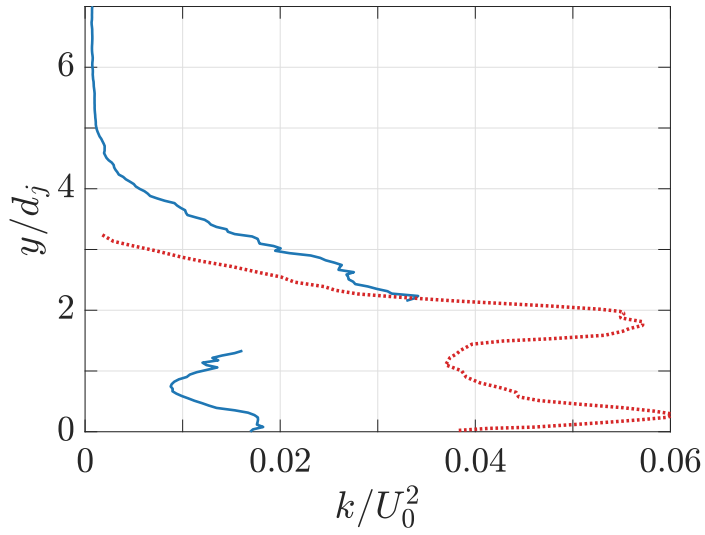

Figure 3.34: Direct comparison of TKE profiles at $x/d_j = 4$ for the same conditions as in Fig. 3.33. —— present study. ····· Kawai and Lele (2010).

Qualitative trends of the shear stresses in Fig. 3.35 also agree between the present study and the computational results by Kawai and Lele (2010). High shear regions in the windward recirculation region, along the windward barrel shock and tentatively in the wake of the jet are detected. One can also discern a weak transition from negative to positive and back to positive shear stresses above the barrel shock region in the streamwise direction. However, this trend is much more pronounced in the computational results, suggesting again that filtering effects remove spectral content from the experimental results.

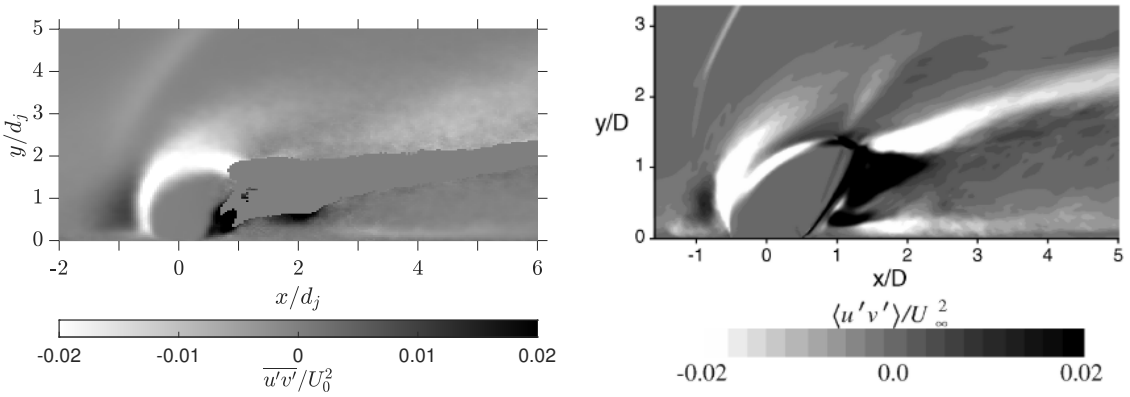

(a) Shear stress of a nitrogen jet at $J = 2.04$ and $\delta/d_j = 2.63$.

(b) Shear stress of an air jet at $J = 1.7$ and $\delta/d_j = 0.775$ from Kawai and Lele (2010).

Figure 3.35: Comparison of the shear stress field, $\overline{u'v'}$, on the symmetry plane of a JISCF. The simulation results by Kawai and Lele (2010) specifically consider a turbulent boundary layer.

A quantitative comparison of PIV results is possible with the fluctuating velocity component data of Choi *et al.* (2012). Their experiment uses an air jet at $J = 3.3$ with $\delta/d_j = 4.5$. The results are compared with current data for an ethylene jet at $J = 4.0$ and $\delta/d_j = 3.73$. Ethylene has a molecular weight similar to that of air (~ 28 g/mol) and a slightly lower specific heat ratio, i.e. 1.237 vs. 1.4. Thus, purely from an injectant perspective the results should be comparable.

In Fig. 3.36, for all three fluctuating velocity statistics, the current study measures larger magnitudes and broader regions of elevated variance and shear stress. It also appears, that the statistical convergence is not as good for the fluctuating velocity component in this

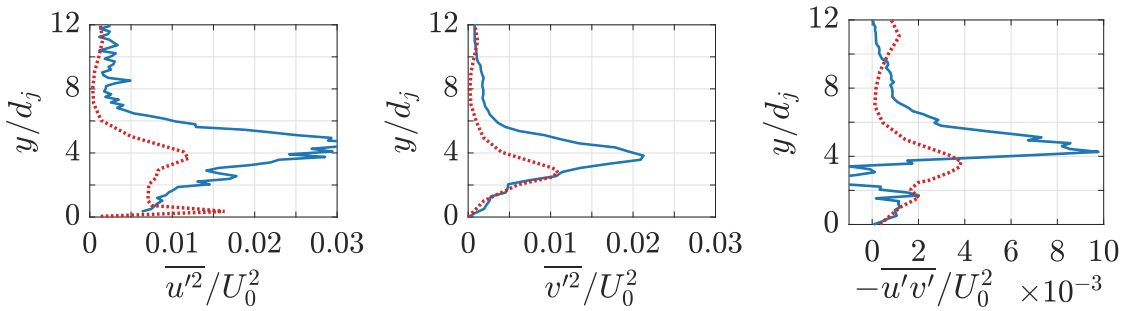

(a) Streamwise velocity variance, $-\overline{u'^2}/U_0^2$.

(b) Wall-normal velocity variance $-\overline{v'^2}/U_0^2$.

(c) Reynolds shear stress, $-\overline{u'v'}/U_0^2$.

Figure 3.36: Comparison of fluctuating velocity statistics at x/d_j = 15. ——— present study, ethylene jet, $J = 4.0$, $\delta/d_j = 3.73$. ····· Choi *et al.* (2012), air jet, $J = 3.3$, $\delta/d_j = 4.5$

study than the reference data.

Given the higher momentum flux ratio in the present study, higher values of fluctuating components over a larger distance are expected. Other factors, such as freestream turbulence and boundary layer details could also play a role. In terms of vector spacing, the resolution in the experiments by Choi *et al.* (2012) is about six times lower than the resolution of this study's data. Because lower resolution means stronger filtering it can account for part of the difference in magnitude.

With the available data, no final conclusion can be made regarding quantitative reliability of fluctuating velocity components in the current PIV data. Qualitatively, differences due to spatial filtering appear consistent. Furthermore, the agreement between data sets is reasonable with respect to trends and the the location of peaks. Thus, it is concluded that fluctuating velocity trends and flow features are reflected correctly by the current PIV data. Only the trends are going to be interpreted in further analysis of injectant properties' influence on turbulent mixing in a JISCF.

CHAPTER 4

TURBULENT JET ENTRAINMENT AND MIXING

To investigate the dependence of jet entrainment and mixing on the properties of the injectant itself, a comparison between different cases and flow conditions has to be possible. To this end, the mean jet trajectory is considered and a new scaling is developed that collapses data points from many different conditions and studies. Subsequently, the fluctuating components (root-mean-square or RMS) of the jet fluid signal and 2-D velocity fields are considered to isolate qualitative trends caused by changes in injectant molecular weight and specific heat ratio. Finally, the convective Mach number is approximated as an additional argument in the presented analysis. To this end, the bow shock shape is extracted, from PIV mean velocity data, together with velocity profiles in front and after the shock, as well as velocity profiles along the jet center streamline,

The crossflow conditions are set as described in Sec. 3.1 and Sec. 3.5. The jet is set according to Sec. 3.1.4 with the resulting measured global momentum flux ratios in Tab. 4.1. The conditions in the table represent all data points presented in this part of the study.

Table 4.1: Measured global momentum flux ratios, J, for each of the jet fluid signal and PIV data sets presented in this chapter. Also given are sonic injection velocities for the measured jet conditions as a reference for further discussion in the results.

	Jet Fluid Signal				PIV				-
J	1	2	4	6	1	2	4	6	a^* [m/s]
Ar	1.14	2.05	3.97	6.34	-	1.90	4.00	6.27	277.30
C_2H_4	1.06	1.98	4.05	5.84	-	2.11	4.00	5.82	311.70
CO_2	1.00	1.97	4.21	5.97	-	2.15	4.13	-	250.70
He	1.03	1.96	4.08	6.03	1.10	2.06	4.10	-	876.90
N_2	1.01	2.22	4.25	6.11	1.08	2.04	3.88	5.70	320.40

4.1 Definition of Jet Penetration

Confusion can arise in existing literature, regarding the effect of jet fluid properties on the jet penetration (or jet trajectory) and the associated mixing processes due to inconsistent definitions.

Usually, the penetration or jet trajectory is measured in terms of some form of concentration/jet fluid signal iso-contour. Only reading the conclusion of two studies, one states that "Since a larger penetration contour implies less freestream entrainment at a given stream- wise location, the ..." (Gruber, Nejad, Chen, *et al.*, 1997a), while the other claims that "The ethylene jet penetrates deeper into the freestream than the hydrogen jet." (Ben-Yakar *et al.*, 2006). In the first case the author is talking about the lower MW gas jet penetrating deeper into the crossflow, while in the second case the author is talking about the higher MW gas. These appear to be contradictory statements even though the result is the same: the higher MW gas jets seem to mix faster with the crossflow medium than the lower MW gas jets.

For the aforementioned examples, one should consider that mean trajectory and crossflow penetration are not the same as instantaneous crossflow penetration by large scale jet structures. Gruber, Nejad, Chen, *et al.* (1997a) consider a somewhat arbitrary mean intensity value corresponding to a jet fluid signal. They base their analysis on the iso-contour derived from this global threshold and come to the conclusion that faster contraction of this iso-contour, or lower penetration, is a sign of faster mixing. On the other hand, Ben-Yakar *et al.* (2006) base their penetration analysis on the identification of the upper edge of the jet in instantaneous schlieren snapshots. Based on the identified large scale structures, the faster mixing jet instantaneously will penetrate deeper into the crossflow, creating a larger spatial variance. The latter manifesting itself in larger RMS values for ensemble averaged results and a faster dropping mean concentration value as one moves along the jet. In neither case is the small scale or molecular mixing quantified, only the large scale entrainment

rate and turbulent mixing.

Further differences in interpretation can arise if jet fluid signal profiles are normalized to the local maximum jet fluid signal, e.g. at a given jet cross section. Whether ensemble averaged jet fluid signal profiles are normalized in this fashion or not varies across literature. A brief survey of studies in Tab. 4.2 shows that the majority of results are not reported with a normalization to local maximum values. Out of the selected studies only Pizzaia and Rossmann (2018) normalize their results and base further evaluation the normalized data. However, some trajectory definitions are ambiguous, e.g. it is not entirely clear how a trajectory based on the maximum signal from OH radicals in reacting jets or schlieren edges in non-reacting jets compare to trajectories based on ensemble averaged normalized and non-normalized jet fluid signal iso-contours.

In the following, a simple turbulent mixing model is considered to explain why normalized and non-normalized jet fluid signal profiles can lead to different conclusions regarding the effect of injectant properties on mixing and entrainment. The model roughly corresponds to turbulent scalar dispersion from a point source governed by a Gaussian process (Pope, 2000). This description is also applicable to the mixing of incompressible jets in quiescent environments (Bertagni *et al.*, 2019). With this model, the 2-D shape of a cross-sectional slice through the concentration field, $C(x, y)$ can be described as,

$$C(x,y) = \frac{2C_0}{\sqrt{\pi}\sigma(x)\left(\mathrm{erf}(y_{lim}) - \mathrm{erf}(-y_{lim})\right)} e^{-y^2/\sigma(x)^2}. \tag{4.1}$$

For the sake of this argument, imagine x to be the coordinate along the jet centerline and y as the transverse coordinate. In the above equation, the spread of the concentration profile is characterized by $\sigma(x)$ and $y_{lim} = 2.576$ is chosen to cover 99% of the area under a bell curve. C_0 is chosen such that at $x = 0$, $C(0, 0) = 1$ and a linear relationship for the growth of the profile spread is assumed, $\sigma = ax + b$. The rate of growth, a is important in the results while the functional form is not. The trends presented do not change for a polynomial, exponential or power law describing $\sigma(x)$.

Table 4.2: Brief survey of different jet penetration/trajectory definitions in the literature. "*Norm?*" refers to whether the jet fluid signal profiles are re-normalized by the local maximum jet fluid signal. The asterisk denotes ambiguity in the definition if it is based on qualitative markers or burning regions.

Trajectory data	Exp. or sim.	Test domain width	Parameters varied	Definition	Norm.?
Rothstein and Wantuck (1992)	Experiment	$>> 3$ cm?	J	max. intensity of averaged OH-PLIF signal	No*
Portz and Segal (2006)	Experiment	2.54 cm	injectant, J, M_∞, δ, $d_j(M_\infty)$	visually identified outer edge of jet from time averaged schlieren records	No*
Lin *et al.* (2010)	Experiment	15.2 cm	J, d_j, injection angle	$\chi = 0.01 \approx Y$ of ethylene from Raman scattering	No
Sun and Hu (2018b)	Simulation	infinite with non-reflecting boundary	J	$Y = 0.02$ of jet fluid	No
Pizzaia and Rossmann (2018)	Experiment	15 cm	d_j, δ, J	5% jet fluid concentration	Yes
Ben-Yakar *et al.* (2006)	Experiment	27 cm	injectant	Outer edge of instantaneous schlieren images	No*
Takahashi *et al.* (2010)	Experiment	3 cm	injectant, J, M_∞	max./50%/10% concentration locus	No
Povinelli *et al.* (1970)	Experiment	9.75 cm	M_j, J	1% helium concentration via sampling probe	No
McClinton (1974)	Experiment	22.84 cm	d_j	max. and $\chi = 0.005$ of hydrogen via sampling probe	No
McDaniel and Graves (1988)	Experiment	2.92 cm	J	1% of iodine LIF signal	No
Gruber, Nejad, Chen, *et al.* (1995)	Experiment	12.7 cm	injector shape, injection angle, J	10% intensity from Mie-scattering	No

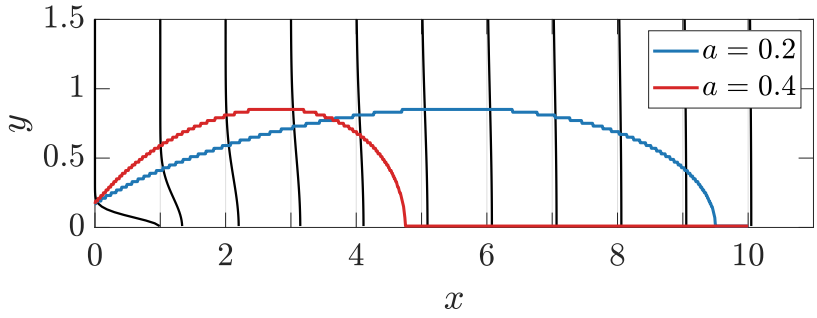

(a) Concentration iso-contours of a Gaussian mixing process. The growth rate a of the profile spread, σ, controls when the y-coordinate starts reducing again after the initial growth.

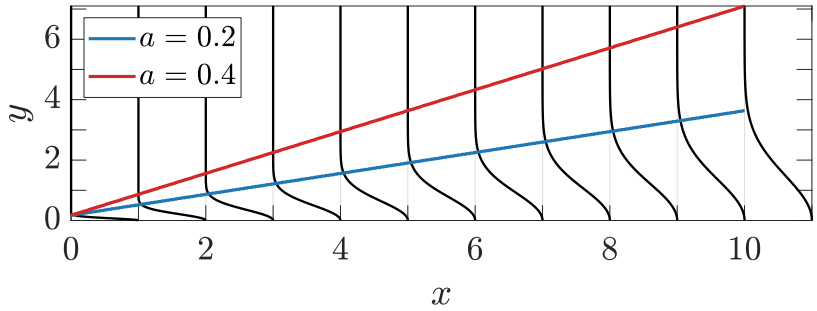

(b) Concentration iso-contours of a Gaussian mixing process for which the profiles at each x-coordinate have been re-normalized by the centerline concentration. The growth rate a of the profile spread, σ, determines how fast the y-coordinate of the iso-contour grows.

Figure 4.1: Examples for the two different approaches with which concentration iso-contour based jet penetration (or jet trajectories) are determined in JISCF literature. The threshold here is $C = 0.05$. The black concentration profiles are plotted proportional to the x-coordinate and only for the lower σ growth rate of $a = 0.2$.

Two pseudo concentration iso-contours ares extracted from the resulting $C(x, y)$ profiles. In one case a global iso-contour threshold is selected as 5%; in the other case the same threshold is selected but the profiles are re-normalized with the local centerline ($y = 0$) concentration value.

The result for the first case is shown in Fig. 4.1a. What is immediately evident is that the y-coordinate of the iso-contour does not grow monotonically. It grows initially and after a certain distance starts contracting again and eventually converges back to the centerline. This is due to the fact that for fast enough mixing the threshold concentration value is eventually equivalent to the maximum centerline concentration value. Away from

the centerline the scalar concentration has been diluted below the threshold value. In fact, even the centerline concentration will be below the threshold for further mixing but it is the closest that local conditions can still get to it. In this scenario, the position of the maximum y-coordinate depends on the rate of growth of σ. This is equivalent to saying that it depends on how fast the fluid mixes. For a slow enough mixing process, y could keep growing beyond the limits of the current example and no contraction towards the centerline would be observable. For a faster process, the maximum y-coordinate is reached faster.

In the second case, Fig. 4.1b, no matter the growth rate of σ, the y-coordinate of the iso-contour will keep increasing. However, the rate at which it increases does depend on the growth rate of σ. Thus, in this case, faster mixing yields a faster growing y-coordinate.

Of course a JISCF is not exactly analogous to a point source. Especially the existence of a CVP downstream of the point at which the jet turns parallel to the crossflow will cause deviations from an ideal Gaussian process and break the axial symmetry assumed in the model, see for example the spanwise measurements of Lin *et al.* (2010). Differences in lateral entrainment and mixing of the jet could also change the trends shown in Fig. 4.1. For example, large enough lateral entrainment could prevent a steady rise of the normalized trajectory and cause it to become parallel to or even to dip towards the line of maximum jet fluid signal (which itself will eventually be parallel to the crossflow). Compressibility effects in the near field of the jet might also play a role.

Nonetheless, on the symmetry plane of JISCF mean jet fluid signal profiles akin to Gaussian distributions have been reported by Sun and Hu (2018b). And even if the JISCF is not correctly described by a Gaussian process, the fact remains that jet penetration or trajectory defined by a locally normalized jet fluid signal should always exceed the non-normalized case in its transverse extent.

To summarize, jet penetration or trajectory results of ensemble averaged jet fluid signal measurements can come to contradicting conclusions depending on the definitions used. In the non-normalized case, a shallower or faster contracting jet fluid signal iso-contour

corresponds to faster or more efficient entrainment. On the other hand, in the normalized case more efficient mixing corresponds to a faster growing, i.e. deeper penetrating, iso-contour/trajectory. Moreover, the selection of the threshold value also influences the rate at which y changes so that small differences have to be expected even between studies that are identical save for the selected jet fluid signal threshold values, see for example Fig. 11 in Watanabe *et al.* (2012).

To the author's best knowledge, if the principles described in this section are applied, studies using different definitions and criteria largely agree on the effect of injectant properties on mixing and entrainment in JISCF flow fields. However, a unified comparison between a wide range of different injectants is still missing to clarify the impact of individual properties such as MW and γ. In this part of the study mainly trajectories based on absolute jet fluid signal iso-contours are considered as it appears to be the norm in the existing literature.

4.2 Development of a Jet Trajectory Scaling

To develop a JISF mean trajectory scaling, the momentum balance technique presented for the incompressible jet in crossflow (JICF) by Muppidi and Mahesh (2005) is extended to a high-speed compressible crossflow. Applying momentum balance analysis to a JISCF to estimate a characteristic scale has been attempted before by Zukoski and Spaid (1964). However, their approach balances the momentum components parallel to the test section wall and neglects the existence of velocity gradients due to the boundary layer and crossflow-dependent shock structures. The analysis presented here could be viewed as an extension and generalization, respectively, of these two studies.

For a meaningful extension of the technique by Muppidi and Mahesh (2005) similarities and differences between incompressible JICF and JISCF have to be considered. In both cases, a wall boundary layer represents a region with lower momentum that allows for an increase in the jet's crossflow penetration. Additionally, in the case of a JISCF, the

interaction of the jet with the supersonic crossflow leads to the formation of a bow-shock in front of the jet. Above the sonic line in the boundary layer, the bow shock will extend the momentum-deficit region as incoming crossflow fluid is shocked to much lower velocities. The change in velocity is especially strong through the almost vertical part of the shock, see Fig. 2.4b and the instantaneous schlieren visualizations in Fig. 4.2. Furthermore, as the sonic underexpanded jet expands into the crossflow, the jet fluid eventually will be forced to match the ambient pressure through the barrel-shock and the Mach-disk, see the mean flow field images in Fig. 4.2 for examples. This reduces the momentum flux of the jet itself, at least temporarily.

Based on these observations, one can expect that at a characteristic penetration height, h_c, the momentum of the jet will be rapidly overwhelmed by the crossflow momentum. This is corroborated by the topology of the RMS fields in Fig. 4.2. The visible jet shear layer in the RMS images can be considered as an indicator of the jet trajectory. At a certain height this trajectory quickly turns and runs almost parallel to the crossflow. The specific height at which this occurs should lie in a region where the bow shock becomes weaker and the jet fluid has passed through the jet shock system. Writing the integral momentum balance up to this penetration height behind the bow shock yields,

$$d_j \int_0^{h_c} \rho_{cf}(x,y) U_{cf}^2(x,y) \mathrm{d}y = C_h \int_{A_j} \rho_j U_j^2(x,z) \mathrm{d}A_j, \tag{4.2}$$

where C_h is a constant of proportionality and crossflow properties (subscript cf) are all functions of the position in the flow field due to the boundary layer and the bow shock. The integral on the right-hand side is taken over the jet orifice area. Because it is postulated that the momentum deficits introduced by the flow's compressibility features control the mean jet evolution, an integration up to regions of entirely constant velocity is not necessary.

As described by Muppidi and Mahesh (2005), the momentum balance in Eq. (4.2) assumes that the pressure gradient imposed on the jet by the crossflow is causing the jet

deflection and that this pressure gradient is proportional to the crossflow momentum flux. Furthermore, it assumes that significant jet deflection occurs once the transversely integrated crossflow momentum is comparable to the initial jet momentum.

To solve this integral relationship several simplifications have to be made. Because this study only deals with choked sonic jets, the jet velocity profile upon injection closely resembles a top-hat velocity profile, i.e. $U_j(x,z) \approx const. = U_j^*$ and $\rho_j = const. = \rho_j^*$. Moreover, as suggested by Muppidi and Mahesh (2005), the crossflow velocity profile in front of the jet is approximated as a linear function $u_{cf}(x,y) \approx u_{cf,2}(y)\, y/\left(\delta + \delta_s\right)$, where the subscript 2 denotes properties after a normal shock. Here, δ is the boundary layer thickness and δ_s is the extension of the boundary layer effects due to the bow shock momentum flux reduction. With these assumptions, the relationship in Eq. (4.2) can be simplified to,

$$\int_0^{h_c} \left(\frac{y}{\delta + \delta_s}\right)^2 \mathrm{d}y = \frac{1}{4} C_h \pi d_j J_2. \tag{4.3}$$

Solving for the characteristic penetration height (h_c) yields,

$$\frac{h_c}{d_j} = \left[\frac{3}{4} J_2 \pi C_h \left(\frac{\delta + \delta_s}{d_j}\right)^2\right]^{1/3}. \tag{4.4}$$

While it is expected that JISCF flow features scale with h_c, the characteristic penetration does not represent any physical features of the flow. Any direct correspondence between geometrical features of the JISCF flow field and h_c should be regarded as coincidental.

The additional momentum deficit region, δ_s, is estimated using a combination of blast-wave theory and oblique shock wave theory. To apply results from blast-wave theory, it is assumed that the JISCF can be viewed as the upper-half of a blunt-nosed cylinder. An assumption which has been made successfully before by Zukoski and Spaid (1964). The approximate radial coordinate, r, of a shock wave around such a body can be computed

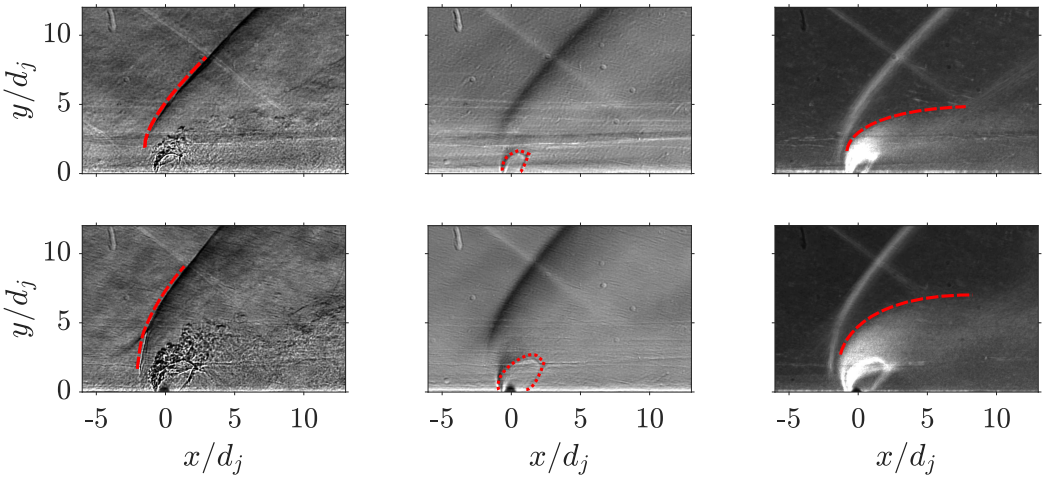

Figure 4.2: Schlieren visualization of a N_2 jet in a Mach 1.71 crossflow. Top row $J = 2$, bottom row $J = 6$. Left column: instantaneous images, middle column: mean images, right column: RMS images. Brighter color corresponds to higher intensity values. Red lines mark flow field features of interest for the scaling developed here. The variations in the salient flow features with J are clearly visible.

from results available in the literature (Anderson, 2006, chap. 4),

$$\frac{r}{d_{cyl}} = 0.795 C_D^{1/4} x^{1/2}, \tag{4.5}$$

where d_{cyl} is the diameter of a blunt-nosed cylinder and C_D is the drag coefficient. It is assumed that the momentum deficit region ends once the crossflow Mach number behind the bow shock is no longer subsonic, i.e. $M_2 = 1.01$. Using planar oblique shock relations the corresponding bow shock angle, β, can be found. As $dr/dx = \tan\beta$, the x-coordinate in Eq. (4.5) can be replaced, yielding,

$$\frac{r}{d_{cyl}} = 0.316 \frac{C_D^{1/2}}{\tan\beta}. \tag{4.6}$$

The two remaining unknowns are the equivalent body size, d_{cyl}, and the drag coefficient. The equivalent body size of the JISCF is replaced by utilizing an empirical observation by Papamoschou and Hubbard (1993) that can be interpreted as $d_{cyl} \propto J_2^{1/3} d_j$, i.e. the

characteristic "size" of the jet is proportional to the momentum flux ratio to the one-third power. With this proportionality, Eq. (4.6), and introducing an additional proportionality constant C_r, an explicit expression estimating the extent of the bow shock momentum deficit region is written in Eq. (4.7).

$$\frac{\delta_s}{d_j} \equiv \frac{r}{d_j} = \frac{0.316}{\tan\beta} C_r C_D^{1/2} J_2^{1/3}. \tag{4.7}$$

The drag coefficient, C_D, of a JISCF as well as two proportionality constants, C_h and C_r, remain to be determined. The drag coefficient is set to $C_D = C_{p,max}/2$, where $C_{p,max}$ is the pressure coefficient relative to the stagnation pressure behind a normal shock wave. This is a result of Lee's modified Newtonian law applied to a spherical body (Anderson, 2006, chap. 3). With regard to the drag coefficient, the latter is similar to a blunt-nosed cylinder. $C_{p,max}$ converges to $C_{p,max} = 2$ in the limit of infinite Mach number and $\gamma_\infty \to 1$.

The constants C_h and C_r are determined by comparing trends of the derived characteristic penetration scale, Eq. (4.4), with the purely empirical results of Portz and Segal (2006). The pre-multiplier of their trajectory curve fit, see Eq. (2.15), is summarized in one expression,

$$\frac{h_C^P}{d_j} = A(J_1)^{B+1/2D} \left(\frac{\delta}{d_j}\right)^E. \tag{4.8}$$

The dependence on the molecular weight is neglected because it is weak and h_c does not account for it either. The additional $0.5D$ factor in the exponent of pre-shock momentum flux ratio is due to the particular form assumed for the relevant x-direction scaling, i.e. $x/J^{1/2}d_j$. It is described and justified in more detail below. Resulting values for h_C^P/d_j are computed over the following parameter range: $M_1 = 1.5 - 3.5$, $\delta/d_j = 0.1 - 10$, $J_1 = 0.1 - 30$.

A three-parameter curve fit is performed using non-linear least squares to fit the developed expression for h_c to the parameter space spanned by h_C^P. For better visualization, the result is shown in Fig. 4.3 as a projection from the four dimensional fitting space with

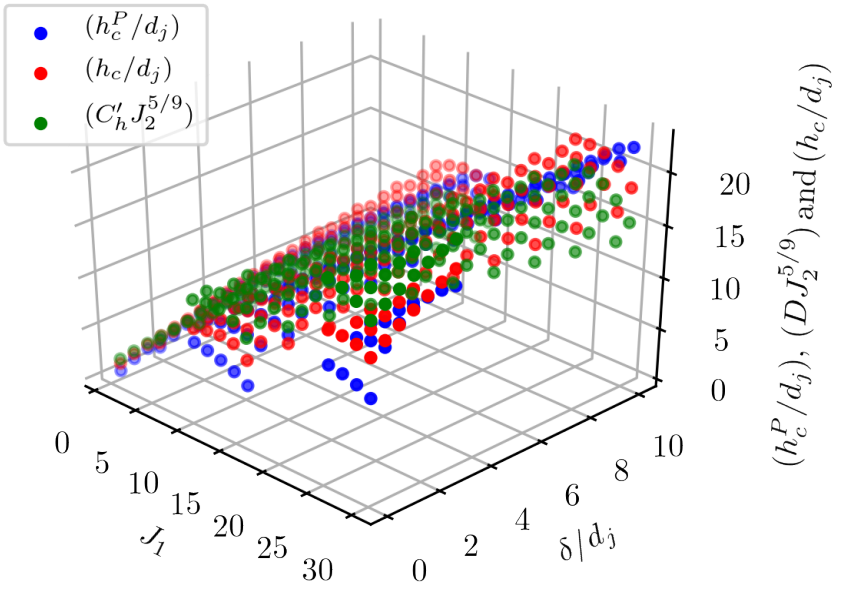

Figure 4.3: Results of curve fitting the expression in Eq. (4.4) to the empirical results of Portz and Segal (2006). Every 41st data point used for the curve fit is shown.

three independent parameters (J_1, δ/d_j and M_1) to three dimensions with two independent parameters. The R^2 value of the fit is 0.89 with $C_h = 0.084$ and $C_r = 17.236$.

The value of the constant C_h determined here is relatively close to the value of 0.05 measured by Muppidi and Mahesh (2005) for incompressible JICF. This could imply that the fundamental interaction between jet momentum and crossflow induced pressure gradients does not change from subsonic to supersonic flows.

To test the validity of a characteristic penetration height, h_c, the approach is applied to JISCF mean trajectory data collected for this study and to a number of already published data sets. It is also compared to several existing JISCF trajectory scalings.

The value of h_c/d_j is used to scale the non-dimensional transverse jet penetration y/d_j. However, the correct scaling for the x-coordinate is subject to an ongoing debate. In non-reacting, subsonic and incompressible JICF studies both x/Jd_j and $x/J^{1/2}d_j$ have been discussed. Theoretical and some experimental results suggest $x/J^{1/2}d_j$ as the more relevant scaling (Broadwell and Breidenthal, 1984; Smith and Mungal, 1998; Hasselbrink

and Mungal, 2001a). However, some studies, such as the one by Gevorkyan *et al.* (2016), achieve better trajectory collapse using a x/Jd_j scaling, suggesting that jet operating conditions have some influence on the ideal scaling parameter. Recently, in a compressible JISCF study, Pizzaia and Rossmann (2018) had success collapsing their jet trajectory relatively well using the $x/J^{1/2}d_j$ scaling. Thus, this study favors the latter scaling but will assess potential improvements in trajectory collapses using the x/Jd_j scaling as well.

Based on the preceding analysis and in the spirit of past JISCF studies, a JISCF trajectory law is proposed utilizing h_c/d_h as,

$$\frac{y}{d_j} = A\left(\frac{h_c}{d_j}\right)\left(\frac{x}{J_2^{1/2}d_j} - C\right)^B . \tag{4.9}$$

The momentum flux ratio after a normal shock is used in the x-coordinate scaling to account for the finding by Portz and Segal (2006). It increases comparability between studies at different crossflow Mach numbers. The coefficients A, B and C are determined in the validation that follows.

While the power-law form and the empirical determination of the coefficients A, B and C represent nothing new, the inclusion of the scaling coefficient, h_c/d_j does. Ideally, within the range of validity for h_c/d_j, the resulting trajectory power-law can make better and more universal predictions than previous attempts. Moreover, because h_c/d_j explicitly considers certain flow field physics, it should be easier for future researchers to identify other controlling factors, should their trajectory data deviate significantly from this power-law result.

Table 4.3: Data sets used for trajectory comparison. In all cases the trajectory is defined at the windward edge of the jet through some kind of jet fluid signal measurement with a threshold varying between 1-10%. For the entry marked with * no direct measurement is available, a reasonable value for $\delta_{95\%}/d_j$ was assumed based on the reported injector diameter, $d_j = 0.48$ mm, and the geometry of their test facility.

Trajectory data	M	J	Gases	d_j [mm]	$\delta_{95\%}$ [mm]	$\delta_{95\%}/d_j$
Rothstein and Wantuck (1992)	1.5	5.9-38.6	H_2	0.48	?	6*
Portz and Segal (2006)	1.6, 2.5	0.5-3	He , H_2 , Ar	1, 1.5, 3.2	3.7, 2.5	0.8-3.7
Lin *et al.* (2010)	2	0.49-1.52	C_2H_4	1.6, 4.8, 7.9	6.4	0.81-4
Sun and Hu (2018b)	2.7	1.85-5.5	Air	2	-	2.56
Pizzaia and Rossmann (2018)	3.4	1.2-5	Air	2.5, 3.1	-	0.6, 6.1
Current study	1.71	1-6	Ar , CO_2, C_2H_4 , He , N_2	2	5.26	2.63

4.2.1 Validation of the Jet Trajectory Scaling

The jet trajectories in this study are determined using the mean jet fluid signal images derived from Mie-scattering results as described in Sec. 3.3.2.4. As mentioned before, the actually measured quantity is $(\rho \cdot f)$, especially in regions of significant dilatation effects, and not purely the mixture fraction f. The trajectories reported are defined as the 2% jet fluid signal iso-contour on the windward side of the jet. The nominal flow conditions for all trajectories reported are summarized in Tab. 4.3.

Two previously published, empirical JISCF correlations by Rothstein and Wantuck (1992) and Lin *et al.* (2010) are considered in Fig. 4.4 and Fig. 4.5, respectively. For consistent comparison the scalings are adjusted to include the $J^{1/2}d_j$ normalization of the x-coordinate. Trajectory data used in the analysis is summarized in Tab. 4.3. All of the current study's results are displayed after processing them with a third order Savitzky-Golay filter to reduce spurious fluctuations.

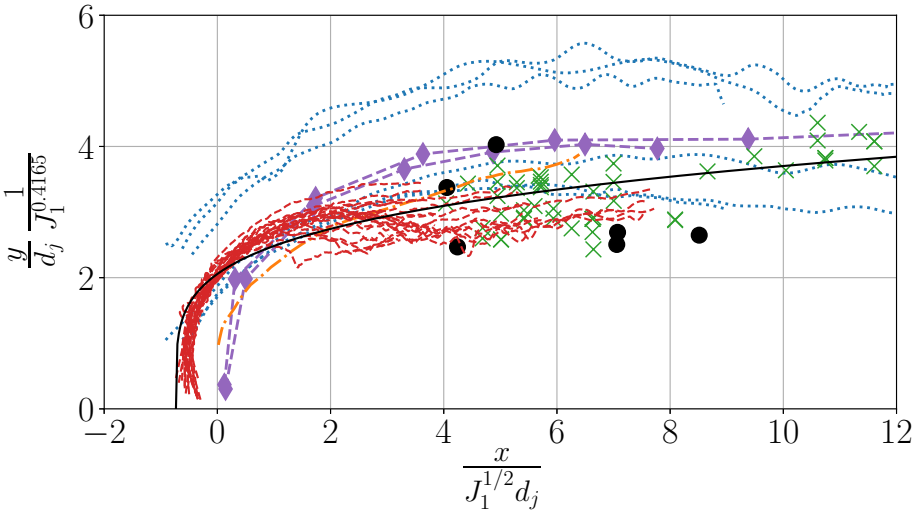

Figure 4.4: Trajectory collapse using the correlation reported by Rothstein and Wantuck (1992). ····· Pizzaia and Rossmann (2018), —◆— Sun and Hu (2018b), ● Lin *et al.* (2010), × Portz and Segal (2006), -·-·- Rothstein and Wantuck (1992), - - - - current study, —— power-law curve fit.

The scaling by Rothstein and Wantuck (1992) (Fig. 4.4) is more effective at collapsing the trajectory data. The data sets by Pizzaia and Rossmann (2018) are an exception, but

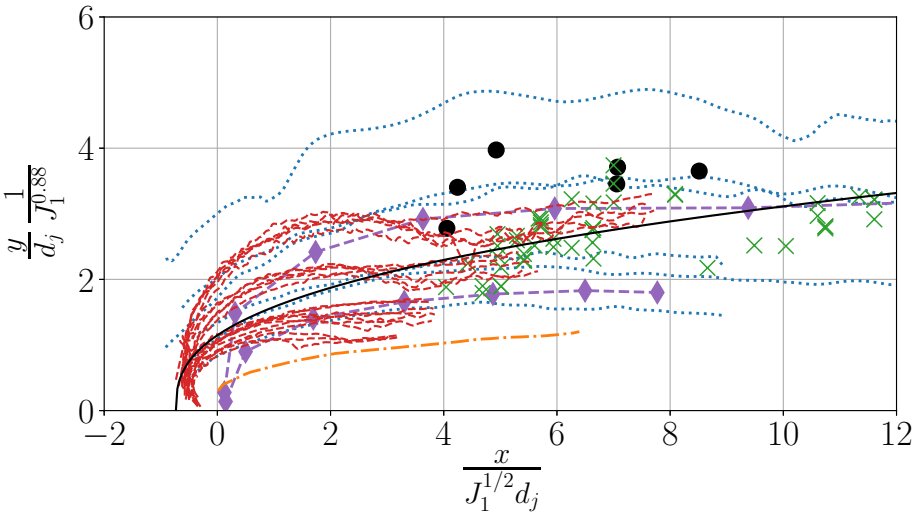

Figure 4.5: Trajectory collapse using the correlation reported by Lin *et al.* (2010). ····· Pizzaia and Rossmann (2018), —◆— Sun and Hu (2018b), ● Lin *et al.* (2010), × Portz and Segal (2006), -·-·- Rothstein and Wantuck (1992), - - - - current study, —— power-law curve fit.

that is not too surprising as they are the only ones reported for normalized jet fluid signal values and significant variation in the boundary layer effects δ/d_j. They show clearly that the Rothstein and Wantuck (1992) scaling does not explicitly consider differences in δ/d_j, i.e. the Pizzaia and Rossmann (2018) trajectories cluster by δ/d_j values (not explicitly shown in the figure), with the higher δ/d_j cases lying around $y/d_j/J_1^{0.4165} \approx 5$ and the thinner boundary layer cases lying around $y/d_j/J_1^{0.4165} \approx 3.5$.

For a more quantitative comparison of the effectiveness of different scalings the coefficient of determination R^2 is computed and summarized in Tab. 4.4. R^2 is a measure of the variance in an independent variable that can be predicted from the dependent variable. Thus, a higher R^2 value for a given trajectory scaling corresponds to a better correlation of the data points by that scaling.

To compute R^2 the data in Tab. 4.3 is first curve fitted using a power-law trajectory of the form $y/d_j = A(h/d_j)(x/J^{1/2}d_j - C)^B$, where (h/d_j) stands for whatever y-coordinate scaling a given correlation/scaling yields. The data set by Pizzaia and Rossmann (2018) is excluded from the curve fit and R^2 computation because it is the only study reporting

trajectories from normalized jet fluid signal profiles, see Tab. 4.2. Nonetheless, the data set is shown in the comparisons as it explicitly considers the effect of the boundary layer on jet penetration.

Thus, quantitatively, the Rothstein and Wantuck (1992) correlation also clearly works better than the Landsberg *et al.* (2016) correlation for the range of data investigated, with an R^2 value of 0.76 in Tab. 4.4. This might be due to the larger range of J values investigated in the Rothstein and Wantuck (1992) study, see Tab. 4.3.

Table 4.4: Coefficient of determination computed for the different correlations and scalings investigated. Only the Pizzaia and Rossmann (2018) data set is excluded from the computation due to the differing trajectory definition. Both x-scalings involving $J^{1/2}$ and J are considered.

	$R^2 - J^{1/2}$	$R^2 - J$
Rothstein and Wantuck (1992)	0.76	0.34
Lin *et al.* (2010)	0.51	0.69
Portz and Segal (2006)	0.69	0.67
Zukoski and Spaid (1964)	0.73	0.7
Current Study	0.77	0.66

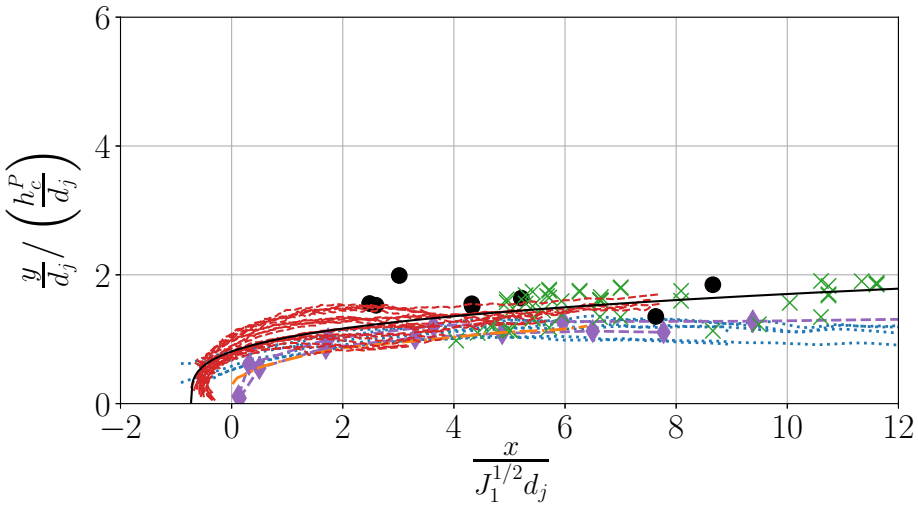

Figure 4.6: Trajectory collapse using the correlation reported by Portz and Segal (2006). Pizzaia and Rossmann (2018), Sun and Hu (2018b), Lin *et al.* (2010), Portz and Segal (2006), Rothstein and Wantuck (1992), current study, power-law curve fit.

Trajectory collapse for the Portz and Segal (2006) correlation is shown in Fig. 4.6. Based on the R^2 value in Tab. 4.4 it performs slightly worse than the Rothstein and Wantuck (1992) result. However, it does seem to account for changes in δ/d_j, as evident in the relatively improved collapse of the Pizzaia and Rossmann (2018) data. The fact that the trajectories cluster close to $y/d_j/(h_c^P/d_j) \approx 1$ suggests that the empirical correlation could be capturing a relevant length scale of the JISCF flow field. An attempt was made to use J_2 in the Portz and Segal (2006) correlation but it worsened the R^2 score significantly, probably due to the fact that it is a purely empirical correlation that was derived for usage with the pre-shock value J_1.

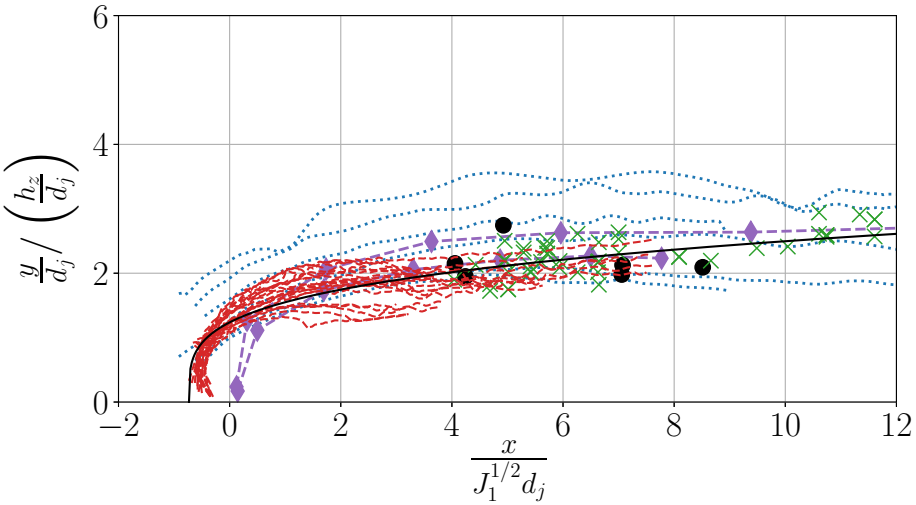

Figure 4.7: Trajectory collapse using the scaling factor reported by Zukoski and Spaid (1964). ····· Pizzaia and Rossmann (2018), —◆— Sun and Hu (2018b), ● Lin *et al.* (2010), × Portz and Segal (2006), -·-·- Rothstein and Wantuck (1992), - - - - current study, —— power-law curve fit.

In Fig. 4.7 the trajectory collapse using the scaling of Zukoski and Spaid (1964) (Eq. (2.13)) is considered. This entirely analytic scaling, devoid of any empirical constants, works well both qualitatively and quantitatively in comparison to correlations shown so far. In terms of R^2, it performs almost as well as the Rothstein and Wantuck (1992) correlation. Thus, a scaling approach based on the streamwise momentum balance between crossflow and jet yields promising results. The only discernible shortcoming is the missing consideration

of boundary layer effects, as evidenced by the spread in the Pizzaia and Rossmann (2018) data.

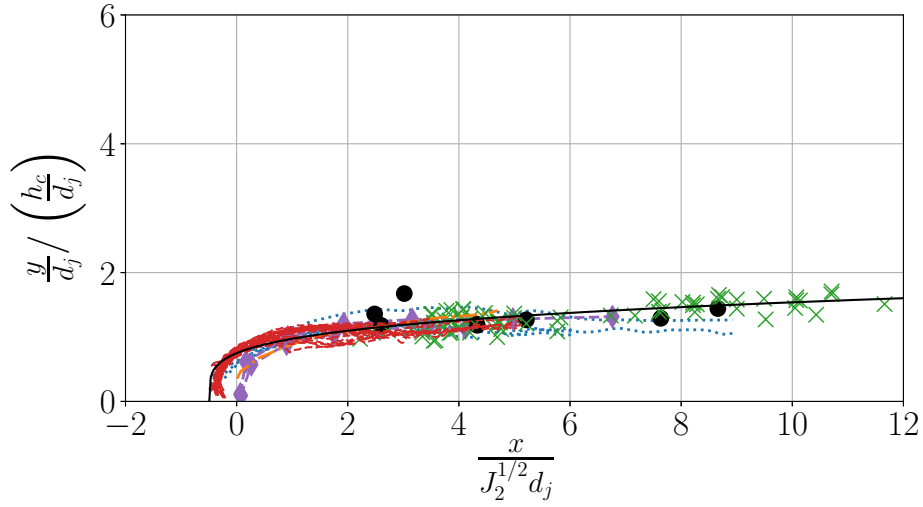

Figure 4.8: JISCF mean trajectories scaled with the h_c parameter presented in this study. The collapse is significantly improved for the entire range of momentum flux ratios, Mach numbers, jet injectants and boundary layer thicknesses. ····· Pizzaia and Rossmann (2018), —◆— Sun and Hu (2018b), ● Lin *et al.* (2010), × Portz and Segal (2006), -·-·- Rothstein and Wantuck (1992), - - - - current study, —— power-law curve fit.

The results for the semi-analytical scaling developed in Sec. 4.2, i.e. $x/(J_2^{1/2}d_j)$ and $y/d_j/(h_c/d_j)$, are presented in Fig. 4.8. Qualitatively, the collapse of all jet trajectories considered is relatively good. The scaling appears to capture boundary layer effects successfully, as evidenced by the collapse of the Pizzaia and Rossmann (2018) data. It also collapses trajectories close to a value of $y/d_j/(h_c/d_j) \approx 1$, i.e. it could represent a relevant flow length scale.

Out of all approaches considered it has the highest R^2 value, see Tab. 4.4. The curve fit constants for Eq. (4.9) are $A = 0.886$, $B = 0.235$, and $C = -0.492$. Close to the jet orifice, the curve fit is biased towards the data collected for this study due to the low amount of data points available in this area from other studies.

Some remaining variability between trajectories can partly be attributed to differences in trajectory definition, diagnostics used (Tab. 4.2), the way in which the jet origin is reported, entrainment/mixing differences between injectants, and experimental uncertainty.

That the Pizzaia and Rossmann (2018) data collapses relatively well with all the other data should be regarded as fortuitous, since the corresponding trajectory definition is very different from the other studies used in this evaluation.

The R^2 improvement over the empirical Rothstein and Wantuck (1992) correlation and the analytical Zukoski and Spaid (1964) scaling is relatively small, the new scaling captures between between 1%-5% more of the variance in the data sets used for comparison. However, the new scaling explicitly considers additional aspects of the flow field controlling the jet trajectory, i.e. the bow shock and the velocity boundary layer. Thus, using the new scaling, it is easier to investigate further parameters' effects on the jet trajectory and potentially extend the model to account for those. For example, the influence of injectant properties on JISCF mean trajectories is discussed in more detail below.

The relative success of the newly presented scaling supports the notion that the effective momentum flux ratio computed for crossflow properties after a normal shock, J_2 (Eq. (2.16)), might be more relevant for the problem than the global, pre-shock momentum flux ratio J or J_1. The comparison of R^2 values for different correlations in Tab. 4.4 also shows that the by far dominant parameter determining the mean jet trajectory is the momentum flux ratio. Thus, the newly developed scaling is particularly useful for cases in which a thick boundary layer is present and J_1 is relatively low ($1 < J_1 < 10$). For higher values of J_1 and thin boundary layers, the empirical Rothstein and Wantuck (1992) correlation and the analytical Zukoski and Spaid (1964) scaling are sufficient.

Data points with $J < 0.5$ have been excluded from the current jet trajectory analysis as they do not collapse with the other data points. Given that the current formulation of h_c emphasizes the importance of the momentum flux reduction in both crossflow and jet, it is likely that such barely choked jets do not result in the required shock strengths for the scaling to work. This is in contrast to the model developed by Heister and Karagozian (1990) for perfectly expanded and barely underexpanded jets. The combination of the physical insights from their approach with the presented study could yield impactful results.

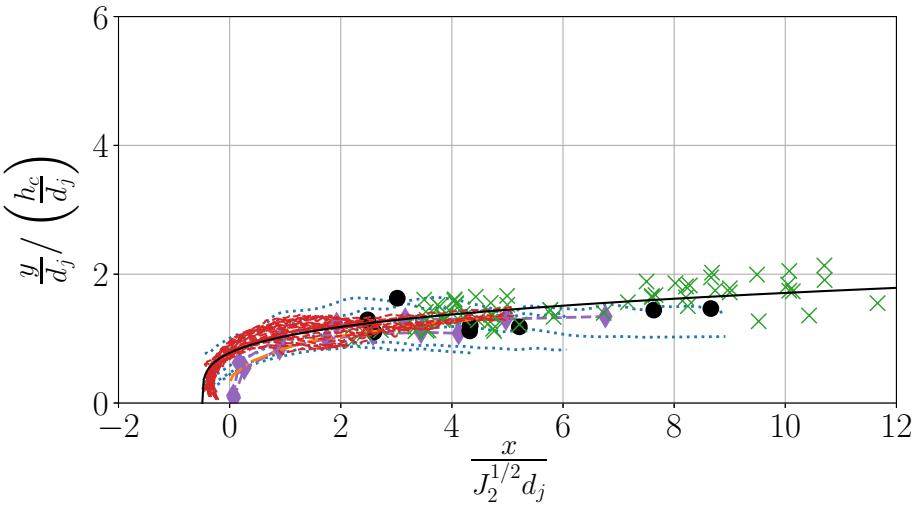

Figure 4.9: Trajectory collapse using a simplified h_c' scaling parameter for engineering estimates. ····· Pizzaia and Rossmann (2018), —◆— Sun and Hu (2018b), ● Lin *et al.* (2010), × Portz and Segal (2006), -·-·- Rothstein and Wantuck (1992), - - - - current study, —— power-law curve fit.

The prominent importance of the momentum flux ratio in determining the mean jet trajectory motivates a simplification of the proposed scaling parameter, h_c, to provide a simpler engineering estimate at the expense of loosing explicit flow field physics representation. Assuming that $\delta < \delta_s$ at large J, a reasonable assumption for thin supersonic boundary layers, one can write a simplified characteristic penetration as,

$$\frac{h_c'}{d_j} = C_h' J_2^{5/9}. \tag{4.10}$$

All of the constant values, the calibration constants, and the weakly Mach number dependent drag coefficient and shock angle β are lumped together into one calibration constant C' in this expression. The analytically derived exponent value of $5/9$ is about 33% higher than the empirical measurement of 0.4165 by Rothstein and Wantuck (1992). Performing the multi-parameter curve fit described in Sec. 4.2 again yields $C_h' = 1.43$ and $R^2 = 0.73$, compared to $R^2 = 0.89$ for the full scaling expression of h_c. See Fig. 4.3 for the resulting fit surfaces.

The JISCF trajectory collapse with this simplified scaling is shown in Fig. 4.9. As

would be expected, the spread in the Pizzaia and Rossmann (2018) data is slightly larger because the boundary layer thickness is no longer considered explicitly. Nonetheless, a $R^2 = 0.75$ is achieved for all other data sets, compared to the $R^2 = 0.77$ of the full scaling expression and $R^2 = 0.76$ of the Rothstein and Wantuck (1992) correlation. The power law constants in Eq. (4.9) are very similar to those of the full scaling expression with $A = 0.936$, $B = 0.256$, and $C = -0.492$.

The analysis briefly returns to the previous section's question about what x-coordinate scaling is the most meaningful one in a JISCF flow field. For the evaluation of the above approaches using J instead of the square-root value all other parameters are adjusted appropriately. The R^2 values in Tab. 4.4 clearly show that using J instead of $J^{1/2}$ deteriorates correlation between trajectories for all cases considered. Thus, $J^{1/2}$ is the more relevant x-coordinate scaling parameter although flow conditions might exist where this is not true.

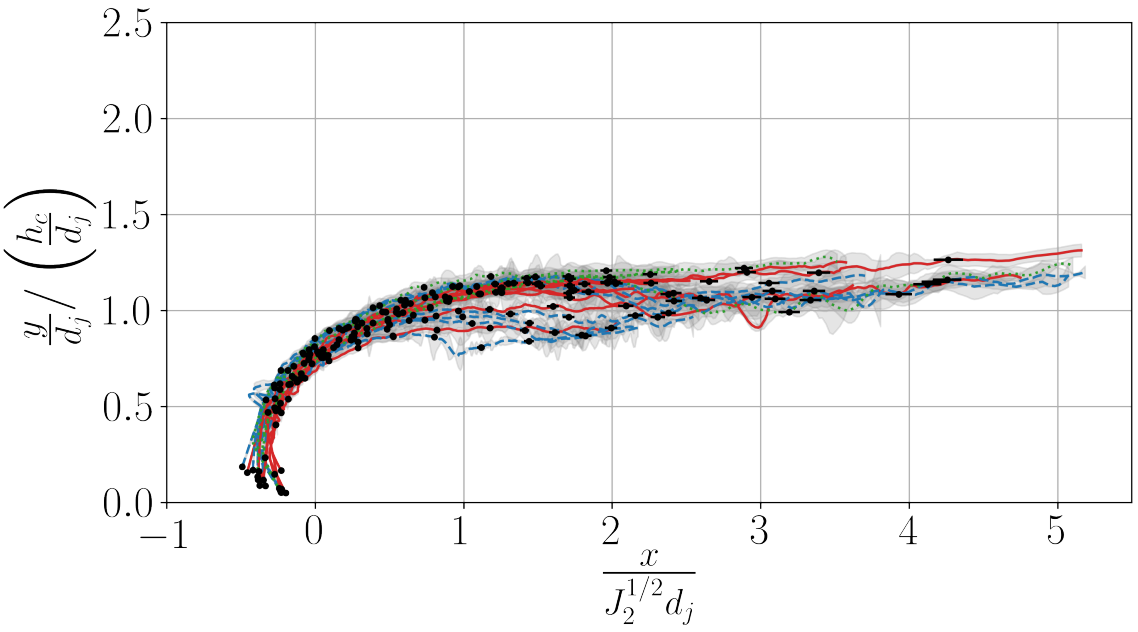

Figure 4.10: Visualization of uncertainties in this study's jet trajectory data and influence of γ on penetration. Lines are the trajectories reported, gray bands are uncertainties in the y-coordinate, and black dots with horizontal lines are uncertainties in the x-coordinate at every 40th data point. —— $\gamma = 1.66$ (Ar & He), ····· $\gamma = 1.4$ (N_2), - - - - $\gamma = 1.28\,\&\,1.237$ (CO_2 & C_2H_4).

With the new scaling at hand, the trajectory data collected in this study is analyzed

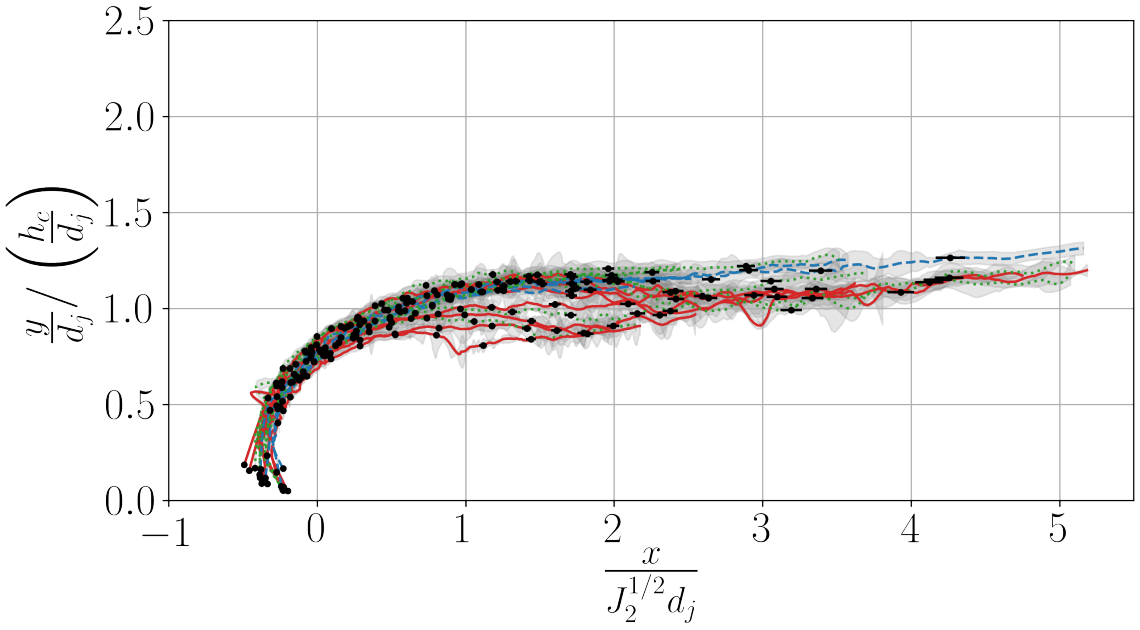

Figure 4.11: Visualization of uncertainties in this study's jet trajectory data and influence of MW on penetration. Lines are the trajectories reported, gray bands are uncertainties in the y-coordinate, and black dots with horizontal lines are uncertainties in the x-coordinate at every 40th data point. —— $MW \approx 40$ g/mol (Ar & CO_2), ····· $MW \approx 28$ g/mol (C_2H_4 & N_2), - - - - $MW = 4$ g/mol (He).

in more detail. Confidence intervals are shown in Fig. 4.10 and Fig. 4.11. The intervals are computed as described in Appendix C. In the normalized y-direction the confidence intervals are relatively small and limited to intervals of roughly $\pm 0.25\, y/d_j/(h_c/d_j)$. Uncertainties in the normalized x-direction grow slowly with downstream distance up to a maximum interval size of about $\pm 0.12\, x/J_2^{1/2}d_j$.

Trajectories in Fig. 4.10 and Fig. 4.11 are marked to emphasize the effect of varying jet fluid specific heat ratio and molecular weight, respectively. Close to the jet orifice, the jet fluid properties (MW and γ) do not seem to have a discernible effect on the mean trajectory. Downstream of the jet bending point, however, the scatter between trajectories increases. The effect of γ on normalized penetration in Fig. 4.10 is weak and suggests that higher γ leads to slightly higher penetration and later drop-offs in the 2% jet fluid signal iso-contour.

Moreover, two of the lowest MW gases used, helium and ethylene, exhibit higher

penetration and later drop-off of the iso-contour than the higher MW gases used, argon and carbon dioxide, see Fig. 4.11. This trend becomes clearer the farther downstream one moves along the jet.

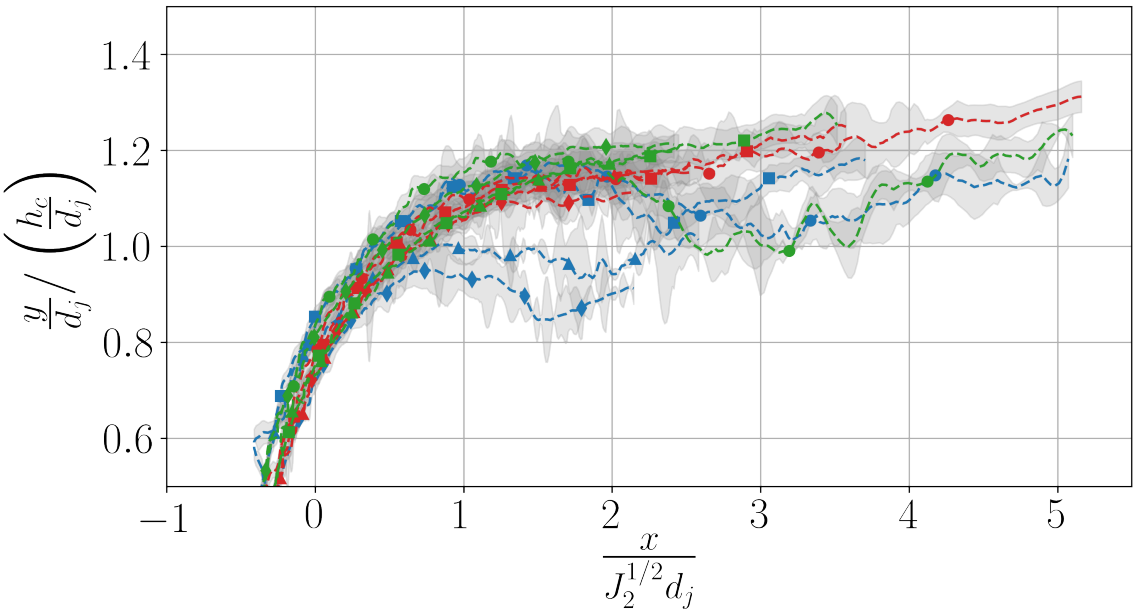

Figure 4.12: Close up of nitrogen and helium trajectories. - - - - N_2 with $MW = 28$ g/mol & $\gamma = 1.4$, - - - - C_2H_4 with $MW \approx 28$ g/mol & $\gamma = 1.237$, - - - - He with $MW = 4$ g/mol & $\gamma = 1.66$. • $J = 1$, ■ $J = 2$, ▲ $J = 4$, ♦ $J = 6$.

Because the trajectories are defined along absolute jet fluid signal iso-contours, and recalling the discussion in Sec. 4.1, the observations imply that gases with lower specific heat ratios mix faster with the crossflow than gases with higher specific heat ratios. These results generally agree with the conclusions in Gruber, Nejad, Chen, *et al.* (1997a), Ben-Yakar *et al.* (2006), and Takahashi *et al.* (2010). They are also supported by the convective Mach number results of (Papamoschou and Roshko, 1988) and Gruber, Nejad, Chen, *et al.* (1997a), where lower MW gases cause a higher convective Mach number which suppresses hydrodynamic instability growth and entrainment.

The trend that injectants with lower specific heat ratio mix faster can potentially also be explained with the convective Mach number model. However, the trend for changing specific heat ratio appears weaker than for changes in the molecular weight. Thus, it will

be analyzed in more detail in the discussions to follow.

Fig. 4.12 focuses on the nitrogen, ethylene, and helium cases. Again, the overall influence of injectant properties appear small. Nonetheless, trends are discernible. Except for $J = 1$, the ethylene trajectories all drop-off faster than the corresponding nitrogen trajectories. This suggests that the higher γ of nitrogen causes a reduction in entrainment and turbulent mixing rates, since its MW is almost identical to that of ethylene. At $J = 1$ the nitrogen and ethylene trajectory evolve closer together, i.e. at this low momentum flux ratio the hydrodynamic instabilities influenced by the convective Mach number might be less important for mixing. Meanwhile, boundary layer interaction might be more important.

Ethylene also clearly mixes faster than the helium jets at all J. Interestingly, the nitrogen trajectories penetrate deeper than the helium trajectories for $J > 1$. This seems to contradict the notion that higher MW injectants should entrain and mix faster. However, there are two logical explanations for this behavior. One, the helium and nitrogen trajectories exhibit very similar penetration overall, i.e.the nitrogen cases penetrating deeper could be a an artifact of experimental uncertainty. For the other explanation, the discussion of jet fluid signal iso-contour behavior in 4.1 is recalled. Then, the nitrogen trajectories penetrating deeper than helium can be interpreted as nitrogen having a larger turbulent mixing rate than helium, but not as high as ethylene, so that the drop-off point in the trajectory is not reached in the experimental FOV for $J > 1$. The latter point also implying that for the presented data, nitrogen has the second lowest turbulent mixing rate overall.

Fig. 4.10 and Fig. 4.11 show that the higher MW gases, argon and carbon dioxide, both do not penetrate as deep as nitrogen and/or reach drop-off points in their trajectories at all J. Thus, supporting the possibility that the observed behavior of the nitrogen trajectories is indeed due to the turbulent mixing rate and not just the experimental uncertainties.

To summarize, the injectant properties' influence on penetration trajectories is relatively weak. However, careful analysis leads to interesting observations that can be used to guide research and to provide better comparability for further mixing studies.

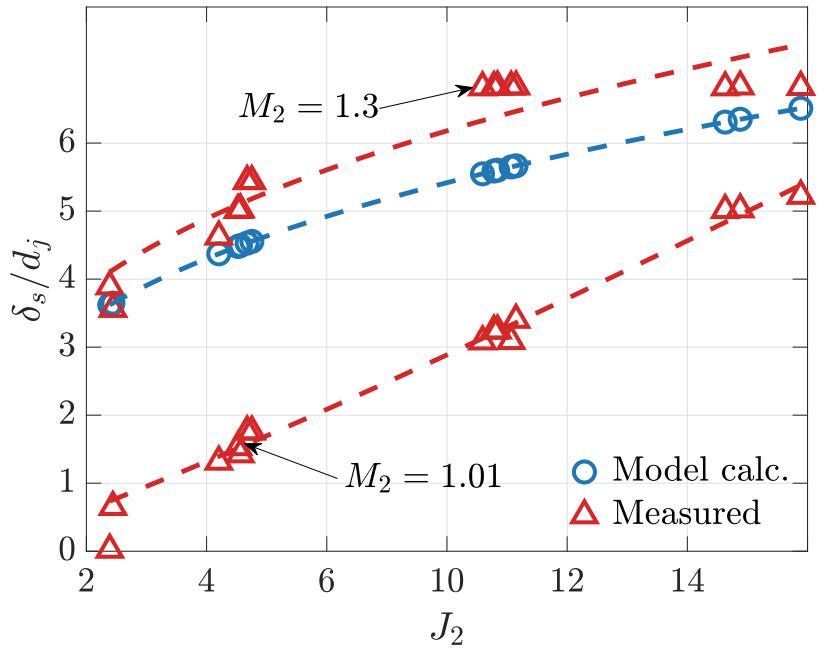

Figure 4.13: Comparison of the δ_s/d_j parameter computed via Eq. (4.7) and derived from PIV results for two different post-shock cut-off Mach numbers.

4.2.2 PIV Bow Shock measurements

PIV records acquired for this study allow for a direct measurement of the parameter δ_s/d_j defined in Eq. (4.7). After bow shock shape extraction, see Sec. 3.6, the angle β at which a certain post-shock Mach number is achieved and the corresponding wall-normal distance can be found directly. Subtracting the boundary layer thickness from this distance should yield an experimental measurement of δ_s.

For the development of the scaling parameter h_c it was assumed that $M_2 = 1.01$ denotes the end of the region with significant momentum deficit, yielding good trajectory collapse over a wide range of conditions. Fig. 4.13 compares the theoretically predicted δ_s/d_j with the experimentally determined values for this cut-off Mach number. The expression in Eq. (4.7) clearly over-predicts the extent of δ_s/d_j but with a smaller growth rate, especially at low J. At larger J the experimental and theoretical values could be converging.

The deviation between experiment and blast wave theory can probably be attributed in part to the shielding effect of the boundary layer. At low J, the jet barely leaves the

boundary layer, i.e. it forces the supersonic part of the crossflow less to deviate from its current flow direction than at higher J. At higher J, the boundary layer effects become less pronounced and the bow shock shape tends towards that predicted by blast wave theory for a solid body.

To obtain values and trends similar to that of Eq. (4.7) from the experiments, a cut-off Mach number of 1.3 has to be used. Thus, for the current experimental setup, blast wave theory predicts a stronger and spatially more extended bow shock than what is actually present. Using an empirical power-law for the Mach 1.3 cut-off measurement yields,

$$\frac{\delta_s}{d_j} = 3.06 J_2^{0.339}. \tag{4.11}$$

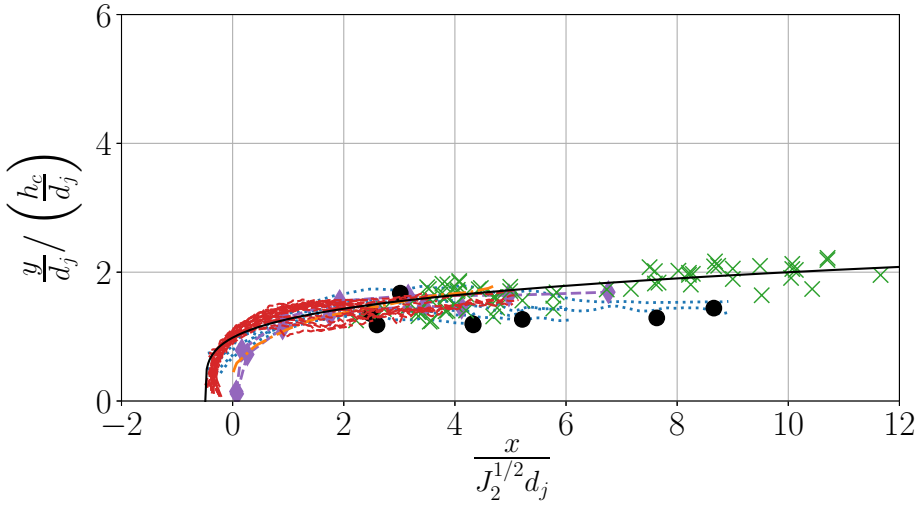

Figure 4.14: JISCF mean trajectories scaled with the h_c parameter presented in Eq. (4.4) using an empirically determined expression for δ_s/d_j. ····· Pizzaia and Rossmann (2018), —◆— Sun and Hu (2018b), ● Lin *et al.* (2010), × Portz and Segal (2006), -·-·- Rothstein and Wantuck (1992), - - - - current study, —— power-law curve fit.

Using the empirical power law in Eq. (4.11) instead of the blast wave based result (Eq. (4.7)) for the calculation of h_c/d_j gives the trajectory collapse in Fig. 4.14. The corresponding value of the required empirical constant is $C_h = 0.0314$, which is still relatively close to the incompressible result of Muppidi and Mahesh (2005). With $R^2 = 0.76$ the degree of correlation for this version of h_c is comparable to that using the blast wave derived

expression for δ_s.

The results suggest that while the presented scaling works reasonably well and the crossflow effects considered (boundary, bow-shock) are relevant, their relative contributions to the scaling are not captured correctly, yet. It is also unlikely that the ad-hoc selected cut-off off Mach 1.3 is universal. Changing δ/d_j and M_∞ will probably change the cut-off and the numerical values of the constants in Eq. (4.11). Thus making at least the multiplier in front of the base of the exponent a function of the freestream Mach number and boundary layer thickness. At high J and/or very thin boundary layers the experimentally measured δ_s/d_j could converge towards the blast wave result.

4.3 Influence of Jet Fluid Properties

To investigate the influence of injectant properties on the JISCF flow field evolution further, RMS jet fluid signals and velocity profiles are extracted. Data is extracted along the jet trajectories determined for each case and along four vertical profiles at the same normalized x/d_j coordinate for each case. The vertical profiles are taken at $x/d_j = 0$, 1.5, 3 and 4.5.

Examples of the mean and RMS jet fluid signal fields are shown in Fig. 4.15a and Fig. 4.15b, respectively, for the case of nitrogen injection. Corresponding examples of nitrogen-jet PIV fields are shown in Fig. 4.16a and Fig. 4.16b, respectively. In all jet signal fluid and PIV fields the coordinates are normalized with the jet diameter and solid black lines indicate the extracted profiles. The results for all remaining cases can be found in Appendix A and Appendix B for jet fluid signals and PIV fields, respectively.

In the PIV fields, magenta solid lines are part of the jet center-streamline used in the convective Mach number calculations discussed below. This streamline is determined by integrating from the $x = 0$, $y = 0$ location forward in time using the mean velocity field data. The dt for the streamline integration is 400 ns, lower values did not yield any more appreciable changes in the streamline paths.

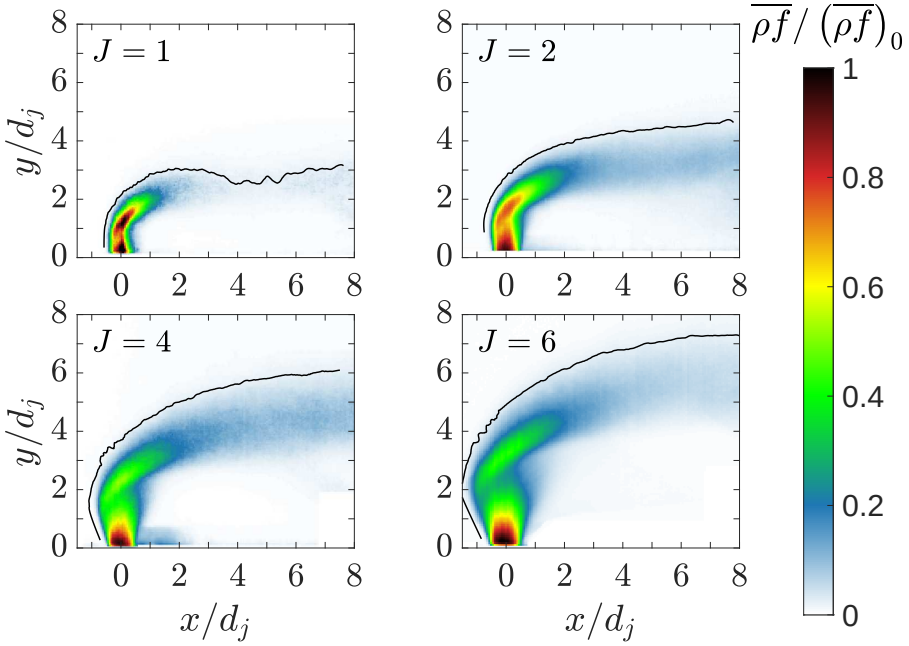

(a) Mean jet fluid signal fields for the N_2 jet. The jet fluid signal is decreasing from the injection point down the jet trajectory as the injectant is entrained into the crossflow. The non-monotonic behavior around $y/h_c = 1 - 2$, with ρf suddenly increasing again shortly, is due to density effects, i.e. the barrel and Mach disk shock formed by the jet.

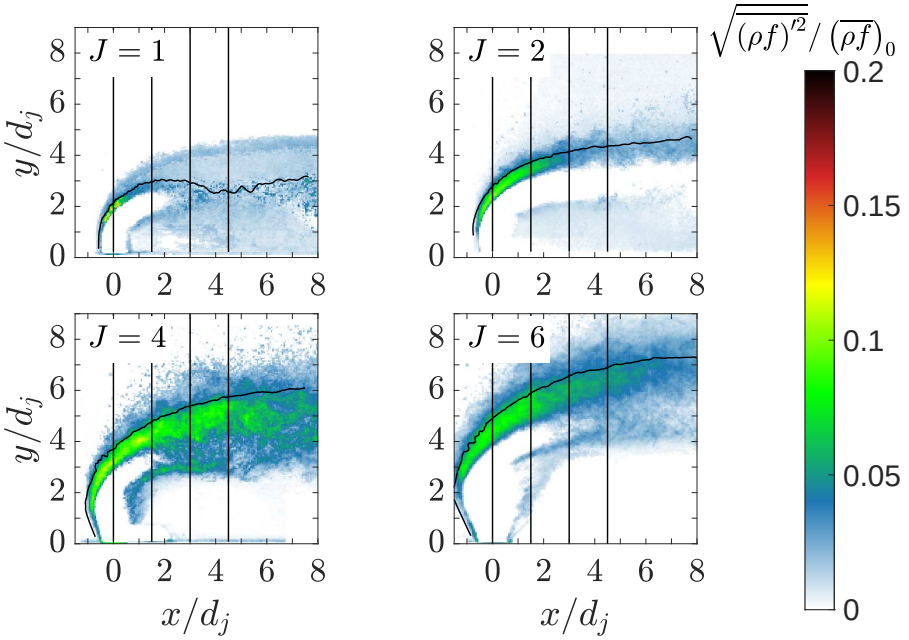

(b) RMS jet fluid signal fields for the N_2 jet. The behavior and extend of jet fluid signal fluctuations can be seen to change qualitatively with increasing J. Likely a consequence of the jets changing interaction with the crossflow boundary layer and changing velocity gradients.

Figure 4.15: Example jet fluid signal fields for N_2 injection. While the details differ between different gas injection cases, general features and trends are similar. Black solid lines represent profiles along which data is extracted in the following analysis.

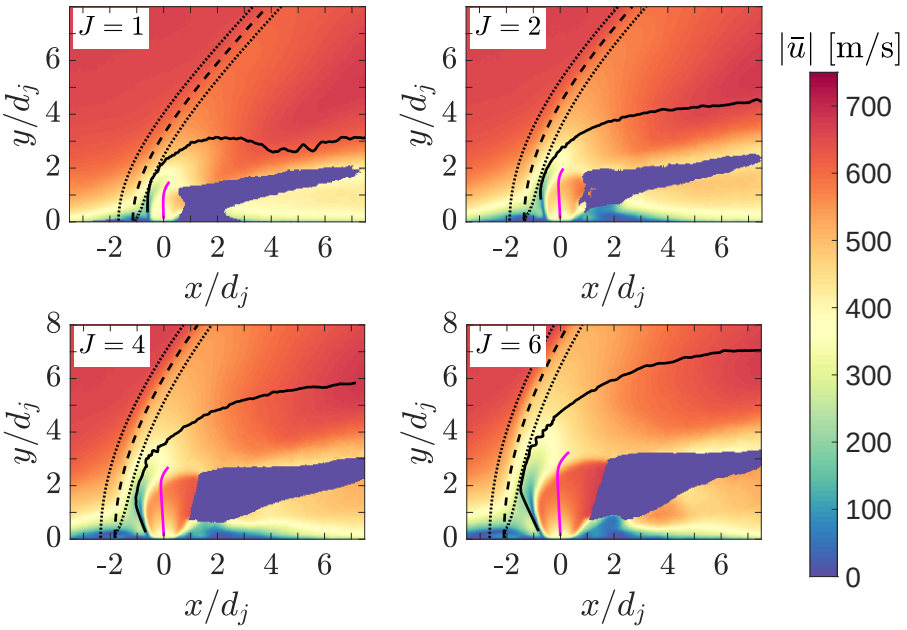

(a) PIV mean velocity fields for the N_2 jet. In all cases the jet velocity increases initially before the jet shock structure is reached, the maximum jet velocity increaases with J. The black dashed line is the PIV derived shock position, black dotted lines are profiles along which pre- and post-shock velocities are extracted, and the magenta line is part of the jet center-streamline along which the jet velocity is extracted.

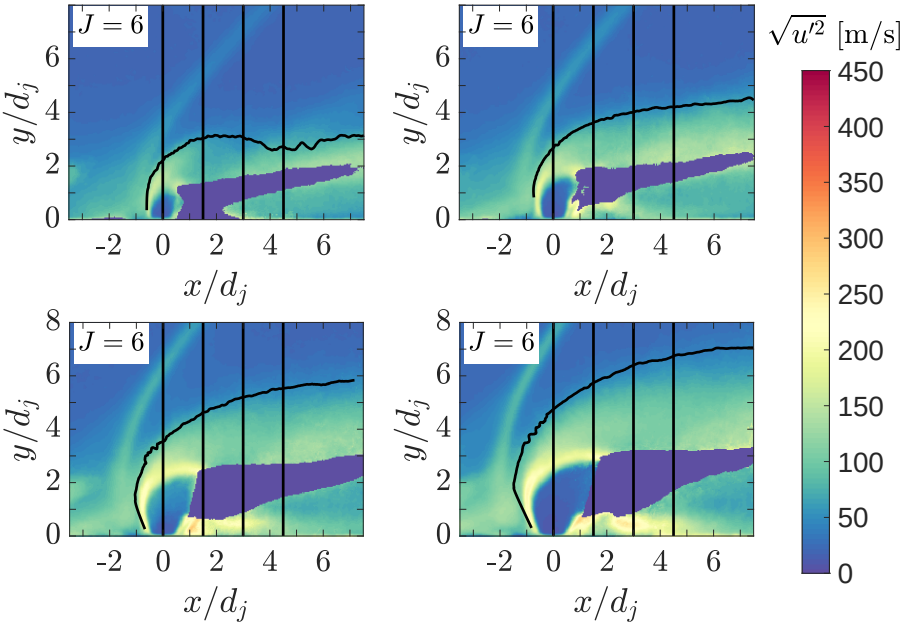

(b) PIV RMS velocity fields for the N_2 jet. The largest fluctuations are present in the vicinity of the jet shock structures where the jet shear layer starts forming and in near-wall regions downstream of the jet.

Figure 4.16: Example PIV velocity fields for N_2 injection. While the details differ between different gas injection cases, general features and trends are similar. Black solid lines represent profiles along which data is extracted in the following analysis.

4.3.1 Jet Fluid Signal and Velocity Statistics along Jet Trajectories

The jet fluid signal RMS development along the jet trajectories is shown in Fig. 4.17. The arc length coordinate used on the x-axis of these plots is defined as,

$$\hat{s} = \sum_i \sqrt{(\mathrm{d}\hat{x_i}^2 + \mathrm{d}\hat{y_i}^2)} \tag{4.12}$$

where $\hat{.}$ indicates variables normalized with the scalings developed in Sec. 4.2. The color coding is primarily designed to highlight the effects of the molecular weight, as the mean trajecory results in Fig. 4.11 suggest a stronger effect with MW than γ. Confidence intervals are computed in accordance with Appendix C.

As can be seen Fig. 4.17, the values of jet fluid signal fluctuations can exhibit large jumps or oscillations over very small spatial regions. The same is true for jet fluid signal fluctuation results along vertical profiles discussed later in this chapter. This noisiness is a result of the PDF method used to retrieve the jet fluid signal from the Mie-scattering signal. It indicates that in some cases/positions either the Mie-scattering PDFs used in the inversion are not sufficiently converged or the regularization approach used is not appropriate. A further source of uncertainty not considered, is the possibility of remaining density fluctuations downstream of the jet turning deeper in the crossflow. Thus, because only the statistical uncertainty, not the actual data uncertainty, of the jet fluid signal is estimated in this study (see Appendix C), the uncertainty bars in the figures appear smaller than they should be.

Another limitation imposed by the presence of these oscillations and the missing data uncertainty is that only qualitative trends and relative changes in the jet fluid signal fluctuations can be considered in the following discussions.

A general feature indicative of the effectiveness of the developed scaling is that the peak jet fluid signal fluctuations collapse for all cases at a value close to $\hat{s} = 1$. At higher momentum flux ratios, the peak appears to move to values slightly smaller than unity. At

the same time, peak jet fluid signal fluctuations are decreasing slightly and almost equalize between the different injectants. This overall decrease in peak fluctuation magnitude could mean that the strongest jet fluid signal fluctuations move away from the edge of the jet defined by the 0.02 contour as J increases.

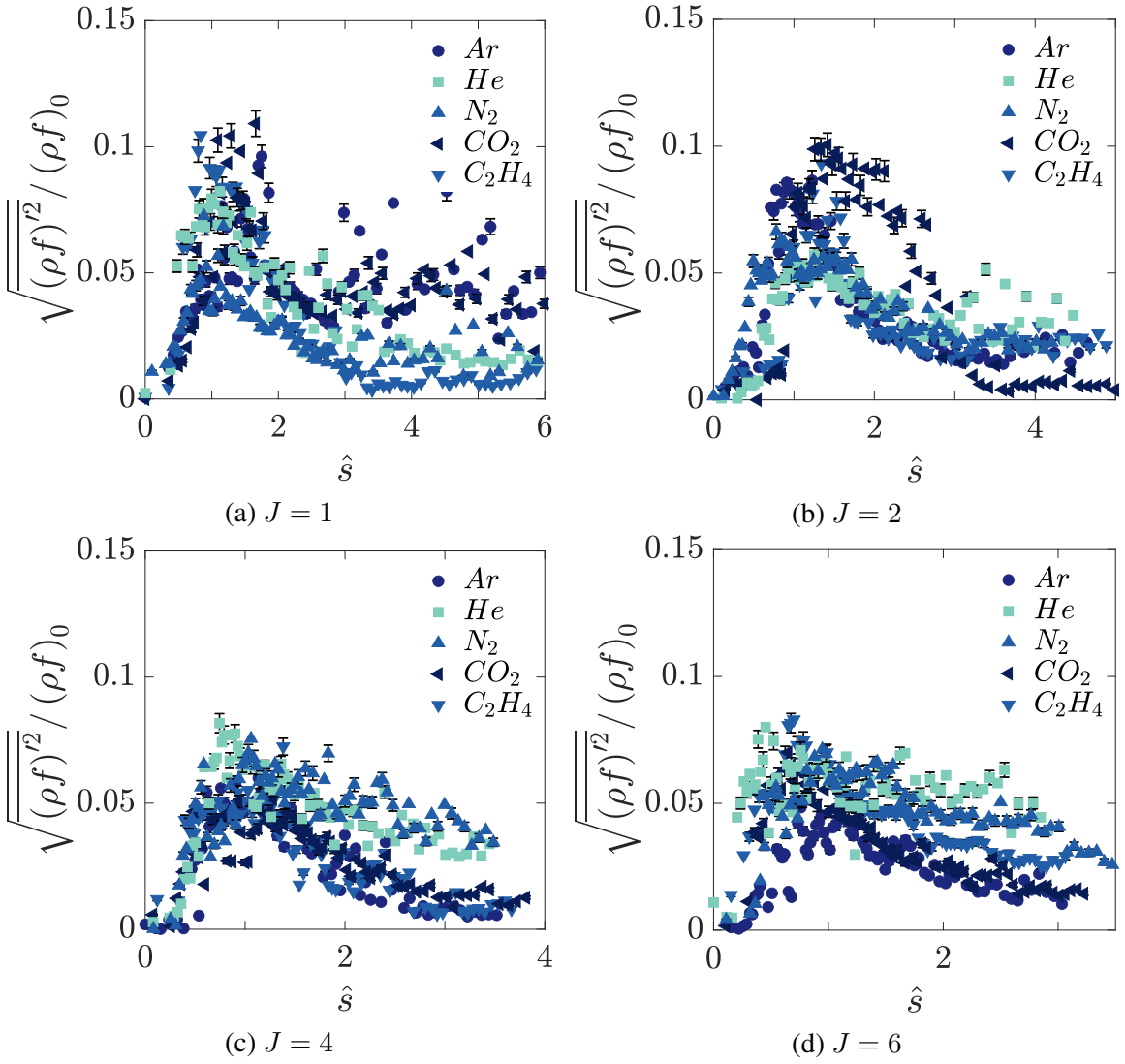

(a) $J = 1$

(b) $J = 2$

(c) $J = 4$

(d) $J = 6$

Figure 4.17: RMS jet fluid signal development along individual jet trajectories for different momentum flux ratios. Darker colors indicate higher MW while the names of the gases in the legend are ordered from highest γ to lowest: ● = 1.66, ■ = 1.66, ▲ = 1.4, ◀= 1.28, ▼ = 1.237. 95% confidence intervals for the statistical uncertainty are shown.

At $J = 1$ (Fig. 4.17a) and $J = 2$ (Fig. 4.17b) the higher MW gases (argon and carbon-dioxide) with higher specific heat ratios (helium and nitrogen) overall exhibit the higher

fluctuations. This trend changes for $J = 4$ (Fig. 4.17c) and $J = 6$ (Fig. 4.17d) where the highest fluctuations occur for the lower MW gases with higher specific heat ratios (helium and nitrogen), especially in the regions downstream of the peak.

Looking at where the trajectories themselves lie with respect to the RMS jet fluid signal fields in Fig. 4.15b and Appendix A gives a reason for these trends. At higher J and for the gases with lower MW, the peak fluctuations seem to move more towards the windward edge of the jet. For the higher MW injectants, the peak fluctuations remain more on the inside of the trajectory contours. The higher MW argon and carbon dioxide gases exhibit stronger and more distributed fluctuations in regions downstream of $\hat{s} = 1$ at lower J, while the lower MW gases have increasingly strong and distributed fluctuations at higher J.

Coming back to Fig. 4.17, one can see an interesting behavior for ethylene injection. Ethylene has an intermediate MW and a γ that is lower than that of nitrogen. In the peak region, the ethylene data remains close to the higher molecular weight injectants (argon and carbon dioxide) at all J. However, downstream of the peak an interesting shift occurs. At low J, the ethylene data clusters more towards the lower MW helium and nitrogen results. For higher J, it starts trending more towards the higher MW argon and carbon-dioxide data. Thus, the lower specific heat ratio of ethylene might allow it to entrain and mix more efficiently at higher J than nitrogen.

At higher investigated values of J the behavior is consistent with the convective Mach number concept and the observations made by Gruber, Nejad, Chen, *et al.* (1997a) for helium and air jets and Ben-Yakar *et al.* (2006) for hydrogen and ethylene jets. The lower MW gases exhibit stronger remaining jet fluid signal fluctuations at $\hat{s} > 1$, suggesting that entrainment and mixing are less effective than for the higher MW gases. However, especially at $J = 1$ this trend is not as clear and higher MW gases have stronger fluctuation peaks and stronger remaining fluctuations downstream of the peak.

Results for the RMS velocities along jet trajectories are shown in Fig. 4.18. It should be noted that the jet fluid signal and PIV measurements are not acquired simultaneously. Thus,

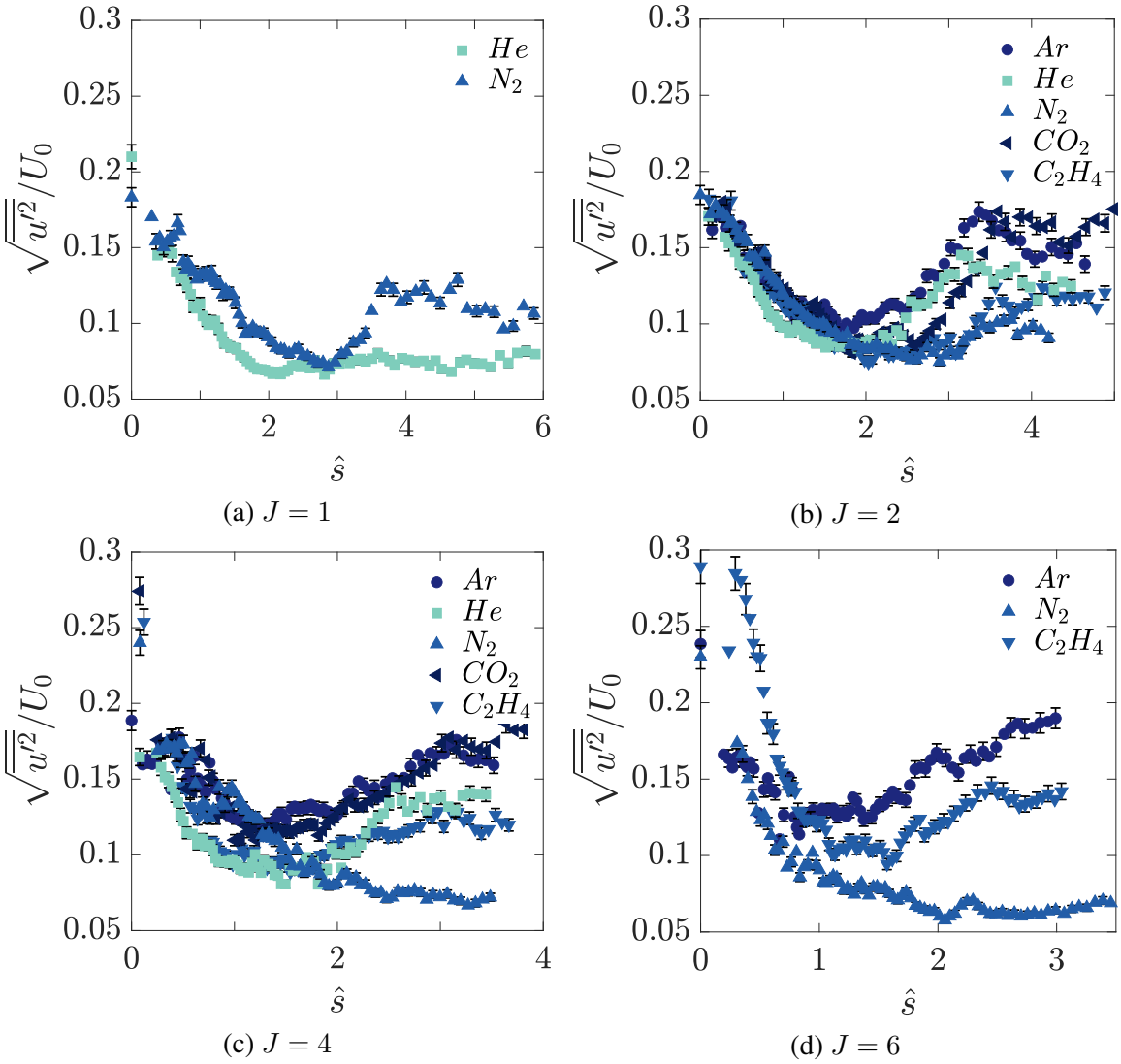

(a) $J = 1$ (b) $J = 2$

(c) $J = 4$ (d) $J = 6$

Figure 4.18: RMS velocity development along individual jet trajectories for different momentum flux ratios. Darker colors indicate higher MW while the names of the gases in the legend are ordered from highest γ to lowest: $\bullet = 1.66$, $\blacksquare = 1.66$, $\blacktriangle = 1.4$, $\blacktriangleleft = 1.28$, $\blacktriangledown = 1.237$. 95% confidence intervals are shown.

part of the differences between the results could stem from small deviations in the targeted momentum flux ratio. Alignment is not an issue because the data is recorded with the same setup without moving the camera. Confidence intervals are computed in accordance with Appendix C.

The developed scaling collapses the peaks close to $\hat{s} = 0$ and a lower plateau in the profiles close to $\hat{s} = 2$, for $J = 1$, and moving further upstream closer to $\hat{s} = 1$ for $J = 2$,

4 and 6. The highest MW gases (argon and carbon dioxide) exhibit the highest RMS velocity fluctuations at all J.

The nitrogen jet at $J = 1$ has a secondary peak around $\hat{s} = 4$ that is mirrored to a smaller extent in the jet fluid signal results, see Fig. 4.17a. At all other momentum flux ratios, nitrogen has some of the lowest velocity RMS values out of all injectants, in contrast to its jet fluid signal properties. This might be due to the consistently lower momentum flux ratios at which PIV data was acquired for the nitrogen jet, especially at nominal $J = 2$ and 4 (Tab. 4.1). Helium has a secondary peak at $J = 2$ and $J = 4$ that is only distinguishable at $J = 2$ in the jet fluid signal results, see Fig. 4.17b.

At $J > 1$, the higher MW gases (argon and carbon dioxide) show the strongest velocity fluctuations in Fig. 4.18. The effect of γ seems to be weak: at $J = 2$ the second peak of carbon dioxide lags behind that of argon but peak magnitudes appear to be similar and at $J = 4$ the two injectants show almost identical behavior overall. Ethylene, with the same MW as nitrogen but a lower γ, displays RMS magnitudes comparable to those of nitrogen at $J = 2$.

Similar to the jet fluid signal results in Fig. 4.17, the velocity fluctuations of the lowest MW gas (helium) increase with J, e.g. see the helium cases in Fig. 4.21a and Fig. 4.21b. However, while helium appears to exhibit higher RMS velocity magnitudes than nitrogen and ethylene at $J = 2$, no complete switch with the highest MW gases (argon and carbon dioxide) occurs. The changes in fluctuation magnitude for helium seem to occur mostly in the region downstream of the first peak in both jet fluid signal and velocity results.

4.3.2 Jet Fluid Signal and Velocity Statistics along Vertical Profiles

Further insight into the controlling processes of the jet fluid signal and velocity fields is provided by taking vertical profiles along constant $x/d_j = 0$, 1.5, 3, and 4.5. These profiles are extracted from the field data and compared for a given J. The normalized coordinate x/d_j is used in this case instead of $\hat{x}$ to compare physically similar locations in the JISCF

flow field.

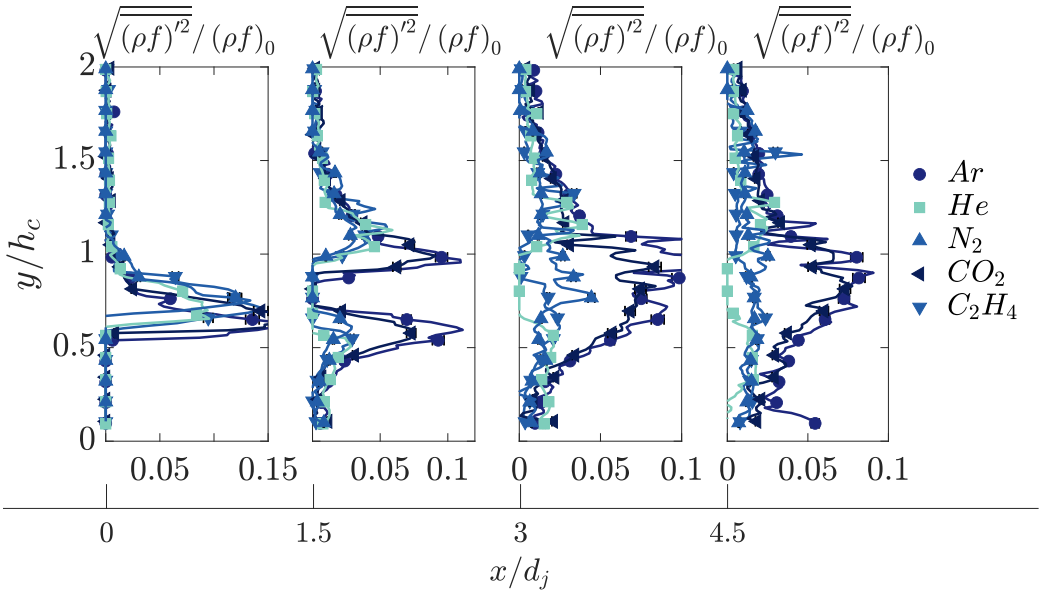

(a) $J = 1$

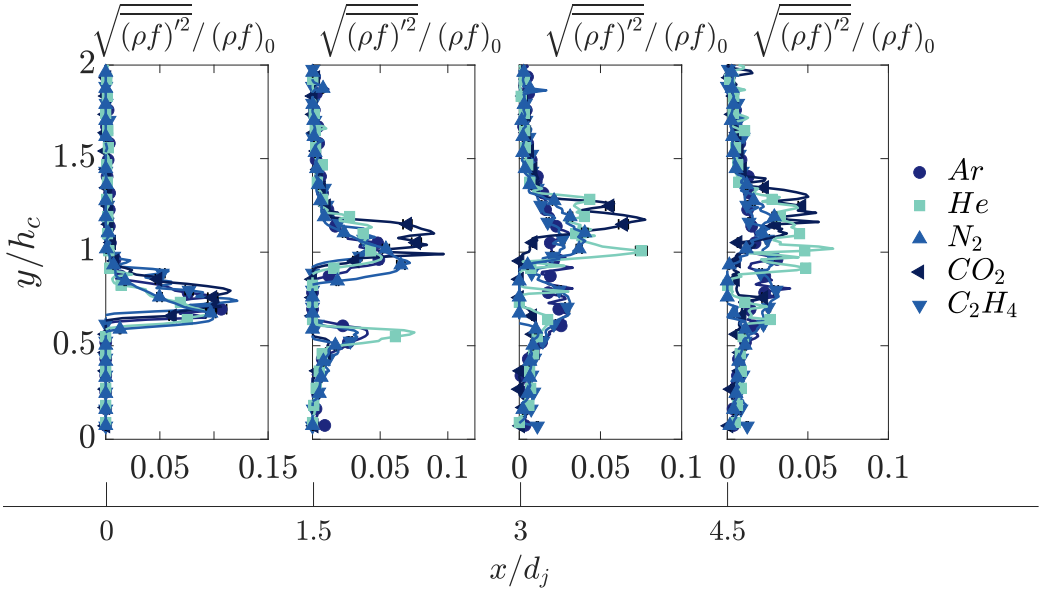

(b) $J = 2$

Figure 4.19: RMS jet fluid signal values along vertical profiles for different momentum flux ratios. Darker colors indicate higher MW while the names of the gases in the legend are ordered from highest to lowest γ : $\bullet = 1.66$, $\blacksquare = 1.66$, $\blacktriangle = 1.4$, $\blacktriangleleft = 1.28$, $\blacktriangledown = 1.237$. 95% confidence intervals for the statistical uncertainty are shown.

Looking at Fig. 4.19 and Fig. 4.20, the normalized $\hat{y} = y/h_c$ coordinate decently collapses major features of the different jet fluid signal profiles between $0.5 < \hat{y} < 1.5$,

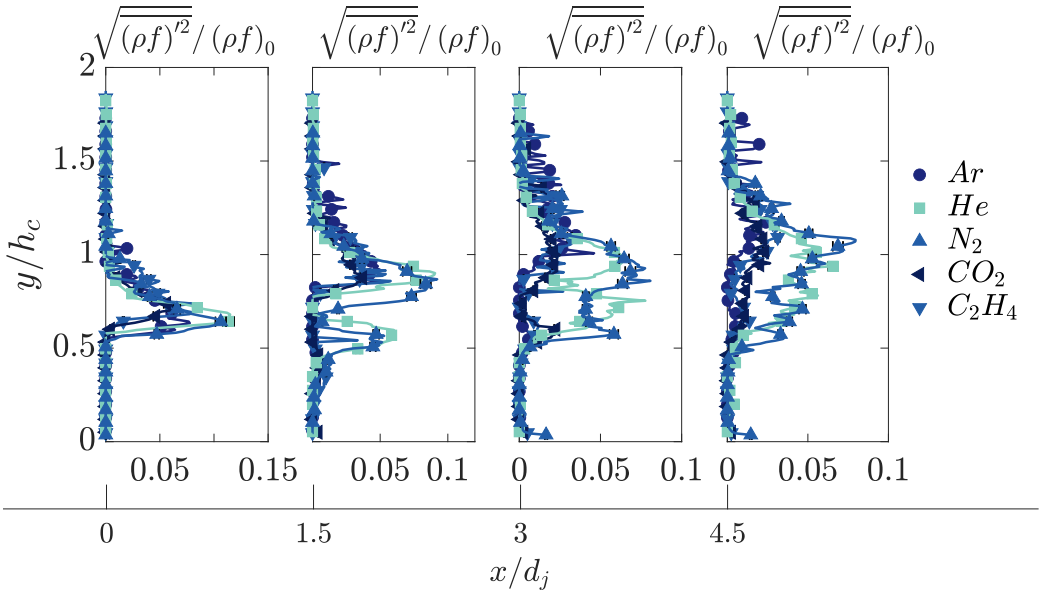

(a) $J = 4$

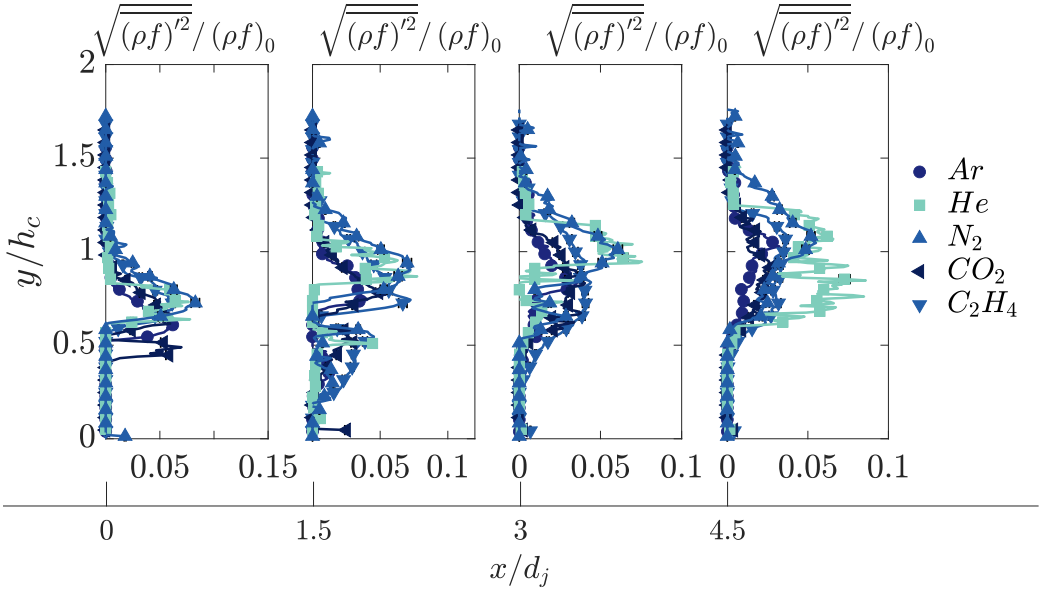

(b) $J = 6$

Figure 4.20: Continuation of Fig. 4.19.

although a stronger influence of injectant properties is now discernible than for the fluctuation profiles along jet trajectories. It is also clearer from the profiles in Fig. 4.19 and Fig. 4.20 that the peak fluctuation magnitude could indeed be reduced as J increases.

The jet fluid signal results largely agree with the trends observed along individual jet trajectories. At the lowest momentum flux ratio, $J = 1$, in Fig. 4.19a the higher molec-

ular weight injectants show the strongest fluctuations at all x/d_j positions. At $J = 2$, in Fig. 4.19b, the magnitude between different gases is fairly equal. At higher momentum flux ratios in Fig. 4.20, $J = 4$ and 6, the lower MW gases display the strongest fluctuations initially and further downstream.

At $J = 1$ in Fig. 4.19 the lower MW gases' (helium, nitrogen, and ethylene) RMS values shrink faster than the ones for the higher MW gases (argon and carbon dioxide), and vice-versa at $J = 4$ and 6 in Fig. 4.20. All cases exhibit the formation of a jet core and subsequent merging of the fluctuation peaks moving downstream.

The trajectory analysis shows that higher MW gases generally entrain and mix with crossflow fluid faster. It also shows that there could be a change in turbulent mixing processes going from $J = 1$ to $J = 2$. The results in Fig. 4.19 and Fig. 4.20 seem to support this as the highest jet fluid signal fluctuations move from the higher MW to the lower MW injectants with increasing momentum flux ratio. However, since the trajectory data suggest that the turbulent mixing rate is higher for the higher MW injectants in all cases the following explanation is proposed based on the convective Mach number model (Papamoschou and Roshko, 1988).

At $J = 1$ (Fig. 4.19a) the jets interact more with the boundary layer region, see Appendix A. Due to the smaller velocity difference between higher MW gas jets (argon and carbon dioxide) and the low speed boundary layer region, instabilities can form and effectively entrain crossflow fluids. In the case of the lower MW gas jets (helium), the velocity difference to the boundary layer region is much larger and the formation of instabilities and turbulent mixing structures is suppressed to some degree. Thus, the higher MW gases would initially experience stronger fluctuations that persist and grow for incomplete turbulent mixing. At the same time, the lower MW gas jets would experience weaker fluctuations with suppressed growth but potentially longer persistence. Since the velocity difference between jet and crossflow only decreases with downstream distance this initiation mechanisms also becomes weaker. Moreover, the lower MW gases could profit from

diffusive processes in the low speed boundary layer zone or stronger coupling to boundary layer vortical structures. The latter two points are purely speculative, though. Nitrogen and ethylene seem to behave more like helium than the two other higher MW gases at these conditions.

At $J = 2$ in Fig. 4.19b an intermediate regime for the specific experimental setup in this study is achieved. Interacting more with the higher flow speeds outside the boundary layer, the higher MW injectants are subjected to some instability suppressing effects but also increasing turbulent mixing rates due to increasing J (Hasselbrink and Mungal, 2001a). At the same time the lower MW gases do not experience too much change which creates the impression that the fluctuations between the different injectants are approximately equal.

In Fig. 4.20a at $J = 4$, one has to assume that while mixing rates are increasing for all gases, the suppression of instabilities on the jet interface grows faster with J for the lower MW gases than the higher MW gases. This assumption is analyzed further in the discussion of the jet shear layer compressibility and calculated convective Mach numbers in Sec. 4.4. If the assumption holds true, then the turbulent mixing of the higher MW gases progresses faster, causing peak fluctuating values to drop off earlier. The lower MW gases continue to exhibit elevated fluctuations further downstream as the turbulent mixing process is still ongoing. For this particular condition, nitrogen behaves very similar to helium which is probably due to its MW being lower than that of argon and carbon dioxide, and its γ being higher than that of ethylene. The latter clustering more towards the higher MW gases argon an carbon dioxide.

Finally, $J = 6$ in Fig. 4.20b is a continuation of the trends at $J = 4$. The higher MW gases are now also subject to stronger instability suppressing effects or the increased amount of jet fluid is starting to take longer to mix completely. Hence the increased fluctuations at $x/d_j = 4.5$ compared to the $J = 4$ cases. At $x/d_j = 4.5$, nitrogen is trending more towards the higher MW gases at these conditions than at $J = 4$. Furthermore, at all downstream locations presented, ethylene clusters more towards the higher MW gases,

argon and carbon-dioxide. Thus, with ethylene's MW similar to that of nitrogen but a $\sim 12\%$ lower specific heat ratio, it could have properties that give it a mixing advantage at all momentum flux ratios investigated in this study.

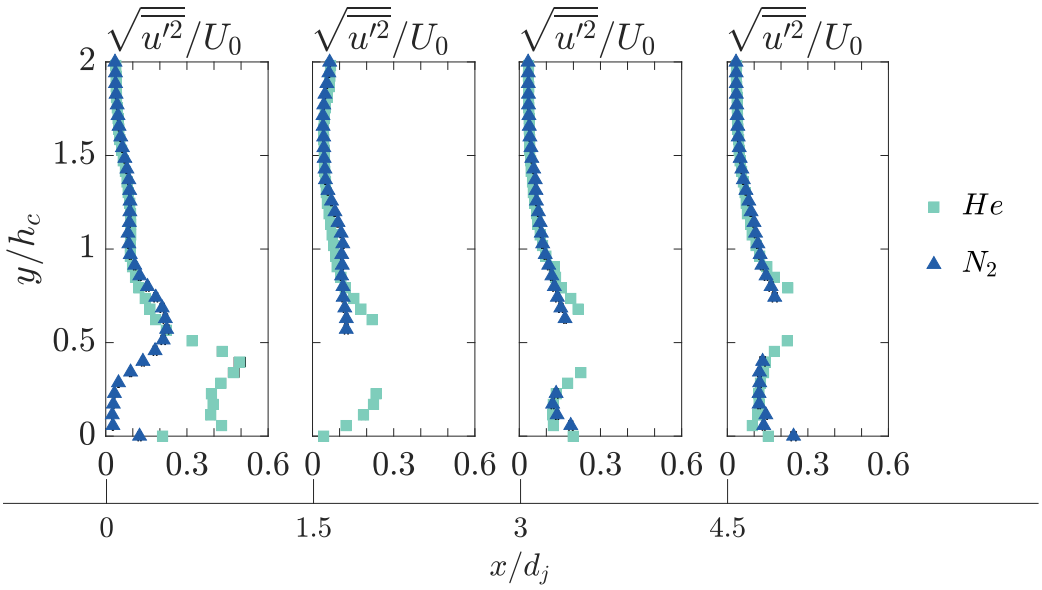

(a) $J = 1$

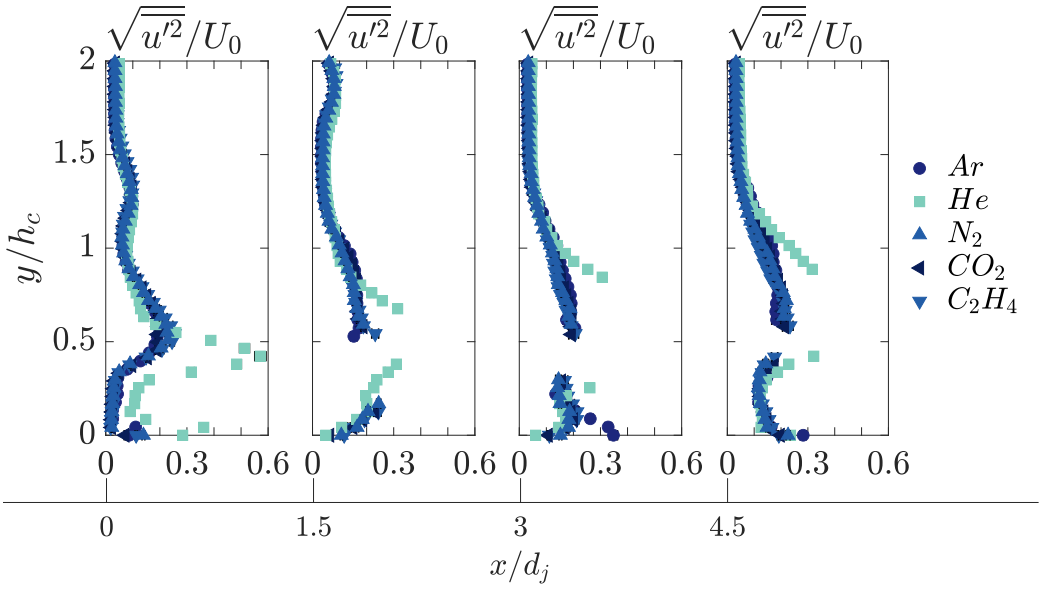

(b) $J = 2$

Figure 4.21: PIV RMS velocity along vertical profiles for different momentum flux ratios. Darker colors indicate higher MW while the names of the gases in the legend are ordered from highest to lowest γ: ● = 1.66, ■ = 1.66, ▲ = 1.4, ◀= 1.28, ▼ = 1.237. 95% confidence intervals are shown.

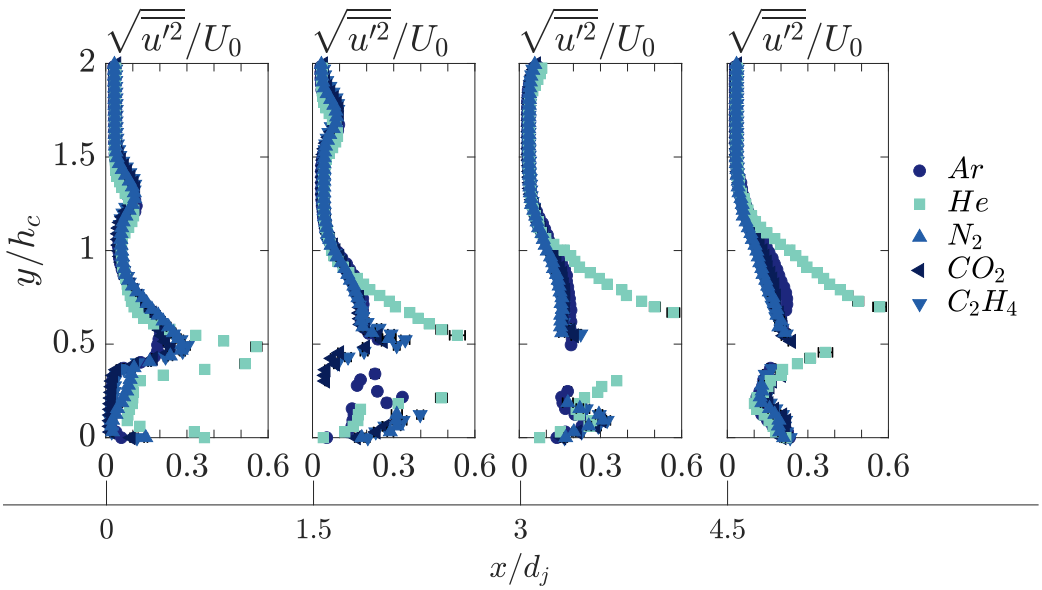

(a) $J = 4$

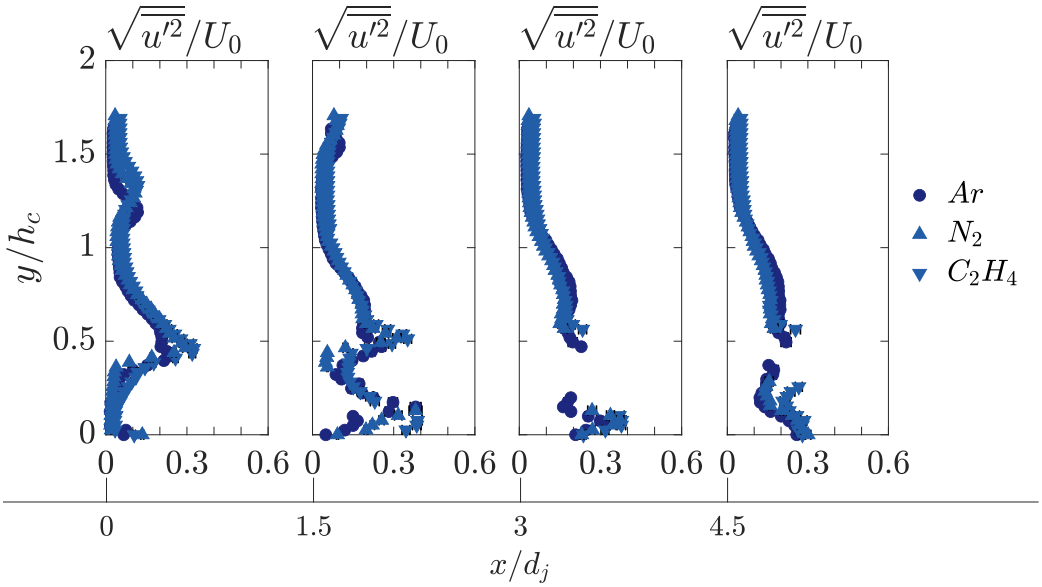

(b) $J = 6$

Figure 4.22: Continuation of Fig. 4.21.

RMS velocity profiles in the y-direction are shown in Fig. 4.21 and Fig. 4.22. In comparison to the data discussed so far, the most striking observation here is that, except for helium, all RMS velocity profiles nearly collapse on top of each other. Because of the missing data in the wake of the jet, no final conclusion can be made regarding this observation but the available trends do not show major deviations between any of the gases at a

fixed J. This also means that some of the differences observed in Fig. 4.18 between gases could be due to deviations in the actual momentum flux ratio during jet fluid signal and PIV measurements for a given nominal J.

The peak fluctuations seem to occur around $y/h_c \approx 0.5$ with a weak upwards trend as x/d_j increases. In the jet fluid signal measurements in Fig. 4.19 and Fig. 4.20 the jet core is discernible between $y/h_c = 0.5 - 1$ for $x/d_j \geq 1.5$, also with a weak upwards trend. Thus, the peak velocity fluctuations appear to be positioned closer to the wall relative to the jet core. For $J \geq 2$ at $x/d_j = 0$ and 1.5 most velocity profiles show a secondary peak starting between $y/h_c = 1 - 1.5$ moving up to $y/h_c = 2$ and beyond. This smaller, secondary peak could be indicative of the windward outer edge of the jet shear layer. In general, the velocity fluctuation peaks are positioned both closer to the wall and further in crossflow than the jet fluid signal fluctuation peaks. Further downstream this difference could be decreasing but the missing vectors in the jet wake make it hard to draw any conclusions on that end.

The sensitivity of fluctuating velocity measurements to injectant properties appears significantly lower than in the fluctuating jet fluid signal measurements. The major controlling factor in Fig. 4.21 and Fig. 4.22 presumably is the jet velocity at the point of injection, see the sonic velocities of the different injected gases in Tab. 4.1. Except for helium they are all within $\sim 22\%$ of each other. The sonic velocity of helium is more than 2.5 times higher than the next highest case due its comparatively low molecular weight.

Moreover, the gas velocity during jet expansion is relatively high for the case of helium injection. Assuming isentropic expansion of the jet up to the barrel shock or Mach disk and combining it with normal shock relations one can estimate the Mach number of the jet before the shock structures from,

$$\frac{p_b}{p_{0,j}} = \left(\frac{2\gamma_j M_{MD}^2}{\gamma_j + 1} - \frac{\gamma_j - 1}{\gamma_j + 1} \right) \left(1 + \frac{\gamma_j - 1}{2} M_{MD}^2 \right)^{-\gamma_j/(\gamma_j - 1)}, \tag{4.13}$$

where p_b is the back pressure after the shock. The back pressure for this study's experimental setup was not measured but is assumed to be ~ 3 times the test section static pressure, $p_\infty \approx 75.8\ \mathrm{kPa}$. This value for p_b is within a reasonable range (Gruber, Nejad, Chen, *et al.*, 1997a) but otherwise arbitrary. Nonetheless, for an order-of-magnitude estimate it should be sufficient. Again invoking an isentropic relationship for temperature (Eq. (3.4)), the actual jet velocity can be calculated. For jet supply pressures corresponding to $J = 2$ all gases except helium have a velocity in the range of 510 - 690 $\mathrm{m/s}$, while helium would be at roughly 1600 $\mathrm{m/s}$. This large difference and the corresponding larger velocity difference to the crossflow is probably responsible for helium being the only case that does not entirely collapse on the rest of the RMS velocity profiles. It also explains the higher normalized RMS magnitude in all of the helium velocity data sets, see Fig. 4.21a, Fig. 4.21b, Fig. 4.22a, and Fig. 4.22b. That is, the lowest MW gas with the highest specific heat ratio will yield the strongest velocity fluctuations, which is in agreement with the simulation results by Watanabe *et al.* (2012).

Besides the influence of the jet exit velocity, a reason for the reduced sensitivity to injectant properties in the velocity measurements, compared to the jet fluid signal results, could be the difference in resolution. Limited spatial resolution acts as a low-pass filter with a cut-off wavenumber on the order of the measurement spacing. Comparing the resolutions for the two measurements (see Ch. 3) yields a ratio of 0.69, i.e. a $\sim 30\%$ lower spatial resolution for the PIV measurements. Thus, the jet fluid signal measurements will definitely resolve more spectral content than the PIV measurements.

It is also possible that the velocity and the scalar jet fluid signal field are fundamentally different. However, in this study, both fields are measured indirectly by techniques employing solid particles with similar properties. Thus, it is unlikely that such differences would show up in the results.

4.4 Compressibility in the Jet Shear Layer

It is desirable to analyze the underlying reasons for the varying mixing behavior of gases with different molecular weight and specific heat ratio further. To this end, the convective Mach number is estimated, M_c, directly from experimental data for cases in which PIV velocity fields are available. The analysis follows a similar logic as the estimate made by Gruber, Nejad, Chen, *et al.* (1997a), however, in this study an additional piece of information is available: the symmetry plane 2-D mean velocity field.

The approach presented here considers the flow setup shown in Fig. 4.23. The goal is to compute the convective Mach number in the shear layer along a line through point **A**. The shear layer is formed between the jet and the incoming crossflow. The variables required to perform the computation are indicated in this sketch and their determination is explained in the following.

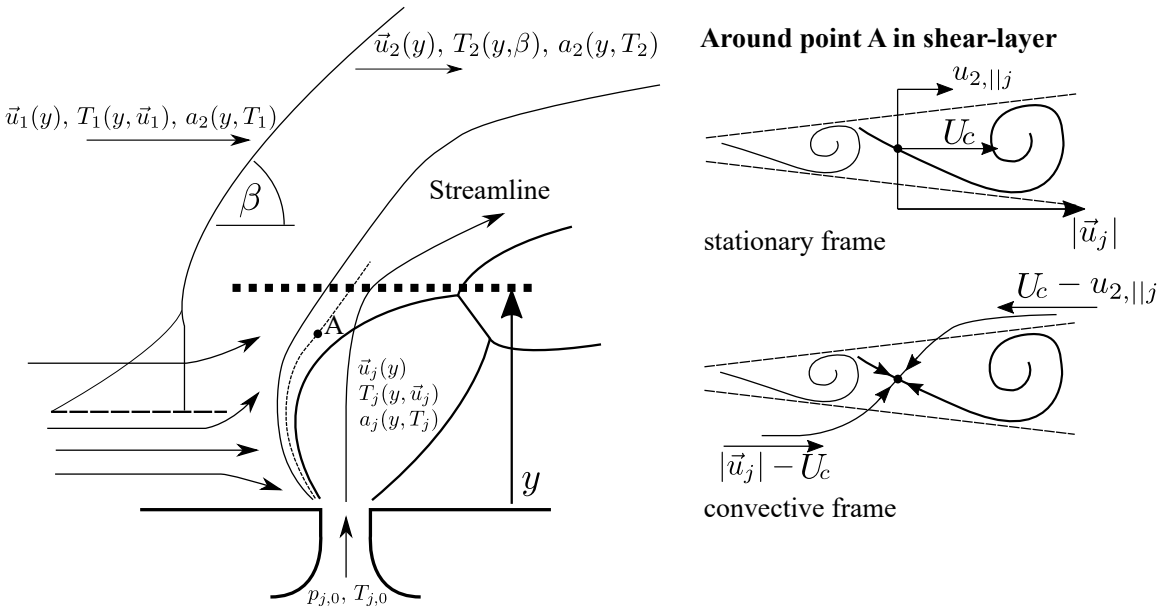

Figure 4.23: Schematic of the flow setup considered for the estimation of the convective Mach number in the jet shear layer.

The crossflow velocity vectors $\vec{u}_1$ (pre-shock) and $\vec{u}_2$ (post-shock) can be directly extracted from PIV results. The profiles along which this is done are indicated by black dotted lines in Fig. 4.16a and Appendix B. The position of these profiles is set with the

measured particle relaxation time, τ_p. The pre-shock profile is set $\Delta x = \tau_p U_\infty$ upstream of the detected shock-edge, where U_∞ is the crossflow velocity magnitude outside of the boundary layer in the core of the flow. Post shock it is set $\Delta x = \tau_p |\vec{u}_1|$ downstream of the shock-edge. This ensures that the extracted velocities are less affected by the "smearing" of the shock due to the finite response time of the PIV tracer particles.

To determine the temperature distribution ahead of the shock the Crocco-Busemann relationship is used (White and Corfield, 2006, chap. 7),

$$T_1(y) = T_w + \left(T_\infty + \frac{U_\infty^2}{2c_p} - T_w \right) \frac{U_1(y)}{U_\infty} - \frac{U_1(y)^2}{2c_p}, \tag{4.14}$$

where T_w is the wall temperature, T_∞ is the crossflow temperature in the core of the flow, and c_p is the specific heat capacity at constant pressure of the crossflow (here air). Strictly speaking, this relationship only holds for zero pressure gradient flows, which is not the case just ahead and behind a shock wave. Thus, the $T_1(y)$ estimate is an approximation of the real values in the flow at best.

The wall can be considered as cold with an approximate temperature of $T_w \approx 430$ K (measured with a thermocouple on the outside of the test section) which yields a reference temperature of $T_{ref} \approx 444$ K (Eckert, 1955). With this reference temperature, the specific heat capacity of the crossflow air evaluates to $c_p \approx 1019.7$ J/kg K. With that, the Mach number distribution in front of the shock can be computed,

$$M_1(y) = \frac{U_1(y)}{\sqrt{\gamma R T_1(y)}}. \tag{4.15}$$

For further computations, it is assumed that over the range of temperatures considered in this analysis ($\sim 300 - 600$ K) the specific heat ratio stays approximately constant. Moreover, planar oblique shock relations are used, instead of the more complicated, three-dimensional conical shock relationship. On the symmetry plane of the flow field, to which the current study is limited, this should yield reasonable results.

With these assumptions, the temperature behind the bow shock can be determined by finding the sonic line and assuming that below it no temperature jump occurs and that above it the measured shock angles (see the black dashed lines in Fig. 4.16a and Appendix B) can be used in the oblique shock relationship,

$$\frac{T_2}{T_1} = \left[1 + \frac{2\gamma}{\gamma+1}\left(M_1^2 \sin^2(\beta)\right)\right] \frac{(\gamma-1)M_1^2 \sin^2(\beta) + 2}{(\gamma+1)M_1^2 \sin^2(\beta)}. \tag{4.16}$$

With this information, the speed of sound behind the bow shock can be computed, too.

The flow properties of the jet are estimated along the jet center-streamline shown as magenta solid lines in Fig. 4.16a and Appendix B. The calculation is only performed up to a point shortly after the barrel shock, see the thick dashed line in Fig. 4.23. Up to this point, an equation that combines the definition of the Mach number with isentropic relationships is used to compute the jet Mach number. Across the shock this would normally not be permissible, but since the total temperature does not change and the PIV measurements smear the shock out, this equation is used as an approximation to solve for $M_j(y)$,

$$U_j(y) = M_j(y)\left[\gamma_j R_j T_{0,j}\left(1 + \frac{\gamma_j - 1}{2} M_j(y)^2\right)^{-1}\right]^{1/2}, \tag{4.17}$$

where $T_{0,j} = 305$ K (see Sec. 3.1.4). Constant γ relationships are used as the drop in temperature during jet expansion will yield a chemically frozen flow and changes in γ due to temperature should be small. Shortly after the jet shock system, a direct measurement of temperature, pressure or Mach number would be required for more accurate results anyway, because the mixing between jet and crossflow affects local thermodynamic conditions. With $M_j(y)$, the jet temperature and speed of sound along the streamline can be computed.

As suggested by Papamoschou and Roshko (1988), in a convective frame of reference there exists a saddle point between large-scale structures in the shear layer that acts as a stagnation point, i.e. where $p_{0,j} = p_{0,2}$, see the schematic in Fig. 4.23 for a visual representation. Assuming, in addition, equal static pressures and steady flow one can solve

the following relationship for the convective velocity and Mach number,

$$\left[1+\frac{\gamma_j-1}{2}\left(\frac{U_j-U_c}{a_j}\right)^2\right]^{\frac{\gamma_j}{\gamma_j-1}}=\left[1+\frac{\gamma_j-1}{2}\left(\frac{U_c-u_{2,||j}}{a_{\infty,2}}\right)^2\right]^{\frac{\gamma_\infty}{\gamma_\infty-1}}. \tag{4.18}$$

For the computation, only the crossflow velocity component parallel to the jet velocity vector, $u_{2,||j}$, is used because perpendicular components do not contribute to the formation of the shear layer. This analysis neglects potential formation and growth of instabilities due to density and pressure differences, such as Rayleigh-Taylor instabilities.

4.4.1 Convective Velocities

The convective Mach numbers computed with the aforementioned methodology are shown in Fig. 4.24. Keeping in mind the assumptions made and accompanying limitations, this estimate is a rough approximation to reality at best. Nonetheless, the trends hopefully shed some light on the observations made in Sec. 4.3.

In Fig. 4.24, the convective Mach number clearly is highest for the lowest molecular weight gas, helium. M_c increases after the injection point while the jet is expanding and drops as the jet fluid crosses the barrel shock. After the jet shock structures, the convective Mach number stays between 0 and 0.2. Helium's convective Mach number is the highest out of all considered injectants. Relative differences in MW of about 30% (argon and carbon dioxide to nitrogen and ethylene) yield only small changes in peak M_c. A relative decrease of 85-90% in molecular weight is required to result in the significant difference between helium and the other injectants.

The influence of γ is weak but between CO_2 and Ar at $J = 4$, CO_2 has a slightly higher convective Mach number, i.e. lower γ yields higher M_c, as expected. This effect is even weaker at $J = 2$, suggesting that it becomes more important at higher momentum flux ratios. The difference between the convective Mach number relative to the high-speed jet side, $M_{c,j}$, and the one relative to the low-speed crossflow side, $M_{c,cf}$, is small and

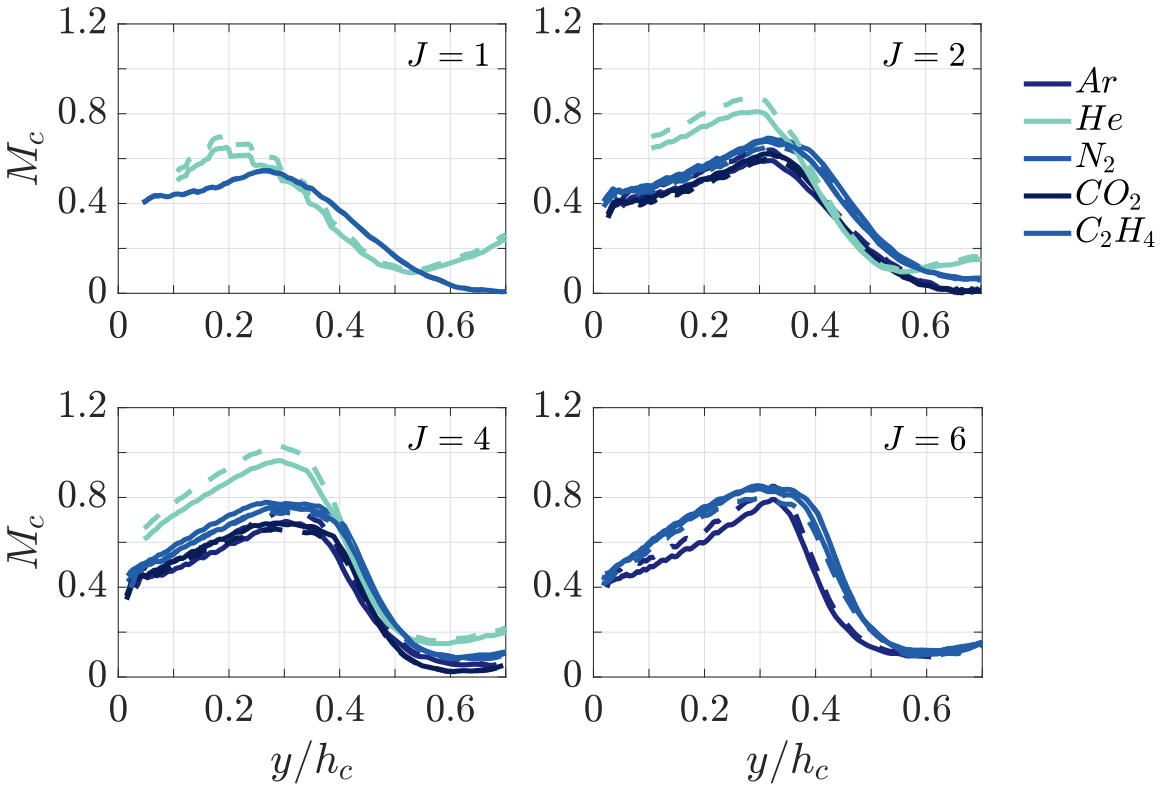

Figure 4.24: Convective Mach numbers in the jet shear layer derived from PIV data. The dip in Mach number arround $y/h_c \approx 0.45$ corresponds to the location of the jet shock system (barrel shock). Solid lines are $M_{c,j}$ (relative to high-speed jet side), dashed lines $M_{c,cf}$ (relative to low-speed crossflow side). Darker colors correspond to higher molecular weight.

corresponds to the relation $M_{c,cf} \approx (\gamma_j/\gamma_\infty)^{1/2} M_{c,j}$ (Papamoschou and Roshko, 1988).

The compressibility of the jet shear layer in terms of M_c generally increases with increasing J but is diminished significantly across the jet shock structure. Convective Mach number peaks collapse around $y/h_c = 0.3$ with helium peaking slightly earlier than the other cases, especially at $J = 1$. Regarding the observations made in Fig. 4.19 and Fig. 4.20, Fig. 4.24 does show that the convective Mach number increases more strongly for the lower MW gases than the higher MW gases. Specifically for helium the peak values increase by $\sim 57\%$ between $J = 1$ and 4, while for nitrogen they increased by $\sim 42\%$, and for argon by $\sim 34\%$ between $J = 2$ and 6. Thus, lending some credibility to the assumption that the suppression of hydrodynamic instability grows stronger with J for the lower MW gases.

The computed peak convective Mach number for helium at $J = 4$ is about 50% smaller than the analytical point estimate made by Gruber, Nejad, Chen, *et al.* (1997a) and Gruber, Nejad, Chen, *et al.* (1997b). $M_c \approx 1$ vs. $M_c = 1.92$ in the current study and the published literature, respectively. On the other hand, the higher MW gases have peak values of M_c at $J = 4$ closer to estimates made for nitrogen as an injectant. $M_c \approx 0.7 - 0.8$ vs. $M_c = 0.66$ in the current study and the same published literature, respectively. In any case, the lower MW injectant's turbulent mixing and entrainment processes are significantly more affected by compressibility in the near-field of the jet.

The M_c trends agree with the general observations made in Sec. 4.2. For the current experimental setup, higher molecular weight of the injectant leads to lower M_c and more effective entrainment and turbulent mixing. Specifically, the convective Mach number results suggest that a major reason for this is the injectant dependent stability of the jet shear layer. As mentioned before, similar trends have been observed in the published literature (Gruber, Nejad, Chen, *et al.*, 1997a; Ben-Yakar *et al.*, 2006; Watanabe *et al.*, 2012).

Conversely, the presented convective Mach number computations do not shed further light on the observation in Fig. 4.10 and Fig. 4.11 that lower specific heat ratio accelerates entrainment and mixing. The computed higher M_c values for gases with lower γ would suggest otherwise. What might come into play here is that $M_{c,cf} > M_{c,j}$ if $\gamma_j > \gamma\infty$ and $M_{c,cf} < M_{c,j}$ if $\gamma_j < \gamma_\infty$. That is, the effective convective Mach number might be lower if γ_j is lower. However, this is a very small effect as can be seen in Fig. 4.24.

The individual velocity components used to compute the convective Mach numbers are shown in Fig. 4.25. That the convective velocities (solid lines) initially are lower than the jet exit velocity agrees with the trends presented in the computational study by Watanabe *et al.* (2012) and the experimental results by Gruber, Nejad, Chen, *et al.* (1997b) and Ben-Yakar *et al.* (2006). As expected, the convective velocity increases as the jet expands and accelerates until the jet barrel shock is reached, the jet velocity is reduced, and a larger component of the jet velocity becomes aligned with the crossflow direction. The convective

velocity magnitude trends towards the freestream velocity at the end of the plots. Further downstream it should approach the actual reference freestream velocity magnitude U_0.

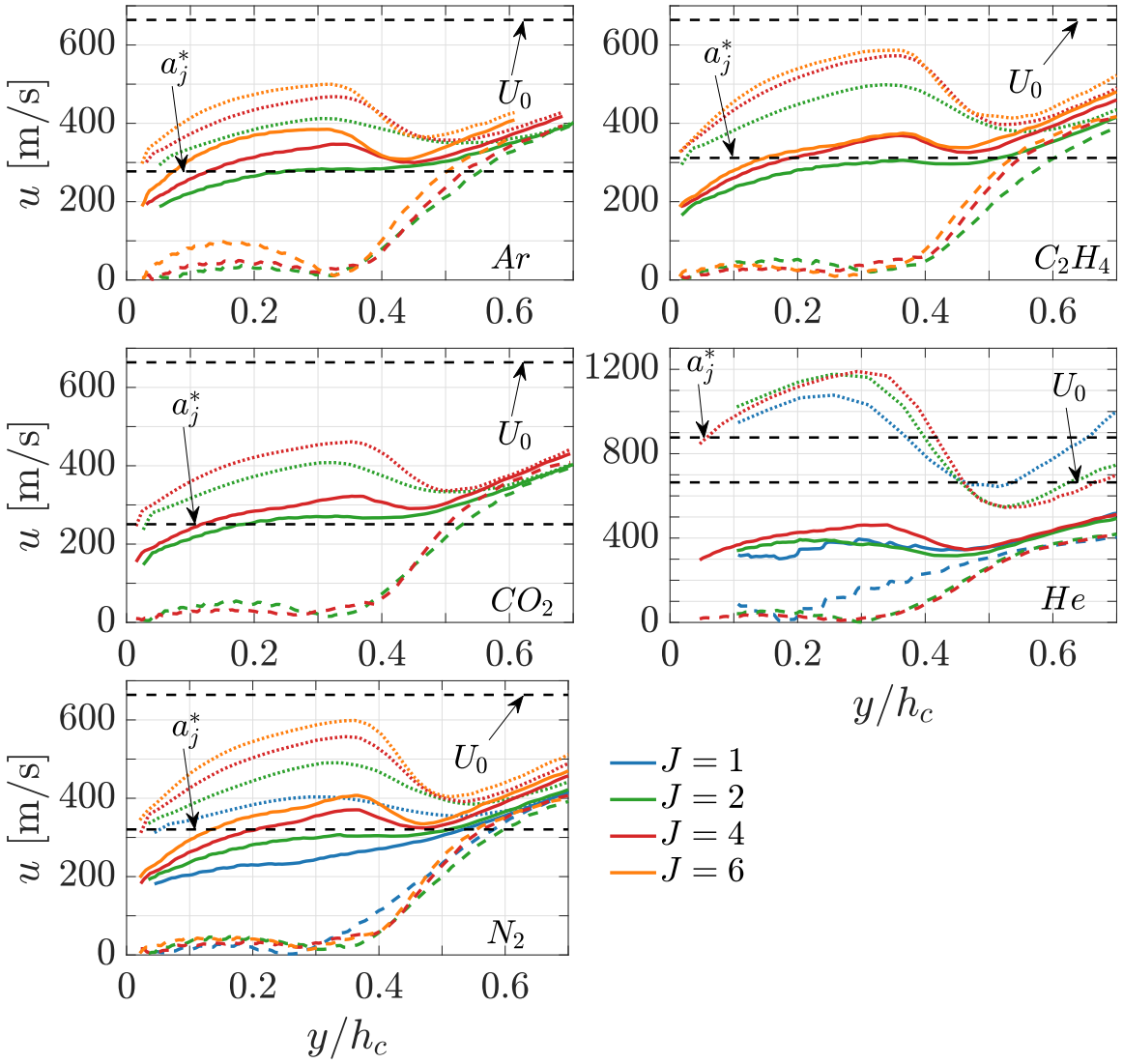

Figure 4.25: Flow speeds used in the determination of convective Mach numbers. Solid lines: convective velocity magnitude, U_c. Dashed lines: freestream velocity component parallel to jet streamline, $u_{2,||j}$. Dotted lines: jet velocity magnitude along centerstreamline, U_j.

Helium is the only gas for which the jet velocity upon injection is higher than the nominal freestream velocity. One of the factors leading to the high convective Mach number in its case. The plots in Fig. 4.25 show that for certain crossflow velocity-sonic injectant combinations, the lower MW injectant, e.g. helium, will probably result in the lower

convective velocities outside of the boundary layer. That is, helium would entrain and mix more efficiently than higher MW injectants in those cases. Thus, in terms of mixing, a scramjet at proper operating conditions with combustor inlet velocities on the order > 1000 $\mathrm{m/s}$ (Smart *et al.*, 2006) might profit from using lower MW gaseous fuels if the boundary layer is very thin.

4.5 Conclusive Remarks

The effect of turbulent entrainment and mixing on JISCF trajectories defined via jet fluid signal iso-contours has been discussed. Specifically, the implications for the interpreting of mixing rates based on trends in the iso-contour behavior were illustrated in detail. JISCF mixing results reported in different ways in the literature can be interpreted consistently using this framework.

A scaling for the mean jet trajectory of gaseous, underexpanded sonic jets in a supersonic crossflow has been presented. The scaling explicitly considers the momentum flux ratio, the influence of the boundary layer, and the bow shock from the jet-crossflow interaction. Especially at lower momentum flux ratios, the boundary layer and changing bow shock influence are important controlling factors for the mean evolution of the jet in the near-field. Two calibration constants and an expression for the Mach number dependent drag coefficient have been determined for the scaling. To validate the scaling, mean jet trajectory data for five different gases were collected in a supersonic windtunnel and data from four other studies was included for comparison. Thus, the validation includes variations in the momentum flux ratio, the molecular weight of the injectants, their specific heat ratio, the crossflow Mach number, the boundary layer thickness and the jet exit diameter. The scaling was also compared to several other existing correlations to assess its efficiency and possible shortcomings in the different approaches.

The newly developed scaling correlates all of the trajectories well and performs the best out of all approaches considered. Because it considers the controlling flow physics

explicitly, it is easier to test its assumptions and find potentially better fitting descriptors than with previous, purely empirical correlations. It is apparent, that at high momentum flux ratios the influence of the boundary layer and changing bow shock is secondary. Thus, a simplified version of the developed scaling, requiring only one calibration constant, is provided for engineering applications and cases with high J values. One major limitation is that the scaling does not work for momentum flux ratios below one, i.e. it only works for clearly choked injection conditions. A comparison of all trajectory scalings considered shows that $x/J^{1/2}d_j$ consistently correlates the data better than x/Jd_j as the x-coordinate normalization.

Building on the strength of considering certain flow physics explicitly, the bow shock parameter in the scaling was directly compared to experimental data. This shows that, while the physics considered in the scaling are relevant to the problem, the contributions of different factors are likely not weighted correctly yet.

Applying the developed scaling to jet fluid signal trajectories collected in this study shows that higher molecular weight and lower specific heat injectants appear to mix faster than lower MW gases with higher specific heat ratios. The effect of the molecular weight is expected and confirms previous studies. The effect of the specific heat ratio is weaker and can be inferred from the convective Mach number concept, but to the best knowledge of the author no other study has attempted to directly probe it.

The fluctuating jet fluid signal profiles show an interesting shift in peak fluctuations with increasing momentum flux ratio from higher MW to lower MW gases. The most likely explanation is a somewhat complex competition between increasing turbulent mixing rates and suppression of hydrodynamic instabilities. Suppression increases with higher momentum flux ratios due to a rising convective Mach numbers. The jet fluid signal field results support the conclusions made in the analysis of the jet trajectories.

RMS velocity values along jet trajectories show trends similar to the fluctuating jet fluid signal results. However, vertical velocity profiles do not exhibit the same sensitivities to

jet injectant properties as their jet fluid signal counterparts. Except for helium, which has a much higher jet exit velocity, the RMS profiles largely collapse on top of each other. Presumably this could be a spatial resolution effect, however, the missing velocity vectors in the jet wake preclude any final conclusions regarding this issue.

Convective Mach number and velocity profiles were computed directly from velocity data. The results yield trends that generally agree with observations in this study and the published literature. They show that compressibility effects likely grow faster for the lower MW gases than for the higher MW gases in this study. This confirms a corresponding assumption made in the interpretation of the fluctuating jet fluid signal results.

The convective Mach number trends also hint at a possible explanation for differences in turbulent mixing between injectants with similar MW but different γ. If the specific heat ratio of the injectant is different from the specific heat ratio of the crossflow, there is a difference between the convective Mach number relative to the low-speed side and relative to the high-speed side. This difference is such that an effective convective Mach number with $\gamma_j < \gamma_\infty$ could be smaller than the effective Mach number for $\gamma_j > \gamma_\infty$, given the same jet injectant molecular weight. However, this hypothesis cold not be further tested and the effect appears to be rather small.

CHAPTER 5

FORCED LASER IGNITION OF A SINGLE ETHYLENE JET

To extend the current work from non-reacting mixing studies to chemical reactions an initial characterization of laser induced ignition in a JISCF is conducted. The LIP setup used here is characterized in more detail in Sec. 3.2. The efforts in this chapter identify regions favorable for sustained chemical reactions in the complicated and often extreme JISCF flow field and to provide a preliminary analysis of the kind of burning that can be expected, if any. LIP ignition is a forced type of ignition and, thus, falls into a similar category as electric spark ignition. Implications of that are considered and described in the discussion of results to follow.

The injectant chosen for this part of the study is ethylene, a pure gas with a relatively high reactivity. As a hydrocarbon it is more interesting for current engineering efforts and, as seen in Ch. 4, might offer some interesting advantages with regard to mixing compared to even more reactive but much lighter fuels such as hydrogen. It is also a major component of cracked liquid kerosene-based fuel, such as JP-10 (Colket III and Spadaccini, 2001). The momentum flux ratio is set to $J = 4$ to achieve a flow regime that takes the jet out of the boundary layer and for which the characteristics of the current setup largely agree with previous studies, see Ch. 4.

To study the impact of flow field conditions on the ignition and combustion process a grid of ignition locations on the flow field centerline is probed. This grid is superimposed on the ethylene $J = 4$ PIV velocity field in Fig. 5.1. Positions in the grid are acquired by mounting the laser focusing lens and two of the preceding mirrors on manual micrometer stages with a measurement accuracy of 5 μm. The real positioning accuracy of the ignition kernel was measured to be ± 0.5 mm in both the x- and y-direction due to the micrometer stages not being connected to each other. Ignition energies are summarized in Sec. 3.2.

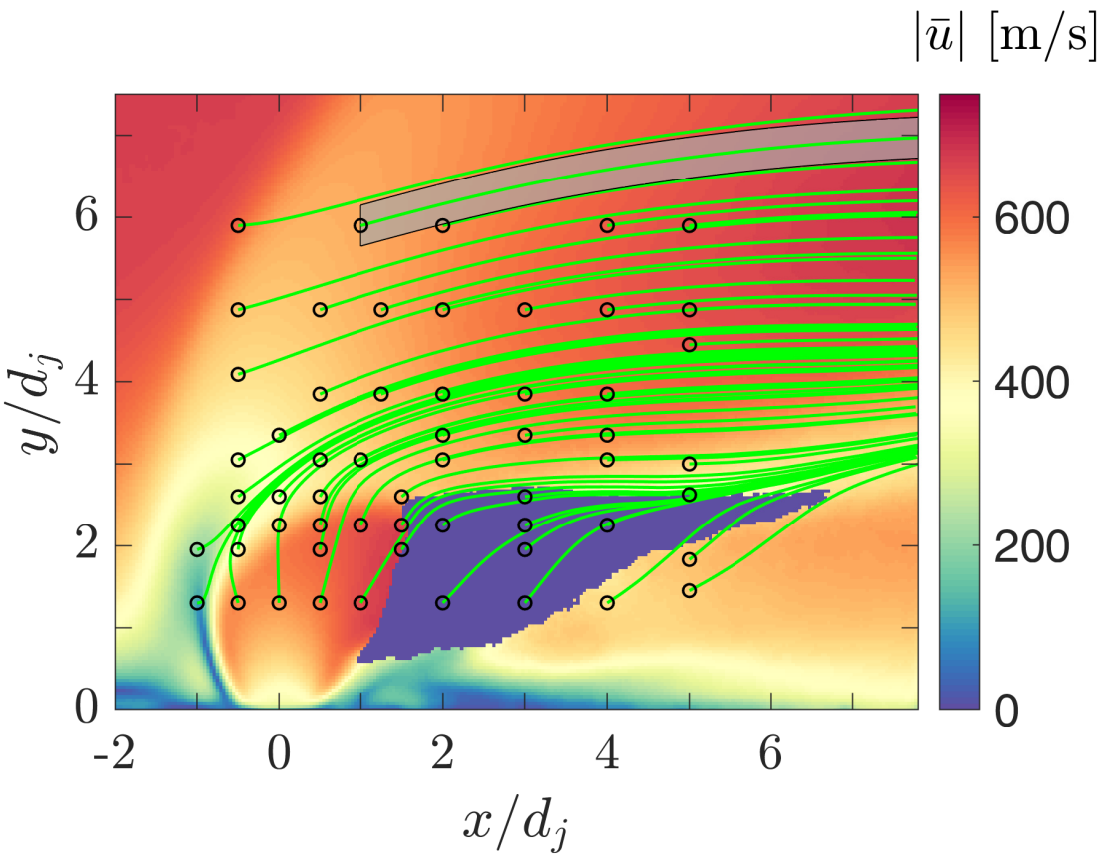

Figure 5.1: PIV mean velocity field for the ethylene jet at $J = 4$ with laser ignition locations superimposed as black empty circles. Green lines are streamlines starting at the ignition locations. The gray shaded area around the streamline starting at (1,5.9) is an example of the region used to extract flow field conditions that the ignition kernel encounters as it advects downstream.

The laser sparks advect with the flow field and are exposed to changing temperatures, pressures and gas compositions. The streamlines plotted in Fig. 5.1 show the average path the sparks/ignition kernels will take after energy deposition at a certain location. The streamlines are determined by integrating from the spark location forward in time using the mean velocity field data. The dt for the streamline integration is 400 ns, lower values did not yield any more changes in the streamline paths. To compute streamlines in the masked region where velocity vectors are missing, the Laplacian of the mean velocity vector field is taken and solved with a least-squares approach. This is done only to determine streamlines; no data interpolated in this way is used in the data analysis presented below.

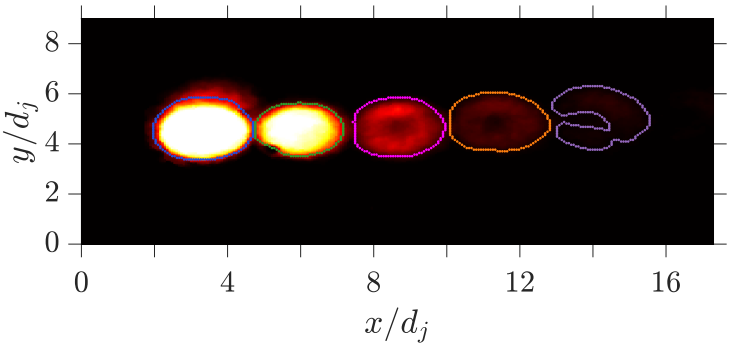

(a) CH*-chemiluminescence reference case without any fuel or jet. In this case, laser energy is deposited close to the center of the cross flow, away from boundary layer effects.

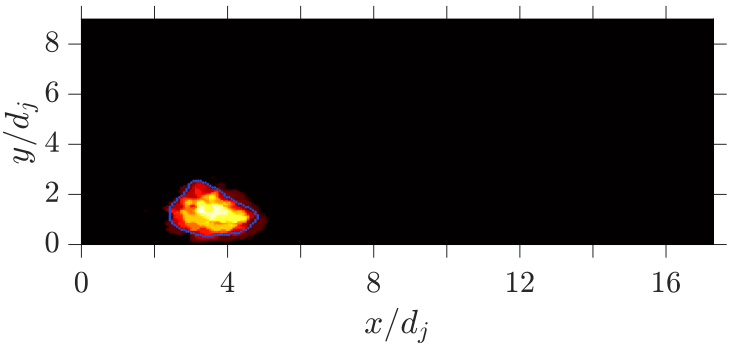

(b) CH*-chemiluminescence for ignition at (0, 2.25). The signal is weaker than for the reference case indicating that processes along the corresponding streamline facilitate the loss of thermal energy and quenching of the plasma.

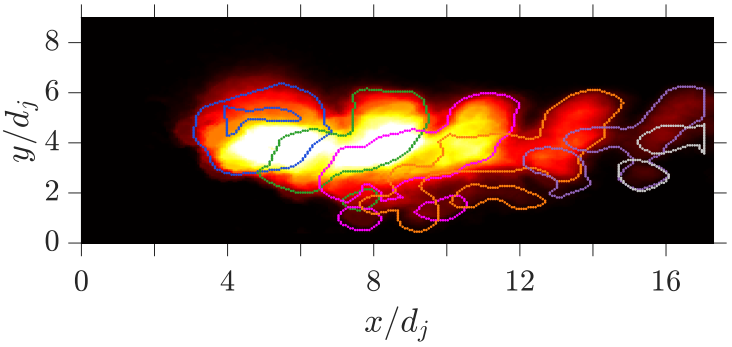

(c) CH*-chemiluminescence for ignition at (1.25, 4.88). The signal is stronger at later times and distributed over a larger spatial region than for the reference case. Along the corresponding streamline, the local conditions are more favorable to sustaining chemical reactions.

Figure 5.2: Time series of CH*-chemiluminescence starting at 10.33 µs with $\Delta t = 8.33$ µs between images. For all examples six subsequent images are shown, some of which do not contain a detectable signal anymore. The signal is normalized to the maximum pixel count of the 12 bit camera used. Darker and lighter colors represent lower and higher signals, respectively. Colored lines in the images represent the edges detected at different Δt for area calculations. $x/d_j = 0$ & $y/d_j = 0$ correspond to the jet location.

It is expected that sparks initiated in or propagating into regions with certain properties are more successful at developing into sustained ignition kernels than in other regions. Such properties include elevated temperatures, low scalar dissipation (i.e. well mixed regions), and low strain rates (Mastorakos, 2009). In the single JISCF flow field, elevated temperatures should occur close to the wall and after shocks. Well mixed air and jet fluid will likely also occur close to the wall, on the windward edge of the jet shear later and in the far field of the jet. Low strain rates are expected on the windward edge of the jet shear layer and in the far field of the jet, but not close to the wall in the wake of the jet. Temperature and scalar dissipation fields cannot be assessed with the data available in this study, but the strain field is analyzed further in terms of the mean velocity divergence, i.e. the dilatational component.

The plasma kernel and associated chemical reactions are imaged using CH*-chemiluminescence. Especially at early times this diagnostic can be influenced by broadband plasma emissions as described in Sec. 3.3.3. Thus, a reference signal is required and care has to be taken in the interpretation of the chemiluminescence recordings to avoid excessive bias due to these broadband emissions.

The reference signal can change as the local flow conditions and chemical compositions change. As a conservative reference, purely the crossflow, without any fuel or jet, is considered. Conservative, because quenching of the plasma spark will be slower in the uniform crossflow than in the strain field of a jet. Thus, a more stringent metric is applied to whether regions support chemical reactions. However, due to the conservative reference, the efficacy of some regions can be underestimated.

Example time series of chemiluminescence recordings are shown in Fig. 5.2. To assess how favorable a given ignition location is to sustained thermal energy release, the spatial extent of the chemiluminescence signal is compared to a reference case. The reference is shown in Fig. 5.2a. The first image in the time series at $\Delta t = 2$ µs is not shown as it is strongly influenced by the initial broadband plasma emissions. However, the images

corresponding to $\Delta t = 10.33$ µs and even $\Delta t = 18.67$ µs also still show these emissions. At later times, the recordings reveal the characteristic donut shape that is expected from this type of LIP (Bradley *et al.*, 2004). That the LIP signal persists beyond the 14 µs, in which visible plasma emissions are detected via schlieren (see Sec. 3.2), is probably due to the lower pressure at supersonic operating conditions. The lower pressure extends the time required for complete recombination and collisional quenching.

An example of an ignition location unfavorable for sustained chemical reactions is shown in Fig. 5.2b. The chemiluminescence signal and its spatial extent are strongly diminished compared to the reference case. For this case, the deposited ignition energy is about 5 mJ higher than in the reference case. However, in the laser focus region and along the corresponding streamline the spark probably encounters conditions that strongly diffuse thermal energy and favor quenching of the plasma. High fuel concentrations, low temperatures close to the termination of the jet expansion region, and strong flow strain can act adversely towards sustained thermal energy release.

On the other hand, an example of an ignition location favorable for sustained chemical reactions is shown in Fig. 5.2c. The chemiluminescence signal remains stronger for a longer time compared to the reference case and is distributed over a larger region. Nonetheless, even with more favorable flow conditions, the signal eventually diminishes. This suggests that the present flow field and configuration cannot reach a steady state with regard to sustaining or stabilizing combustion. That is the ignition kernel can grow but does not become a self-sustaining flame.

The majority of the ignition kernel growth itself, given the present time scales, is likely due to flow advection and strain. Assuming a turbulent flame speed of 10 $\mathrm{m/s}$, which is rather generous for the burning of ethylene (Chaudhuri *et al.*, 2013), the propagation distance at the latest time delay in Fig. 5.2c (~ 44 µs) is roughly 0.4 mm. This corresponds to three pixels on the camera chip and is smaller than the maximum possible image shift during exposure.

It is also important to mention, that the resulting kernel size and CH* signal intensity is a result, not only of the spark location, but also the time history of the kernel as it advects to the point at which it is imaged. Sparks introduced at different locations will take different times to interact with flammable mixtures and experience different flow field states. This history can also change to some degree for individual spark initiated at the same flow location, leading to variability in instantaneous results. Moreover, Mastorakos (2009) mentions that the size of the initial spark (see Sec. 3.2) can affect results and the overdriven state of the laser spark leads to burning properties different from those of steady state combustion. All of these points are considered further in the interpretation of results below.

Because this study is considering forced ignition, the classifications given by Mastorakos (2009) suggest that, if burning occurs, it is likely premixed burning in a stratified mixture before a transition to a diffusion controlled non-premixed burning process is possible. The nature of the burning processes induced by the laser spark are considered in more detail throughout the rest of the study.

5.1 Spatial Distribution of CH* Chemiluminescence

As mentioned before, the enhancement in luminous area compared to the reference case is used to quantify favorable ignition locations. The comparison to a reference case is required due to the LIP induced broadband emissions. Even if there is no significant burning of ethylene the broadband signal is recorded through the CH* chemiluminescence band-pass filter. By quantifying the relative increase in luminous area it is attempted to account for that in determining whether the spark and ignition kernel grow.

The relative increase is defined in Eq. (5.1). For cases in which the relative change is smaller than zero, it is set to zero. The areas are computed by first finding the edges of the luminous region in each frame, then binarizing the images based on the detected edges and calculating the area of the binarized pixels. Examples of the edge detection results are

shown in Fig. 5.2. The method is further described in Sec. 3.3.3. The edges are not shown for the last case as the image starts looking confusing with overlapping regions and lines.

$$r_{CH} = \frac{A_{CH} - A_{ref}}{A_{ref}} \geq 0. \tag{5.1}$$

The areas in Eq. (5.1) are computed as,

$$A = \sum_{\Delta t_i}^{\Delta t_j} A_i(\Delta t_i). \tag{5.2}$$

In this fashion, different subsets of the CH*-chemiluminescence time-series can be evaluated. The results are shown in Fig. 5.3. Also shown are the average position of the pseudo stoichiometric air-ethylene contour and the average 2% jet fluid signal contour, which is used in the determination of the jet trajectories in Ch. 4.

The pseudo stoichiometric contour does not necessarily correspond to the actual stoichiometric mixture fraction contour. As discussed in Ch. 3 the measured jet fluid signal is affected by the varying density in the compressible JISCF flow field. Thus, the pseudo contour shown is an orientation for the phenomenological analysis of the results, but it does not represent the real position of the stoichiometric contour.

The mixture fraction value of the stoichiometric surface can be determined from the chemical equation for air-ethylene combustion at a equivalence ratio of $\phi = 1$,

$$\mathrm{C_2H_4} + 3(\mathrm{O_2} + 3.76\mathrm{N_2}) \longleftrightarrow 2\mathrm{CO_2} + 2\mathrm{H_2O} + 11.28\mathrm{N_2}. \tag{5.3}$$

$$f_{st} = \left[\frac{1}{1 + \frac{Y^0_{\mathrm{C_2H_4}} MW_{\mathrm{O_2}} \nu'_{\mathrm{O_2}}}{Y^0_{\mathrm{O_2}} MW_{\mathrm{C_2H_4}} \nu_{\mathrm{C_2H_4}}}} \right] \approx 0.064. \tag{5.4}$$

In Eq. (5.4), ν' is the stoichiometric coefficient. Together with the chemical equation, the

stoichiometric mixture fraction is calculated to be $f_{st} = 0.064$.

For visual representation, values of r_{CH} have been interpolated between the discrete ignition locations in Fig. 5.3 using biharmonic spline interpolation. However, the only measured values correspond to the actual laser focus set points.

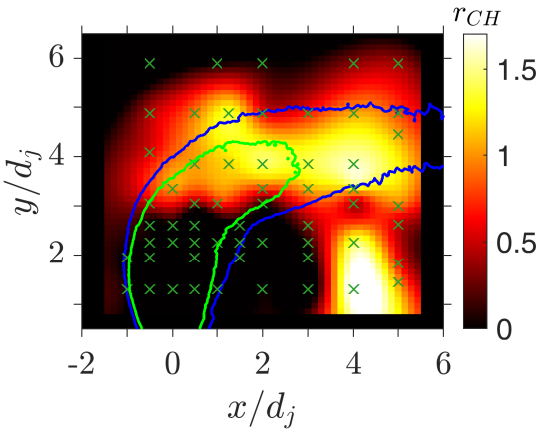

(a) Visual representation of r_{CH} for times $\Delta t = 10.33 - 27$ µs.

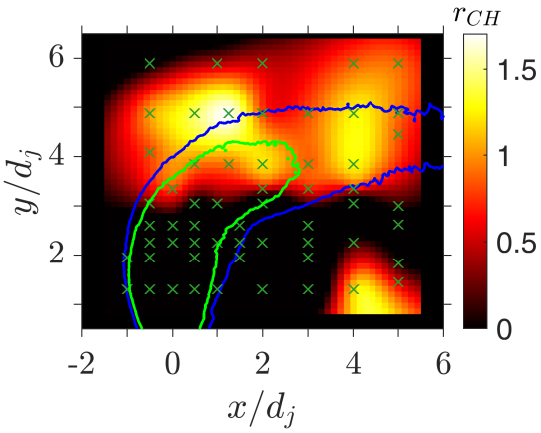

(b) Visual representation of r_{CH} for times $\Delta t = 18.67 - 35.33$ µs.

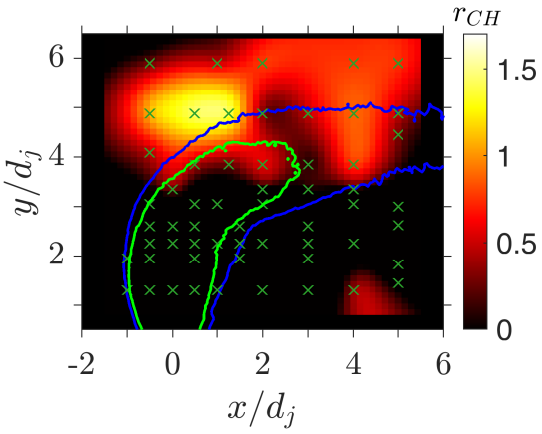

(c) Visual representation of r_{CH} for times $\Delta t = 27 - 43.67$ µs.

Figure 5.3: Visualization of r_{CH} at different time intervals from the deposition of the laser energy in the flow. Green $\times$: ignition locations. Green solid lines: pseudo stoichiometric contour. Blue solid lines: 0.02 jet fluid signal contour.

Uncertainties for r_{CH} are estimated as described in Appendix C. For $\Delta t = 10.33 - 27$ µs the average normalized uncertainty is 24.5% of the value of r_{CH}. Four data points have uncertainties comparable to the value of r_{CH} itself, the remaining points are all below 50%. In the intermediate range, $\Delta t = 18.67 - 35.33$ µs, the average normalized uncertainty is

21.6%. Three data points have uncertainties comparable to the reported r_{CH} values, the rest all fall below 50%. At the later time series entries, $\Delta t = 27 - 43.67$ µs, the average normalized uncertainty is 18%. Only one data point has an uncertainty comparable to the actual r_{CH} value, the rest are all below 50%.

The uncertainty of r_{CH} represents the statistical uncertainty in the average chemiluminescent area and the influence of variations in energy deposited per ignition spark. Since at later time series entries the average uncertainty is only 18%, it is the most reliable in terms of identifying regions that favor sustained release of thermal energy. At earlier times, the larger uncertainties probably reflect more of the transient and statistical nature of spark and ignition kernel development. This is especially true in regions with highly variable fuel content, such as the outer edge of the windward shear layer. Here it takes a finite time for the spark to interact with flammable gases and the interaction can be intermittent.

To evaluate how reactions involving air and ethylene are sustained, it is desirable to exclude plasma broadband emission effects. Based on the trends in Fig. 5.2c and the evolution of the reference case in Fig. 5.2a the time interval $\Delta t = 27 - 43.67$ (corresponding to the fourth to sixth image in the time series) will be used in the subsequent correlations to flow field quantities.

The most pronounced feature of all the plots in Fig. 5.3 is that inside the core region of the jet and on both the windward and leeward side close to the jet orifice, thermal energy from the laser spark is rapidly diffusing and radicals are quenched. The flow expansion inside the jet and the high compressive strain rates in the vicinity of shock structures are probably responsible for that, see Fig. 5.4b. Strong flow expansion will lead to lower temperatures and pressures, diffusing thermal energy, increasing the minimum ignition energy and lengthening ignition delays. It also accelerates the flow and increases dilatational strain rates. Strong flow compression and associated higher pressures accelerate collisional energy exchange, quenching the laser spark plasma faster. However, compression is probably less detrimental to the initiation of combustion since higher pressure and temperature also

increase the rate of ethylene reacting with oxygen (Shao *et al.*, 2018).

That temperature changes along the path of an ignition kernel are a dominant factor makes sense when considering single-step chemistry. With single-step chemistry, the rate constant can be reasonably described by an Arrhenius relation,

$$k = Ae^{-E_a/RT}. \tag{5.5}$$

Here, k is the rate constant, A is a reaction dependent pre-exponential factor, E_a is a reaction dependent activation energy, and R is the specific gas constant. Changing the temperature T results in a change of the reaction rate equal to,

$$\frac{k_2}{k_1} = e^{E_a/R(1/T_1 - 1/T_2)}. \tag{5.6}$$

With a temperature increase of $\sim 170\ \mathrm{K}$ across a Mach 1.71 normal shock in the current experiment and an activation energy of roughly $110\ \mathrm{kJ/mol}$ (Xu and Konnov, 2012), the reaction rate would increase by a factor $\sim \exp(11) \approx 60,000$. A drop in temperature would have similar dramatic effects. At the same time, the pressure probably never drops significantly below 0.7 atm or rises above 2.4 atm, i.e. close to the Mach 1.71 crossflow value and the pressure behind a normal shock. A range over which k is not significantly affected by pressure.

As the time interval is shifted, it can be seen that the distribution and peak values of the area ratio r_{CH} change. In general the peak values are reduced as the time interval shifts to later times. This due to chemical reactions being quenched eventually in all cases, see the example in Fig. 5.2c. It also agrees with the trends observed by Brieschenk *et al.* (2013a), where at later times indicators for hot combustion products fade.

The shift of the most favorable regions further upstream in the windward jet shear layer (compare Fig. 5.3a and Fig. 5.3c) represent a possible bias of the current evaluation methodology. A laser spark deposited further upstream and further away from the average

edge of the jet will take longer to interact with a flammable gas mixture. Thus, any burning processes associated with such a spark will show up at later times than for a spark initiated closer to instantaneously available flammable mixtures. Nonethless, such a bias does not appear to invalidate general trends that can be identified in Fig. 5.3.

Another obvious change in Fig. 5.3 is the reduction of r_{CH} in the jet wake region around the point (4, 2.25) as the time interval is shifted. This suggests that the flow conditions in this region help sustain the initial plasma kernel but do not allow it to transition to a propagating ignition kernel or flame. Looking at the mean velocity field in Fig. 5.4a it is likely that this point is in a low velocity region. Moreover, based on the mean jet fluid signal field in Fig. 5.5a and the RMS jet fluid signal field in Fig. 5.5b it is a region into which basically no ethylene is getting.

On the other hand, a spark initiation at the point (4, 1.3) seems to sustain some form of chemical reaction beyond the initial plasma deposition even though the ignition location is very close to the previously mentioned (4,2.25). Interestingly, no point around (4, 1.3) shows the same elevated r_{CH} values. Moreover, looking at the streamlines in Fig. 5.1 ignition kernels initiated at these two points largely seem to take the same path. A similar type of intermittent burning has been identified by Gamba and Mungal (2015) in an auto-igniting JISCF.

Another interesting region is situated around a line between (2, 6) and (3, 4). Both up- and downstream of this region r_{CH} is significantly higher than in the region itself. Fig. 5.4b shows that ignition points in this region lie at the beginning of an expansion region following the bow shock and jet shock structure. Since spark deposition further downstream is more successful, the rarefaction appears to have a strongly detrimental effect on sustaining chemical reactions. Moreover, the total time the spark or ignition kernel has to travel through the expanding regions seems to influence ignition kernel growth. This relatively strong effect of flow expansion agrees with the analysis that locally lower temperatures and pressures are probably more detrimental to sustained chemical reactions than the quenching

due to higher pressures in compressive flow regions. It also agrees with observations made by Gamba and Mungal (2015) for an auto-igniting JISCF, where a specific region close to the jet turning point along the windward shear layer exhibited significantly reduced thermal energy release.

The above observations regarding ignition locations around (2, 6) and (3, 4) also emphasize the importance of the time history of the ignition kernel. From its deposition to the start of the chemiluminescence measurements the spark and kernel interact with the surrounding flow field. The success of the ignition process to large degree depends on whether the spark can interact with flammable gases before it cools down too much (Sforzo *et al.*, 2015).

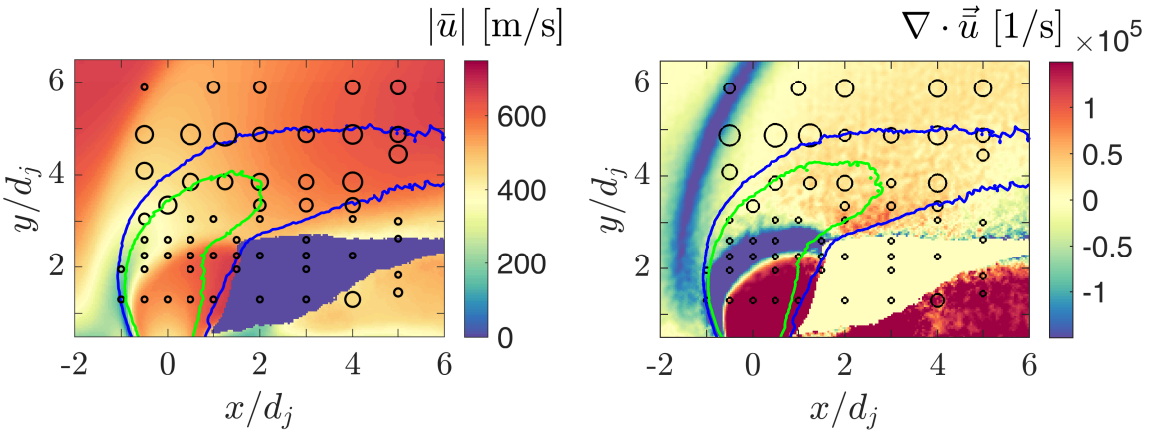

(a) Mean velocity field.

(b) Mean flow divergence.

Figure 5.4: PIV derived mean velocity and flow divergence in relation to the increase in CH* luminous area. Circles indicate the positions at which laser energy is deposited, their size is proportional to r_{CH}. Green solid lines: pesudo stoichiometric contour. Blue solid lines: 0.02 jet fluid signal contour. The momentum flux ratio for the PIV and jet fluid signal data is $J = 3.99$ and $J = 4.05$ respectively, as they were not acquired simultaneously.

Based on the current observations, the most promising conditions for sustaining chemical reactions exist in the windward shear regions, close to the 0.02 jet fluid signal contour, and towards the pseudo stoichiometric contour, see Fig. 5.5a. On one hand, the growing chemiluminescence signal of some points away from the strongest average dilatation effects (Fig. 5.4b) and close to the average stoichiometric surface seem to make obvious

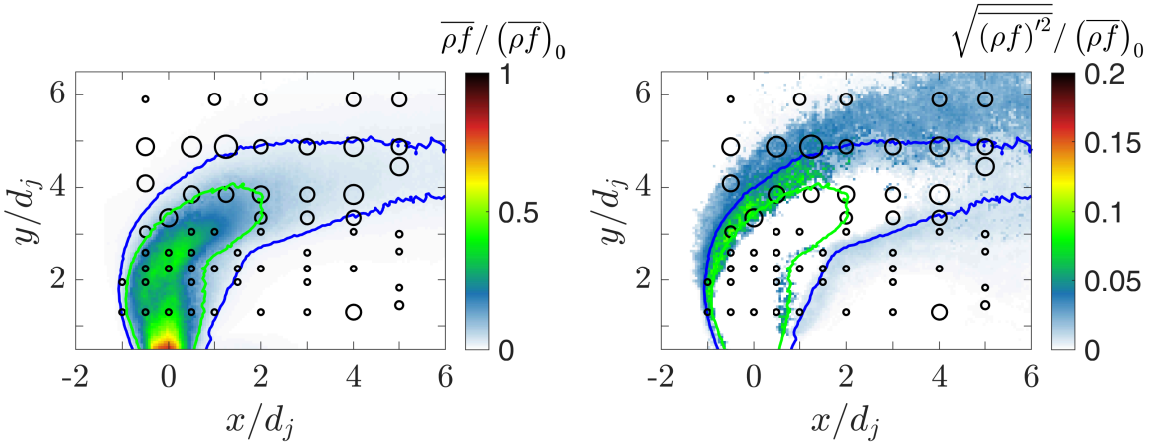

(a) Mean jet fluid signal field.

(b) RMS jet fluid signal field.

Figure 5.5: Mean and RMS jet fluid signal in relation to the increase in CH* luminous area. Circles indicate the positions at which laser energy is deposited, their size is proportional to r_{CH}. Green solid lines: pseudo stoichiometric contour. Blue solid lines: 0.02 jet fluid signal contour.

sense. The lower strain rates prevent the ignition kernel from being diffused immediately. On the other hand, the large values of r_{CH} closer to and even beyond the 0.02 contour are unlikely to be a result of the average properties of the flow field.

Looking at Fig. 5.5b, the ignition points closer to the 0.02 contour and beyond predominantly occur in regions with comparatively stronger jet fluid signal fluctuations. This suggests that the plasma kernel, as it advects with the flow, could initiate premixed ethylene burning along the interface of crossflow and the instantaneous large-scale jet structures penetrating the crossflow. The instantaneous jet fluid signal field in Fig. 5.6a confirms that along the jet-crossflow interface the fuel-air ratio is closer to favorable burning conditions further in the crossflow than expected from the average jet fluid signal field. Instantaneously, values of $\rho f/(\overline{\rho f})_0 \rightarrow 0.064$ (pseudo stoichiometric) occur at vertical coordinates up to $y/d_j \sim 6$ as opposed to $y/d_j \sim 4$ on average.

Interestingly, even an ignition kernel initiated at (-1,4.9), outside the regions of increased jet fluid signal fluctuations, has an elevated value of r_{CH}. Looking at the streamlines (Fig. 5.1) of spark points in this region, the plasma could be transported into the jet shear layer within a sufficiently small time frame to initiate burning for a limited amount

of time. Indeed, the time series for the point (-1,4.9) in 5.6c is an example of that. Initially the ignition kernel is loosing energy and shrinking compared to Fig. 5.6b. It follows a short period of growth, increased CH* luminescence and final extinction. The tilting and stretching along the y-axis due to velocity differences of the ignition kernel is not as pronounced in this case due to the initially limited growth. Initiation of a spark even further upstream will eventually lead to failed ignition attempts as the spark will not reach flammable gas mixtures before being too cold to ignite them.

Comparing the instantaneous jet fluid signal in Fig. 5.6a with the average shape of chemiluminescence emitting regions in Fig. 5.6b, shows that the shape of the chemically reacting regions is governed by velocity differences in the y-direction. The lower parts of the luminous regions is advecting with lower speeds after the jet barrel shock and Mach disk. The upper parts are situated in the re-accelerating region of the crossflow, after the bow shock. However, the jet structures could change their orientation further downstream and a larger field of view is required to make conclusive observations.

Another factor that could influence the results is the alteration of the flow field due to the spark deposition itself. The laser spark is accompanied by a shock wave, rarefaction wave, and a region of strong thermal expansion, see Fig. 3.9. Such phenomena can disrupt and alter the processes from the undisturbed flow field. Unfortunately, no simultaneous measurements were possible in this study, to ascertain the influence of the laser spark deposition on the JISCF flow field. Thus, all flow field properties discussed subsequently are strictly valid only in the non-reacting case.

Any chemical reactions occurring in addition to the initial plasma deposition are due to the plasma spark igniting flammable regions of the flow around it. These are most likely small regions in which premixing of air and ethylene has already occurred. The thin reacting layers characteristic of diffusion burning along the jet-crossflow interface are not observed directly.

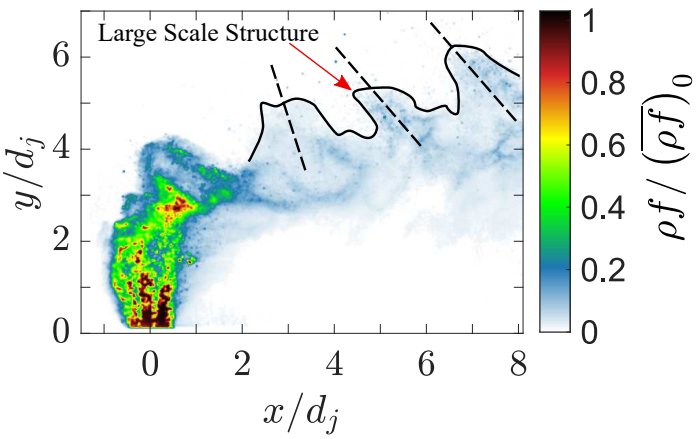

(a) Representative example of an instantaneous jet fluid signal field for the ethylene jet at $J = 4$. The solid black lines are a visual aid following part of the contour of the jet. The dashed black lines are a qualitative indication of the large-scale structure oritentation.

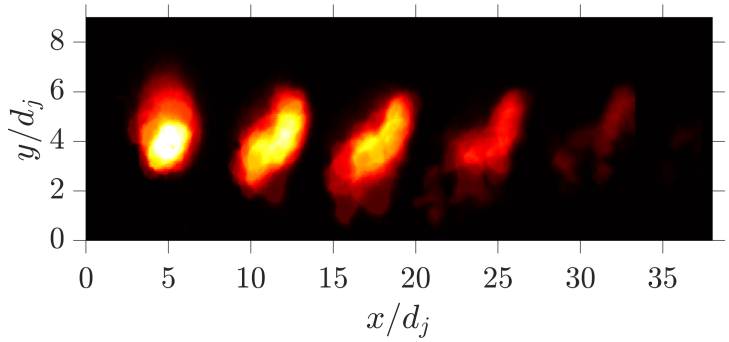

(b) Average time series of a spark deposited at (1.25, 4.88) with high r_{CH} values.

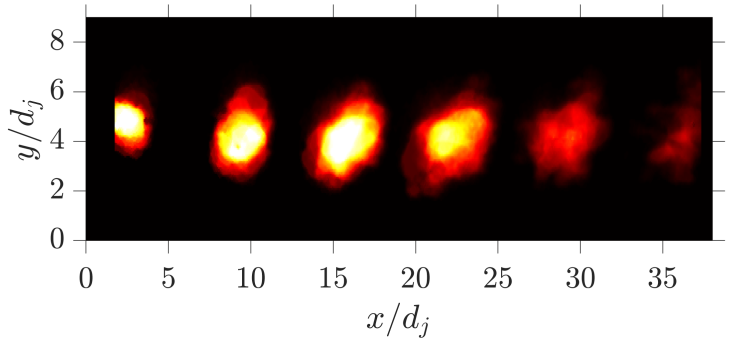

(c) Average time series of a spark deposited at (-0.5, 4.88) with high r_{CH} but an initial position outside the jet shear layer.

Figure 5.6: Instantaneous jet fluid signal field and CH* time series starting at 10.33 µs. Results for each Δt are shifted by an additional $x/d_j = 2$ with respect to the previous Δt data to avoid overlap and make the average shapes more clearly distinguishable. The true extent of the luminous regions is roughly $2 > x/d_j > 17$. The CH* data in (b) is the same as in Fig. 5.2c.

5.2 Influence of Flow Field Variables on CH* Chemiluminescence

Given the previous qualitative observations, it is desirable to have a more quantitative measure of what flow field history will yield enhanced CH* luminescence, i.e. potential burninging in a JISCF configuration. To this end, bivariate histograms of r_{CH} and relevant flow field variables are created and analyzed.

The flow field conditions encountered by the ignition kernel as it advects downstream are analyzed along the respective streamlines, see Fig. 5.1. Because the spark/ignition kernel has a certain size and the focal point of the laser beam is placed in the flow with a finite position accuracy a region of $\pm 0.5\ \mathrm{mm}$ in both coordinate directions is considered around each point along the streamline. This analysis, therefore, does not consider the effect of the velocity difference in the vertical direction explicitly.

The time interval $\Delta t = 27 - 43.67$ is considered to obtain values of r_{CH}. Due to the finite extent of the PIV and jet fluid signal field-of-view there could be a bias towards the early evolution of the ignition kernel, as some ignition locations are closer to the downstream end of the field-of-view than others.

With this methodology $\sim 255,000$ samples are available to compute the histograms. The resulting bivariate histograms are interpreted as the likelihood of certain flow conditions being encountered for a given increase in CH*-chemiluminescence emitting area. Specifically, it considers flow conditions encountered from the point at which the laser energy is deposited up to the downstream field-of-view limit of the PIV and jet fluid signal data. Normalized RMS uncertainties, calculated as described in Appendix C, are below 1% for all histograms presented.

The histograms for normalized mean and RMS velocity magnitude are shown in Fig. 5.7a and Fig. 5.7b, respectively. Since most of the more successful ignition attempts lie on the windward side of the jet and further away from the wall, higher values of r_{CH} tend to coincide with mean velocities closer to the crossflow velocity and lower RMS velocities. There

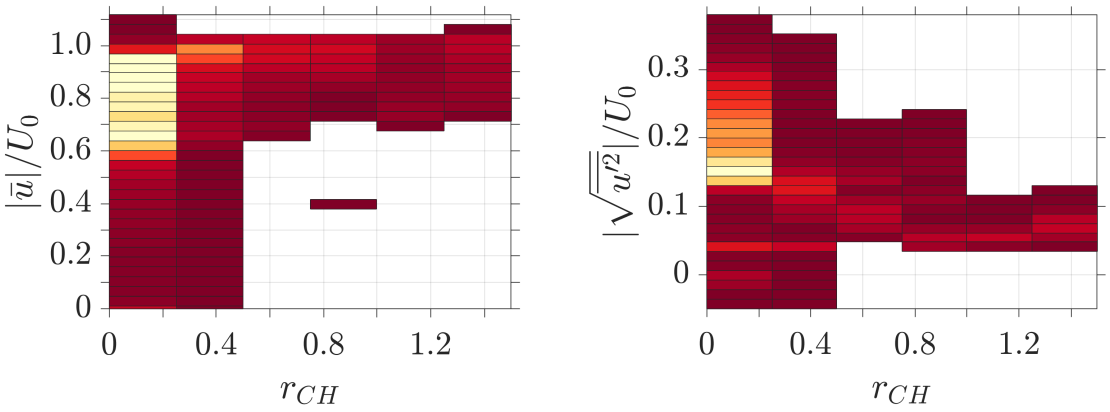

(a) Mean velocity. Average normalized error

(b) RMS velocity.

Figure 5.7: Bivariate histograms for two quantities characterizing the mean flow field and how it acts on regions possibly containing chemical reactions. Darker and lighter colors correspond to lower and higher event counts, respectively.

is a set of cases which provide values of $r_{CH} \approx 0.88$ at lower mean velocities and higher RMS velocities. These correspond to ignition on the upper end of the average stoichiometric contour and the one case in the jet wake around (4,1.3).

To normalize the values of different strain rate components, the extinction strain rate of a non-premixed ethylene-air flame at the undisturbed, static crossflow conditions of this study is used. Computation of the extinction strain rate is accomplished by applying the extinction simulator in Chemkin Pro 19.1 to the opposed flow flame model utilizing the GRI 3 mechanism (Smith, Golden, *et al.*, 2020). The simulator yields an extinction strain rate of $\kappa_{ext} \approx 4,000\ 1/\text{s}$.

While the extinction strain rate gives an idea of the comparative magnitude of strain in the JISCF flow field, it does not have any real relevance to the combustion physics of the ignition kernel here. Based on the work of Bradley *et al.* (2004) and Ochs and Menon (2020), the ignition kernel in this study never reaches a steady state and remains in the transient from overdriven to steady. As long as the overdriven state is relevant, the steady state flame extinction strain rate is not and the ignition kernel can potentially withstand much larger strain rates before quenching (Bradley *et al.*, 2004).

The result for the flow divergence is presented in Fig. 5.8. The divergence is defined as,

$$\nabla \cdot \vec{\bar{u}} = \frac{\partial \bar{u}}{\partial x} + \frac{\partial \bar{v}}{\partial y}. \tag{5.7}$$

A positive value of the divergence corresponds to a flow region experiencing expansion, a negative value to compression. Generally, it is equivalent to the trace of the strain rate tensor, i.e. it measures the normal part of the aerodynamic strain present in the flow field or the dilatation. However, due to filtering effects and the missing third velocity component, the quantity presented here is not the true dilatation and numerical values probably underestimate the true strain in the flow field. Thus, only trends are discussed. The derivatives are computed with a second-order central difference scheme. The scheme is chosen based on the study by Foucaut and Stanislas (2002). However, this process is inherently noisy, as can be seen in the presented data.

Fig. 5.8 exemplifies the high dilatational strain rates present in some parts of the JISCF flow field. Even so, the higher values of r_{CH} all correlate with dilatation rates close to zero. This makes sense, given that higher possible strain rates can diffuse deposited energy and extinguish chemical reactions more quickly. At the flow temperatures and pressures in this study (see Sec. 3.1 and Sec. 3.5), the dilatational strain rates easily exceed the extinction strain rates of steady state ethylene-air flames (Egolfopoulos and Dimotakis, 2001; Sarnacki *et al.*, 2012).

Although the ignition kernel is still in an overdriven state, the existence of such high strain rates makes premixed burning more likely than non-premixed burning. The latter is extinct at much lower strain rates than the former (see Lieuwen (2012, chap. 9)). To support this claim, further extinction rate calculations with Chemkin are performed. According to these calculations, a stoichiometric, premixed ethylene-air flame can withstand strain rates up to $\sim 11,500\ 1/\mathrm{s}$ and $\sim 42,000\ 1/\mathrm{s}$ at the present static flow and stagnation conditions, respectively. In contrast, non-premixed ethylene air flames extinguish at $\sim 4,000\ 1/\mathrm{s}$ and $\sim\ 27,000\ 1/\mathrm{s}$ for static flow and stagnation conditions, respectively. It is emphasized

again, that the actual numerical values of the extinction strain rates are not relevant for an overdriven ignition kernel.

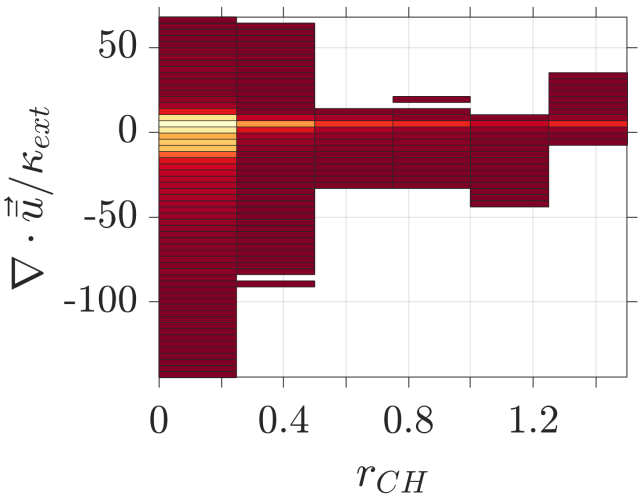

Figure 5.8: Bivariate histogram for the flow divergence. The histogram characterizes the effect of dilatational strain acting on regions possibly containing chemical reactions. Darker and lighter colors correspond to lower and higher event counts, respectively.

The histogram of the mean jet fluid signal in Fig. 5.9a confirms the qualitative observation made in Fig. 5.5a. The highest r_{CH} cases lie on the edge of the jet plume in regions with $\overline{\rho f}/\left(\overline{\rho f}\right)_0 = 0.02$ or less. However, decent growth of CH* luminescent regions is still observed close to the average pseudo stoichiometric contour.

Finally, the results for jet fluid signal fluctuations in Fig. 5.9b supports the conjecture made in connection to Fig. 5.5b and Fig. 5.6a. For all values of $r_{CH} > 0.25$ the jet fluid signal RMS exhibits a preference towards non-zero values (~ 0.03) and the spread is not reducing significantly. This indicates that large scale structures advecting in the vicinity of the spark and ignition kernel play an important role in propagating chemical reactions. The "ignition" of (potentially premixed) gas around large scale jet structures is the primary mechanism to support chemical reactions in the jet shear layer. Nonetheless, the interface between the jet structures and the crossflow does not actually seem to ignite and burn under the present conditions, probably due to the flow field being too cold.

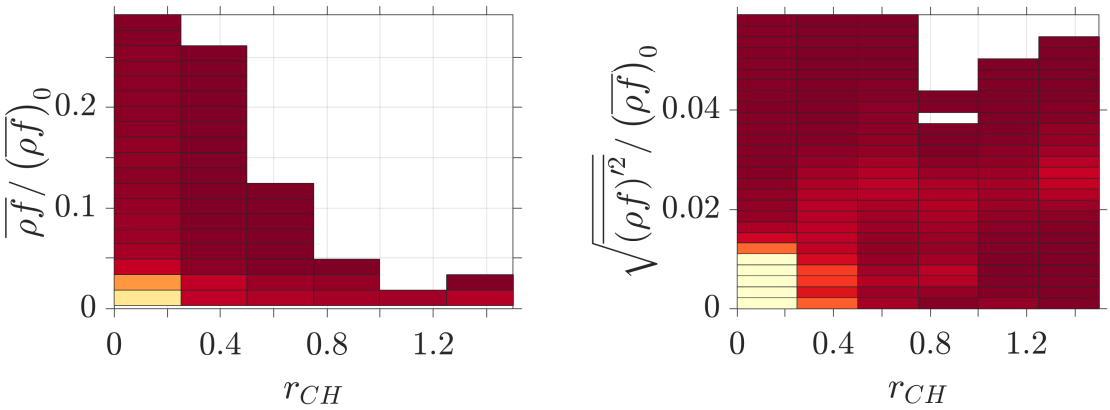

(a) Mean jet fluid signal.

(b) RMS of the jet fluid signal.

Figure 5.9: Bivariate histograms for two quantities characterizing the distribution of jet fluid in the flow field and its effect on regions possibly containing chemical reactions. Darker and lighter colors correspond to lower and higher event counts, respectively.

5.3 Conclusive Remarks

The ignition study on a single ethylene jet in crossflow at $J = 4$ revealed several important trends. Broadband plasma emissions strongly influence the results up to $\Delta t = 18.67$ µs and then fall of rapidly.

Accounting for this effect, the conditions most favorable to burning are located close to the top of the average pseudo stoichiometric contour and in the windward shear layer away from jet shock structures. Some regions near the wall could also provide a suitable environment but the governing processes here are likely the result of more complex three-dimensional phenomena as well as boundary layer interactions. The present study does not provide enough data to characterize this region completely and further investigation is desirable.

Due to the dependence of ignition kernel evolution on the corresponding flow field history, trends in r_{CH} can be weakly biased towards certain ignition locations for different time windows analyzed. The success of a laser spark transitioning to an ignition kernel strongly depends on the time it takes to get in contact with flammable gas mixtures and the strain rates it experiences. With regard to the instantaneous flow field, this aspect introduces

a statistical component into the measured growth of the ignition kernel as it advects with the flow. It also allows laser sparks deposited in an inert region to result in an ignition kernel at later times, if they advect into a flammable gas region fast enough.

The observed trends also suggest that the dilatational strain rate history has a strong influence on chemical reactions mostly through associated temperature changes. Changes in temperature can have a significant effect on the rate constant of ethylene combustion according to an argument relying on single-step Arrhenius kinetics. Compressive regions exhibit elevated temperatures while expansive regions cause a drop in temperature. The former increasing values of the rate constant, the latter decreasing them.

Extinction strain rates of non-premixed and premixed flames were considered for order of magnitude comparisons. However, within the time available to perform measurements, the ignition kernel is unlikely to transition into a steady state and remains in an overdriven state. This overdriven state could allow combustion processes around the kernel to withstand higher strain rates than a steady state flame.

In the favorable regions close to the pseudo stoichiometric contour and the windward shear layer, the ignition kernel did not result in a steady state flame. Instead, the ignition kernel appears to burn small pockets of premixed reactants formed around large scale jet structures as the jet fluid is entrained into the crossflow. Given the time scales considered, the dominating factor for a growing ignition kernel's size, shape, and orientation seem to be the mean flow velocity gradients in the surrounding flow field. The structure of the large scale entrainment features appear to have no significant effect as chemical reactions are not seen to stabilize in thin flamelets along the instantaneous jet fluid - crossflow interface.

CHAPTER 6

STAGED JETS IN A SUPERSONIC CROSSFLOW

The insight gained in Ch. 4 and Ch. 5 is used to investigate the possibility of enhancing burning in a relatively cold JISCF system by using laser ignition (see Sec. 3.2) on a staged setup of two jets (also referred to as dual jets/injectors or DI in the following). Two staged configurations are used, both with the jet orifices in the plane of symmetry but different spacings between the jets.

Table 6.1: Measured global momentum flux ratios, J, for each of the jet fluid signal and PIV data sets presented in this chapter. "DI" stands for dual injector, i.e. injectors with two staged jet orifices. PLIF measurements have been performed with all of the available injectors using ethylene and a momentum flux ratio of 4.07 ± 0.1.

	Jet Fluid Signal				PIV			
Injector	SI	SI*	DI1	DI2	SI	SI*	DI1	DI2
Species	N_2	C_2H_4	C_2H_4	C_2H_4	C_2H_4	C_2H_4	C_2H_4	C_2H_4
d_j [mm]	2.00	1.41	1.41	1.41	2.00	1.41	1.41	1.41
J	2.28/4.03	4.10	3.95	4.12	4.00	4.04	3.95	3.99

The jet orifices of the dual jets are 1.41 mm in diameter to maintain the approximate total mass flow rate of the single jet/injector (SI) used in Ch. 4 and Ch. 5. The spacing between the jets is chosen based on results in Ch. 4. Using the previously discussed x-coordinate scaling, the separations are $x/J_2^{1/2}d_j = 1$ and 3 for DI1 and DI2, respectively. In physical coordinates, the separation distances between the jets are 4.2 mm and 12.6 mm, respectively. Given the situation in Fig. 4.11, this puts the second jet of DI1 in the near field of the first jet before it turns completely into the crossflow. The second jet of DI2 is further downstream, interacting with the first jet only after it has turned almost completely into the crossflow. Schematics of the staged injectors are shown in Fig. 3.5. For reference, some data points are also collected with a single jet having the same jet diameter as the dual

injectors, which will be referred to as SI*. For all data sets in this part of the study the boundary layer thickness remains unchanged, i.e. δ/d_j increases to 3.73 (from 2.63) for the injectors with the smaller jet diameter.

The non-reacting data sets collected in this part of the study are summarized in Tab. 6.1. Primarily, a global momentum flux ratio of $J = 4$ is targeted for which the jet is expected to definitely leave the boundary layer. The non-reacting data sets are used as a reference, for validation of the previous discussions and to relate the influence of flow field properties on the development of the LIP induced ignition kernel.

Investigated ignition locations are chosen based on the results in Ch. 5. They are summarized in Tab. 6.2. Position IDs 1, 2 and 3 correspond to promising cases, in terms of likelihood to support ignition, with large increases in luminous area. Position ID 4 is used for comparison as a location that seemed detrimental to the initiation of sustained thermal energy release. Only positions 1,2 and 3 are used in the experiments with staged injection as the goal is to maximize the likelihood of sustained thermal energy release. The laser spark locations are adjusted for the smaller diameter injectors based on the jet trajectory scaling in Ch. 4 to ensure similar local conditions.

Table 6.2: Ignition positions used in this part of the study. The positions (x, y) are given in $[\mathrm{mm}]$ relative to the first jet orifice center. Positioning accuracy is ± 0.5 mm as explained in Ch. 5.

d_j	2.00 mm				1.41 mm			
ID	1	2	3	4	1	2	3	4
Position	(-1.0,10.0)	(2.0,10.0)	(8.0,10.0)	(3.0,5.2)	(-0.7,9.1)	(1.4,9.1)	(5.7,9.1)	-

In the reacting cases, OH-PLIF data are collected on the symmetry plane of the JISCF flow field. This yields a planar measurement of regions containing the product of potential hydrocarbon burning that is not line-of-sight averaged. Thus, it can be related more directly to the planar measurements of jet fluid signal and velocities. Statistically independent ensembles of PLIF images are collected at different time delays from laser energy deposition as summarized in Tab. 6.3 and Tab. 6.4. The single injectors in Tab. 6.3 are primarily in-

tended as a reference for the staged injection cases. The latter, summarized in Tab. 6.4, are used to investigate the influence of the second jet as well as the effects of changing jet spacing on the evolution of the laser spark and the possibly associated thermal energy release.

Due to the fast advection of the ignition kernel downstream, the jet fluid signal and PIV FOV is increased to achieve more overlap between Mie-scattering/PIV and PLIF data. The new FOV is roughly 38 $\mathrm{mm}\times$32 mm vs. the previous 25 $\mathrm{mm}\times$21 mm.

Table 6.3: Summary of ignition locations and time delays from energy deposition investigated for the single injector setups.

Injector	SI				SI*
ID	1	2	3	4	2
Times [µs]	19, 35	19, 35	19, 35	19, 35	19, 35

Table 6.4: Summary of ignition locations and time delays from energy deposition investigated for the dual/staged injector setups.

Injector	DI1		DI2	
ID	1	2	2	3
Times [µs]	19, 27, 35	19, 27, 35	19, 27, 35	19, 27, 35

6.1 Non-reacting Dual Jet Characteristics

Initially, the jet trajectories of the $d_j = 1.41$ mm jets are compared to the already discussed cases in Ch. 4. This serves to establish a baseline for the following experiments and also to further validate the jet trajectory scaling approach already presented. Then mixing and velocity statistics are compared between single jets and dual jets by extracting profiles similar to the approach in Ch. 4. This yields further insight into similarities and differences between single jets with changing diameters and staged jets.

6.1.1 Dual Jet Trajectories

Fitting trajectory data from Ch. 4 is compared with data in this chapter for nitrogen and ethylene jets at $J = 2$ and $J = 4$ using the two single injectors, SI and SI*. A direct comparison using the 0.02 jet fluid signal trajectory definition and the scaling from Fig. 4.8 yields Fig. 6.3. The quality of the trajectory collapse is good between cases with the same d_j but significantly reduced between the $d_J = 2\,\mathrm{mm}$ and $d_j = 1.41\,\mathrm{mm}$ cases. Specifically, the penetration of the SI* injector trajectories drops off faster than for the Si injector.

Based on the discussion of jet trajectories in Sec. 4.1, the faster drop-off means that the jet fluid signal downstream of injection decreases faster in the SI* cases. The faster decrease can have two main reasons. The total amount of jet fluid introduced into the flow field is reduced by $\sim 50\%$ for the smaller jet diameter (see Eq. (3.4)) at a given J and turbulent mixing characteristics can be different due to the difference in δ/d_j. This suggests that an absolute jet fluid signal contour (here $\overline{(\rho f)}/\overline{(\rho f)}_0 = 0.02$) might not be the best choice to compare jet trajectories from experiments with different jet mass flow rates and δ/d_j.

A trajectory that might be more generally indicative of the jet penetration is the maximum jet fluid signal location. However, especially close to the jet orifice, this type of measurements is strongly impacted by dilatation effects and changing density in the compressible flow field. Fig. 6.2 shows a comparison of trajectories based on the maximum jet fluid signal location at a given jet cross section. The qualitative collapse of cases with different d_j is improved employing this approach. Thus, as expected, the change of d_j from SI to SI* does not change the underlying mechanisms responsible for jet penetration significantly. Moreover, this implies the developed trajectory scaling captures the effects of changing d_j and δ/d_j.

It is still desirable to compare jet trajectories based on iso-contours to reduce dilatation effects. Normalization with the maximum jet fluid signal at a given jet cross section should remove the effect of changing global $\dot{m}_j/\dot{m}_\infty$ to some degree (the maximum signal will

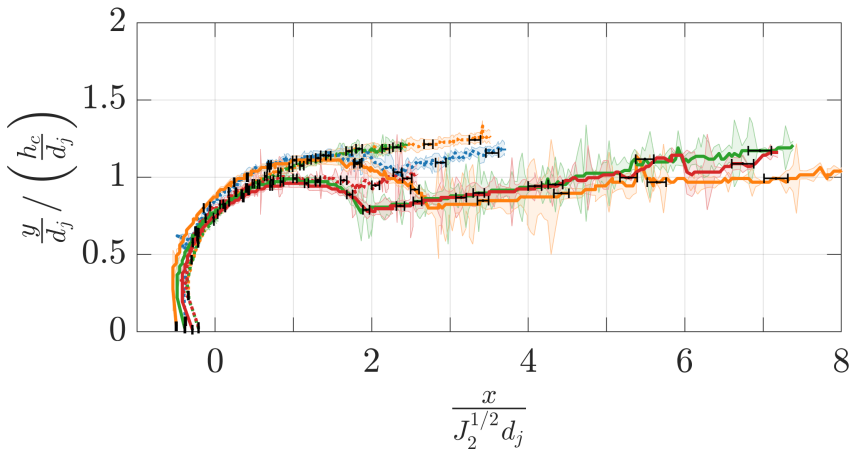

Figure 6.1: 2% jet fluid signal trajectories of single jet injectors. Dotted lines correspond to data presented in Ch. 4 with $d_j = 2$ mm. Solid lines represent data taken with a larger FOV and $d_j = 1.41$ mm. — N_2 $J = 2$, — N_2 $J = 4$, — C_2H_4 $J = 2$, — C_2H_4 $J = 4$.

still be impacted strongly by dilatation effects in the jet's near field). Note that this approach changes the interpretation of mixing rates from jet trajectory trends according to the discussion in Sec. 4.1. That is, higher turbulent mixing rates should now generally result in trajectories with higher penetration.

In Fig. 6.3 trajectories based on the normalized 10% jet fluid signal contour are shown. The 10% cut-off is chosen for comparison with the data by Pizzaia and Rossmann (2018). For the trajectory data in this study, the normalized contour collapse is qualitatively about as good as that in Fig. 6.2 and better than that in Fig. 6.1. Nonetheless, data of matching d_j still seems to correlate the best.

The SI trajectories reflect the familiar result that ethylene should experience enhanced turbulent mixing over nitrogen. On the other hand, the SI* trajectories do not exhibit the same trend. The nitrogen and ethylene trajectories pretty much collapse on top of each other. This could be a resolution effect since the SI* data was acquired with a larger FOV and the differences are small to begin with. According to Tab. 3.3 the resolution is $\sim 20\%$ lower for the larger FOV.

Also shown for comparison in Fig. 6.3 are the normalized trajectories of Pizzaia and

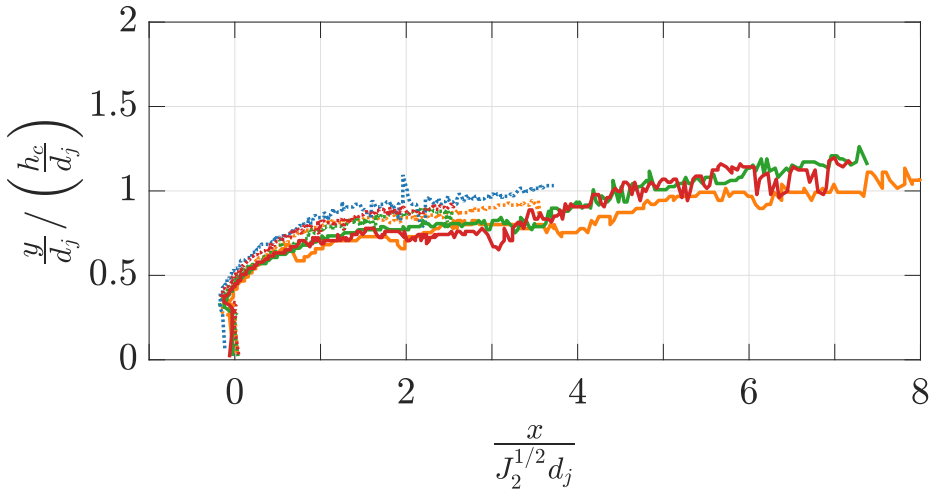

Figure 6.2: Maximum jet fluid signal trajectories of single jet injectors. Dotted lines correspond to data presented in Ch. 4 with $d_j = 2$ mm. Solid lines represent data taken with a larger FOV and $d_j = 1.41$ mm. — N_2 $J = 2$, — N_2 $J = 4$, — C_2H_4 $J = 2$, — C_2H_4 $J = 4$.

Rossmann (2018). Interestingly, downstream of $x/J_2^{1/2}d_j = 3.5$ their trajectories do not collapse with the trajectories determined in this study. Initially, the trajectories agree well, but further downstream of the injection point the Pizzaia and Rossmann (2018) data shows a much flatter normalized contour evolution. Based on the discussion in Sec. 4.1 this could mean that the jet fluid in the Pizzaia and Rossmann (2018) experiments experiences stronger lateral mixing or flow expansion than the jet fluid in the present study. It is not entirely clear why that would be the case. Their trajectory is a 5% normalized jet fluid signal contour and except for the larger lateral extent of their test section (see Tab. 4.2) their experimental geometry is similar to the one in this study. Their lower normalized signal cut-off, if anything, should yield larger penetrations. Stronger expansion effects might be a possible factor due the higher crossflow Mach number in the Pizzaia and Rossmann (2018) experiments (Mach 3.4) and the corresponding stronger bow shock.

The presented results show that the correlation of jet trajectories with different global mass flow ratios improves using the maximum jet fluid signal trajectory or a normalized jet fluid signal contour. However, between different experimental setups and crossflow Mach numbers, these types of trajectories appear to be influenced by factors that are not

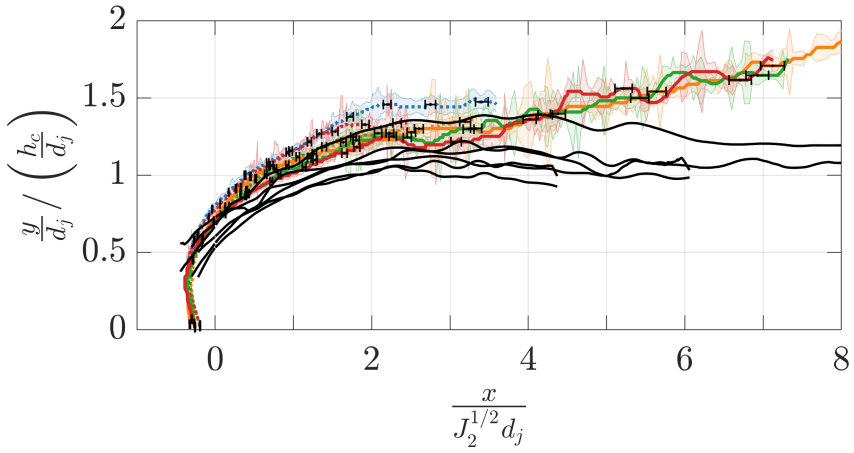

Figure 6.3: Normalized 10% jet fluid signal trajectories of single jet injectors. Dotted lines correspond to data presented in Ch. 4 with $d_j = 2$ mm. Solid lines represent data taken with a larger FOV and $d_j = 1.41$ mm. — N_2 $J = 2$, — N_2 $J = 4$, — C_2H_4 $J = 2$, — C_2H_4 $J = 4$, — Pizzaia and Rossmann (2018).

accounted for in the developed penetration scaling. Unfortunately, a comparison of normalized contour trajectories is not possible for all of the data presented in Fig. 4.8 in this study, as the required data is not available in the published literature.

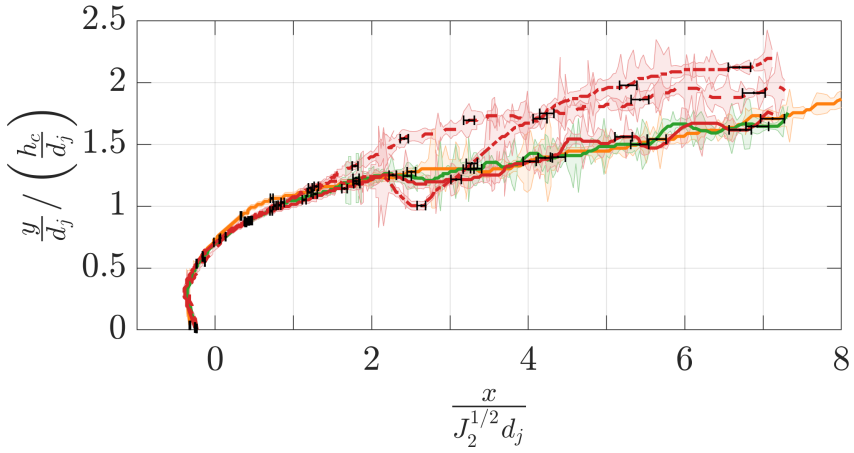

Figure 6.4: Normalized 10% jet fluid signal trajectories of single and staged injectors. The jet diameter for all data sets is $d_j = 1.41$ mm. All red lines refer to C_2H_4 at $J = 4$ as injectant. — N_2 $J = 2$, — N_2 $J = 4$, — C_2H_4 $J = 4$, - - - DI1, ····· DI2.

The normalized 10% jet trajectories for the single and staged injectors with $d_j = 1.41$ mm are compared in Fig. 6.4. Acquiring this data, both jets of the dual injectors are seeded. Penetration is enhanced for both staged injectors over the single injector case. For jet

interaction in the near field (DI1), the penetration monotonically grows beyond the single injector cases around $x/J_2^{1/2}d_j = 1.5$. In the case of a second injector farther downstream (DI2), the normalized trajectory first exhibits a dip just ahead of the second jet, close to $x/J_2^{1/2}d_j = 2.5$, and subsequently penetrates deeper into the crossflow than both the single injector cases and the DI1 case. The dip is due to the additional jet fluid from the second jet temporarily moving the locations of highest jet fluid signal closer to the test section wall.

The observations suggest that entrainment and turbulent mixing is generally enhanced by staged jets within a certain distance of each other, in agreement with the experimental result by Hollo *et al.* (1994) and the computational results by Lee (2006a). Furthermore, in this particular case, the injector with the larger jet spacing (DI2) exhibits the overall largest penetration. According to the work by Lee (2006a) this is due to the existence of an optimal distance between jets for blockage effects, provided by the first jet, to influence the second jet, resulting in higher penetration and faster mixing. This optimal distance depends on the momentum flux ratio and at even larger separations penetration and mixing could be reduced below the values observed for the DI2 case.

6.1.2 Dual Jet Mixing and Velocity Statistics

In the following, jet fluid signal and velocity field data of the smaller d_j injectors are investigated in more detail and compared to the SI results already discussed.

6.1.2.1 Jet Fluid Signal Fields

The mean jet fluid signal fields of SI ($d_j = 2$ mm) and SI* ($d_j = 1.41$ mm) are shown in Fig. 6.5 and Fig. 6.6, respectively. They are similar, but the SI* data shows slightly more extended regions with elevated jet fluid signals in the near field. The RMS jet fluid signal field in the right panel of the same figures also shows some differences in the near field, primarily in the windward shear layer where the SI* jet experiences stronger fluctuations over a more extended region. The fluctuations drop off rapidly further downstream. The

reason for the differences might be the enhanced interaction with the boundary layer as δ/d_j is larger for the smaller jet diameters. On average, the jet contours still collapse well as demonstrated in Fig. 6.3.

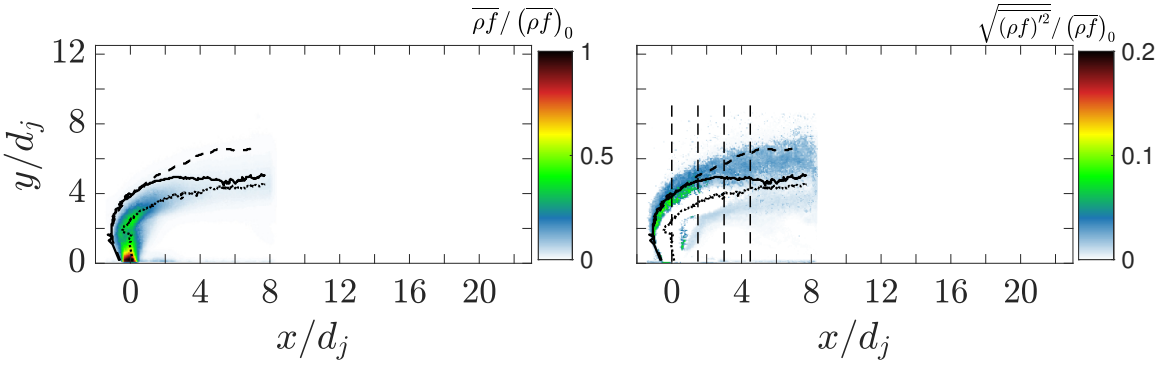

Figure 6.5: Mean and RMS jet fluid signal field for the SI-jet at $J = 4$. Dotted line: max. jet fluid signal location. Solid line: 0.02 contour. Dashed line: normalized 0.1 contour. Vertical dashed lines: locations of data extraction for y-profiles comparing the $d_j = 2$ mm injectors. This is the same data as shown in Fig. A.2a and Fig. A.2b for $J = 4$.

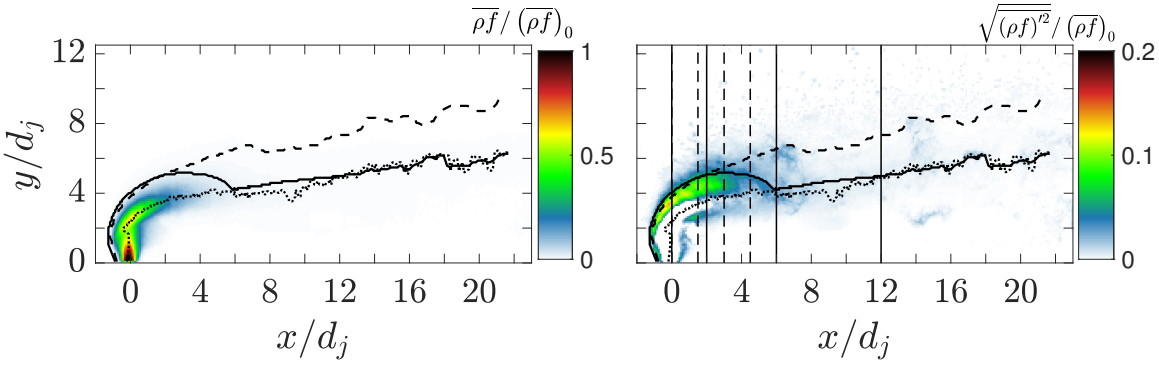

Figure 6.6: Mean and RMS jet fluid signal field for the SI*-jet at $J = 4$. Dotted line: max. jet fluid signal location. Solid line: 0.02 contour. Dashed line: normalized 0.1 contour. Vertical dashed lines: locations of data extraction for y-profiles comparing the $d_j = 2$ mm injectors. Vertical solid lines: locations of data extraction for y-profiles comparing the $d_j = 1.41$ mm injectors.

The jet fluid signal fields for the DI1 injector are shown in Fig. 6.7. The two jets are clearly visible as are the formation of two compression regions, presumably after jet shock structures terminating the jet expansion into the crossflow. The second jet has a straighter trajectory and turn slightly later into the crossflow than the first jet, as would be expected due to the blockage effect of the first jet partly shielding the second jet from the crossflow.

The regions of more intense jet fluid signal fluctuations are more distributed and extend slightly further downstream than in the SI* case in Fig. 6.6. This is probably due to the additional jet fluid introduced and the additional disturbances caused by the second jet. It can be clearly discerned how the second jet pushes and extends the 0.02 jet fluid signal contour further into the crossflow. Moreover, elevated and more continuous fluctuations of ρf are visible closer to the wall in the jet wake region after $x/d_j = 12$ when compared with the SI* case.

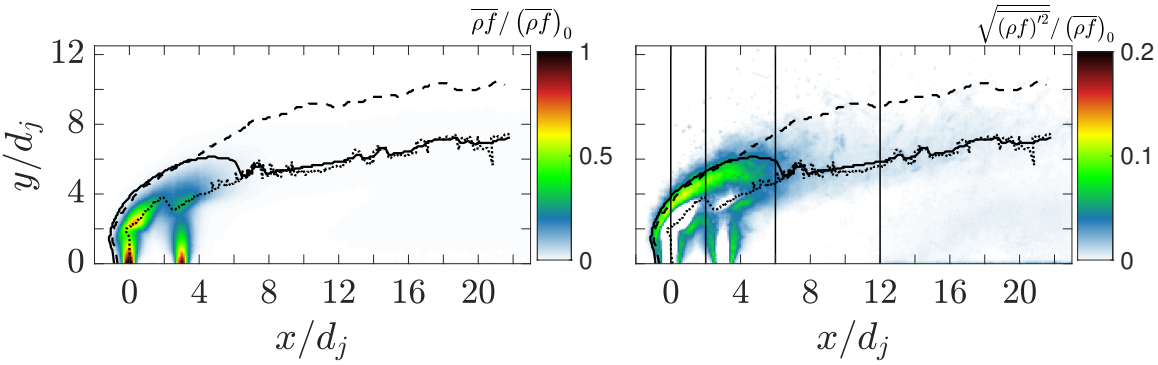

Figure 6.7: Mean and RMS jet fluid signal field for the DI1-jets at $J = 4$. Dotted line: max. jet fluid signal location. Solid line: 0.02 contour. Dashed line: normalized 0.1 contour. Vertical solid lines: locations of data extraction for y-profiles comparing the $d_j = 1.41$ mm injectors.

Several clear differences between the DI2 and the DI1 injector can be seen comparing Fig. 6.8 and Fig. 6.7. The topology of the first jet resembles more that of a single jet (Fig. 6.6), i.e. as expected from the increased jet spacing the first jet seems to interact much less directly with the second jet. Differences in the second jet's appearance are presumably due to differences in the pressure field outside the second jet orifice. Specifically, the second jet in the DI1 case should experience a much lower pressure than the second jet in the DI2 case, see the wall pressure results by Kawai and Lele (2010) and Sun and Hu (2018a). The larger separation between the jets allows the second jet to "use" the obstruction formed by the first jet more effectively and penetrate even further than in the DI1 case. Two distinct regions of peak RMS fluctuations can be identified, one on the first jet resembling that of the SI* case and one around the second jet. In the vicinity of the second jet the fluctuation

magnitude remains moderate but overall elevated indicating that the jet-jet interaction facilitates a spatially distributed mixing process. Except for a small region around $x/d_j = 14$, which does not appear to be an artifact, much less near wall fluctuations are visible here than in the DI1 case. This is due to the upward motion induced by the second jet causing jet fluid to be advected away from the wall over a more extended spatial region.

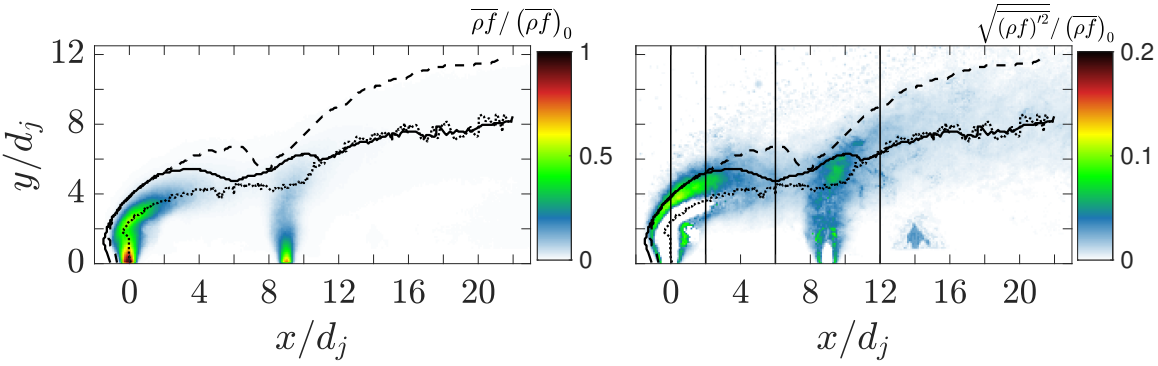

Figure 6.8: Mean and RMS jet fluid signal field for the DI2-jets at $J = 4$. Dotted line: max. jet fluid signal location. Solid line: 0.02 contour. Dashed line: normalized 0.1 contour. Vertical solid lines: locations of data extraction for y-profiles comparing the $d_j = 1.41$ mm injectors.

A more quantitative analysis is conducted using the same techniques as in Ch. 4. RMS jet fluid signals are compared along the absolute 2% jet fluid signal contour in Fig. 6.9, where $\hat{s}$ is again the normalized arc length along the trajecory computed from the scaled $x-$ and y-variables. The absolute contour is chosen instead of the normalized one to investigate differences in mixing and entrainment.

In the comparison between the two single jet injectors in Fig. 6.9a it appears that along the 2% contour the RMS fluctuation magnitude and evolution is comparable. In the near field the smaller jet diameter tends to slightly higher values which corresponds to the observations made in Fig. 6.5 and Fig. 6.6, presumably due to the enhanced boundary layer interaction.

The comparison of RMS fluctuations between single and staged injectors in Fig. 6.9b corroborates the qualitative observations made about the presented field information. The SI*, DI1 and DI2 cases largely match near the injector and far downstream. After the peak

around $\hat{s} = 1.5$, the DI1 case exhibits continuously elevated fluctuations in the intermediate region around $\hat{s} = 2 - 5$. Clearly, this is due to the interaction between the two jets positioned very close to each other. Their vicinity broadens the region in which vigorous entrainment and turbulent mixing are occurring.

Surprisingly, the DI2 case has a slightly higher peak at $\hat{s} = 1.5$ than the SI* and DI1 cases, which could be the consequence of an extended low-speed region between the two jets allowing the second jet to influence the evolution of the first one. Downstream of the main peak the fluctuation magnitude of the DI2 case largely matches that of the SI* case up tp $\hat{s} = 4$. At this point the RMS magnitude of the DI2 case increases to another peak due to the presence of the second jet. This secondary peak is not as high as the first one. Judging from Fig. 6.8 the peak fluctuations are lower around the second jet due to a more distributed stirring process. This stirring process is probably caused by vortex structures initiated at the first jet's flow obstruction. After the second peak the RMS magnitude decreases again and seems to converge with the SI* and DI1 cases.

The convergence of the RMS values donwstream of the second DI2 peak suggests that the spacing of the two injectors can control the distribution of the fluctuation intensity and its peak values but eventually results in the same far field state, at least within the FOV observed. This makes sense, if in the far field small scale diffusion processes dominate.

The jet fluid signal fluctuations are investigated further by extracting vertical profiles at several downstream locations, presented in Fig. 6.10. Between the single jet injectors in Fig. 6.10a the smaller d_j jet tends to have its peak RMS values closer to the wall. This suggests that the change in δ/d_j from 2.63 to 3.73 causes a change in mixing and entrainment that is not entirely captured by the y/h_c scaling. Furthermore, the peak values at all four x/d_j locations are larger for the smaller d_j jet indicating that the change in δ/d_j actually enhances turbulent mixing in the near field of the jet, in agreement with the study conducted by Pizzaia and Rossmann (2018).

The staged jet profiles in Fig. 6.10b agree well with each other at $x/d_j = 0$ as would

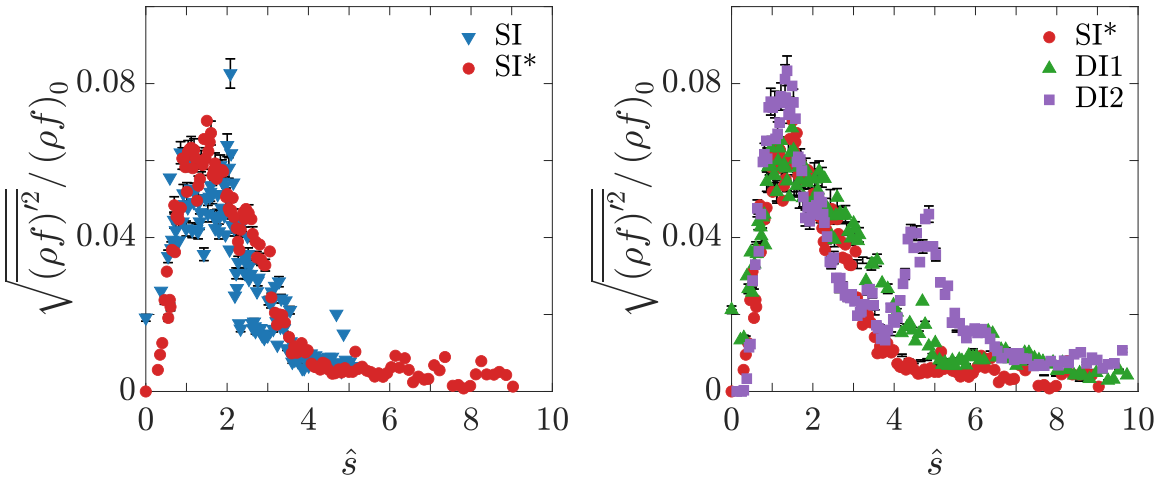

(a) Comparison between $d_j = 2$ mm and 1.41 mm single injectors.

(b) Comparison between single and staged injectors with $d_j = 1.41$ mm.

Figure 6.9: RMS jet fluid signal evolution along the 2% jet fluid signal contour. In all cases the injectant is ethylene at $J = 4$.

be expected. This figure also shows that the higher peak discussed for DI2 in Fig. 6.9b is most likely an artifact of the 0.02 trajectory determination: upstream of $x/d_j = 6$ the DI2 case always has RMS magnitudes similar to or slightly lower than the SI* case.

As would be expected, the DI1 case deviates from the other two cases first (see data shown for $x/d_j = 2$). However, the presence of the second jet does not seem to modify the RMS trends in the y-direction significantly, except for the near wall increase due to the jet itself. Instead the effect seems limited to an overall increase in RMS magnitude.

The presence of the second jet in the DI2 case does not appear to cause major changes in the y-profile upstream of the secondary jet when compared to the SI* case. Nonetheless, downstream the RMS magnitude and evolution deviates significantly from the SI* and DI1 injectors. Specifically, the elevated fluctuations reach much deeper into the crossflow. This makes sense considering the overall enhanced penetration of the DI2 injector over the other two injectors. The later re-introduction of jet fluid signal fluctuations also means that they will persist the furthest downstream for the DI2 injector.

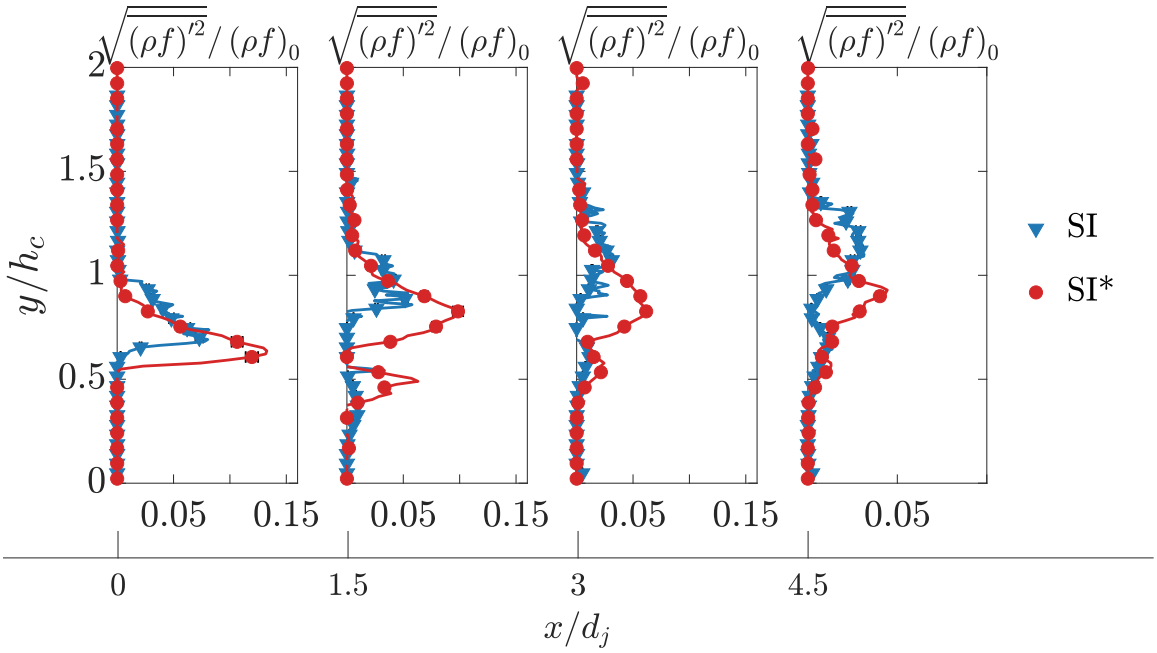

(a) Single jet injectors SI and SI*.

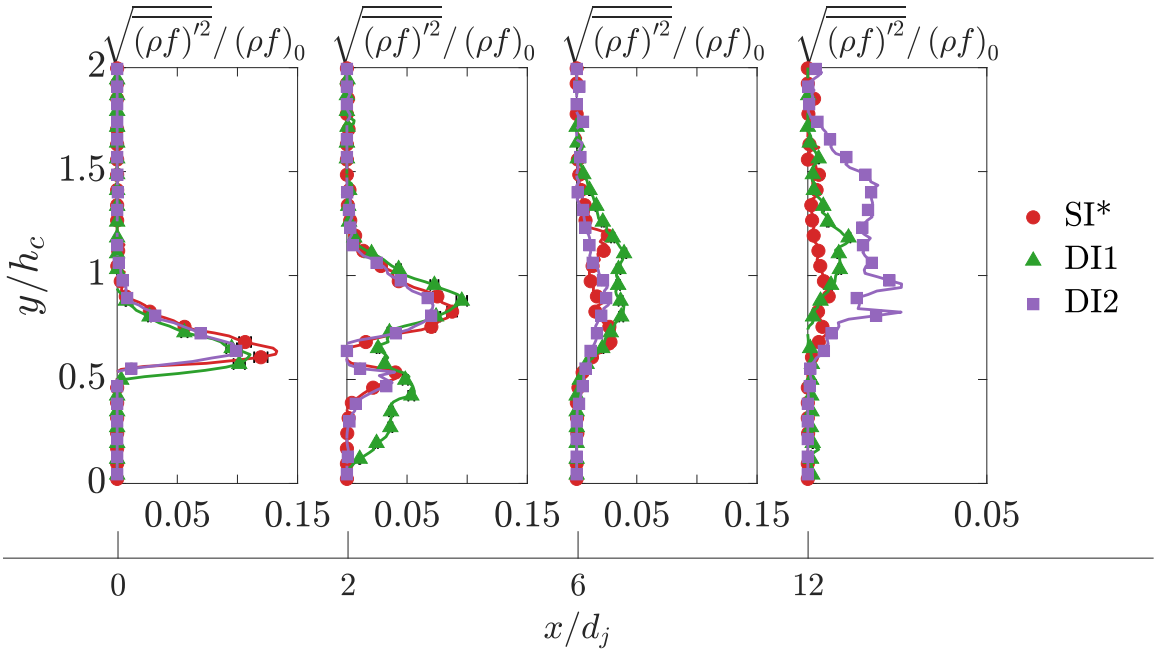

(b) Single and staged jet injectors SI*, DI1, and DI2.

Figure 6.10: RMS jet fluid signals along vertical profiles for ethylene injection at $J = 4$.

6.1.2.2 *Velocity Fields*

Complementary to the jet fluid signals, velocity field data is discussed below. The two single jet injectors SI and SI* in 6.11 and 6.12 have qualitatively very similar velocity fields. Interestingly, the transverse extend of the masked low-seeding density region is smaller for the smaller d_j case, again hinting at an increase in mixing due to the changing jet orifice diameter relative to the rest of the flow system. The tractory based on normalized jet fluid signal penetrates deeply into the crossflow beyond the point of highly elevated velocity fluctuations. Unfortunately, deterioration of the test section windows lead to an artificial increase in the velocity fluctuations detected by the PIV diagnostic, which is especially in flow regions downstream and above the jet influenced regions. This fact will be considered in the following data interpretation and the uncertainty estimate.

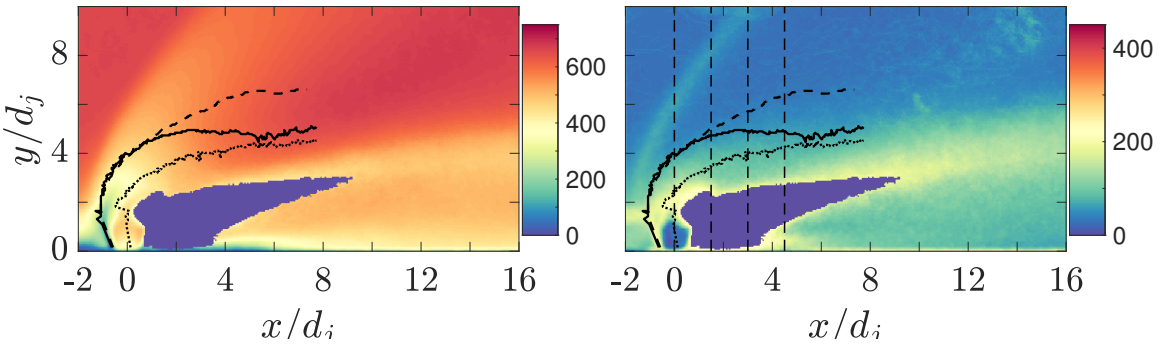

Figure 6.11: Mean and RMS velocity field for the SI-jet at $J = 4$. Dotted line: max. jet fluid signal location. Solid line: 0.02 contour. Dashed line: normalized 0.1 contour. Vertical dashed lines: locations of data extraction for y-profiles comparing the $d_j = 2$ mm injectors.

Comparing the DI1 injector velocity field in Fig. 6.13 with the SI* injector field in Fig. 6.12 one can immediately notice the increased low velocity regions and the increased penetration of velocity fluctuations into the cross flow. The second jet in Fig. 6.13 appears to expand more and penetrate deeper than the first jet due to the flow blockage of the latter. The shape of the bow shock, qualitatively, is not changed significantly but appears more well-defined. A very low speed region exists between the two jets with high RMS velocity values.

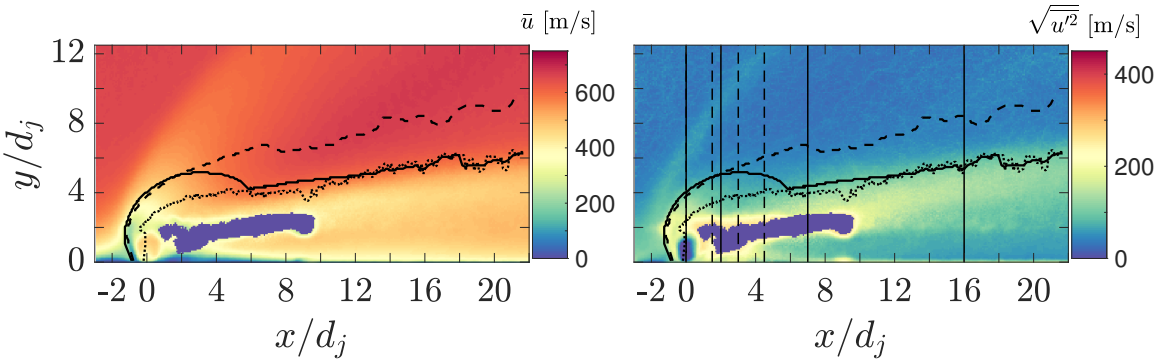

Figure 6.12: Mean and RMS velocity field for the SI*-jet at $J = 4$. Dotted line: max. jet fluid signal location. Solid line: 0.02 contour. Dashed line: normalized 0.1 contour. Vertical dashed lines: locations of data extraction for y-profiles comparing the $d_j = 2$ mm injectors. Vertical solid lines: locations of data extraction for y-profiles comparing the $d_j = 1.41$ mm injectors.

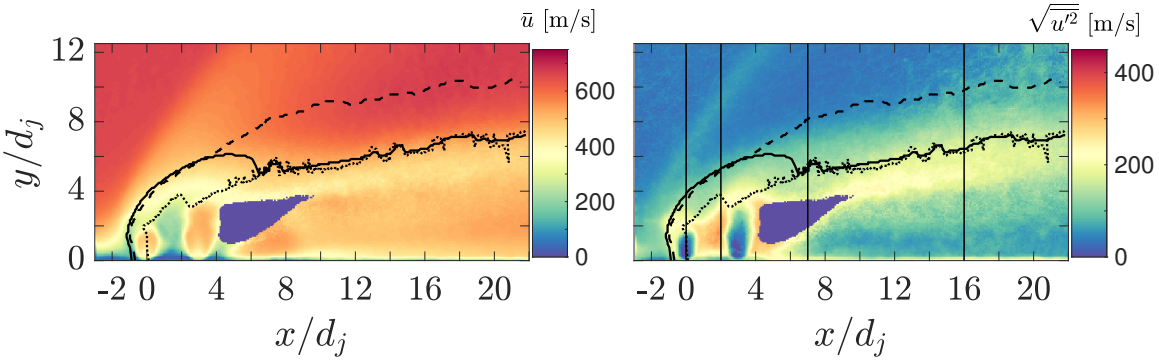

Figure 6.13: Mean and RMS velocity field for the DI1-jets at $J = 4$. Dotted line: max. jet fluid signal location. Solid line: 0.02 contour. Dashed line: normalized 0.1 contour. Vertical solid lines: locations of data extraction for y-profiles comparing the $d_j = 1.41$ mm injectors.

The expansion and penetration of the second jet of the DI2 injector in Fig. 6.14 is further increased over the DI1 case. Corroborating the observation that with the current configuration the larger distance between the two jets allows the second jet to "profit" more from the first jet's flow blockage. An extended low speed, high RMS region between the two jets exists that could allow the two jets to influence each other. The existence of two bow shocks, one ahead of the first jet, and one originating at the second jet suggests that the increased separation between the jets leads to a different interaction regime between the jets compared to the DI1 injector.

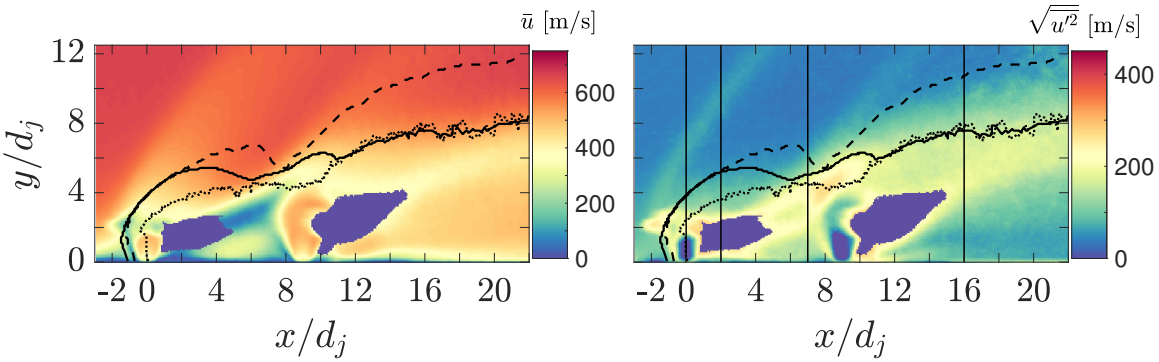

Figure 6.14: Mean and RMS velocity field for the DI2-jets at $J = 4$. Dotted line: max. jet fluid signal location. Solid line: 0.02 contour. Dashed line: normalized 0.1 contour. Vertical solid lines: locations of data extraction for y-profiles comparing the $d_j = 1.41$ mm injectors.

RMS velocity profiles of the single jet injectors along the absolute 0.02 contour trajectory are compared in Fig. 6.15a. For the SI injector two data sets are available, one with a zoomed in FOV of 25 mm×21 mm (SIin) and one further zoomed out with 38 mm×32 mm (SIout). The agreement between the single injector cases is overall good, the largest disagreement occurring downstream of $\hat{s} = 3$. The elevated RMS values in the SI* case beyond $\hat{s} = 3$are most likely the result of the deteriorating window quality because at that point any additional influence of the boundary layer should be relatively weak.

The trends of single and staged injectors with $d_j = 1.41$ mm in Fig. 6.15b support the observations made for the jet fluid signal field in Fig. 6.9b. Closer to the injector the RMS values along the 0.02 jet trajectory agree, with the staged injectors trending slightly higher than the single injector at the peak. The peak itself occurs earlier than in the mixing cases around $\hat{s} = 0.5$ vs. $\hat{s} = 1.5$.

Downstream of the peak, the DI1 case deviates the earliest from the other two cases with elevated RMS velocities. Then, around $\hat{s} = 3$, the velocity fluctuations of the DI2 case start rising above the other two cases, due to the presence of the second jet, before converging towards the RMS values of the DI1 case. The latter point again suggests that the spacing of the two injectors can control the distribution of the fluctuation intensity and its peak values but eventually results in the same far field state. What is clearer in the

velocity field, though, is the overall elevated fluctuation intensity for the staged injectors within the FOV recorded.

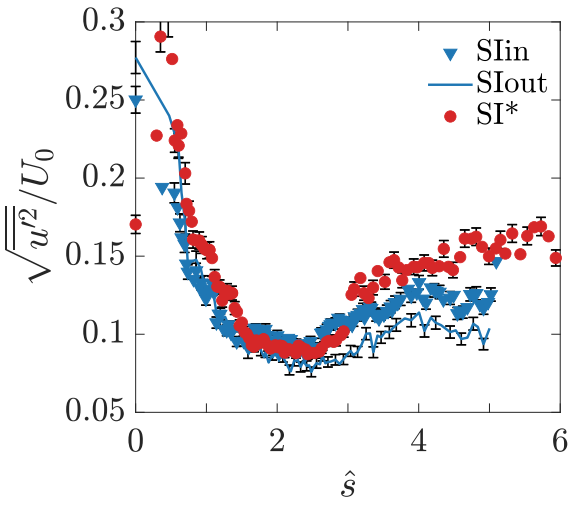

(a) Comparison between $d_j = 2$ mm and 1.41 mm single injectors. SIin refers to the zoomed in FOV, SIout to the zoomed out FOV.

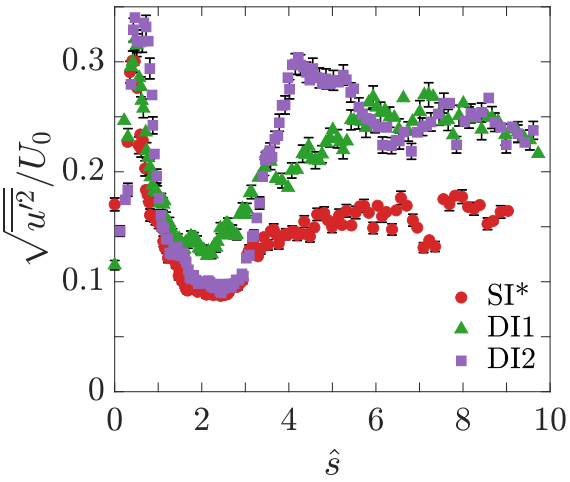

(b) Comparison between single and staged injectors with $d_j = 1.41$ mm.

Figure 6.15: RMS velocity evolution along the 2% jet fluid signal contour. In all cases the injectant is ethylene at $J = 4$.

Looking at the vertical RMS velocity profiles of the SI and SI* injectors in Fig. 6.16a it appears that the velocity field is less influenced by the change of the jet diameter than the jet fluid signal field in Fig. 6.10a. However, due to the missing data in the jet wake it is hard to make a conclusive statement in this case. An interesting difference between SIin and SIout can be observed at the $x/d_j = 0$ station, where the SIin RMS velocity values start to increase at a higher location than the SIout value, before merging with the other two single injector cases. The only explanations available for this behavior at this points are small differences in repeated experiments or resolution effects, as the vector resolution drops from 0.16 mm to 0.24 mm for SIin and SIout, respectively.

The comparison of single and staged injectors in Fig. 6.16b again shows good agreement close to the injector orifice of the first jet, i.e. at $x/d_j = 0$. Moreover throughout all transverse profile locations the SI and SI* data largely agree with each other.

At $x/d_j = 2$, just before the second jet of the DI1 injector, the second jet helps to

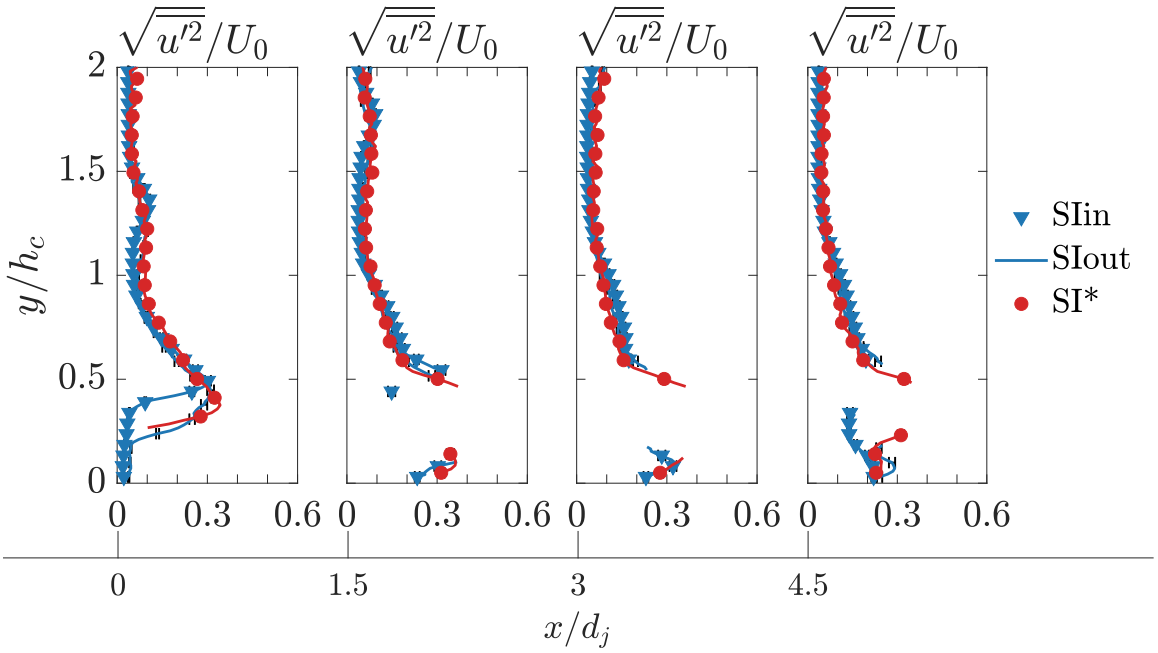

(a) Single jet injectors SI and SI*.

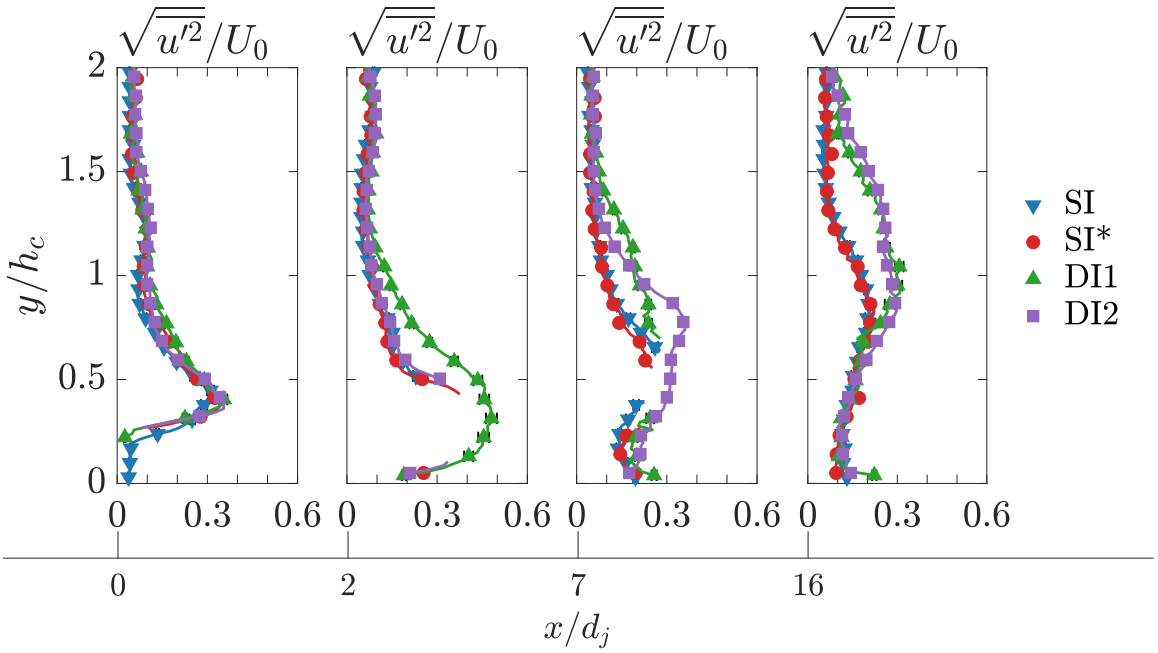

(b) Single and staged jet injectors SI*, DI1, and DI2.

Figure 6.16: Velocity RMS values along vertical profiles for ethylene injection at $J = 4$.

avoid a low seeding density region in the DI1 case. Furthermore, the RMS profiles show that the second DI1 jet also appears to enhance velocity fluctuations over the SI* and DI2 cases. Just ahead of the second jet of the DI2 injector, at $x/d_j = 7$, the RMS velocities

of the DI2 case are growing larger than for the other two cases up to $y/h_c \approx 1.25$, above which higher fluctuations are sustained for the DI1 case. The final profile at $x/d_j = 16$, far downstream of any secondary jet, further exemplifies the convergence towards a far field state dependent on the number of injectors, but not on the jet diameter or spacing between the jets.

6.2 OH-PLIF Measurements

To address the initiation and enhancement of burning in a relatively cold JISCF system, a laser spark is introduced into the flow field using LIP ignition. Promising locations for laser energy deposition are identified in Ch. 5 and the subsequent evolution of the ignition kernel and potentially burning regions is evaluated in more detail here with OH-PLIF to visualize regions containing hot products. Ensembles of OH-PLIF data are collected at three time delays from laser energy deposition: 19, 27, and 35 µs. In some cases data is only collected for 19 and 35 µs.

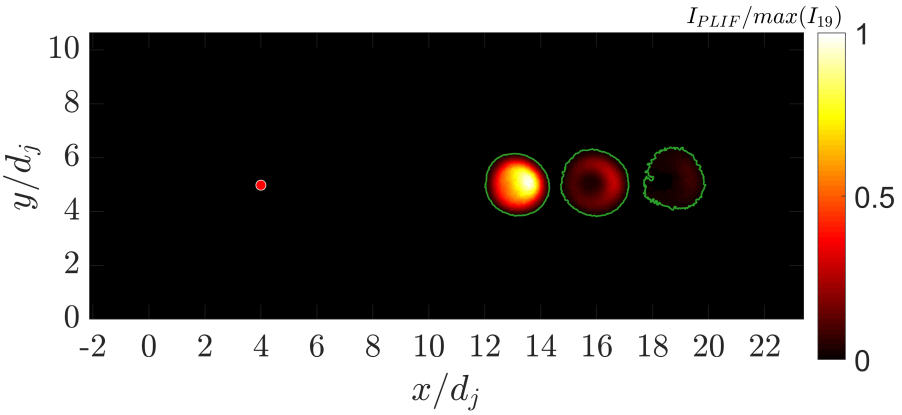

Figure 6.17: Mean reference OH-PLIF signal taken in the crossflow without any jet or fuel added. Time of recordings after laser energy deposition: 19, 27 and 35 µs. The laser spark point is denoted by a red dot at (4,5), with positions $(x/d_j, y/d_j)$ given relative to the first jet orifice center and $d_j = 2$ mm. The signal is normalized to the maximum intensity at the first time delay to emphasize the decay of the plasma kernel. Green lines indicate the contour found by the edge-detection algorithm used. For all PLIF recordings shown in this chapter the same colormap is used but normalization differs as described in each case.

As with CH* chemiluminescence, the PLIF recordings are influenced by the laser

plasma broadband emissions. In the following discussions, when OH fluorescence is mentioned, it does not automatically imply that the recorded signal necessarily comes from OH molecules but rather that a signal is recorded that makes it through the utilized OH-PLIF bandpass filter. The OH-PLIF gating time is shorter and the band-pass filter is slightly narrower than in the CH* case, i.e. the influence is going to be lower. Nonetheless, all results will be interpreted relative to the signal recorded for a non-burning reference case.

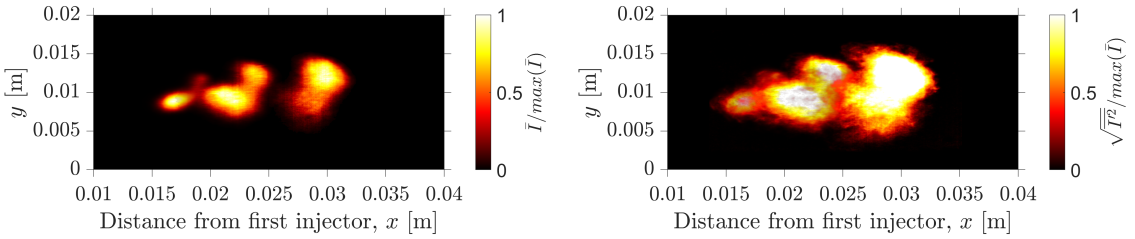

(a) Mean OH-PLIF signal.

(b) RMS OH-PLIF signal

Figure 6.18: Statistics of the PLIF records for injector DI2 with LIP sparking at ID 2. Normalization is achieved with the maximum intensity of the mean at each time delay

The mean signal of the reference case is presented in Fig. 6.17. Although the schlieren results in Fig. 3.10 showed no more visible plasma signal after 14 µs the OH-PLIF system still picks up on the existence of the hot plasma region at times > 19 µs. This is most likely due to longer recombination times at lower densities during supersonic tunnel operation. Recording the reference case without turning the PLIF laser on results in a weaker absolute signal, suggesting that the UV laser sheet is exciting exciting some molecules in the hot gases of the laser plasma. Over the time interval investigated here the plasma emissions decay significantly. At 27 µs after energy deposition the donut shape characteristic of the expanding hot gas region of laser induced plasmas can be discerned (Bradley *et al.*, 2004). The PLIF active regions move in a straight line from the ignition point, as would be expected for the undisturbed crossflow.

The the line-of-sight averaged CH*-chemiluminescence measurements showed that ignition and potential burning events are relatively repeatable, see Sec. 3.3.3. On the other hand, the planar OH-PLIF measurements clarify the highly three-dimensional nature of the

JISCF flow field and associated chemical reactions. The mean and RMS of a representative OH-PLIF record are shown in Fig. 6.18a and Fig. 6.18b, respectively. In contrast to the CH* results, the OH-PLIF RMS signal has a higher intensity count than the mean signal at all times. The difference increases with time from the LIP spark event. Thus, a large amount out-of-plane motion is probably taking place and thermal energy release regions are very intermittent and spatially distributed. The latter is to be expected in a JISCF flow field below auto-ignition conditions due to the occurrence of high aerodynamic strain.

This part of the dissertation introduces ignition attempts in the flow field of staged injectors. While larger flow strain peaks are expected, the enhanced turbulent mixing of staged jets (see preceding sections) should provide more favorable conditions for burning than the single injector. The modified flow history in the case of staged injectors might also have a positive impact on the development of the ignition kernel with regard to growth and burning rate. A dependence of the OH-PLIF statistics on the jet spacing it expected.

6.2.1 Positioning in the Jet Fluid Signal Field

In Fig. 6.19, the development of the ignition kernel in the SI* flow field is shown as a composite of OH-PLIF recordings and a representative jet fluid signal image. Laser energy is deposited at ignition ID 2. For both measurements, instantaneous recordings are chosen. The results in Ch. 5 indicate that, in this case, the instantaneous properties are probably more important than the time averaged properties. That is, the ignition kernel interacts with the instantaneous jet structures as it advects downstream to the point of measurement. The jet fluid signal colormap is truncated at 0.5 to make the downstream structures better visible.

It is important to note that these are example images from individual recordings. Jet fluid signal and OH-PLIF measurements are not conducted simultaneously and the PLIF results are from individual ensembles, not recorded during the same ignition event. Moreover, some of the OH-regions are slightly cut-off at the downstream border. This is because

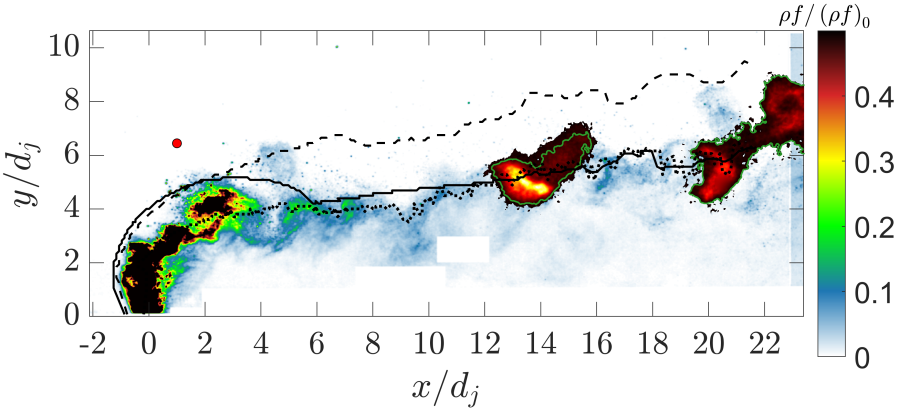

Figure 6.19: Composite image of instantaneous jet fluid signal field and instantaneous OH-PLIF signal for the SI* injector ($d_j = 1.41$ mm) using ethylene at $J = 4$. PLIF signals are recorded at 19 and 35 µs from ignition at ID 2, denoted by the red dot. The PLIF colormap is the same as in Fig. 6.17 with normalization by the maximum signal at the first time delay. Green lines indicate the contour found by the edge-detection algorithm used. Dotted line: max. jet fluid signal location. Solid line: 0.02 contour. Dashed line: normalized 0.1 contour.

the FOV in some cases is not large enough to cover the entirety of the most downstream occuring OH-PLIF emitting regions.

Because of the composite nature of the images, the jet fluid signal data does not reflect the impact that the laser spark deposition has on the flow field. Effects of the laser spark shock wave and subsequent gas expansion have not been characterized in this study.

Qualitatively, regions emitting OH-PLIF signals elongate in the transverse direction and tilt streamwise at the top, while parts nearer to the wall seem to trail behind. A similar trend has been observed using CH* chemiluminescence in Ch. 5. This tilt was mainly attributed to the velocity difference in the wall-normal direction where the gradient slowly shears the chemically active regions. The observations possible with the larger FOV also suggest that the orientation of the instantaneous windward jet structures could eventually align with the OH-PLIF emitting regions.

Stronger tilting of the large scale jet structures into the streamwise direction would agree with the observations made by Ben-Yakar *et al.* (2006) for jet in a much faster cross-flow. Whether this implies the possibility of non-premixed burning along the jet interface

is a question that requires further analysis. The OH fluorescing regions generally appear spatially distributed as opposed to filament- or layer-like. Thus, being more indicative of a form of premixed or partially premixed burning than non-premixed flamelets. However, the limited resolution might play a factor in this assessment as well.

The data in Fig. 6.19 shows the OH-signal becoming weaker at later times, although it does not disappear completely. The signal's center of mass seems to stay close to the maximum mean jet fluid signal trajectory which, at this point, has merged with the mean "0.02" contour. Instantaneously, of course, higher jet fluid signals are still possible up to around 10%.

Fig. 6.20 shows results for the same spark location using the SI injector with a larger jet diameter. Evidently, using the scaling developed in Ch. 4 the re-scaled ID 2 ignition location in Fig. 6.19 is not in the same place (in x/d_j space) relative to the different jet trajectories. This is a result of the previously discussed differences in jet fluid availability due to changes in the mass flow rate. The spark appearing to be closer to the jet for the SI case, it could be subject to higher strain rates. Jet fluid signal data downstream of $x/d_j = 8$ is not available for this case because the focus of this part of the study is on the new injectors and the corresponding velocity fields. The OH fluorescing regions appear slightly larger and more uniformly bright for the larger SI injector. Nonetheless, their centroid also stays close to the maximum mean jet fluid signal trajectory.

Moving to the DI1 injector in Fig. 6.21, several interesting differences to the SI* case can be observed. The OH-PLIF emitting regions appear strongly elongated in the wall-normal direction and much less tilted. The regions still follow the maximum jet fluid signal trajectory but instead of simply becoming dimmer, there seems to be a possibility for OH-PLIF emissions to increase again, indicating the presence of sustained chemical reactions.

The lack of tilt suggests that the velocity gradient in the wall-normal direction is not the only governing factor. The increase in mixing due to the second jet probably provides more premixed fuel regions that burn upon contact with the ignition kernel. However, the close

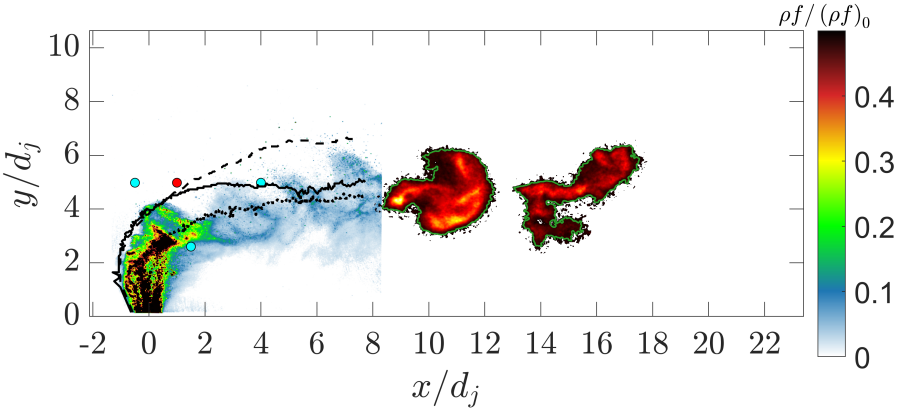

Figure 6.20: Composite image of instantaneous jet fluid signal field and instantaneous OH-PLIF signal for the SI injector ($d_j = 2$ mm) using ethylene at $J = 4$. PLIF signals are recorded at 19 and 35 µs from ignition at ID 2, denoted by the red dot. Other spark locations investigated for this configuration are indicated by turquoise dots. The PLIF colormap is the same as in Fig. 6.17 with normalization by the maximum signal at the first time delay. Green lines indicate the contour found by the edge-detection algorithm used. Dotted line: max. jet fluid signal location. Solid line: 0.02 contour. Dashed line: normalized 0.1 contour.

second jet can also result in more flow strain which would make the onset of non-premixed burning less likely (Lieuwen, 2012, chap. 9). Up to the times investigated, the significant near wall mixing region seems to have had no positive influence on the combustion process so far.

The influence of increased flow strain is also visible for the DI2 injector in 6.22. The OH signal appears more corrugated and the overall signal intensity lower, especially at the last time delay. The relative increase in tilt compared to DI1 at the earliest time suggests that, at this point in time, the mixing enhancement due to the presence of the second jet has had no significant impact yet.

The result for the ignition location identified in Ch. 5 as detrimental to sustained burning is shown in Fig. 6.23. Clearly, the ignition kernel has been torn up and the overall signal intensity is very low compared to the ID 2 cases discussed so far. A big factor is the strong aerodynamic strain directly at the spark location. It is likely responsible for the fast quenching and significant "shredding" of the ignition kernel as it advects downstream.

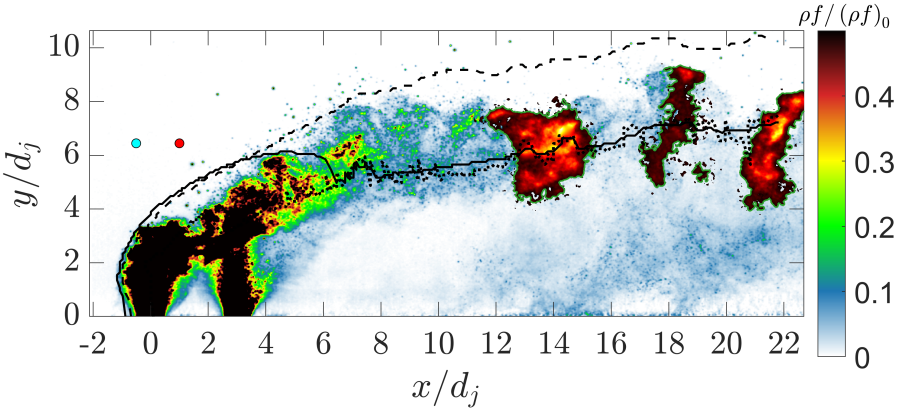

Figure 6.21: Composite image of instantaneous jet fluid signal field and instantaneous OH-PLIF signal for the DI1 injector using ethylene at $J = 4$. PLIF signals are recorded at 19, 27, and 35 µs from ignition at ID 2, denoted by the red dot. Other spark locations investigated for this configuration are indicated by a turquoise dot. The PLIF colormap is the same as in Fig. 6.17 with normalization by the maximum signal at the first time delay. Green lines indicate the contour found by the edge-detection algorithm used. Dotted line: max. jet fluid signal location. Solid line: 0.02 contour. Dashed line: normalized 0.1 contour.

6.2.2 Positioning in the Velocity Field

Considering the influence of the velocity field, Fig. 6.24 shows results for the SI* injector. Laser energy is deposited at ignition ID 2. The ensemble averaged velocity field is shown with the ensemble averaged OH-PLIF signals because the results in Ch. 5 point to two things. One, the mean velocity field having a strong influence on the average shape of regions containing hot combustion products. Two, whether chemical reactions are sustained depends strongly on the presence of flow expansion and compression in the path of the laser spark/ignition kernel.

It is important to note that the results presented here are ensemble averages from individual data acquisitions. Velocity and OH-PLIF measurements are not conducted simultaneously and the PLIF results are from individual data sets, not recorded during the same experimental run. The average OH-PLIF signal is normalized to a range from zero to one and interpreted as the likelihood for hot products to exist in a given region of the flow. One corresponding to a region in which strong PLIF signals are detected in the majority of

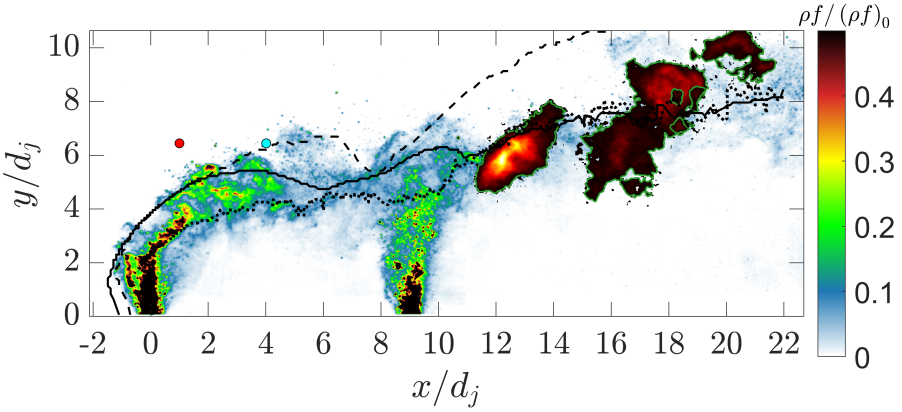

Figure 6.22: Composite image of instantaneous jet fluid signal field and instantaneous OH-PLIF signal for the DI2 injector using ethylene at $J = 4$. PLIF signals are recorded at 19, 27 and 35 µs from ignition at ID 2, denoted by the red dot. Other spark locations investigated for this configuration are indicated by a turquoise dot. The PLIF colormap is the same as in Fig. 6.17 with normalization by the maximum signal at the first time delay. Green lines indicate the contour found by the edge-detection algorithm used. Dotted line: max. jet fluid signal location. Solid line: 0.02 contour. Dashed line: normalized 0.1 contour.

samples, zero being a region in which no PLIF signal is detected at all. An alpha map is used in the composite images, such that a zero mean PLIF signal corresponds to complete transparency and a mean PLIF signal of one to complete opaqueness.

Clearly visible in Fig. 6.24 is the preferential alignment of the longer axis of the mean OH-PLIF regions with the mean flow direction. Presumably, this confirms that the evolution of chemically reacting regions is strongly influenced by the wall-normal velocity gradient. The velocity gradient is clearly discernible in the figure: the lower part of the average PLIF signal extends into a region with velocities around 500 $\mathrm{m/s}$ while the upper part reaches into areas moving at 600 $\mathrm{m/s}$ and above. On average, OH is more likely to be detected close to the maximum mean jet fluid signal trajectory, similar to the observation made in the instantaneous samples.

The corresponding results for the SI injector are shown in Fig. 6.25. The low speed regions in the vicinity and wake of the jet appear less pronounced than in the SI* case. This could lead to the slightly reduced tilt that is observed for the mean PLIF signal. Morever, the OH active regions exhibit a more pronounced bi-modal distribution at 35 µs.

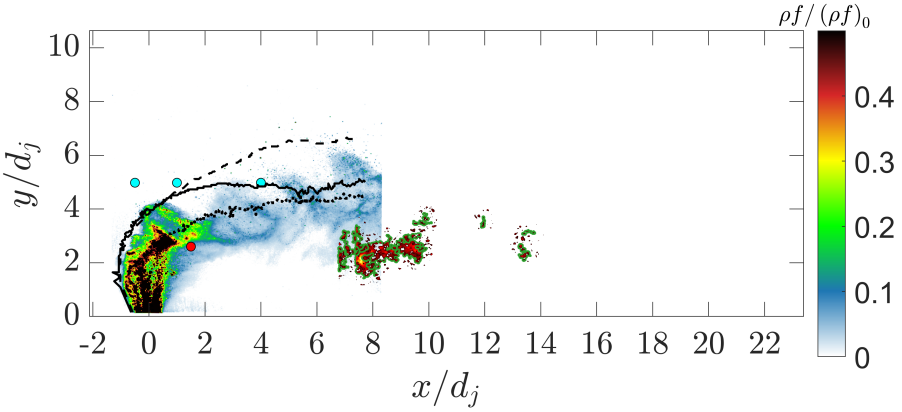

Figure 6.23: Composite image of instantaneous jet fluid signal field and instantaneous OH-PLIF signal for the SI injector ($d_j = 2$ mm) using ethylene at $J = 4$. PLIF signals are recorded at 19 and 35 µs from ignition at ID 4, denoted by the red dot. Other spark locations investigated for this configuration are indicated by turquoise dots. The PLIF colormap is the same as in Fig. 6.17 with normalization by the maximum signal at the first time delay. Green lines indicate the contour found by the edge-detection algorithm used. Dotted line: max. jet fluid signal location. Solid line: 0.02 contour. Dashed line: normalized 0.1 contour.

For the same configuration as in Fig. 6.24, Fig. 6.26 shows the mean two-dimensional divergence of the flow field. For the SI* injector, the ID 2 location puts the laser spark into a weakly compressive region after the bow shock, followed by an expansion. The measured OH signal itself falls mostly into compressive regions. In contrast, for the SI injector in 6.27, the ID 2 spark location appears to be positioned more towards the expansive region. Nonetheless, in both cases the measured mean OH-PLIF signal is confined mostly to compressive regions.

The first staged injector, DI1, yields the results in Fig. 6.28. As observed for the instantaneous results, the tilt of the mean OH regions is reduced in this case. Further downstream and at 35 µs after ignition, the spatial extent of hot products appears to be smaller than in the single injector case. What remains, though, is that the peak OH-PLIF signal favors locations around the maximum mean jet fluid signal trajectory.

Another similarity between the DI1 and the single jet injectors is the confinement of the mean OH signal to compressive regions in Fig. 6.29. In fact, it appears to be clearer that the regions exhibiting more thermal energy release grow laterally as the compressive

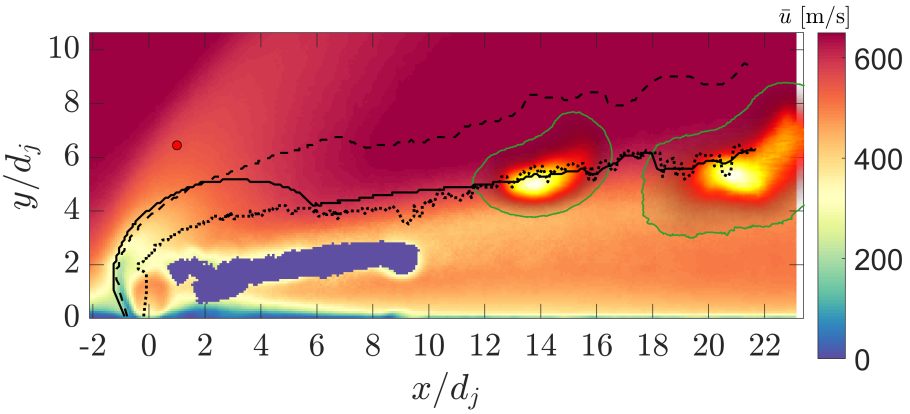

Figure 6.24: Composite image of the mean velocity field and the mean OH-PLIF signal for the SI* injector using ethylene at $J = 4$. PLIF signals are recorded at 19 and 35 µs from ignition at ID 2, denoted by the red dot. The PLIF colormap is the same as in Fig. 6.17 with normalization by the individual maximum signal at each time delay. Green lines indicate the contour found by the edge-detection algorithm used. Dotted line: max. jet fluid signal location. Solid line: 0.02 contour. Dashed line: normalized 0.1 contour.

region spreads, starting at $x/d_j \sim 9$. Given the flame speed limitations discussed in Ch. 5, this might not be the result of burning but rather stretching of the chemically active regions by the mean velocity field. Moreover, the second jet extends the region off influence of the bow shock, putting the spark location clearly in a compressive strain region.

The results in Fig. 6.30 show further changes in the average OH-PLIF signal for the DI2 injector. At 27 µs and 35 µs after energy deposition the regions over which OH-PLIF signals are measurable appear to be more extensive than for either the SI* or the DI1 case. Especially at 35 µs, the tilt is significantly reduced compared to the other two injector cases. Both of these observations suggest that mixing is enhanced and the chemically reacting regions are experiencing significantly increased flow strain after the secondary jet.

Interesting is also that the regions most likely to contain hot products shift from being situated below the maximum jet fluid signal trajectory to being situated above it. A trend that is most notable at 35 µs and that is also present, to a lesser degree, in the other injector configurations. Generally, the OH signal region's centroid is still situated close to the maximum mean jet fluid signal trajectory.

An additional observation for all injectors is that the OH fluorescing regions never seem

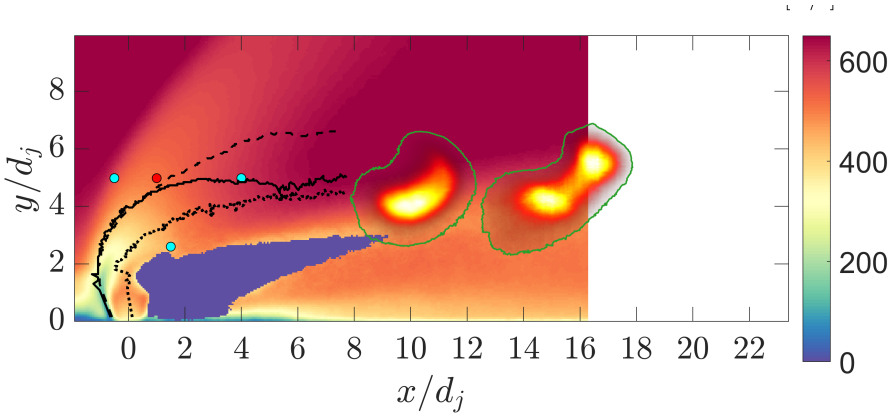

Figure 6.25: Composite image of the mean velocity field and the mean OH-PLIF signal for the SI injector using ethylene at $J = 4$. PLIF signals are recorded at 19 and 35 µs from ignition at ID 2, denoted by the red dot. Other spark locations investigated for this configuration are indicated by turquoise dots. The PLIF colormap is the same as in Fig. 6.17 with normalization by the individual maximum signal at each time delay. Green lines indicate the contour found by the edge-detection algorithm used. Dotted line: max. jet fluid signal location. Solid line: 0.02 contour. Dashed line: normalized 0.1 contour.

to extend beyond the normalized 10% jet fluid signal trajectory. While the 10% cut-off is somewhat arbitrary, one could argue that a trajectory defined in such a way, with a comparable cut-off, can be used to determine a-priori the maximum penetration of chemically reacting regions into the crossflow. However, with the available data this is somewhat speculative and further data is required to substantiate the claim.

The DI2 divergence field in Fig. 6.31 shows the second jet providing a further region of elevated compressive and expansive strain. As in the DI1 case, the OH signal regions are growing laterally into the expanding compressive strain region downstream of the second injector. It is also clearer that the locus of the strongest PLIF signal is moving towards regions of moderate compressive strain, away from peak values in the wake of the second jet around $y/d_j \sim 5 - 6$.

Ignition location ID 4 is shown in Fig. 6.32. It is a fast quenching region with very low signal intensity compared to the other cases. The hard cut-off on the left side of the figure showing the normalized mean signal is somewhat misleading as the results are strongly influenced by noise. The FOV does not actually cut-off individual realizations significantly

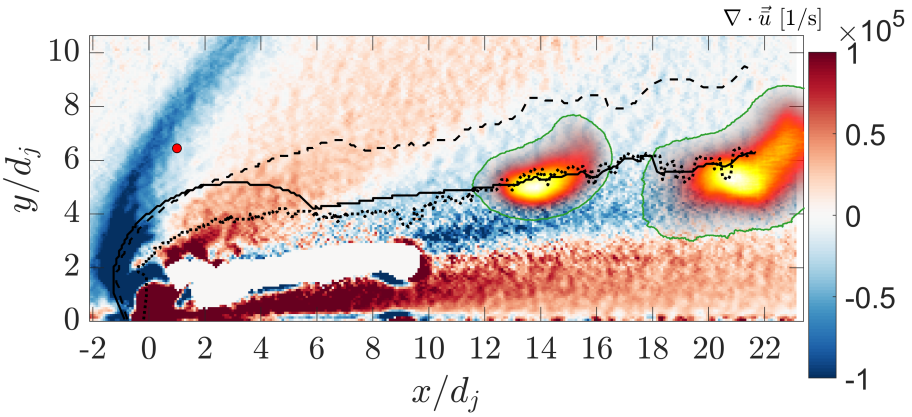

Figure 6.26: Composite image of the divergence field and the mean OH-PLIF signal for the SI* injector using ethylene at $J = 4$. PLIF signals are recorded at 19 and 35 µs from ignition at ID 2, denoted by the red dot. The PLIF colormap is the same as in Fig. 6.17 with normalization by the individual maximum signal at each time delay. Green lines indicate the contour found by the edge-detection algorithm used. Dotted line: max. jet fluid signal location. Solid line: 0.02 contour. Dashed line: normalized 0.1 contour.

at the edge of the image. Unfortunately, the relevant velocity data is incomplete for the flow region pertaining to spark initiation at ID 4. However, from Fig. 6.33 it is very likely that the spark and ignition kernel experience high expansive strain rates.The results clarify that ignition at ID 4, close to a very high flow strain region and high expansive strains, is detrimental to sustaining chemical reactions. It leads to a rapid loss of the hot spark plasma. This observation corroborates the importance of flow strain on the evolution of an ignition kernel as it advects downstream.

The remaining ignition locations ID 1 and ID 3 exhibit similar qualitative behavior as the data presented for ID 2. They all lie on the windward side of the jet shear layer and differ in details such as emission intensity and growth of the hot product containing regions. Therefore, they are not presented individually but statistical properties for all cases investigated will be analyzed in the following section.

6.2.3 Statistics of OH-active Regions

To investigate further, whether any of the ignition locations and injector configurations actually lead to enhanced burning, statistical trends for the extent of OH fluorescing regions

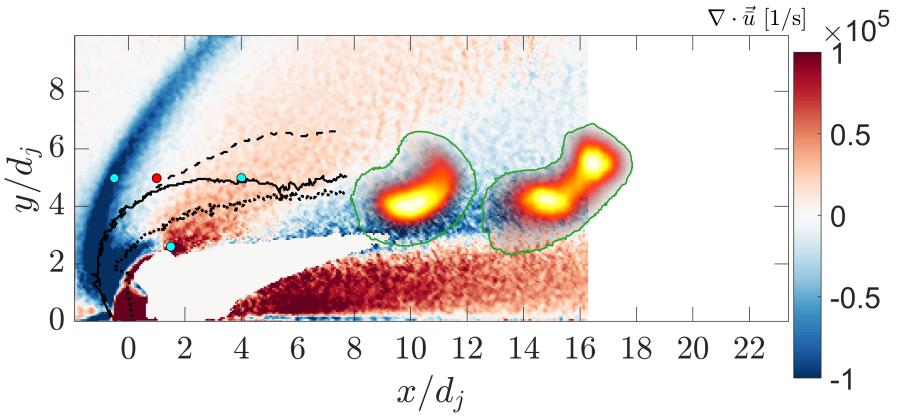

Figure 6.27: Composite image of the divergence field and the mean OH-PLIF signal for the SI injector using ethylene at $J = 4$. PLIF signals are recorded at 19 and 35 µs from ignition at ID 2, denoted by the red dot. Other spark locations investigated for this configuration are indicated by turquoise dots. The PLIF colormap is the same as in Fig. 6.17 with normalization by the individual maximum signal at each time delay. Green lines indicate the contour found by the edge-detection algorithm used. Dotted line: max. jet fluid signal location. Solid line: 0.02 contour. Dashed line: normalized 0.1 contour.

and their signal intensity are investigated.

The instantaneous area of the OH-PLIF signal is found using the approach described in Sec. 3.3.4. After the edge of the OH fluorescence is found, the area of the interior pixels is calculated. Then, the average area of the region, $\bar{A}$ is calculated for each individual data set. An example of instantaneous areas for one data set is shown in Fig. 6.34a. Due to the highly three-dimensional nature of the flow field the fluctuations are rather large.

The signal intensity is quantified in terms of the integrated intensity. The integrated intensity is calculated for each instantaneous OH-PLIF record and then averaged to get $\overline{\sum I}$. An example of an integrated intensity record is shown in Fig. 6.34b.

The standard deviation of $\bar{A}$ and $\overline{\sum I}$ as well as the variation in deposited ignition energy (see Sec. 3.2) are considered in the uncertainty estimate. More details about the computation of confidence intervals for this section can be found in C.

Results for the change in area of the OH-PLIF signal are presented in Fig. 6.35. The computed average area is normalized by the corresponding non-reacting reference value, see Fig. 6.17. Therefore, a value of $\bar{A}/\bar{A}_{ref} < 1$ means that the average fluorescing area of

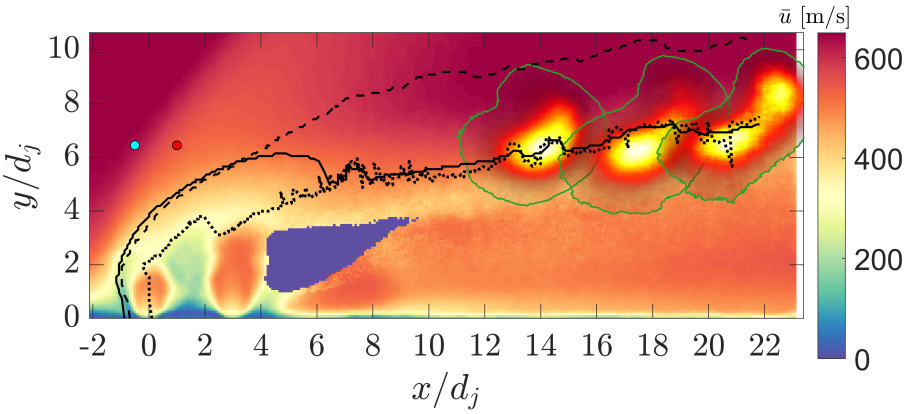

Figure 6.28: Composite image of the mean velocity field and the mean OH-PLIF signal for the DI1 injector using ethylene at $J = 4$. PLIF signals are recorded at 19, 27, and 35 µs from ignition at ID 2, denoted by the red dot. Other spark locations investigated for this configuration are indicated by a turquoise dot. The PLIF colormap is the same as in Fig. 6.17 with normalization by the individual maximum signal at each time delay. Green lines indicate the contour found by the edge-detection algorithm used. Dotted line: max. jet fluid signal location. Solid line: 0.02 contour. Dashed line: normalized 0.1 contour.

a data set is lower than that of the reference case at the same time after ignition.

Several investigated configurations probably do not lead to any sustained chemical reactions, quenching the spark or ignition kernel soon after energy deposition. For ignition at ID 4 using the SI injector this is actually expected and further confirms some of the trends identified in the initial investigation, see Ch. 5.

Generally, Fig. 6.35 shows that more promising ignition locations are further downstream of the jet orifices, see the ordering of symbols at 19 µs. For a given injector, laser energy deposition further downstream consistently yields greater area growth. This supports the notion that the very high strain rates in the JISCF flow field are detrimental to burning. Additionally, it also supports the previous claim that the dominant burning mode is premixed. The formation of flammable mixtures at the molecular level takes some time and the flow conditions are not able to support non-premixed burning. That is, in the present experiments, the diffusive and convective processes outweigh the thermal energy release due to chemical reactions significantly for the non-premixed case.

The staged injector with little separation between the jets, DI1, overall performs the

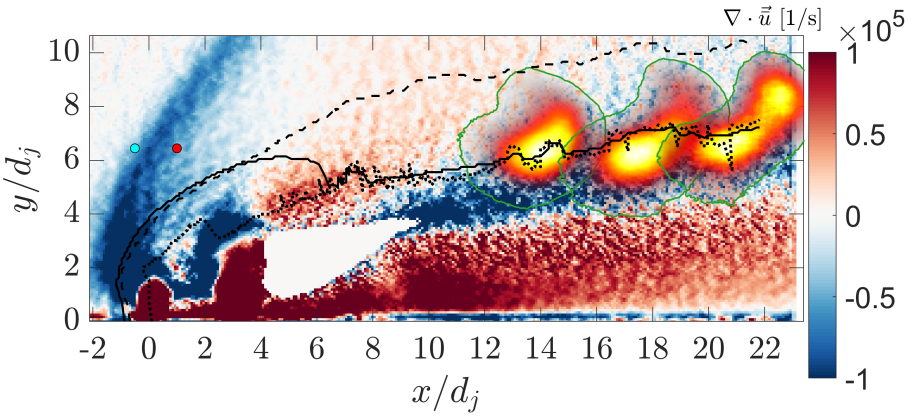

Figure 6.29: Composite image of the divergence field and the mean OH-PLIF signal for the DI1 injector using ethylene at $J = 4$. PLIF signals are recorded at 19, 27 and 35 µs from ignition at ID 2, denoted by the red dot. Other spark locations investigated for this configuration are indicated by a turquoise dot. The PLIF colormap is the same as in Fig. 6.17 with normalization by the individual maximum signal at each time delay. Green lines indicate the contour found by the edge-detection algorithm used. Dotted line: max. jet fluid signal location. Solid line: 0.02 contour. Dashed line: normalized 0.1 contour.

worst. In most cases even worse than the single jet injector SI and only slightly better at 35 µs for ignition at ID 2.

DI2 performs slightly better with the best setup being ignition further downstream of the first jet, i.e. at ID 3. It presumably provides larger $\bar{A}/\bar{A}_{ref}$ values due to the ignition kernels being initiated in regions of lower strain/shear than in the case of the DI1 injector. However, a look at 6.31 shows that might not necessarily be true. Surprisingly, for ignition at ID 2 the area growth at 35 µs is smaller than for ignition at ID 1 using the SI injector. Further analysis is required to explain some of these trends.

The most unexpected result is that the smaller diameter, single jet injector SI* outperforms every other configuration at the latest time recorded. With the spark location used, ID 2, the OH fluorescing region is initially (19 µs) slightly smaller than that of the reference case and about half the size of the larger diameter SI measurement. In fact, the difference in area between SI* and SI corresponds roughly to the difference in area between the to injectors, $A_{SI*} = 0.5A_{SI}$. However, at the latest time the area of the SI* case is about three times larger than that of the SI case and almost four times larger than that of the reference

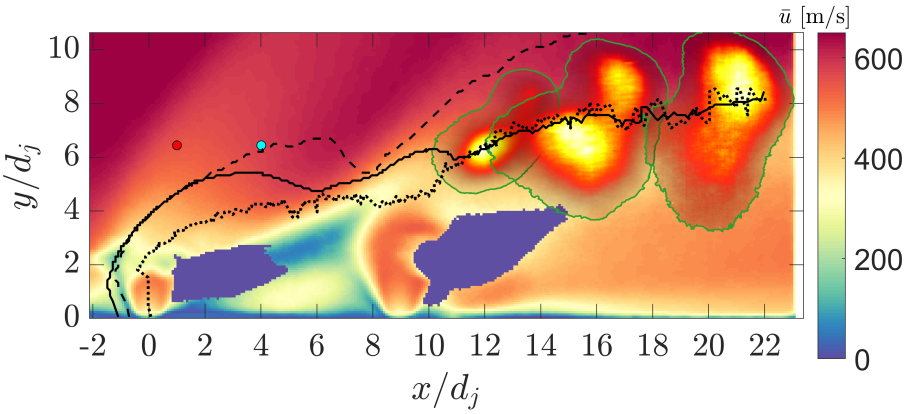

Figure 6.30: Composite image of the mean velocity field and the mean OH-PLIF signal for the DI2 injector using ethylene at $J = 4$. PLIF signals are recorded at 19, 27, and 35 µs from ignition at ID 2, denoted by the red dot. Other spark locations investigated for this configuration are indicated by a turquoise dot. The PLIF colormap is the same as in Fig. 6.17 with normalization by the individual maximum signal at each time delay. Green lines indicate the contour found by the edge-detection algorithm used. Dotted line: max. jet fluid signal location. Solid line: 0.02 contour. Dashed line: normalized 0.1 contour.

case.

A possible explanation may be found in the trends observed for the non-reacting jet fluid signal and velocity fields. As described earlier, the SI* jet seems to interact more strongly with the boundary layer structures, resulting in enhanced jet fluid signal fluctuations over the SI case, see Fig. 6.10a. At the same time though, the velocity fluctuations remain at similar values, see 6.16a. Thus, the SI* jet potentially provides an environment with a comparatively higher amount of premixed fuel-oxidizer in the far field without imposing additional flow strain, as the staged injectors would do. However, considering the limited growth of a deflagration at the considered time scales, the reason for the large area is probably also connected to the wall normal velocity gradient stretching the ignition kernel more in the SI* case. Because the SI* case was intended purely as a reference case between injector diameters and this result is somewhat unexpected, only the two presented data points are available at this point in time.

One final interesting feature is the sudden increase in area of the SI case ignited at ID 1. Fig. 6.27 and Fig. 6.29 show that a possible explanation might lie with the ignition location.

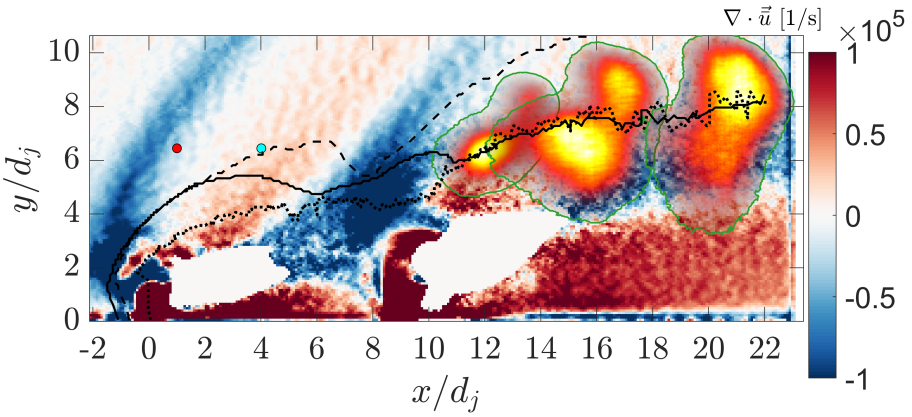

Figure 6.31: Composite image of the divergence field and the mean OH-PLIF signal for the DI2 injector using ethylene at $J = 4$. PLIF signals are recorded at 19, 27 and 35 µs from ignition at ID 2, denoted by the red dot. Other spark locations investigated for this configuration are indicated by a turquoise dot. The PLIF colormap is the same as in Fig. 6.17 with normalization by the individual maximum signal at each time delay. Green lines indicate the contour found by the edge-detection algorithm used. Dotted line: max. jet fluid signal location. Solid line: 0.02 contour. Dashed line: normalized 0.1 contour.

For the smaller diameter jets, the spark at ID 1 is forced to traverse the entirety of the extended bow shock, while for the single, larger jet the spark is initiated right after the bow shock and probably experiences less extreme compressive strain values, thus expanding more with the flow.

In Fig. 6.36 the mean integrated PLIF signal is plotted against the time from laser spark deposition. This data confirms that the configurations SI-ID 4 and DI1-ID 1 are the worst performing ones. Moreover, it confirms that ignition further away from the jet orifice along the windward shear layer seems to be overall beneficial. Several cases exhibit both significant area and integrated intensity increase relative to the reference cases over time, see SI*-ID 2 and DI2-ID 3. This suggests that at least for those cases some form of chemical to thermal energy release reaction continues to occur.

Coming back to case SI-ID 1, the integrated intensity exposes that the significant area increase in Fig. 6.35 is probably not a sign of increased thermal energy release. Instead, it is more likely a manifestation of straining and stretching of the initial ignition kernel only.

To summarize, using the growth of OH-PLIF emitting areas and the integrated PLIF

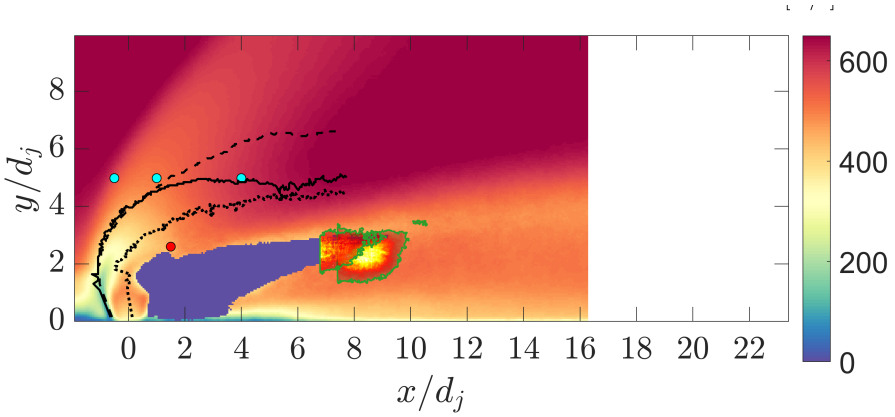

Figure 6.32: Composite image of the mean velocity field and the mean OH-PLIF signal for the SI injector using ethylene at $J = 4$. PLIF signals are recorded at 19 and 35 µs from ignition at ID 4, denoted by the red dot. Other spark locations investigated for this configuration are indicated by turquoise dots. The PLIF colormap is the same as in Fig. 6.17 with normalization by the individual maximum signal at each time delay. Green lines indicate the contour found by the edge-detection algorithm used. Dotted line: max. jet fluid signal location. Solid line: 0.02 contour. Dashed line: normalized 0.1 contour.

signal intensity as criteria, the two best performing injector designs are SI* and DI2. Presumably, both provide an enhanced mixing environment and relatively low or more distributed flow strain. The SI* injector through increased interaction with the boundary layer and by virtue of being a single injector. The DI2 injector through the more optimized interaction between the two jets and the larger separation between the jets. The latter point avoiding one single region of highly concentrated strain as opposed to the DI1 injector.

6.2.4 Orientation of OH-active Regions

To better understand the interaction between the plasma kernel and the flow field, the orientation and eccentricity of the averaged OH-PLIF signals are evaluated. The shape of the averaged fluorescing regions is treated approximately as an ellipse for this purpose, see Fig. 3.24b for an example of the data processing.

From the implicit equation for a conical section, Eq. (3.17), the angle between the

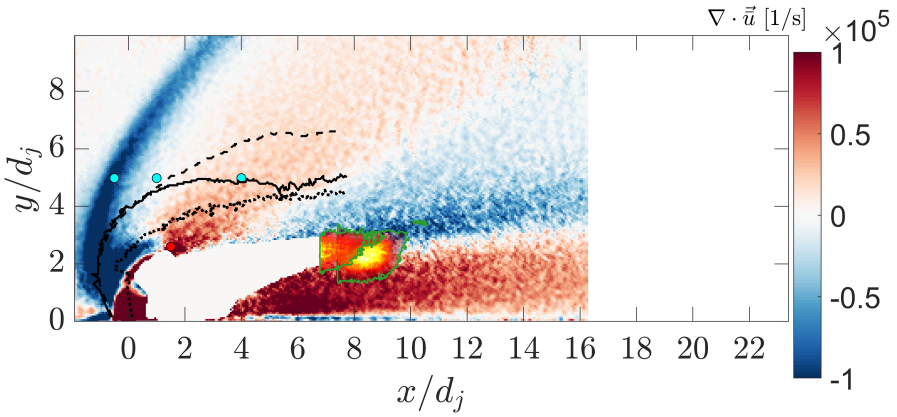

Figure 6.33: Composite image of the divergence field and the mean OH-PLIF signal for the SI injector using ethylene at $J = 4$. PLIF signals are recorded at 19 and 35 µs from ignition at ID 4, denoted by the red dot. Other spark locations investigated for this configuration are indicated by turquoise dots. The PLIF colormap is the same as in Fig. 6.17 with normalization by the individual maximum signal at each time delay. Green lines indicate the contour found by the edge-detection algorithm used. Dotted line: max. jet fluid signal location. Solid line: 0.02 contour. Dashed line: normalized 0.1 contour.

horizontal x-axis and the semi-major axis can be determined as,

$$\theta = \arctan\left(\frac{C - A - \sqrt{(A-C)^2 + B^2}}{B}\right), \tag{6.1}$$

which yields a measure of the orientation. The eccentricity can be computed from the semi-minor, b, and semi-major axis, a, as,

$$\varepsilon = \sqrt{1 - \left(\frac{b}{a}\right)^2}. \tag{6.2}$$

The orientation in terms of θ is shown in Fig. 6.37. The most significant trend, over the time observed, is that all single injector cases, i.e. injectors SI and SI*, start and stay at relatively low angles, $\sim 15° - 60°$. As time goes by the stretched and tilted reacting regions tend to align at an angle of roughly $\theta = 30°$, as exemplified by the results in Fig. 6.24. Interestingly, this angle corresponds to the vortex line orientation in the far field of an incompressible JICF at $J = 4$, as reported by Sykes *et al.* (1986) and Hasselbrink and Mungal (2001a). Since the far field of a JISCF is not that different from an incompressible

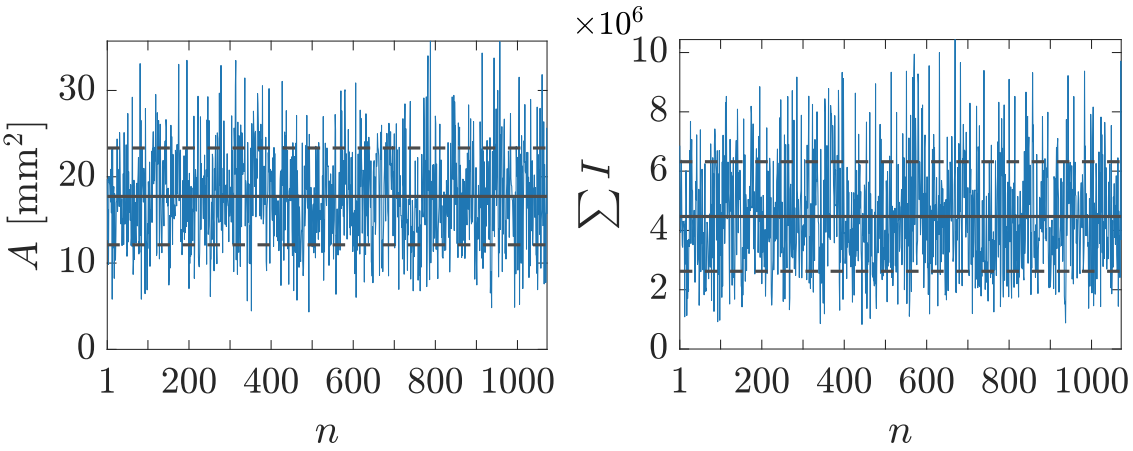

(a) Sample record of instantaneous areas detected via edge finding.

(b) Sample record of instantaneous integrated intensities.

Figure 6.34: Representative examples of instantaneous area and integrated intensity for one data set. Horizontal full line: mean value. Horizontal dashed lines: $\pm 1 \cdot \sigma$.

JICF, the advected reacting regions could be aligning with the dominant vortex structures.

Both DI2 cases have an initial preferential alignment with the crossflow direction but then experience a rotation, propagation or stretching in the transverse direction, orienting the semi-major axis at almost $90°$ to the crossflow direction. Given the different distances from the second jet at which ID 2 and ID 3 are igniting, and the difference in the shift of their corresponding cases' orientation, this change is probably a result of three things acting together. One is that the mean flow velocity gradient in the y-direction in the wake of the jet is weakening with downstream distance. Two, the vortex line orientation is probably disturbed significantly by the second jet. And three, the second jet probably accelerates the lower part of the ignition kernel for a limited amount of time, reducing the tilt. Given the differences in the physical ignition and jet locations it is also possible that the orientation of the DI2 cases will converge back towards that of the other cases further downstream, if the reactions do not cease entirely before that.

The average reacting regions for both SI-ID 1 and DI1-ID 1 exhibit a major change in their orientation. At 19 µs they have a relatively high tilt angle. In fact, in the DI1-ID 1 case the ellipse is leaning against the flow. At later times, however, the orientation changes

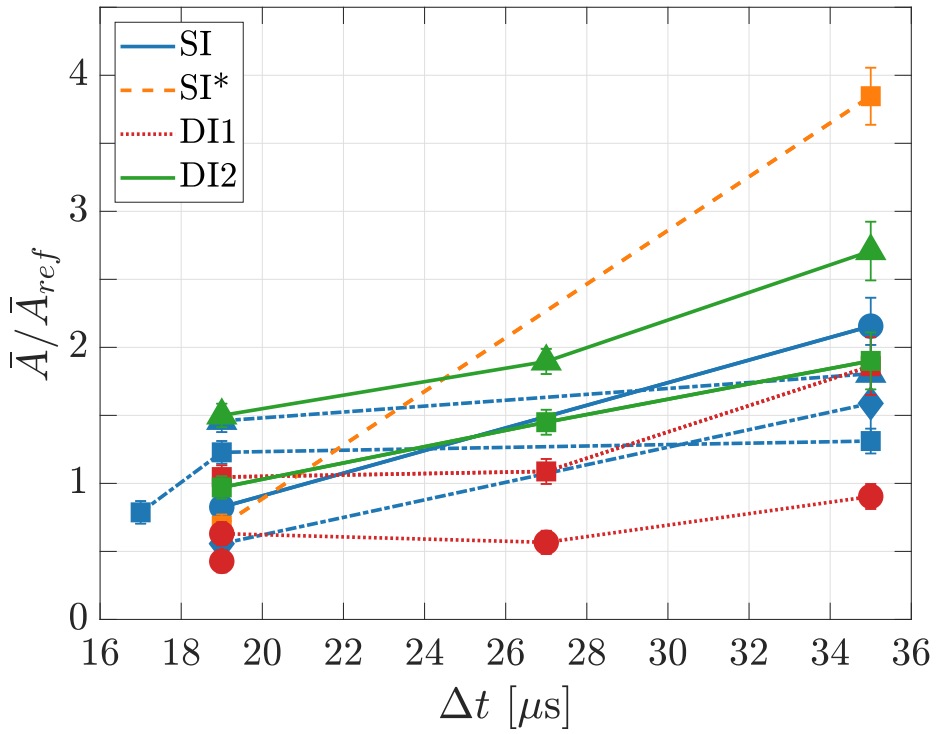

Figure 6.35: Evolution of the mean area of the OH-PLIF signal as a function of time from laser energy deposition. Ignition locations: • =ID 1, ■ =ID 2, ▲ =ID 3, ♦ =ID 4. 95% confidence intervals are shown.

such that the structures preferentially align their elongated axis with the crossflow direction. Given the actual ignition locations, the initially higher angle can probably be attributed at least partly to a stronger influence of the vertical jet velocity component. In the case of DI1-ID 1, this influence is stronger and spatially more extended due to the existence of the second jet very close to the first one.

The eccentricity of the fitted ellipses is shown in Fig. 6.38. Most cases exhibit either a relatively constant eccentricity or an increasing one. The most extreme case being SI-ID 4 for which the OH-PLIF emitting region has a weak signal and is highly stretched by the high strain in the vicinity of the spark.

DI1-ID 1 and DI2-ID 2 exhibit a drop in eccentricity at 27 µs, i.e. the shape of the average fluorescing region becomes closer to a circle. For the DI1 case this drop coincides with the change in orientation discussed for Fig. 6.37. Therefore, the change in orientation is accompanied by a shift from an ellipse to a more circular shape of the hot region, and

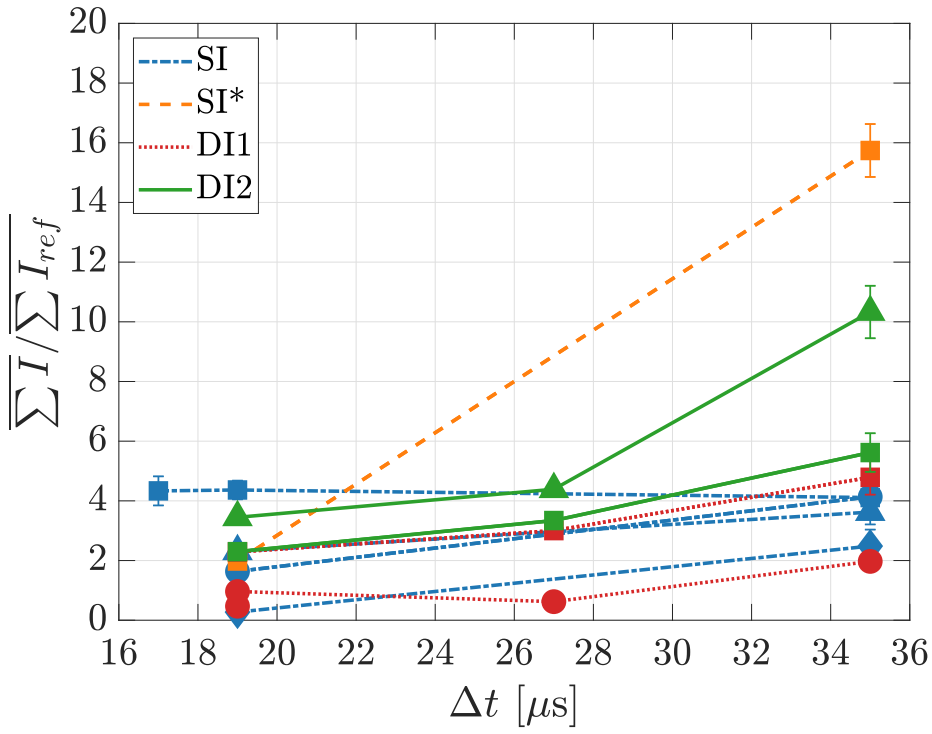

Figure 6.36: Evolution of the integrated intensity of the OH-PLIF signal as a function of time from laser energy deposition. Ignition locations: • =ID 1, ■ =ID 2, ▲ =ID 3, ♦ =ID 4. 95% confidence intervals are shown.

back to an ellipse. This corroborates the notion that changes in the dominant mean flow velocities occur. As the vertical component of the jets becomes weaker, the velocity defect in the wake of the jet becomes more relevant, so that the lower part of the advected hot region is decelerated while upper part is accelerated by the faster crossflow. A change in the orientation of mixing structures might accompany this but the velocity gradient is probably a much stronger influence.

For the DI2-ID 2 case the change in shape is less clear. However, given that all DI2 cases experience a continuous increase in OH fluorescing area and signal intensity, the sudden drop in eccentricity could represent simply the influence of the second jet. The subsequent increase in eccentricity presumably is a continuation of the stretching and tilting of hot regions due to remaining y-direction velocity gradients and the distribution of favorable flow strain regions.

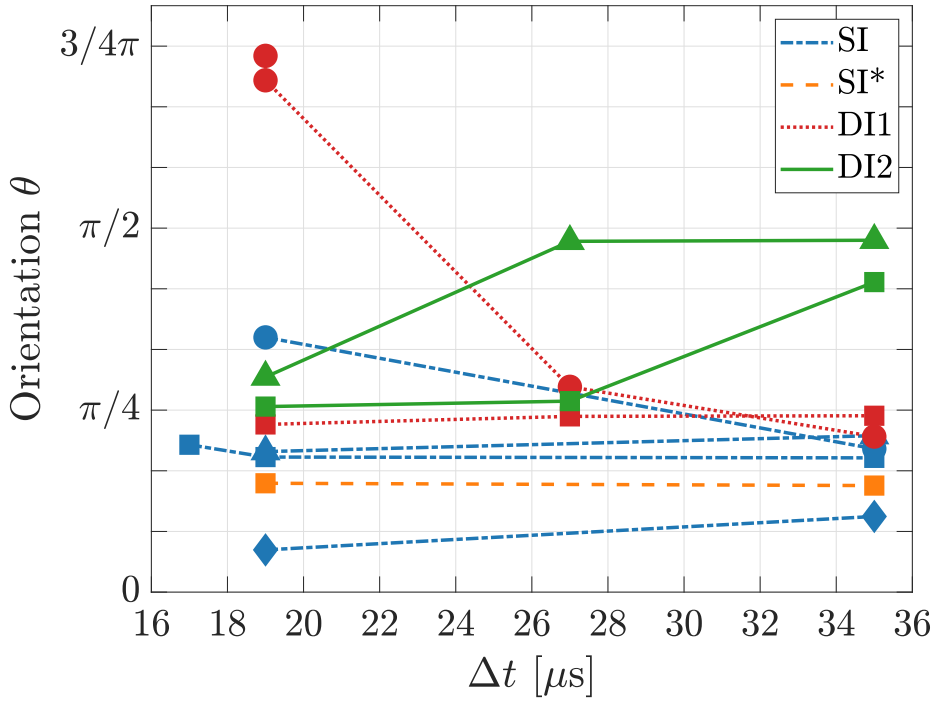

Figure 6.37: Plot of the angle between the horizontal x-coordinate and the semi-major axis of an ellipse, as a function of the time from ignition. The ellipse is fitted to the average shape of the recorded OH-PLIF signals. Ignition locations: ● =ID 1, ■ =ID 2, ▲ =ID 3, ♦ =ID 4.

6.2.5 Statistics of Dilatational Strain and PLIF Signals

Aerodynamic strain appears to play a big role in sustaining and propagating chemically reacting regions in the present experimental setup. Specifically, the effects of flow compression and expansion, measured by the divergence, have a large influence, see discussions above and results in Ch. 5. This section seeks to analyze the influence of dilatational strain on the results in Fig. 6.35 and Fig. 6.36 in greater detail.

Fig. 6.39a shows the spatial distribution of dilatational strain for the SI injector measured by the divergence of the velocity flow field. The dilatational strain is extracted along streamlines starting from investigated ignition locations, similar to what is presented in Ch. 5. The average normalized uncertainty, computed as described in Appendix C, is 26% between all SI data sets. The streamline from ID 4 is located close to the region of missing vectors but does not actually pass through it so that data could be extracted.

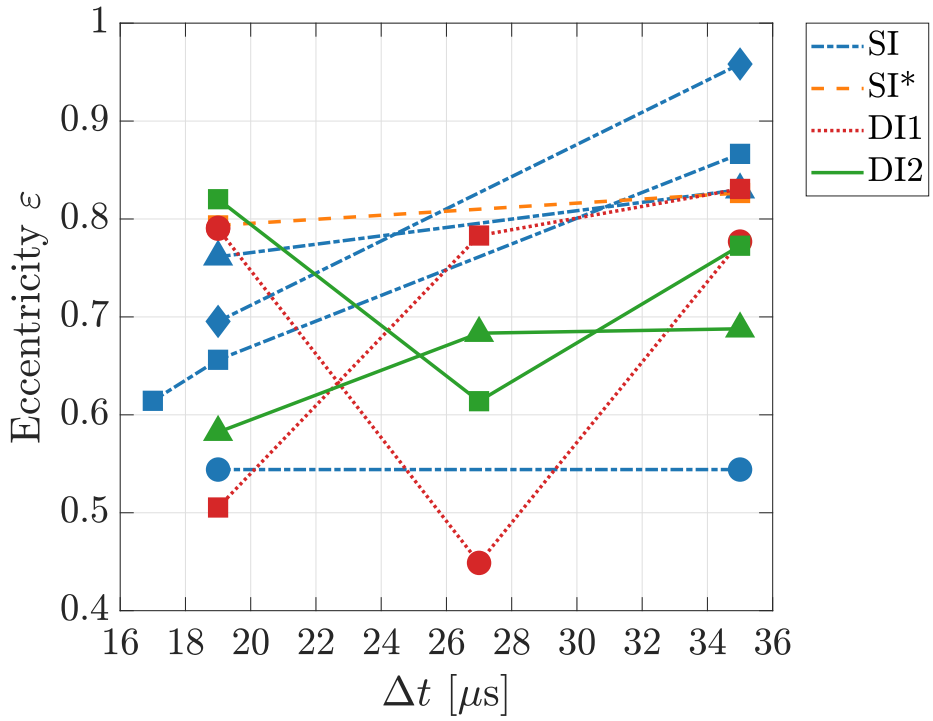

Figure 6.38: Plot of the eccentricity of an ellipse as a function of the time from ignition. The ellipse is fitted to the average shape of the recorded OH-PLIF signals. Ignition locations: • =ID 1, ■ =ID 2, ▲ =ID 3, ♦ =ID 4.

Measurements of the flow divergence are normalized by the extinction strain rate of a non-premixed ethylene-air flame. At the undisturbed, static crossflow conditions given in this study the extinction strain rate is $\kappa_{ext} \approx 4,000\ 1/\text{s}$, see Sec. 5.2. However, besides a sense of scale, the concept of a steady state extinction strain rate has no real significance, due to the overdriven nature of the ignition kernels investigated. Moreover, the reported values of the normalized divergence should be treated with care because of relatively high uncertainties and the noisiness of the differentiation process. Thus, only the trends are of significant interest in the following discussions.

The ignition kernel of SI-ID 1, which exhibits the largest recovery with regard to area growth and intensity, starts out in a highly compressive region close to the bow shock, moves through an expanding region and finally enter a weakly compressive region again. SI-ID 2 has a similar strain history but a shorter initial exposure to lower compression values. The spark of ID-3 is deposited even further downstream so that it experiences no

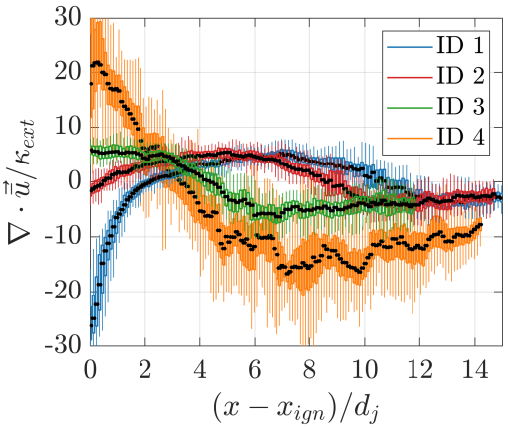

(a) Comparison of the four ignition locations of the SI injector.

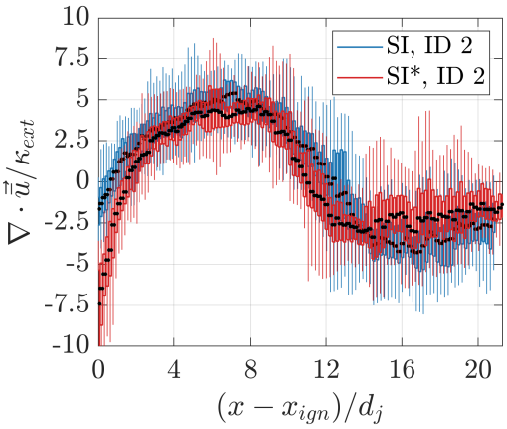

(b) Comparison of the SI and SI* single jet injectors.

Figure 6.39: Dilatational strain history for the single jet injectors along streamtubes starting at the spark locations. Black dots are the median value along the streamtubes. Bars indicate the 25th and 75 percentile, lines the minimum and maximum value in the data range.

initial compression, but a shorter history of positive dilatational strain and an extended region of weaker compressive strain. These observations correlate directly with the results in Fig. 6.35 and Fig. 6.36. Compressive strain helps sustain chemical reactions while expansion suppresses it. A history of flow expansion followed by compression can distribute chemically active regions over a larger area of the flow and sustain the thermal energy release to some degree, if the expansion does not diffuse it completely. This supports the notion that the positive effects of temperature and pressure increase in a compressive region outweigh the quenching effects of increasing molecular collisions. Moreover, it again shows that the change in temperature associated with compression and expansion is one of the dominant factors in determining whether thermal energy release is sustained.

The adverse effects of expansive strain is further illustrated by ignition at ID 4. It is the only case where the laser spark experiences an initially very high positive strain rate. The ignition kernel is then advected into regions of elevated compressive strain but the flow history at that point seems to have diffused the initially deposited energy too much for reactions to be sustained. ID 3 has a similar time history but with lower positive and negative strain rate peaks. In this case, the ignition kernel has a much easier time surviving,

presumably grows in the expansion region and is sustained in the compressive region.

The strain histories of SI-ID 2 and SI*-ID 2 in Fig. 6.39b are very similar both in trends and magnitude. The initial compression is stronger for the SI* injector since the position of the spark is closer to the bow shock, however, it is questionable whether this is sufficient to explain the significant increase in OH fluorescing area and intensity over the SI case. The enhanced turbulent mixing due to boundary layer interaction probably plays a large role as well. The average normalized uncertainty for the SI* data set in Fig. 6.39b is 32%.

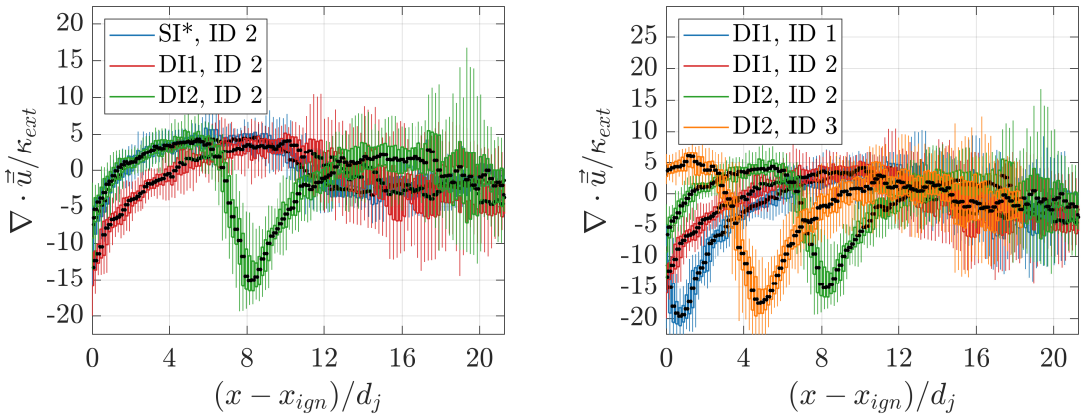

(a) Dilatational strain history of the $d_j = 1.41$ mm injectors for sparks at ID 2.

(b) Dilatational strain histories of the dual jet injectors for all spark locations used.

Figure 6.40: Dilatational strain history of the $d_j = 1.41$ mm injectors. Black dots are the median value along the streamtubes. Bars indicate the 25th and 75 percentile, lines the minimum and maximum value in the data range.

In Fig. 6.40a, the strain history of the three $d_j = 1.41$ mm injectors is compared for ignition at ID 2. Unsurprisingly, the DI1 injector case initially experiences stronger compression than the other cases. Further downstream the strain history of DI1 and SI* are very similar as the influence of the second jet in the DI1 case fades. DI2 on the other hand exhibits a sudden increase in compressive strain due to the secondary bow shock and a second region of positive strain further downstream. The strong compression followed by a secondary expansion probably suppresses growth and reaction rates in the DI2 case to some extent. The large area growth and high intensities for the SI* case suggest that moderate levels of compression and limited exposure to expansion regions are most favorable

to sustain chemical reactions and grow/stretch the ignition kernel.

The dual injector cases are directly compared in Fig. 6.40b. The previously discussed area growth and intensity results for the DI1 injector support the idea that moderate levels of compressive strain are more favorable than very high levels. The ID 2 ignition location experiences basically the same positive strain history as ID 1 but reduced negative strain peak values. The earlier availability of mixed, flammable gases for ID 2 might also be a factor.

For the DI2 injector, a spark at ID 3 initially experiences a shorter region of positive dilatational strain and a longer region of moderate compressive strain values. This seems to favor thermal energy release processes over a short initial compressive regime followed by a longer expansion. Peak strain rate values experienced by ignition kernels coming from ID 2 and ID 3 are roughly equal.

The normalized uncertainties for DI1 and DI2 data sets are larger than for the single injectors and can approach the magnitude of the calculated divergence values themselves. Average normalized uncertainties are 42% and 48% for DI1 and DI2 data respectively.

Premixed burning is more likely to be present than non-premixed burning in all cases discussed. In the far field, the dilatational strain tends to be compressive. For ignition IDs 1,2 and 3 the median far field strain values fall in the range $\nabla \cdot \vec{u} = (0 - (-5)) \cdot \kappa_{ext}$, where the extinction strain rate of a non-premixed flame at static flow conditions is considered. Thus, premixed burning is generally more likely to be sustained. Note that the divergence does not exactly correspond to the aerodynamic strain experienced by the flame, as strain components both normal and tangential to the flame surface would have to be considered for a proper quantification. Therefore, this arguments rests on an order of magnitude comparison.

Further correlations between OH signal intensity and dilatational strain rate are investigated using joint probability density functions of the normalized mean OH signal and the divergence of the average velocity field. The analysis is limited to the ID 2 spark location

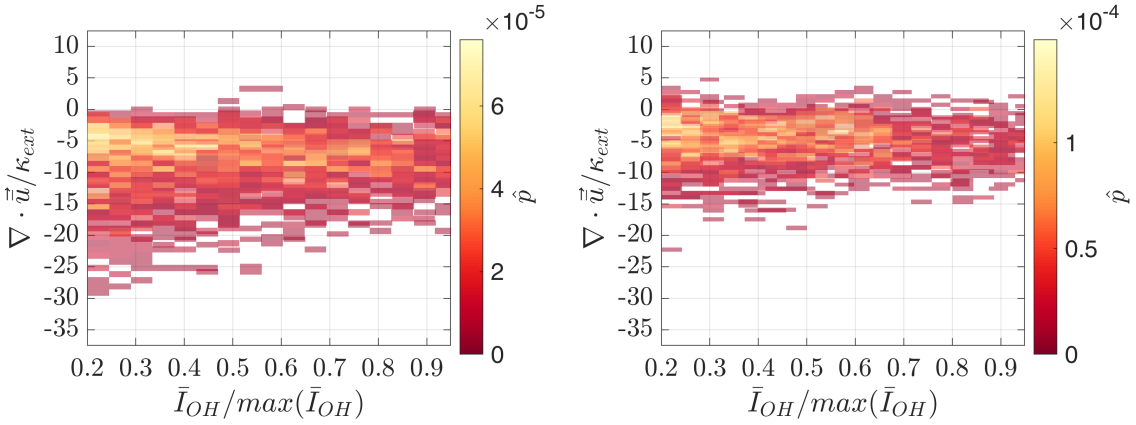

(a) SI injector with laser spark at ID 2.

(b) SI* injector with laser spark at ID 2.

Figure 6.41: Joint PDFs of the single jet injector cases between normalized average OH-PLIF signal intensity and velocity field divergence. Available times after laser energy deposition are 19 and 35 µs. The alpha of each data set is set to 0.5 so that more saturated colors correspond to higher probabilities at all times.

for the SI, SI*, DI1 and DI2 injectors. Measurements at different times from ignition are overlayed in the same figure and each data set is plotted with the same colormap and an alpha-value of 0.5. Thus, more saturated colors correspond to higher probabilities across the time delays considered. Based on the approach in Appendix C, the maximum normalized RMS uncertainty of the presented PDFs is 10%. The average normalized uncertainty of the measured divergence values themselves varies from 29% for the single jet injectors, over 49% for the DI1 injector, to 59% for the DI2 injector.

The SI injector results are shown in Fig. 6.41a, the SI* injector in Fig. 6.41b, the DI1 injector in Fig. 6.42a, and the DI2 injector in Fig. 6.42b. The single jet cases show narrower strain distributions at all OH signal intensities. This makes sense as the secondary jet introduces significant additional strain into the flow field as well as enhanced mixing. The latter potentially allowing chemical reactions to take place in regions with higher strain rates than in the single jet cases. The SI* case has an even narrower strain distribution than the SI case. This is due to the positioning of the ID 2 spark, the smaller diameter causing an overall smaller flow disturbance, and the weaker bow shock (i.e. lower peak compressive strain).

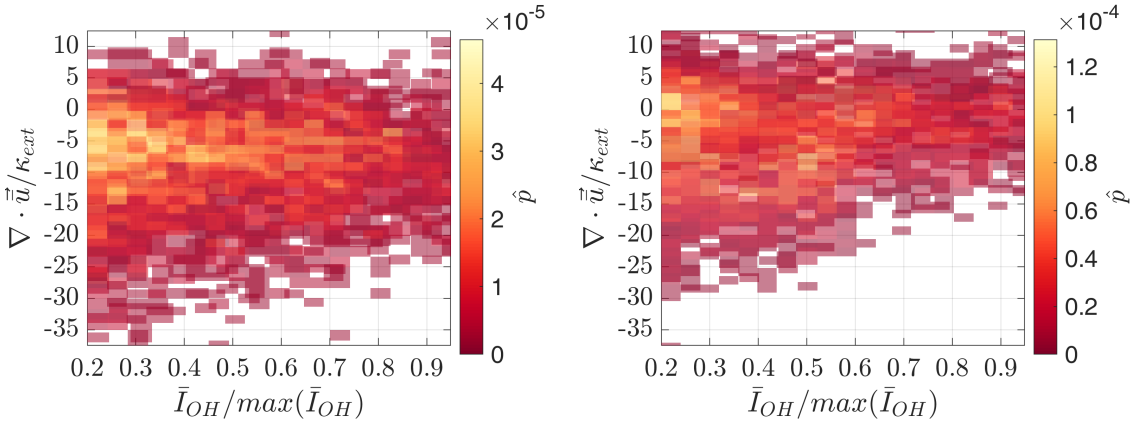

(a) DI1 injector with laser spark at ID 2.

(b) DI2 injector with laser spark at ID 2.

Figure 6.42: Joint PDFs of the dual jet injector cases between normalized average OH-PLIF signal intensity and velocity field divergence. Available times after laser energy deposition are 19, 27 and 35 µs. The alpha of each data set is set to 0.5 so that more saturated colors correspond to higher probabilities at all times.

Interestingly, the PDFs show that OH signals of all intensities favor moderately compressive regions, in agreement with the preceding analysis. The DI2 injector case is the least well defined with regard to this trend, but it can be discerned that the higher OH signal intensities do occur more regularly at normalized compressive strain rates between 0 and $-10 \cdot \kappa_{ext}$.

6.3 Conclusive Remarks

Experiments with single injectors having different jet diameters showed that changes in the jet mass flow rate can influence the jet fluid signal iso-contour trajectories. A potentially more meaningful trajectory for comparison is the maximum jet fluid signal trajectory or a normalized jet fluid signal iso-contour trajectory. Interestingly, while normalized trajectory data correlates well within a respective study, the data sets show distinct behavior in direct comparison. This suggests that there might be differences in the mixing and flow expansion process that the current data alone cannot capture and that influences the normalized trajectory.

These results highlight the need for more JISCF experiments using a standardized ap-

proach to compare jet trajectories and varying additional parameters, including such things as test section width. Collecting trajectory data further downstream can make deviations between data sets more evident. Moreover, a more detailed characterization of the influence of flow expansion after the bow shock for different crossflow Mach numbers is of interest.

The jet fluid signal and velocity field data showed that the smaller diameter single injector enhances mixing but leaves the velocity field largely unchanged. It is conjectured that the mixing enhancement occurs due to an increased interaction with the boundary layer as δ/d_j increases.

The OH-PLIF data indicated that a stabilized flame is most likely not achieved for any of the investigated configurations, i.e. no balance between thermal energy release and diffusive/convective transport is possible and chemical reactions will always be quenched at some point downstream. The plasma spark seems to predominantly ignite and burn premixed regions around the large scale entrainment structures of the jet. Nonetheless, the SI*-ID 2 and the DI2 configurations yield significantly enhanced OH-PLIF signals over the reference case, with regard to both fluorescing area and OH-PLIF signal intensity.

The larger separation between jets (DI2 injector) resulted in shorter positive strain regions and lower peak compressive strain rates, enhanced mixing and more encouraging burning statistics compared to the DI1 injector. Together with the studies in Lee (2006a) and Lee (2006b) for auto-igniting JISCF, it is conjectured that at even larger separations this trend might reverse. Moreover, for a given momentum flux ratio, there should indeed be an ideal separation distance between the jets, even for the predominantly premixed burning mode found in this study.

In the majority of cases, the average distribution of OH fluorescing regions seemed to align with the vortex lines of the JISCF further downstream of the fuel injection point. And while the presented data suggests predominantly premixed burning, no conclusive argument could be made to completely rule out non-premixed burning. Furthemore, because this study has a limited FOV and a limited amount of ignition locations, it is possible that

some of the trends change further downstream or for different ignition locations.

As would be expected, the most important factors contributing to enhancement of the OH-PLIF signal are faster mixing between fuel and oxidizer (jet + crossflow), moderate compressive strain rates, and limited exposure of the ignition kernel to flow expansion regions. Thus, moving towards sustained burning without cavity stabilization or sufficient enthalpy for auto-ignition, it could be beneficial to attempt the following engineering solutions. Introduce the fuel jets far upstream of the combustor to allow for sufficient mixing time. Provide sources of moderate compression such as bumps or waves along the combustor wall or isolator. Introduce vortex generators and methods to artificially thicken the boundary layer upstream of the fuel jet, such as shock-boundary layer interaction. Use a larger number of small diameter fuel injectors. Some of these suggestions are naturally implemented in radical farming scramjet concepts (Boyce *et al.*, 2012).

CHAPTER 7
CONCLUSIONS AND FUTURE WORK

7.1 Conclusions

This study furthers the understanding of jets in compressible high-speed crossflows, both in the non-reacting and reacting flow cases. A stagnation temperature of ~ 600 K and crossflow Mach number of 1.71 places the current experimental setup in a relatively low enthalpy regime, i.e. there is no auto-ignition occurring within the length of the test section using flammable injectants. Thus, the findings in this study are applicable to many ground test facilities and operating regimes at which auto-ignition is not possible.

A semi-empirical approach was used to develop a jet trajectory scaling that is valid for a wide range of JISCF experimental conditions. The advantages of this scaling include explicit consideration of flow physics and improved comparability between different studies and flow conditions. The trajectory scaling performs as good or better than all other empirical and analytical approaches considered for comparison.

To systematically investigate the influence of jet injectants' molecular weight and specific heat ratio on turbulent mixing, five different gases were used: argon, ethylene, carbon dioxide, helium, and nitrogen. Planar laser Mie-scattering records were collected to obtain non-intrusive measurements of jet fluid signal and velocity fields on the symmetry plane of the flow field. To the author's best knowledge, the investigated range of values for MW and γ in a single study is unprecedented, with $MW = 4 - 44$ g/mol and $\gamma = 1.24 - 1.66$; as is the availability of both mixture fraction and velocity field data. The usage of a blow-down windtunnel with a relatively long run time yields enough samples for statistically converged data sets. These data sets are not only of interest for the current experimental study but could also prove valuable for the validation of computational results and models

and the design of future experiments.

Extending the study of non-reacting JISCF to the reacting case, laser sparks were introduced in the flow field of a $J = 4$ ethylene jet. Time series of resulting ignition kernels were collected using line of sight averaged CH* chemiluminescence. This study is the first to employ a traversable laser ignition system on a JISCF setup, systematically testing different spark locations for the resulting thermal energy release patterns. Moreover, in contrast to many previous studies, the chemical conversion of ethylene was investigated instead of hydrogen. The use of a gas with a molecular weight higher than that of hydrogen fuel brings this study a step closer to translating the study of fundamental physics to engineering applications.

Based on results from the non-reacting single jet investigations, two streamwise staged jet injectors were designed. The non-reacting flow field measurements are repeated to establish a comprehensive baseline comparing the single and dual jet injectors. To the author's knowledge, this is the first experimental study to report on the specific effects of jet spacing on turbulent mixing and velocity fields.

Information from the single jet CH* measurements were used to select three laser spark locations conducive to sustained heat release and one location exhibiting fast quenching for comparison. Focusing again on the $J = 4$ ethylene jet, OH planar laser induced fluorescence measurements were recorded. Visualizing regions of hot combustion products, both instantaneous and statistical properties of OH-PLIF emitting regions were investigated. The PLIF signal was also related to non-reacting measurement of jet fluid signal and velocity fields to understand the underlying processes better. A characterization of this kind, having jet fluid signal and velocity field information available, is unique in the literature. The results show a way towards further research on combustion processes in compressible, high-speed flows using low-enthalpy ground-test facilities.

7.1.1 Turbulent Entrainment and Mixing of Single and Staged JISCF

The semi-empirical trajectory scaling developed explicitly considers the post-shock momentum flux ratio, boundary layer thickness and bow shock presence. Qualitatively, of the scalings considered for comparison, it correlates all available trajectory data the best. Quantitatively, based on a measure of R^2, the developed scaling shows a slight improvement ($\sim 1 - 51\%$) over all other empirical and analytical approaches examined. Two big advantages of the developed scaling are the direct inclusion of boundary layer thickness effects and the crossflow Mach number. Thus, with regard to hypothesis one in Ch. 1, the physics informed, semi-empirical scaling performs as good or better than fully empirical relationships. The results show that the developed scaling is particularly useful at the lower momentum flux ratios common for JISCF, i.e. $1 \leq J \leq 10$. For high enough J, the boundary layer and bow shock play only a secondary role. A simplified version of the developed scaling, that relies on the dominant influence of high J, is given for engineering estimates.

A comparison of all trajectory scalings considered shows that $x/J^{1/2}d_j$ consistently correlates the data better than x/Jd_j as the x-coordinate normalization. This agrees with large parts of the incompressible JICF literature, however, there could be configurations or specific regions of the flow field for which a scaling with J is still more effective or useful.

The momentum deficit introduced by the presence of the bow shock was quantified as a length scale denoted as δ_s. Its value was estimated using modified blast wave relationships. A comparison with experimentally determined results shows that the developed scaling likely considers the correct flow physics but not in the right proportions at all momentum flux ratios. Specifically, the blast wave prediction and experimental results appear to converge at higher J.

Analytical considerations for the behavior of JISCF trajectories with changing mixing rates and definitions were presented. They provide guidelines for a consistent interpretation of jet trajectories reported across the existing literature. Using these guidelines and the developed scaling, higher MW injectants with lower specific heat ratios are seen to exhibit

faster turbulent mixing. The influence of molecular weight and specific heat ratio can be anticipated from literature results and the convective Mach number concept. The influence of the specific heat ratio, however, is relatively weak and warrants further investigation.

Salient features in the fluctuating jet fluid signal and velocity profiles collapse with the developed scaling. The jet fluid signal reveals that peak fluctuations in the far field switch from the higher MW gases to the lower MW gases with increasing momentum flux ratio. Since the higher MW gases appear to consistently enhance turbulent mixing rates, this shift is attributed to boundary layer interactions at low J and a faster increasing M_c for gases with lower MW. The velocity data largely agrees with the jet fluid signal but shows a lower level of sensitivity to injectant property changes. This might be due to spatial filtering effects, as the velocity vector spacing is larger than the jet fluid signal resolution.

General trends in computed M_c profiles agree with conclusions drawn from the trajectory and jet fluid signal fluctuations data, regarding the influence of jet injectant properties. The suppression of hydrodynamic instabilities changes with compressibility levels in the jet shear layer. The peak M_c values computed for the higher MW gases are comparable to point estimates made by other authors in JISCF flow fields. However, for helium, the lowest MW gas, the calculated M_c is significantly lower than the point estimates with $M_c \approx 1$ vs. $M_c = 1.92$. The results show that the convective Mach number indeed grows faster with J for the lower MW gases than the higher MW gases. The results also suggest a possible explanation for the influence of lower specific heat ratios, if the molecular weight of injectants is more or less identical; an effective convective Mach number might be lower for $\gamma_j < \gamma_\infty$ cases than for $\gamma_j \geq \gamma_\infty$ cases. The value of this effective convective Mach number would lie in between the M_c values calculated with respect to the crossflow and the jet stream. Finally, the computations suggest that the convective Mach number tends towards zero once the injectant flow crosses the jet shock structure, i.e. compressible suppression of hydrodynamic instability should play a role only close to the jet orifice. Thus, with regard to the second part of hypothesis one, the trajectories do exhibit a sensitivity to

jet injectant properties, and the jet fluid signal fluctuations and the convective Mach number all agree on the sensitivities observed.

Additional jet trajectories were measured for jets with smaller diameters (1.41 vs. 2 mm). Contrasting the jet fluid signal contour trajectories shows that changing the jet mass flux, for a given experimental setup, can influence the progression of jet trajectories. This observation motivated further analysis using normalized jet fluid signal contour trajectories and maximum jet fluid signal trajectories. Using these definitions improves comparability for JISCF with changing jet mass flux rates that are otherwise identical.

The fluctuating jet fluid signal shows higher initial values for the smaller diameter single jet injector, presumably due to more boundary layer interaction (Pizzaia and Rossmann, 2018). The velocity field results are largely unchanged between the two jet diameters.

The staged jets exhibit deeper crossflow penetration with increasing jet spacing ($x/d_j =$ 3 and 9), using ethylene as the injectant at $J = 4$. Apparently, the larger separation allows the second jet to profit more from the shielding effect and the upstream low speed flow region caused by the first jet. Based on the properties of different trajectory definitions discussed, this implies stronger turbulent mixing due to the presence of the secondary jet. The fluctuating jet fluid signal and velocity profiles corroborate the presence of stronger fluctuations. This is not unexpected, however, the results of Lee (2006a) suggest that for even larger jet spacings, or different J, this trend will eventually reverse.

Thus, with regard to hypothesis three formulated in Ch. 1, the results confirm that staged jets enhance turbulent mixing and that the enhancement is a function of the separation of the two jets. However, results for the single, smaller diameter jet suggest that increasing the interaction of the jet with the boundary layer, i.e. increasing δ/d_j, could also increase turbulent mixing rates.

7.1.2 Forced Ignition of Single and Staged JISCF

A large number of ignition locations on the symmetry plane of a $J = 4$ ethylene jet were characterized using CH* chemiluminescence recordings. A spark was introduced at each location using a traversable laser ignition system. The most favorable conditions for sustained thermal energy release are found on the windward side of the jet along the average pseudo stoichiometric contour and in the windward shear layer away from jet shock structures. Very specific regions close to the wall in the jet wake also appear promising.

Dilatation strain rates appear to have a strong influence on whether chemical reactions can be sustained or not. A possible explanation is the temperature change induced by flow compression and expansion. Due to the exponential dependence of combustion rate constants on temperature, even moderate changes caused by dilatation can change the reaction rate constant by orders of magnitude. Thus, moderate compressive strain rate can be beneficial to sustain ethylene burning, while any type of flow expansion and the associated drop in temperature are very detrimental.

Further investigations using planar laser induced OH fluorescence show that, even in favorable regions, the ignition kernel does not result in a stabilized flame. It appears that the primary mode of burning is premixed in regions around large scale structures of the jet shear layer. The characteristic, propagating thin flamelets of non-premixed combustion were not observed, instead OH fluorescing regions were spatially distributed.

The growth, average shape and orientation of the ignition kernel is governed mainly by mean flow velocity gradients in its vicinity. However, far downstream, the orientation also appears to align with the direction of large scale vortex structures in incompressible JICF, i.e. $\sim 30^{\circ}$ relative to the undisturbed crossflow direction. Thus, the vortex structures could play an important role and non-premixed burning along them cannot be ruled-out entirely.

The reacting single jet results confirm hypothesis two, defined in Ch. 1. The success of an ignition event depends highly on its flow field history, which, in turn, changes with ignition location. Fuel distribution, dilatational strain and velocity gradients play the

biggest roles in determining ignition kernel size, orientation, and combustion product signal strength.

Moving from the single to the dual jet injectors, the jet diameter was reduced. The developed trajectory scaling was used to adapt the ignition locations to the smaller d_j. This should have placed the laser spark at similar locations with regard to the jet fluid signal and velocity field properties. However, qualitative observations show that this might not be the correct approach to ensure ignition location similarity. Instead, a scaling with only the jet diameter could yield better similarity.

With the staged injectors, the ignition locations farthest downstream in the jet shear layer provide the largest enhancements in OH-PLIF emission area and signal intensity. The turbulent mixing enhancement and additional flow disturbance due to the second jet also has a clear influence on mean ignition kernel shape, causing a more vertical orientation. The staged injector with the larger jet spacing provides more favorable conditions for sustained thermal energy release. However, the overall largest improvements are observed simply for the single jet injector with a smaller jet diameter.

The larger separation between jets results in shorter positive strain regions and lower peak compressive strain rates, enhanced mixing and more encouraging burning statistics. Together with the studies in Lee (2006a) and Lee (2006b) for auto-igniting JISCF, it is conjectured that at even larger separations this trend might reverse. Moreover, for a given momentum flux ratio there is indeed an ideal separation distance between the jets, even for the predominantly premixed burning mode found in this study.

The smaller single jet producing the largest enhancement in overall OH fluorescent area and signal intensity is somewhat surprising. The result can be explained with peak strain rates being lower than in the dual injector cases and turbulent mixing being enhanced compared to the large diameter single jet. It is also possible, that the small difference of the spark location relative to the upstream bow shock plays a role.

The forced ignition results for the smaller diameter single jet and the staged jets show

that resulting burning processes are not necessarily enhanced using the staged jets. This is in contrast to hypothesis three of this dissertation. The larger jet spacing does exhibit enhancements over the smaller spacing. However, ignition location and turbulent mixing rates play an equally important, if not more important role, than jet staging, with regard to OH-PLIF signal strength and size. Overall, as expected, the most important factors contributing to enhancement of OH-PLIF signals are: enhanced turbulent mixing between fuel and oxidizer, moderate compressive strain rates, and limited exposure of the ignition kernel to flow expansion regions.

While the presented data suggests predominantly premixed burning, no conclusive argument can be made to rule out non-premixed burning. Furthermore, because this study probed a limited field-of-view and a limited number of ignition locations, it is possible that some of the trends change further downstream or for different ignition locations.

7.2 Limitations and Future Work

The solid particle Mie-scattering approach employed here has the drawback of limited tracer response time. Both the jet fluid signal and velocity fields are affected by this. It is unlikely that temporal dynamics beyond that of the largest scales are captured in their entirety. There is also room for improvement with regard to seeding uniformity and mean particle size.

The low seeding density on the leeward side of the jet close to the wall is an issue for PIV measurements, leading to masked regions in which very few reliable vectors could be computed. This also excludes an interesting part of the velocity fields from analysis. An extension for future studies should include the usage of high-speed cameras to supplement the statistical data with time-resolved flow field dynamics. Specifically, the temporal evolution of the large scale structures as a function of injectant properties is of interest.

Given the shortcomings of the solid particle seeding technique, it is desirable to develop gas-phase based measurements of concentration and velocity fields. These could be based

on approaches such as iodine/nitric oxide/acetone PLIF, Rayleigh scattering, or molecular tagging velocimetry. A combination of PLIF and high resolution background oriented schlieren measurements might also be able to yield interesting insights into turbulent mixing processes by quantifying density gradients and tracer concentrations simultaneously. In this fashion, one could differentiate dilatation from true jet fluid transport effects.

The current study focuses solely on the JISCF symmetry plane. Since the flow field is highly three-dimensional, future studies should repeat some of the measurements done here either to gather data along cross-sectional views or to provide tomographic flow field information. This can shed light on the role of the CVP as injectant properties are changing and the measurements can be used to investigate (near wall) burning processes further.

While the developed jet trajectory scaling works reasonably well in its current form it can be improved in several ways. It is shown that the blast wave relationship does not capture the JISCF bow shock behavior in its entirety and that the contributions of different physical phenomena to the scaling might not be weighted correctly. Thus, it would be of interest to perform a study focusing on the relationship between bow shock geometry, boundary layer thickness, and jet momentum flux ratio to better characterize the dependencies. Moreover, extending the scaling to barely choked jets or perfectly expanded jets would not only make it more useful but probably also provide an opportunity to better understand the controlling parameters.

Comparison between this study's trajectory data and data from existing literature showed that there are additional influences that may need to be considered. Specifically, the turbulent mixing model discussed suggests that, in some setups, the lateral mixing might be stronger than in others. The comparisons highlight the need to make available larger sets of consistently defined and analyzed jet trajectory data.

Because the success of the smaller diameter single jet in the reacting flow experiments was unexpected, only a few data points were collected. Naturally, it is of interest to extend the current study by collecting more data points and better identifying the differences with

the larger diameter single jet. This includes a more detailed experimental characterization of the boundary layer influence in both cases, e.g. by varying the boundary layer thickness, boundary layer state or jet diameter further.

A simple yet rewarding extension of the current work is to perform simultaneous PIV and OH-PLIF measurements. These measurements could yield direct correlations between chemically reacting regions and the local velocity strain field. Thus, allowing for a better characterization of the influence of flow expansion, compression and shear strain on thermal energy release in the compressible JISCF flow field. Moreover, the data could potentially be used to develop and/or validate computational models for reacting, compressible flow fields.

While the data collected suggests predominantly premixed burning, no definitive conclusion can be drawn with the available information. An interesting research project would be to perform simultaneous acetone/NO and OH-PLIF with higher spatial resolutions to attempt distinguishing the two burning regimes more clearly. In general, any approach combining scalar concentration measurements with thermal energy release indicators should be suitable. The development of an acetone PLIF system also synergizes well with the desire to compare the current Mie-scattering results with gas-phase measurements.

Characterizing two staged injectors confirmed computational predictions that increasing the jet spacing can increase mixing rates and jet penetration. However, the optimal distance is predicted to be a function of the momentum flux ratio and a peak in jet penetration is not identified in this study. Thus, more staged injectors with even larger spacings should be investigated including variations of the momentum flux ratio.

Regarding the engineering of supersonic combustion systems, the current study points towards several interesting research opportunities. One is the usage of a high-speed ignition laser to investigate the possibility of continuous forced ignition for efficient supersonic combustion, as also suggested by Brieschenk *et al.* (2013a). Furthermore, the relatively good performance of the single smaller jet in the reacting flow experiments suggests that

spanwise arrays of jets could be more successful in achieving efficient supersonic burning than staged jets. Such arrays have been characterized to some degree in the past but it would be interesting to extend the currently presented approach to such configurations, including the usage of planar laser diagnostics. The artificial thickening of boundary layers or vortex generators positioned ahead of the jet could be investigated as means to enhance burning efficiency with the current setup as well. Finally, it could be rewarding to investigate the introduction of tailored regions experiencing moderate compressive strain, e.g. through the introduction of textured, curved or bumpy walls. The compressive strain supports thermal energy release reactions and an ideal configuration might exist in terms of compression length, frequency and subsequent re-expansion.

Appendices

APPENDIX A

MIXTURE FRACTION MEAN AND RMS FIELDS

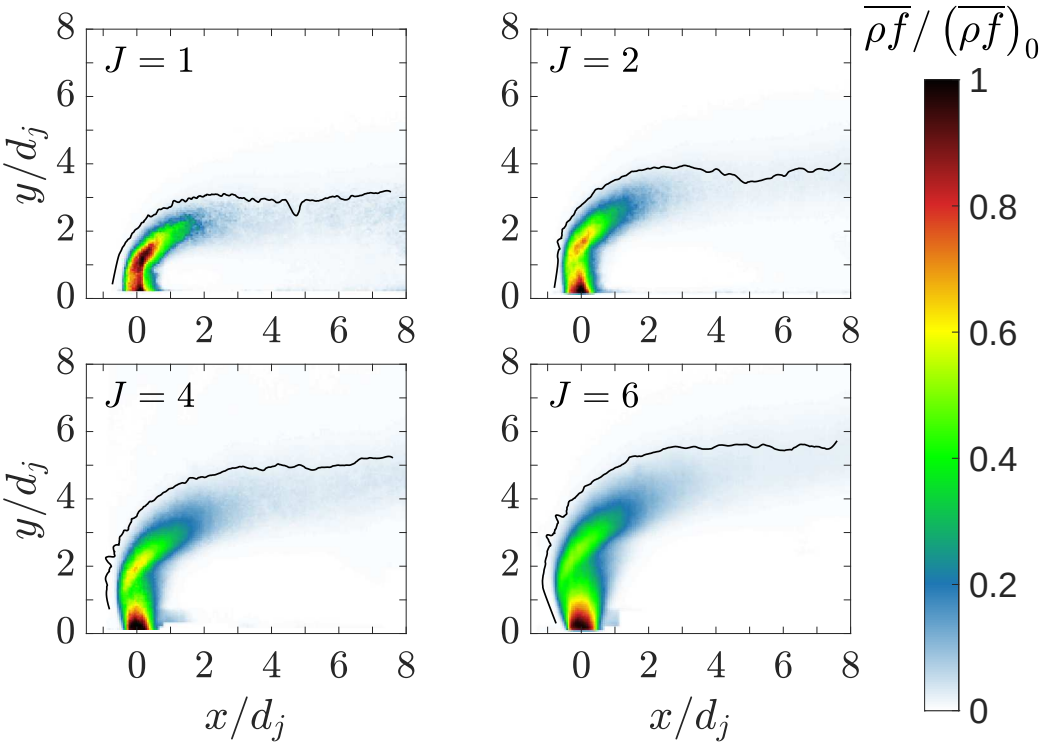

(a) Mean mixture fraction fields for argon.

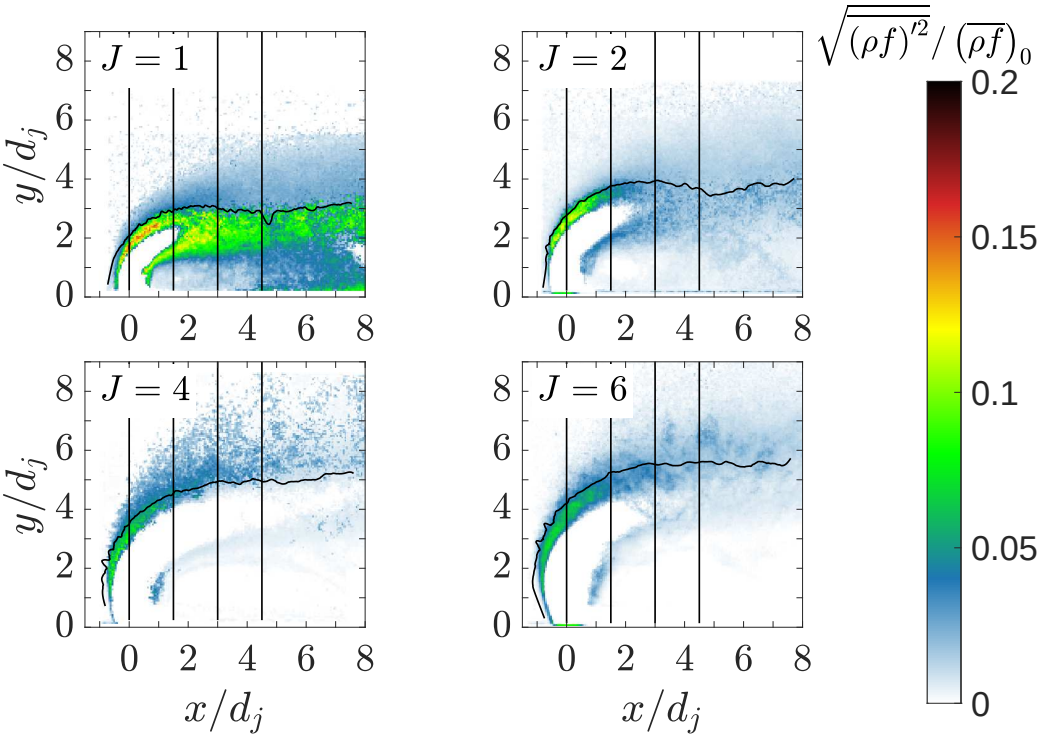

(b) RMS mixture fraction fields for argon.

Figure A.1: Mixture fraction results for argon. The nominal momentum flux ratio is indicated in the upper left corner.

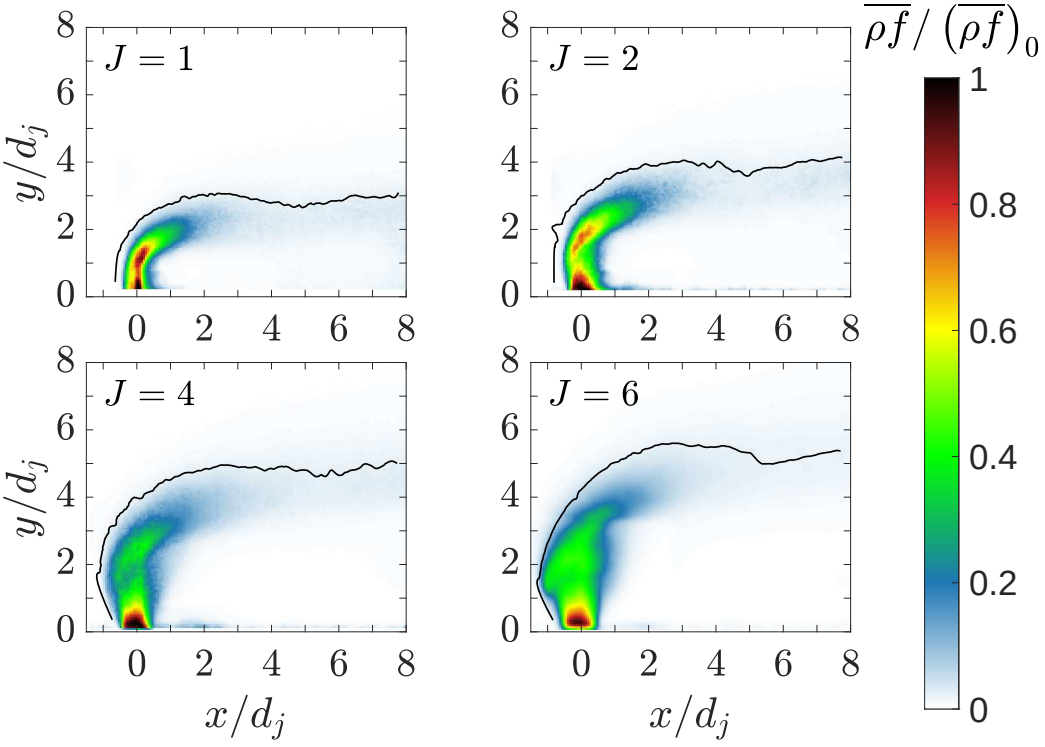

(a) Mean mixture fraction fields for ethylene.

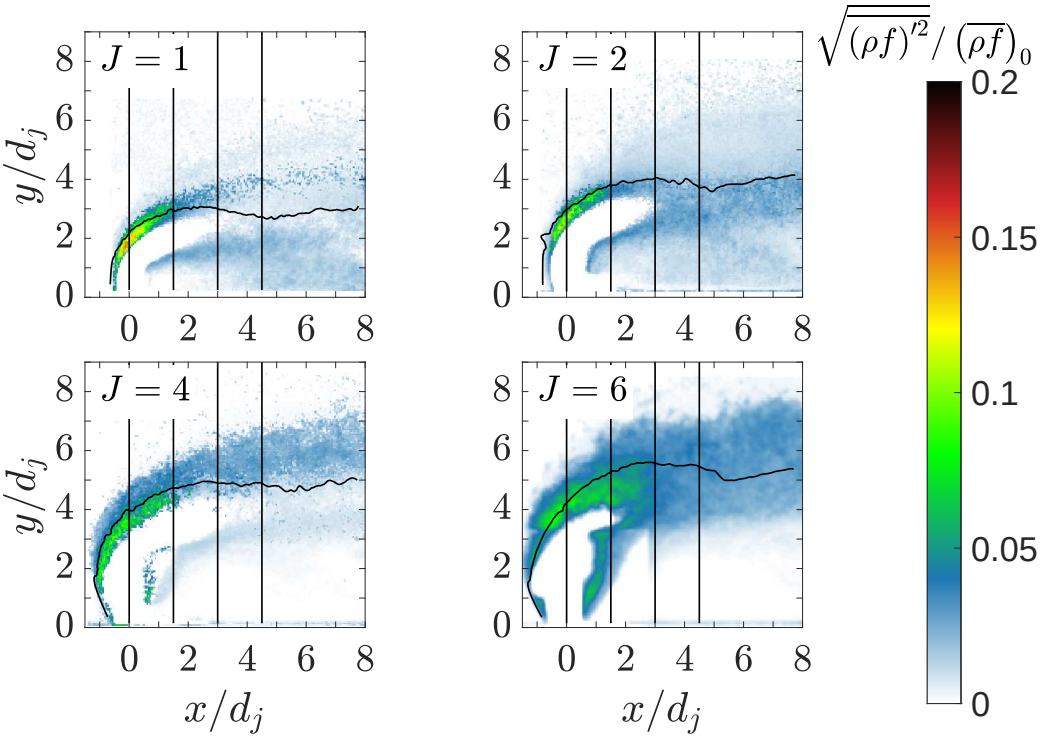

(b) RMS mixture fraction fields for ethylene.

Figure A.2: Mixture fraction results for ethylene. The nominal momentum flux ratio is indicated in the upper left corner. The $J = 6$ case had to be processed with a stronger Gaussian filter than the other cases to achieve convergence in the solution of the inverse problem yielding the mixture fraction field.

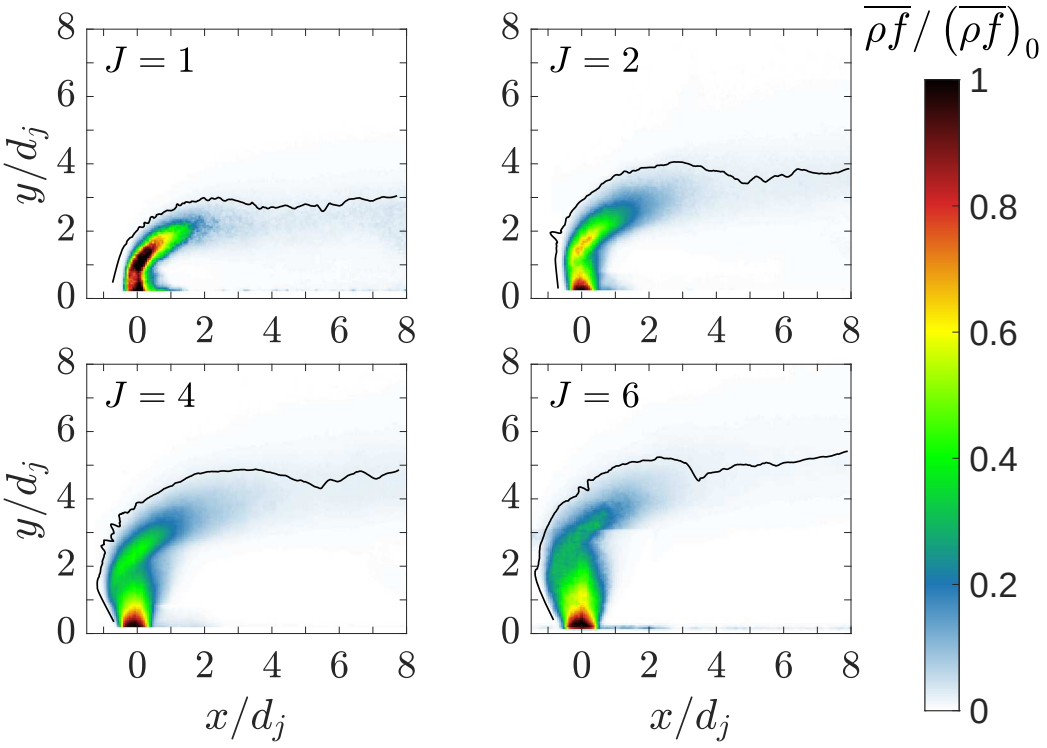

(a) Mean mixture fraction fields for carbon-dioxide.

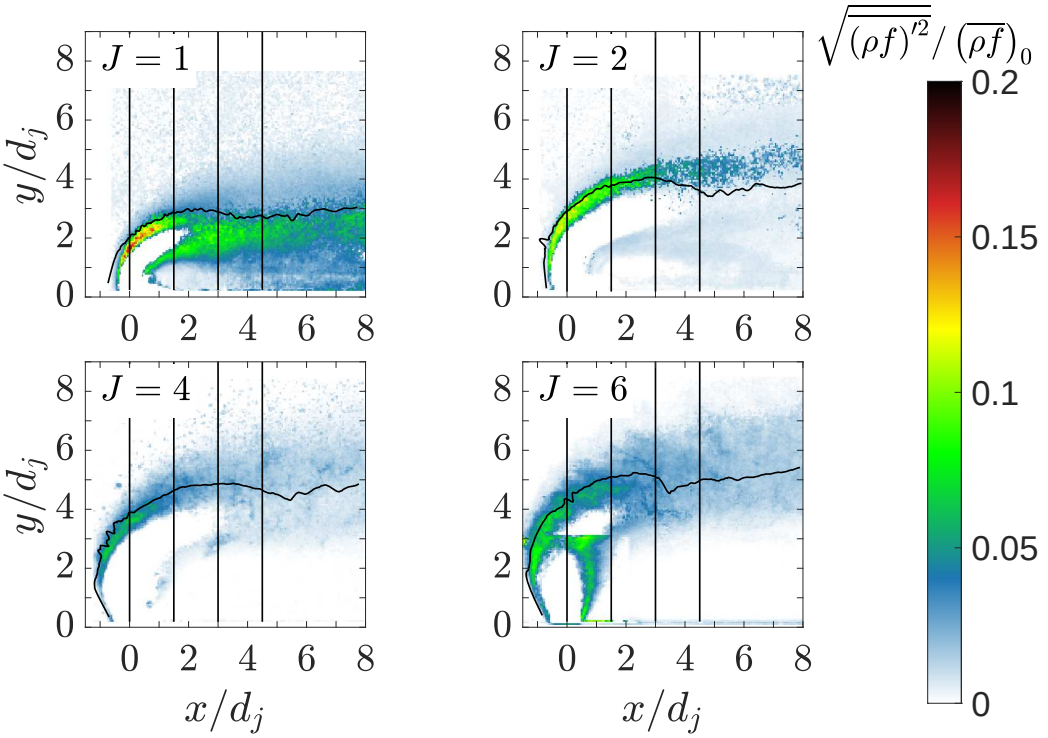

(b) RMS mixture fraction fields for carbon-dioxide.

Figure A.3: Mixture fraction results for carbon-dioxide. The nominal momentum flux ratio is indicated in the upper left corner.

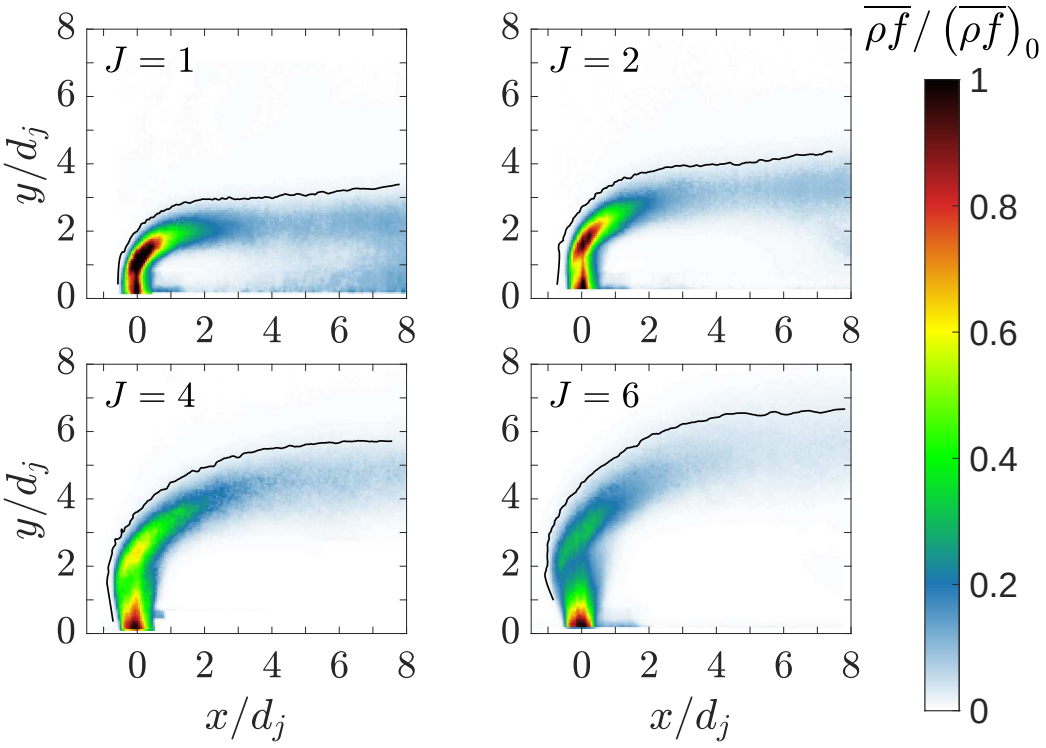

(a) Mean mixture fraction fields for helium.

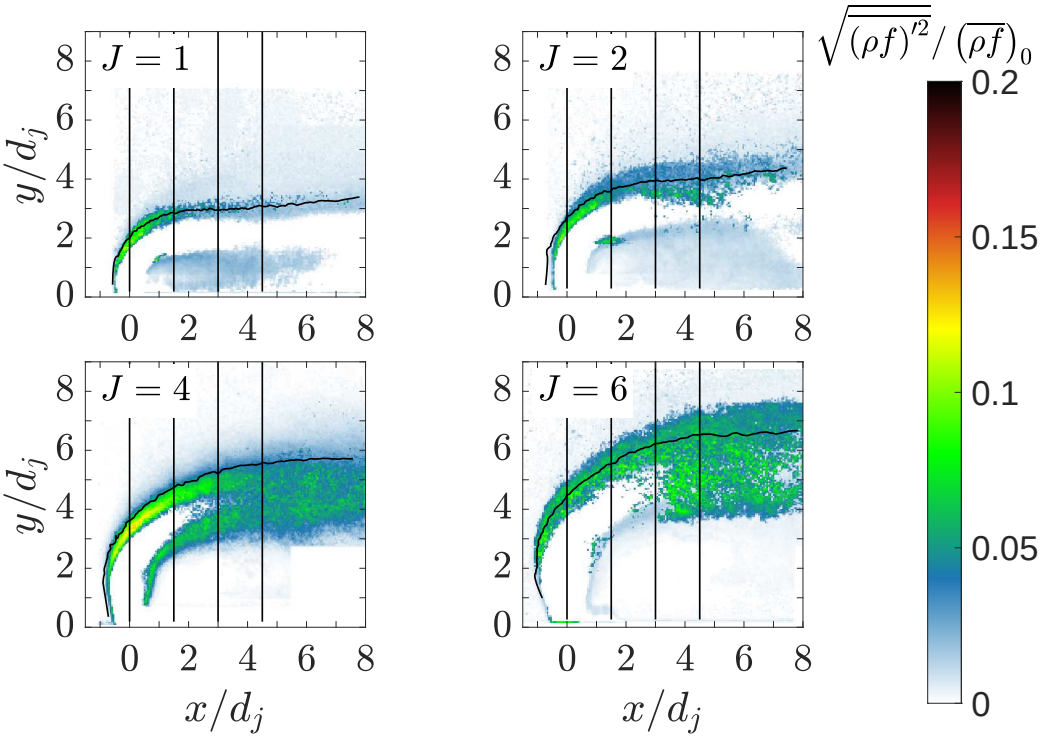

(b) RMS mixture fraction fields for helium.

Figure A.4: Mixture fraction results for helium. The nominal momentum flux ratio is indicated in the upper left corner.

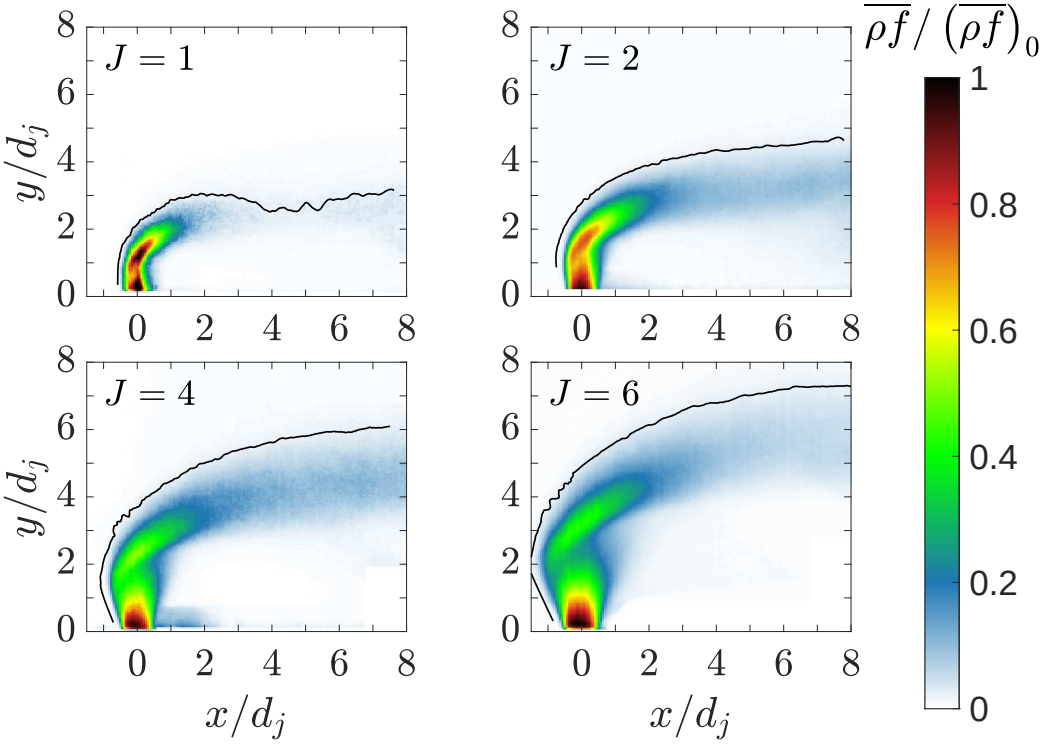

(a) Mean mixture fraction fields for nitrogen.

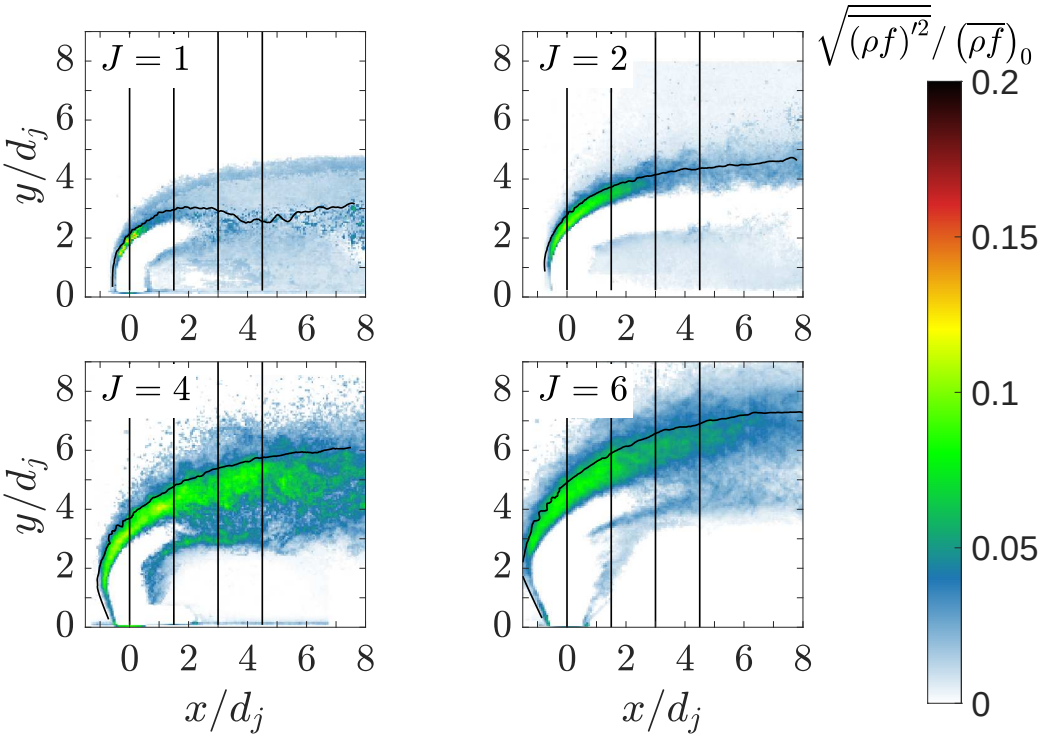

(b) RMS mixture fraction fields for nitrogen.

Figure A.5: Mixture fraction results for nitrogen. The nominal momentum flux ratio is indicated in the upper left corner.

APPENDIX B

PIV MEAN AND RMS FIELDS

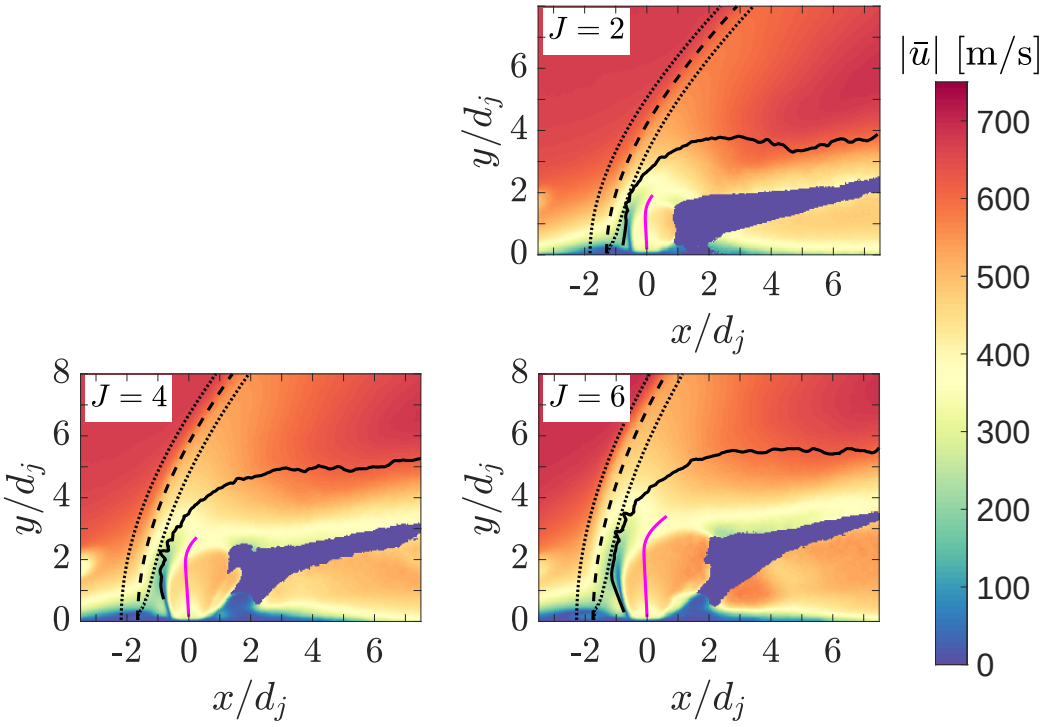

(a) Mean PIV velocity fields for argon.

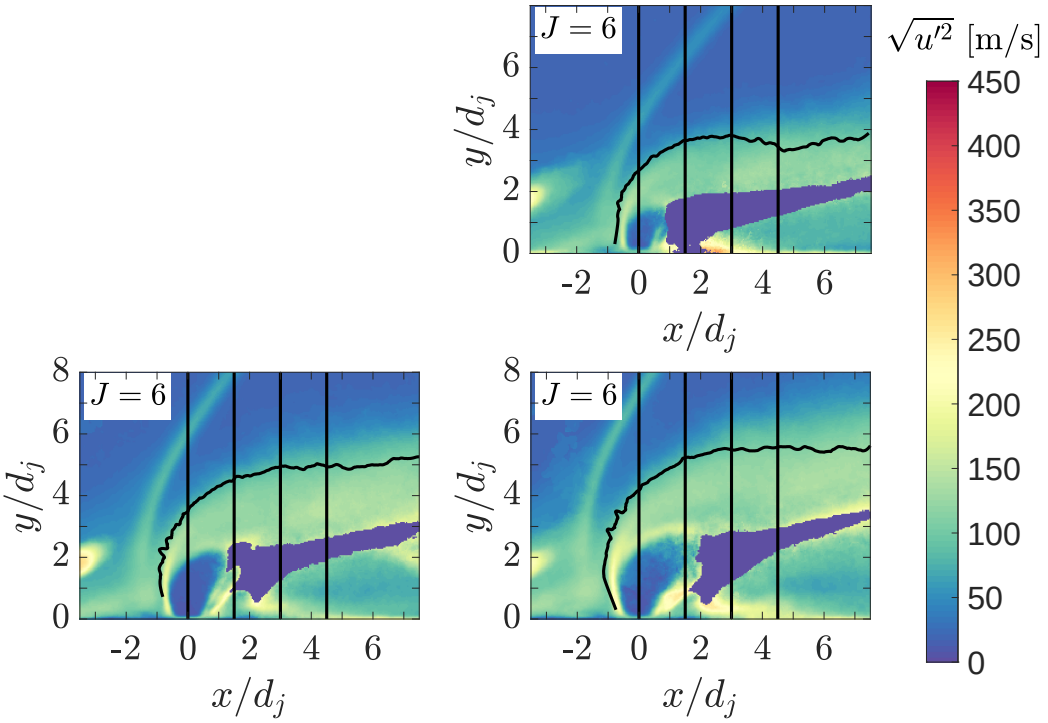

(b) RMS PIV velocity fields for argon.

Figure B.1: PIV velocity results for argon. The nominal momentum flux ratio is indicated in the upper left corner.

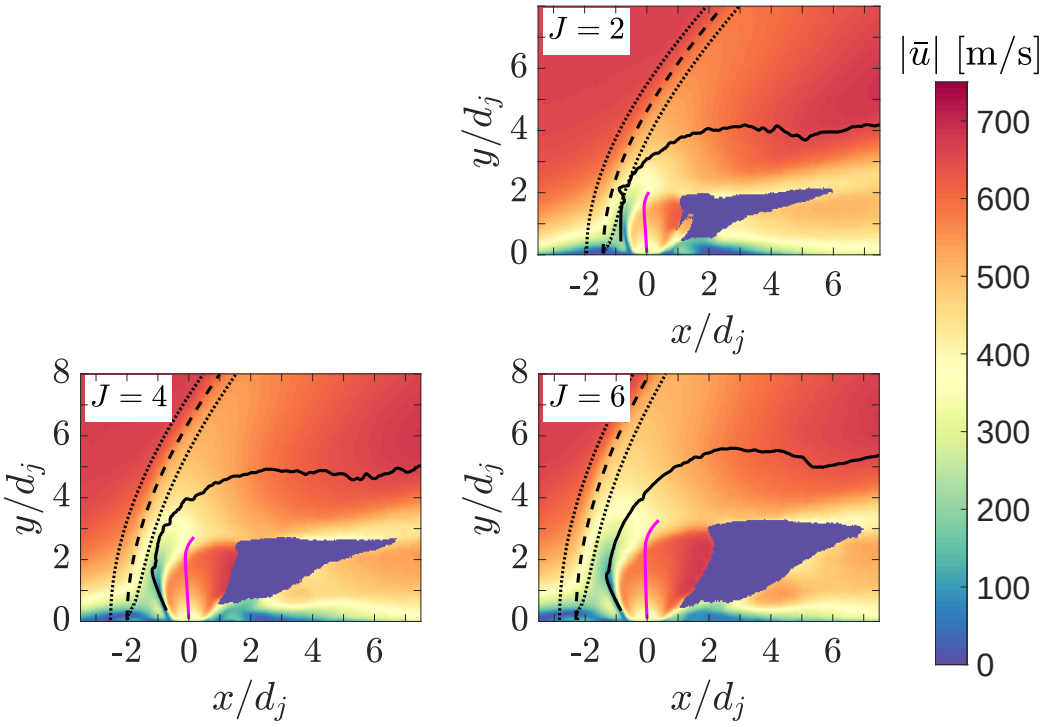

(a) Mean PIV velocity fields for ethylene.

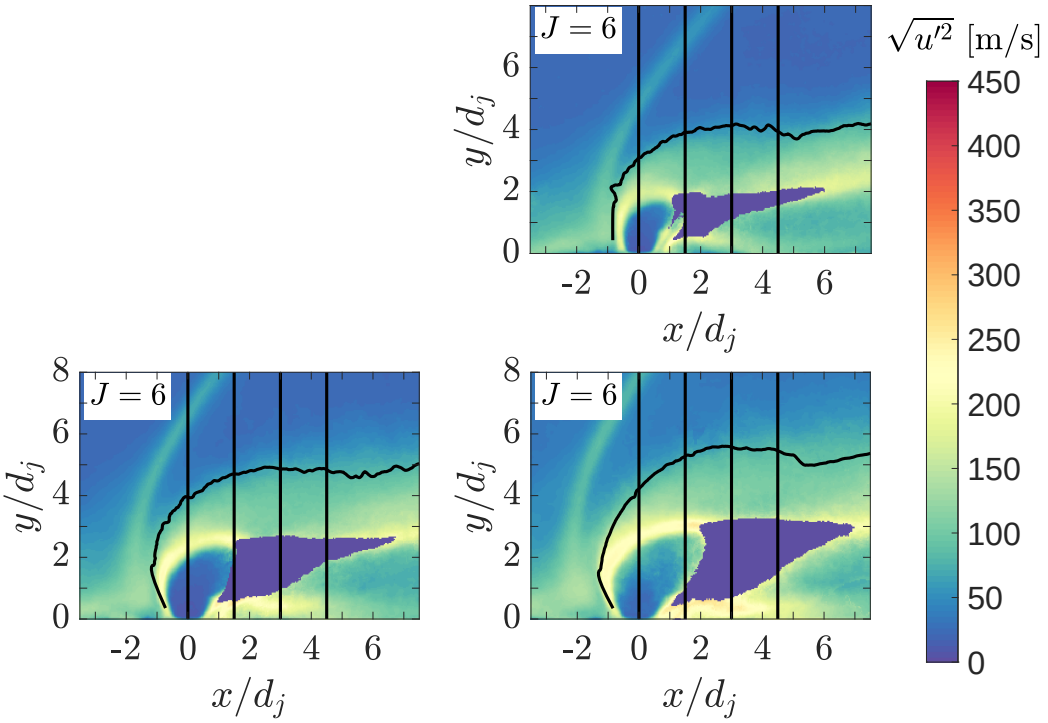

(b) RMS PIV velocity fields for ethylene.

Figure B.2: PIV velocity results for ethylene. The nominal momentum flux ratio is indicated in the upper left corner.

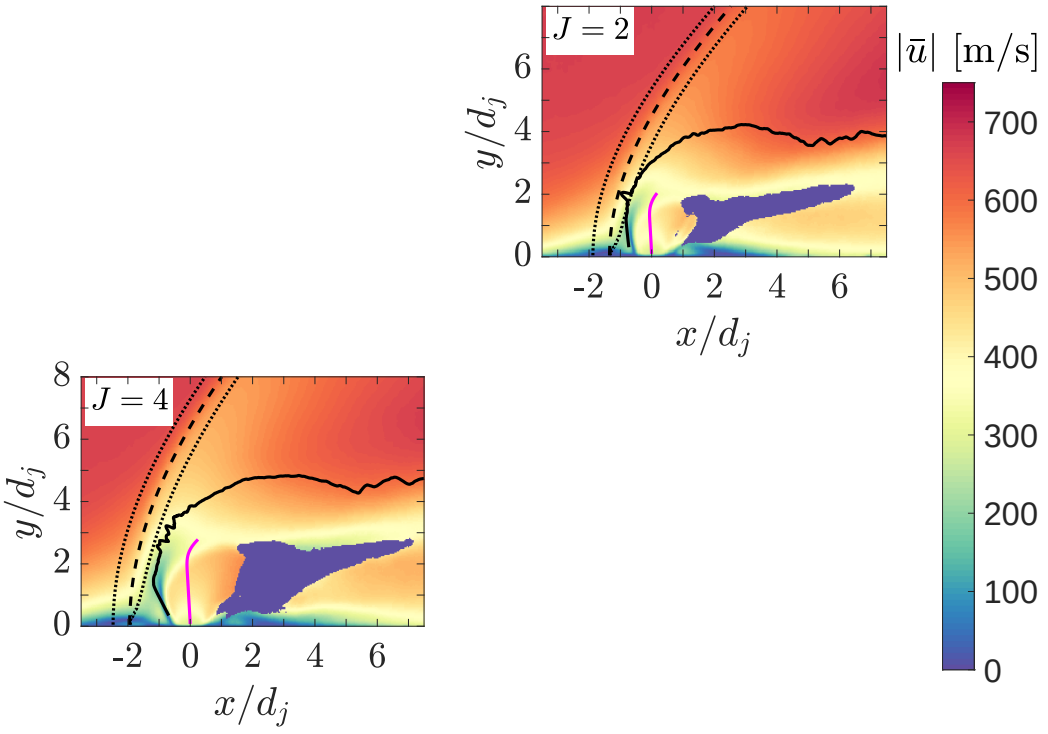

(a) Mean PIV velocity fields for carbon-dioxide.

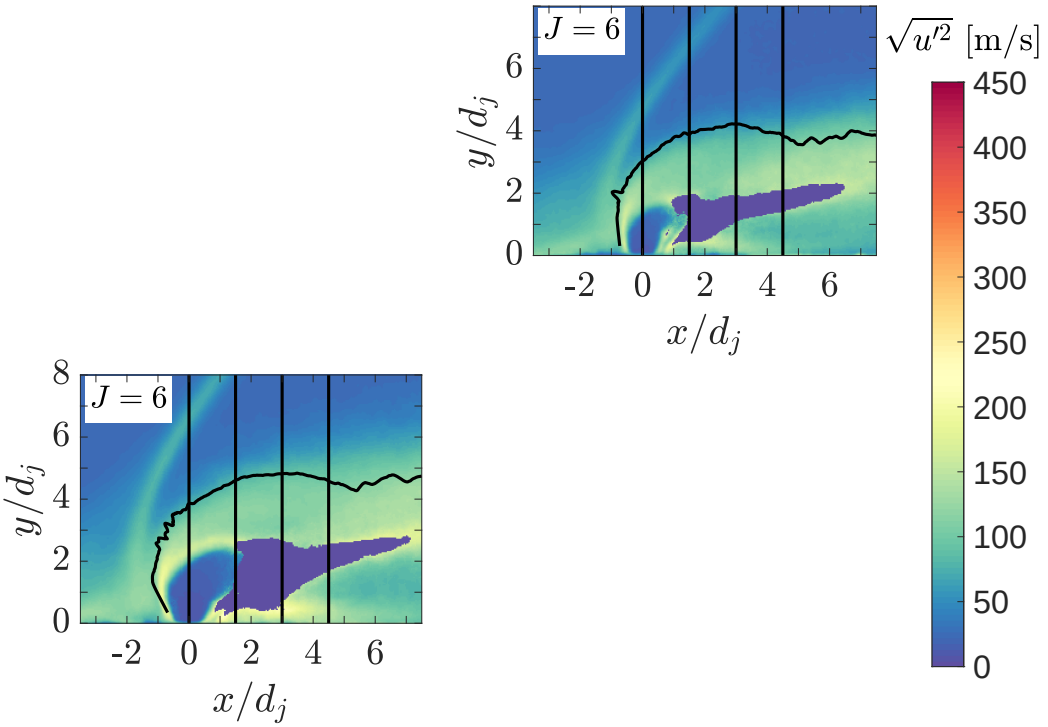

(b) RMS PIV velocity fields for carbon-dioxide.

Figure B.3: PIV velocity results for carbon-dioxide. The nominal momentum flux ratio is indicated in the upper left corner.

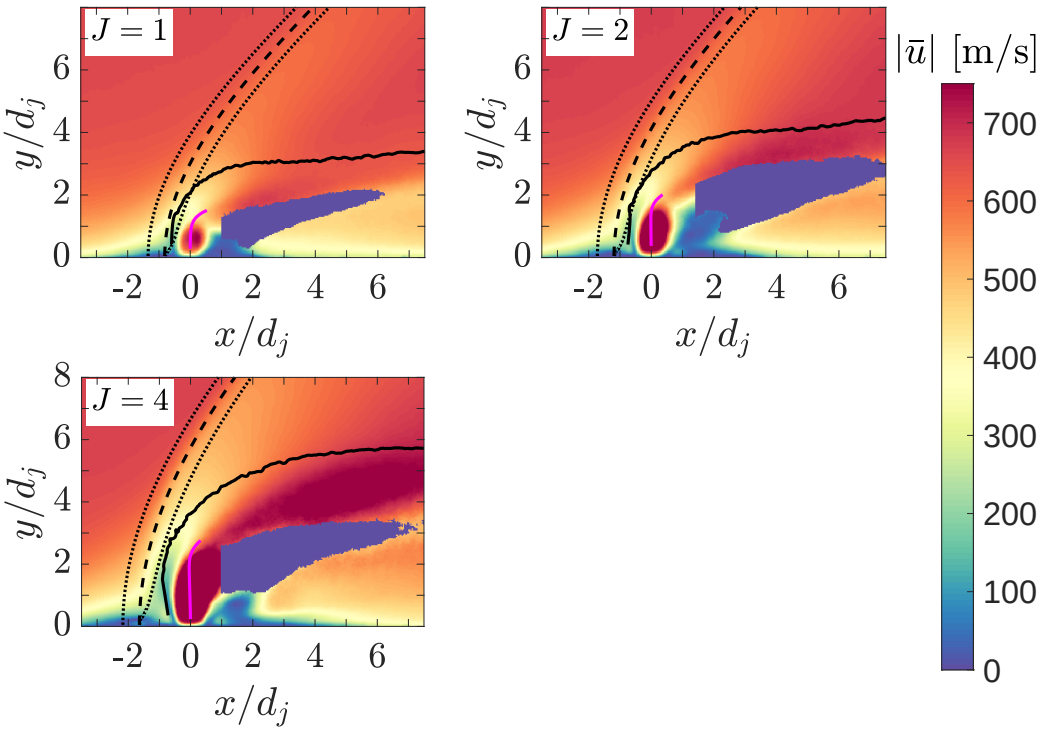

(a) Mean PIV velocity fields for helium.

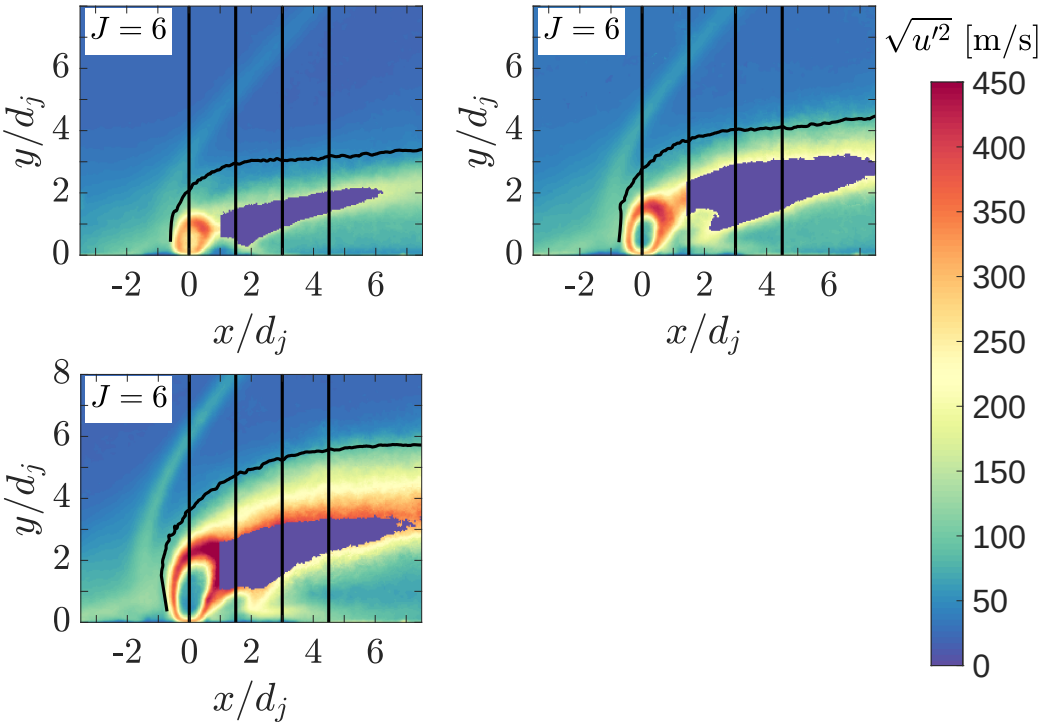

(b) RMS PIV velocity fields for helium.

Figure B.4: PIV velocity results for helium. The nominal momentum flux ratio is indicated in the upper left corner.

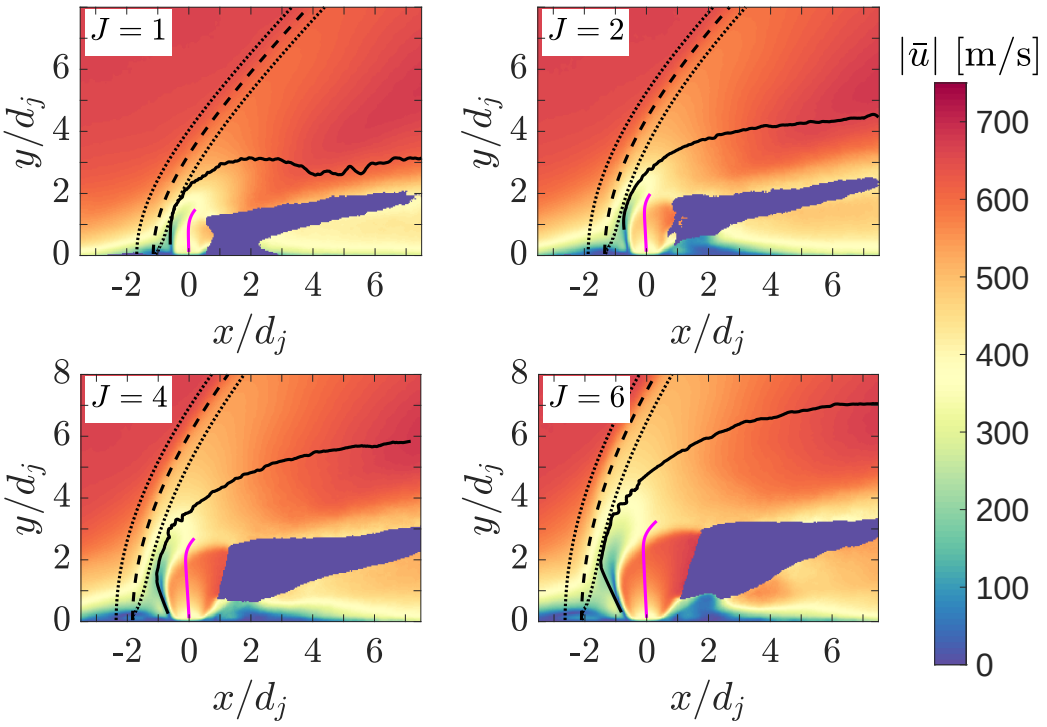

(a) Mean PIV velocity fields for nitrogen.

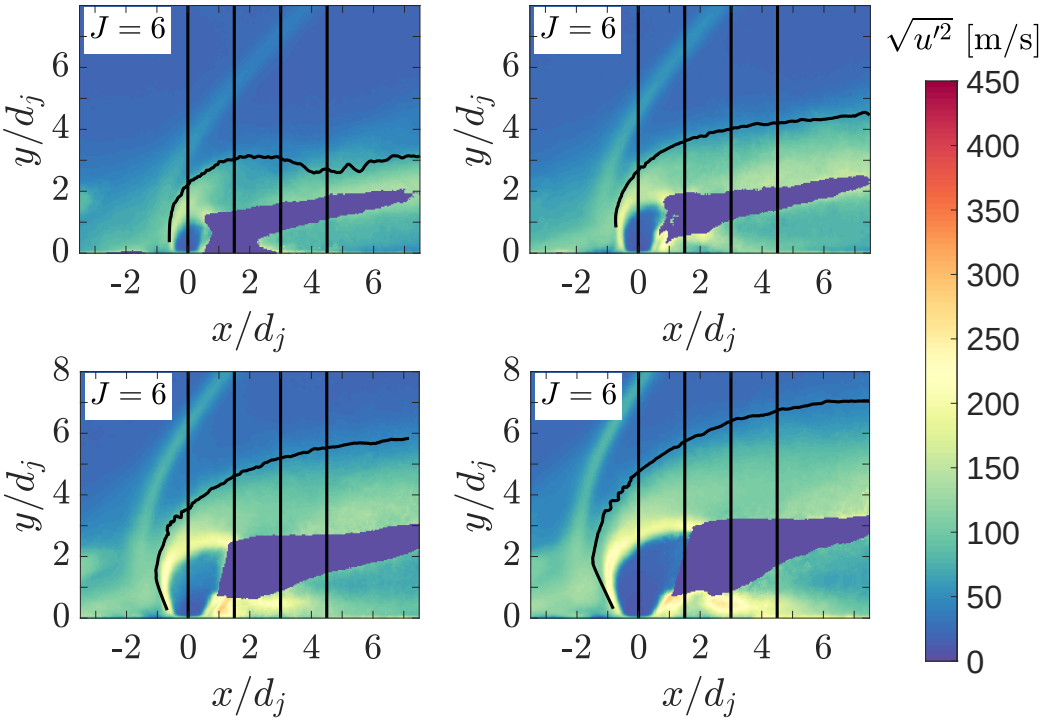

(b) RMS PIV velocity fields for nitrogen.

Figure B.5: PIV velocity results for nitrogen. The nominal momentum flux ratio is indicated in the upper left corner.

APPENDIX C

UNCERTAINTY QUANTIFICATION

Uncertainties generally denoted as U. They give the full confidence interval.

Any total pressure loss in the flow is neglected as the measured 3% drop (see Sec. 3.5) lies within the combined uncertainty of the pressure transducers used in its measurement.

C.1 Uncertainty Estimates for Jet Trajectories

The total uncertainty of jet trajectories based on absolute mixture fraction contours is computed via basic uncertainty propagation principles (Coleman and Steele, 2009) and estimates of statistical confidence intervals (for a 95% confidence level) where appropriate. Unless otherwise stated, it is assumed that confidence intervals can be estimated assuming a normal distribution for the quantity of interest. Since at least 900 samples are available for any computed quantity, this is a reasonable assumption.

For the x-coordinate the following sources of uncertainty are considered: crossflow Mach number, crossflow stagnation pressure, and jet stagnation pressure. The resulting expression is,

$$U^2_{x/J_2^{0.5}d_j} = \left(\frac{\partial}{\partial J_2} \left(\frac{x}{J_2^{0.5} d_j} \right) U_{J_2} \right)^2 . \tag{C.1}$$

With,

$$U^2_{J_2} = \left(\frac{\partial J_2}{\partial J_1} U_{J_1} \right)^2 + \left(\frac{\partial J_2}{\partial M_{\infty,1}} \sigma_{M_{\infty,1}} \right)^2 . \tag{C.2}$$

Where $\sigma_{M_{\infty,1}} = 0.06$ from the static wall pressure measurements in Sec. 3.5 is used and,

$$U^2_{J_1} = \left(\frac{\partial J_1}{\partial p_{0,\infty}} \sigma_{p_{0,\infty}} \right)^2 + \left(\frac{\partial J_1}{\partial p_{0,j}} \sigma_{p_{0,j}} \right)^2 + \left(\frac{\partial J_1}{\partial M_{\infty,1}} \sigma_{M_{\infty,1}} \right)^2 . \tag{C.3}$$

The crossflow stagnation pressure uncertainty is the combined measurement and run

uncertainty, $\sigma_{p_{0,\infty}} \approx 9.4\,\text{kPa}$, as is the jet stagnation pressure uncertainty $\sigma^2_{p_{0,j}} = \left(U_{meas}\left(p_{0,\infty}\right)\right)^2 + \left(1.96\sigma_{p_{0,\infty}}/\sqrt{n}\right)^2$, where n is the number of samples (here always > 900) and the first term is determined via the pressure transducer calibration.

For the y-coordinate the statistical uncertainty in the position of the 2% trajectory itself, uncertainties in the boundary layer thickness measurement, and the correlation between uncertainties in the 2% trajectory position and uncertainties in the post-shock momentum flux ratio are considered in addition. A correlation coefficient of $\rho' = 1$ is assumed between y and J_2, both as a worst-case estimate and because the two quantities are generally strongly correlated. This yields the following expression,

$$U^2_{y/h_c} = \left(\frac{\partial y/h_c}{\partial J_2} U_{J_2}\right)^2 + \left(\frac{\partial y/h_c}{\partial y}\sigma_y\right)^2 + \left(\frac{\partial y/h_c}{\partial \delta}\sigma_\delta\right)^2 + 2\frac{\partial y/h_c}{\partial y}\frac{\partial y/h_c}{\partial J_2}\rho'\sigma_y U_{J_2}. \quad \text{(C.4)}$$

The uncertainty of the trajectory position is estimated using the y-derivative of the mean mixture fraction field and the mixture fraction standard deviation in the following way,

$$\sigma_y = \frac{1.96}{\sqrt{N}}\left[\frac{dy}{d(\overline{\rho f})}\sigma_{(\overline{\rho f})}\right]_{\overline{\rho f}=0.02}. \quad \text{(C.5)}$$

The uncertainty of the boundary layer thickness is estimated in a similar fashion assuming a linear velocity profile yielding,

$$\sigma_\delta = \frac{1.96}{\sqrt{N}}\frac{\delta_{95\%}}{u_\infty}\,\sigma_u|_{\delta_{95\%}} \approx 0.02\,\text{mm}. \quad \text{(C.6)}$$

C.2 Uncertainty Estimates for Mixture Fraction and Velocity Field Data

Confidence intervals for the field data are estimated considering statistical uncertainties, instantaneous uncertainties according to Sciacchitano and Wieneke (2016), and uncertainties due to experimental conditions influencing velocities, where appropriate.

The uncertainty of the mean mixture fraction field is simply estimated as,

$$U^2_{\overline{\rho f}} = 1.96^2 \frac{\sigma^2_{\rho f}}{N}. \tag{C.7}$$

This assumes that fluctuations in f and ρ due to changes in the crossflow in jet conditions are all quantified sufficiently by the standard deviation of the mixture fraction field itself.

Similarly the uncertainty of the RMS of the mixture fraction field fluctuations evaluates to this simple relationship,

$$U^2_{\sqrt{\overline{(\rho f)'^2}}} = 1.96^2 \frac{\overline{(\rho f)'^2}}{2N}. \tag{C.8}$$

Using the principles of uncertainty propagation as before, the square of the total uncertainty, U^2, of the mean velocity magnitude, $\bar{U}$, is,

$$U^2_{\bar{U}} = \left(1.96\frac{\sigma_{\bar{U}}}{\sqrt{N}}\right)^2 + \left(\frac{\partial \bar{U}}{\partial M_2}\sigma_{M_1}\right)^2 + \left(\frac{\partial \bar{U}}{\partial T}\sigma_T\right)^2 + \left(\frac{\varepsilon_p}{N}\right)^2. \tag{C.9}$$

The last term on the right hand side is the uncertainty due to subpixel interpolation: $\varepsilon_p = 0.1\Delta/\Delta t$, where Δ is the PIV vector spacing and Δt is the temporal image pair spacing. The first derivative on the right hand side evaluates to $\sqrt{\gamma R\bar{T}}$, for crossflow quantities and using the general definition of the speed of sound. Likewise, the second derivative is evaluated as ${}^1\!/\!_2\overline{M}_1\sqrt{{}^{\gamma R}\!/\!_{\bar{T}}}$. These terms represent the velocity uncertainty due to temperature fluctuations during an experiment and remaining shocks waves in the test section, as described in Tab. 3.1.

Similarly the total uncertainty of the variance components are computed as,

$$U^2_{\overline{u'^2}_{corr}} = \frac{2}{N}\left[1.96^2\overline{u'^2}^2 + \left(\sqrt{2}\sigma_{U_u}\bar{U}_u\sqrt{1+\frac{\sigma^2_{U_u}}{2\bar{U}^2_u}}\right)^2\right] + \frac{2}{N}\varepsilon^4_p. \tag{C.10}$$

Here all captial U refer to uncertainties and not velocity magnitudes. The subscript "$corr$" denotes bias corrected quantities, see Sciacchitano and Wieneke (2016) for details. For the

velocity variances, the influence of fluctuations in temperature cancels if $\overline{M} >> \sigma_M$. For this study, the inequality holds and the corresponding terms are neglected in $U^2_{\overline{u'^2}_{corr}}$.

The uncertainty of the TKE and the velocity standard deviation magnitude is calculated as the sum of the velocity variance uncertainties yielding,

$$U^2_{TKE} = \frac{1}{4}\left(U^2_{\overline{u'^2}_{corr}} + U^2_{\overline{v'^2}_{corr}}\right), \tag{C.11}$$

$$U^2_{|\sqrt{\overline{\vec{u}'^2}}_{corr}|} = \left(U_{\overline{u'^2}_{corr}} + U_{\overline{v'^2}_{corr}}\right)\sqrt{\frac{N}{2}}\frac{1}{2N}. \tag{C.12}$$

The weighting of samples has to be changed for the uncertainty estimate of the standard deviation (Benedict and Gould, 1996).

Since the mean flow divergence is estimated using a central difference for the derivatives, its uncertainty can be estimated as,

$$U^2_{\nabla\cdot\bar{\vec{u}}} = 2\left(\frac{1}{2\Delta}\right)^2 [1-\rho(2\Delta)]\left(U^2_{\bar{u}} + U^2_{\bar{v}}\right). \tag{C.13}$$

In this equation the spatial auto-correlation coefficient, $\rho(2\Delta)$, is estimated directly from the previously determined uncertainty fields $U_{\bar{u}}$ and $U_{\bar{v}}$. To simplify discussions, the spatial average of the normalized velocity divergence uncertainty of a data set or data sub-set is defined as $\varepsilon = \langle U^2_{\nabla\cdot\bar{\vec{u}}}/|\nabla\cdot\bar{\vec{u}}|\rangle$.

C.3 Uncertainty Estimates for Chemiluminescence and PLIF Results

For the confidence interval of r_{CH} the statistical uncertainty and changes in the chemiluminescent area due to fluctuations in the deposited ignition energy are considered. This yields the expression,

$$U^2_{r_{CH}} = \left(t_{95\%,8}\frac{\sigma_{r_{CH}}}{\sqrt{N}}\right)^2 + \left(\frac{1}{A_{ref}}\frac{\partial A_{ell}}{\partial E_d}\sigma_{E_d}\right)^2. \tag{C.14}$$

The 95% confidence level t-distribution value is used because only nine samples per chemiluminescence time series are available, $t_{95\%,8} = 2.262$. The sensitivity of the chemilumi-

nescent area to the deposited laser energy is equated with the sensitivity of the laser spark size, see Sec. 3.2, with $\partial A_{ell}/\partial E_d = 1.07 \cdot 10^{-4}$ m^2/J and $\sigma_{E_d} = 4$ mJ. Finally, the variance $\sigma^2_{r_{CH}}$ is approximated as σ_A/A_{ref}, where σ_A is computed from the areas found in instantaneous chemiluminescence recordings after applying the CH* edge finding technique.

A similar expression for the uncertainty of $\bar{A}/\bar{A}_ref$ can be derived in the case of OH-PLIF results. Again, accounting for the statistical uncertainty and changes in the PLIF active area due to fluctuations in the deposited ignition energy, one obtains this uncertainty,

$$U^2_{\bar{A}/\bar{A}_{ref}} = \left(1.96\frac{\sigma_{\bar{A}}}{\bar{A}_{ref}\sqrt{N}}\right)^2 + \left(\frac{1}{\bar{A}_{ref}}\frac{\partial A_{ell}}{\partial E_d}\sigma_{E_d}\right)^2. \tag{C.15}$$

Here, $\sigma_{\bar{A}}$ is directly computed from individual data sets and Gaussian statistics are applicable due to the large enough sample size. For the OH-PLIF data $\sigma_{E_d} = 10$ mJ.

Using the same logic as for $\bar{A}/\bar{A}_ref$, the uncertainty of $\overline{\Sigma I}/\overline{\Sigma I_{ref}}$ can be written as,

$$U^2_{\overline{\sum I}/\overline{\sum I_{ref}}} = \left(1.96\frac{\sigma_{\overline{\sum I}}}{\overline{\sum I_{ref}}\sqrt{N}}\right)^2 + \left(\frac{1}{\overline{\sum I_{ref}}}\frac{\partial\overline{\sum I}}{\partial E_d}\sigma_{E_d}\right)^2. \tag{C.16}$$

Again, $\sigma_{\overline{\sum I}}$ is directly computed from individual data sets. To evaluate the derivative in the second term on the right hand side, it is assumed that $\partial\overline{\sum I}/\partial E_d \propto \partial A_{ell}/\partial E_d$. Since the integrated intensity is considered, the assumption that a change in this quantity is proportional to a change in OH emitting area is reasonable. The integrated intensity is related directly to the emitting area by calculating the average integrated intensity per unit area of a given data set,

$$\frac{\partial\overline{\sum I}}{\partial E_d} = \overline{\left(\frac{\sum I}{A}\right)} \cdot \left(\frac{\partial A_{ell}}{\partial E_d}\right). \tag{C.17}$$

Technically, all of the quantities measured with CH* chemiluminescence and OH-PLIF should also exhibit some sensitivity to the availability of fuel and the turbulent mixing rates. To quantify this sensitivity, changes in the results with changing jet momentum flux

ratio have to be analyzed. This task is outside the scope of the current study and, thus, uncertainties due to fuel availability and turbulent mixing rates are neglected.

For all bivariate PDFs presented in Ch. 5 and Ch. 6, the bin width is $W < 0.2\sigma$ of the evaluated random variables to reduce the bias error below 1% (Bendat and Piersol, 2010). The normalized RMS uncertainty of the joint PDF estimate scales as $\varepsilon 1/\sqrt{NW_xW_yp(x,y)}$, where $p(x,y)$ is the real PDF of the two random variables X and Y (Bendat and Piersol, 2010). Since the real PDF is not available, the estimated PDF is used in the computation of the average normalized RMS uncertainty.

REFERENCES

Abbitt III, J. D., Segal, C., McDaniel, J. C., Krauss, R. H., and Whitehurst, R. B. (1993). "Experimental supersonic hydrogen combustion employing staged injection behind a rearward-facing step". *J. Propul. Power* 9.3, pp. 472–478.

Adrian, L., Adrian, R. J., and Westerweel, J. (2011). *Particle image velocimetry*. 30. Cambridge University Press.

Ali, M. Y. and Alvi, F. (2015). "Jet arrays in supersonic crossflow—An experimental study". *Phys. Fluids* 27.12, p. 126102.

An, B., Wang, Z., Yang, L., Li, X., and Zhu, J. (2017). "Experimental investigation on the impacts of ignition energy and position on ignition processes in supersonic flows by laser induced plasma". *Acta Astronaut.* 137, pp. 444–449.

An, B., Yang, L., Wang, Z., Li, X., Sun, M., Zhu, J., and Yan, W. (2020). "Characteristics of laser ignition and spark discharge ignition in a cavity-based supersonic combustor". *Combust. Flame* 212, pp. 177–188.

Anderson, J. D. (2006). "Hypersonic and high-temperature gas dynamics". AIAA.

Anderson, J. D. (1990). *Modern compressible flow: with historical perspective*. Vol. 12. McGraw-Hill New York.

Ben-Yakar, A., Mungal, M. G., and Hanson, R. K. (2006). "Time evolution and mixing characteristics of hydrogen and ethylene transverse jets in supersonic crossflows". *Phys. Fluids* 18.2, p. 026101.

Bendat, J. and Piersol, A. (2010). *Random Data: Analysis and Measurement Procedures*. 4th ed. John Wiley and Sons, Hoboken NJ.

Benedict, L. H. and Gould, R. D. (1996). "Towards better uncertainty estimates for turbulence statistics". *Exp. Fluids* 2, pp. 129–136.

Bertagni, M. B., Marro, M., Salizzoni, P., and Camporeale, C. (2019). "Solution for the statistical moments of scalar turbulence". *Phys. Rev. Fluids* 4.12, p. 124701.

Billig, F. S. (1967). "Shock-wave shapes around spherical-and cylindrical-nosed bodies." *J. Spacecraft Rockets* 4.6, pp. 822–823.

Billig, F. S. and Schetz, J. A. (1994). "Penetration and mixing of gas jets in supersonic cross flow". *AIAA J.* 32.7, pp. 1533–1535.

Boyce, R. R., Mudford, N. R., and McGuire, J. R. (2012). "OH-PLIF visualisation of radical farming supersonic combustion flows". *Shock Waves* 22.1, pp. 9–21.

Bradley, D., Sheppard, C. G. W., Suardjaja, I. M., and Woolley, R. (2004). "Fundamentals of high-energy spark ignition with lasers". *Combust. Flame* 138.1-2, pp. 55–77.

Brieschenk, S., O'Byrne, S., and Kleine, H. (2014). "Ignition characteristics of laser-ionized fuel injected into a hypersonic crossflow". *Combust. Flame* 161.4, pp. 1015–1025.

Brieschenk, S., O'Byrne, S., and Kleine, H. (2013a). "Laser-induced plasma ignition studies in a model scramjet engine". *Combust. Flame* 160.1, pp. 145–148.

Brieschenk, S., O'Byrne, S., and Kleine, H. (2013b). "Visualization of jet development in laser-induced plasmas". *Opt. Lett.* 38.5, pp. 664–666.

Broadwell, J. E. and Breidenthal, R. E. (1984). "Structure and mixing of a transverse jet in incompressible flow". *J. Fluid Mech.* 148, pp. 405–412.

Castellanos, J. L., Gómez, S., and Guerra, V. (2002). "The triangle method for finding the corner of the L-curve". *Appl. Numer. Math.* 43.4, pp. 359–373.

Chaudhuri, S., Wu, F., and Law, C. K. (2013). "Scaling of turbulent flame speed for expanding flames with Markstein diffusion considerations". *Phys. Rev. E* 88.3, p. 033005.

Chauhan, K. A., Monkewitz, P. A., and Nagib, H. M. (2009). "Criteria for assessing experiments in zero pressure gradient boundary layers". *Fluid Dyn. Res.* 41.2, p. 021404.

Choi, B., Takae, K., Kouchi, T., and Masuya, G. (2012). "Mean and Turbulent Velocity Field for Jet Injected into Supersonic Flow with Pseudo-Shock Wave". *J. Propul. Power* 28.5, pp. 971–981.

Cohen, L. S., Coulter, L. J., and Egan, W. J. (1971). "Penetration and Mixing of Multiple Gas Jets Subjected to a Cross Flow". *AIAA J.* 9.4, pp. 718–724.

Coleman, H. W. and Steele, W. G. (2009). *Experimentation, Validation, and Uncertainty Analysis for Engineers*. John Wiley and Sons, Hoboken NJ.

Colket III, M. B. and Spadaccini, L. J. (2001). "Scramjet fuels autoignition study". *J. Propul. Power* 17.2, pp. 315–323.

Crist, S., Glass, D. R., and Sherman, P. M. (1966). "Study of the highly underexpanded sonic jet." *AIAA J.* 4.1, pp. 68–71.

Dimotakis, P. E. (2005). "Turbulent mixing". *Annu. Rev. Fluid Mech.* 37, pp. 329–356.

Donohue, J. M. and McDaniel Jr., J. C. (1996). "Computer-controlled multiparameter flowfield measurements using planar laser-induced iodine fluorescence". *AIAA J.* 34.8, pp. 1604–1611.

Donzis, D. A. and Maqui, A. F. (2016). "Statistically steady states of forced isotropic turbulence in thermal equilibrium and non-equilibrium". *J. Fluid Mech.* 797, pp. 181–200.

Eckert, E. R. G. (1955). *Engineering relations for friction and heat transfer to surfaces in high velocity flow*.

Egolfopoulos, F. N. and Dimotakis, P. E. (2001). "A comparative numerical study of premixed and non-premixed ethylene flames". *Combust. Sci. and Technol.* 162.1, pp. 19–35.

Elsinga, G. E., Oudheusden, B. W. van, and Scarano, F. (2005a). "Evaluation of aero-optical distortion effects in PIV". *Exp. Fluids* 39.2, pp. 246–256.

Elsinga, G. E., Oudheusden, B. W. van, and Scarano, F. (2005b). "The effect of particle image blur on the correlation map and velocity measurement in PIV". *Optics and Photonics 2005, Optical Diagnostics*. Vol. 5880, p. 588010.

F-Chart Software (Jan. 1, 2018). *EES - Engineering Equation Solver*. Version 10.341.

Fitzgibbon, A., Pilu, M., and Fisher, R. B. (n.d.). "Direct least square fitting of ellipses". *IEEE T. Pattern Anal.* 21.5 (), pp. 476–480.

Foucaut, J.-M. and Stanislas, M. (2002). "Some considerations on the accuracy and frequency response of some derivative filters applied to particle image velocimetry vector fields". *Meas. Sci. Technol.* 13.7, p. 1058.

Fric, T. F. and Roshko, A. (1994). "Vortical structure in the wake of a transverse jet". *J. Fluid Mech.* 279, pp. 1–47.

Fries, D., Ochs, B. A., Saha, A., Ranjan, D., and Menon, S. (2019). "Flame speed characteristics of turbulent expanding flames in a rectangular channel". *Combust. Flame* 199, pp. 1–13.

Gamba, M. and Mungal, M. G. (2015). "Ignition, flame structure and near-wall burning in transverse hydrogen jets in supersonic crossflow". *J. Fluid Mech.* 780, pp. 226–273.

Gevorkyan, L., Shoji, T., Getsinger, D. R., Smith, O. I., and Karagozian, A. R. (2016). "Transverse jet mixing characteristics". *J. Fluid Mech.* 790, pp. 237–274.

Glass, M. and Kennedy, I. M. (1977). "An improved seeding method for high temperature laser Doppler velocimetry." *Combust. Flame* 29, pp. 333–335.

Gruber, M. R. and Nejad, A. S. (1995). "New supersonic combustion research facility". *J. Propul. Power* 11.5, pp. 1080–1083.

Gruber, M. R., Nejad, A. S., Chen, T. H., and Dutton, J. C. (1997a). "Compressibility effects in supersonic transverse injection flowfields". *Phys. Fluids* 9.5, pp. 1448–1461.

Gruber, M. R., Nejad, A. S., Chen, T. H., and Dutton, J. C. (1997b). "Large structure convection velocity measurements in compressible transverse injection flowfields". *Exp. Fluids* 22.5, pp. 397–407.

Gruber, M. R., Nejad, A. S., Chen, T. H., and Dutton, J. C. (1995). "Mixing and penetration studies of sonic jets in a Mach 2 freestream". *J. Propul. Power* 11.2, pp. 315–323.

Gruber, M. R., Nejad, A. S., Chen, T. H., and Dutton, J. C. (2000). "Transverse injection from circular and elliptic nozzles into a supersonic crossflow". *J. Propul. Power* 16.3, pp. 449–457.

Hanson, R. K., Seitzman, J. M., and Paul, P. H. (1990). "Planar laser-fluorescence imaging of combustion gases". *Appl. Phys. B-Lasers O.* 50.6, pp. 441–454.

Hasselbrink, E. F. and Mungal, M. G. (2001a). "Transverse jets and jet flames. Part 1. Scaling laws for strong transverse jets". *J. Fluid Mech.* 443, pp. 1–25.

Hasselbrink, E. F. and Mungal, M. G. (2001b). "Transverse jets and jet flames. Part 2. Velocity and OH field imaging". *J. Fluid Mech.* 443, pp. 27–68.

Heister, S. D. and Karagozian, A. R. (1990). "Gaseous jet in supersonic crossflow". *AIAA J.* 28.5, pp. 819–827.

Hollo, S. D., McDaniel, J. C., and Hartfield Jr., R. J. (1994). "Quantitative investigation of compressible mixing-staged transverse injection into Mach 2 flow". *AIAA J.* 32.3, pp. 528–534.

Howison, J. C. and Goyne, C. P. (2010). "Assessment of Seeder Performance for Particle Velocimetry in a Scramjet Combustor". *J. Propul. Power* 26.3, pp. 514–523.

Hsu, A. G., Srinivasan, R., Bowersox, R. D. W., and North, S. W. (2009). "Molecular tagging using vibrationally excited nitric oxide in an underexpanded jet flowfield". *AIAA J.* 47.11, pp. 2597–2604.

Huang, W. (2016). "Transverse jet in supersonic crossflows". *Aerosp. Sci. Technol.* 50, pp. 183–195.

Huete, C., Sánchez, A. L., and Williams, F. A. (2017). "Diffusion-flame ignition by shock-wave impingement on a hydrogen–air supersonic mixing layer". *J. Propul. Power*, pp. 256–263.

Kailasanath, K. (2000). "Review of propulsion applications of detonation waves". *AIAA J.* 38.9, pp. 1698–1708.

Kamotani, Y. and Greber, I. (1972). "Experiments on a turbulent jet in a cross flow". *AIAA J.* 10.11, pp. 1425–1429.

Karagozian, A. R. (1986). "An analytical model for the vorticity associated with a transverse jet". *AIAA J.* 24.3, pp. 429–436.

Karagozian, A. R. (2014). "The jet in crossflow". *Phys. Fluids* 26.10, pp. 1–47.

Karimi, M. and Girimaji, S. S. (2016). "Suppression mechanism of Kelvin-Helmholtz instability in compressible fluid flows". *Phys. Rev. E* 93.4, p. 041102.

Kawai, S. and Lele, S. K. (2010). "Large-eddy simulation of jet mixing in supersonic cross-flows". *AIAA J.* 48.9, pp. 2063–2083.

Kelso, R. M., Lim, T. T., and Perry, A. E. (1996). "An experimental study of round jets in cross-flow". *J. Fluid Mech.* 306, pp. 111–144.

Kobayashi, H., Tamura, T., Maruta, K., Niioka, T., and Williams, F. A. (1996). "Burning velocity of turbulent premixed flames in a high-pressure environment". *International symposium on combustion*. Vol. 26. 1, pp. 389–396.

Kobayashi, K., Bowersox, R. D. W., Srinivasan, R., Carter, C. D., and Hsu, K.-Y. (2007). "Flowfield studies of diamond-shaped fuel injector in a supersonic flow". *J. Propul. Power* 23.6, pp. 1168–1176.

Koike, S., Takahashi, H., Tanaka, K., Hirota, M., Takita, K., and Masuya, G. (2007). "Correction method for particle velocimetry data based on the Stokes drag law". *AIAA J.* 45.11, pp. 2770–2777.

Kovasznay, L. S. G. (1953). "Turbulence in supersonic flow". *J. Aeronaut. Sci.* 20.10, pp. 657–674.

Landsberg, W. O., Wheatley, V., and Veeraragavan, A. (2016). "Characteristics of cascaded fuel injectors within an accelerating scramjet combustor". *AIAA J.*, pp. 3692–3700.

Lauer, M. and Sattelmayer, T. (2011). "Determination of turbulent flame temperature from vibrationally resolved OH chemiluminescence measurements".

Laven, Philip (Oct. 19, 2016). *MiePlot*. Version v4614.

Lee, J., Lin, K.-C., and Eklund, D. (2015). "Challenges in fuel injection for high-speed propulsion systems". *AIAA J.* 53.6, pp. 1405–1423.

Lee, J. G. and Santavicca, D. A. (2003). "Experimental diagnostics for the study of combustion instabilities in lean premixed combustors". *J. Propul. Power* 19.5, pp. 735–750.

Lee, M. P., McMillin, B. K., Palmer, J. L., and Hanson, R. K. (1992). "Planar fluorescence imaging of a transverse jet in a supersonic crossflow". *J. Propul. Power* 8.4, pp. 729–735.

Lee, S.-H. (2006a). "Characteristics of dual transverse injection in scramjet combustor, part 1: Mixing". *J. Propul. Power* 22.5, pp. 1012–1019.

Lee, S.-H. (2006b). "Characteristics of dual transverse injection in scramjet combustor, Part 2: Combustion". *J. Propul. Power* 22.5, pp. 1020–1026.

Lefkowitz, J. K and Ombrello, T. (2017). "An exploration of inter-pulse coupling in nanosecond pulsed high frequency discharge ignition". *Combust. Flame* 180, pp. 136–147.

Lele, S. K. (1994). "Compressibility effects on turbulence". *Annu. Rev. Fluid Mech.* 26.1, pp. 211–254.

Lieuwen, T. C. (2012). *Unsteady combustor physics*. Cambridge University Press.

Lin, K., Ryan, M., Carter, C., Gruber, M., and Raffoul, C. (2010). "Raman scattering measurements of gaseous ethylene jets in a Mach 2 supersonic crossflow". *J. Propul. Power* 26.3, pp. 503–513.

Ma, L., Lei, Q., Wu, Y., Xu, W., Ombrello, T. M., and Carter, C. D. (2016). "From ignition to stable combustion in a cavity flameholder studied via 3D tomographic chemiluminescence at 20 kHz". *Combust. Flame* 165, pp. 1–10.

Mahesh, K. (2013). "The interaction of jets with crossflow". *Annu. Rev. Fluid Mech.* 45, pp. 379–407.

Mai, T., Sakimitsu, Y., Nakamura, H., Ogami, Y., Kudo, T., and Kobayashi, H. (2011). "Effect of the incident shock wave interacting with transversal jet flow on the mixing and combustion". *P. Combust. Inst.* 33.2, pp. 2335–2342.

Margason, R. J. (1993). "Fifty years of jet in cross flow research". *In AGARD, Computational and experimental assessment of jets in cross flow 41 p (see N94-28003 07-34).*

Mastorakos, E. (2009). "Ignition of turbulent non-premixed flames". *Prog. Energ. Combust.* 35.1, pp. 57–97.

Matsubara, Y., Takita, K., and Masuya, G. (2013). "Combustion enhancement in a supersonic flow by simultaneous operation of DBD and plasma jet". *P. Combust. Inst.* 34.2, pp. 3287–3294.

McClinton, C. R. (1974). *Effect of ratio of wall boundary layer thickness to jet diameter on mixing of a normal hydrogen jet in a supersonic stream*. Tech. rep. NASA-TM-X-3030. Contract No.: RTOP 501-04-03-03. Washington (DC): NTRS, NASA Langley Research Center (US).

McDaniel, J. C. and Graves, J. (1988). "Laser-induced-fluorescence visualization of transverse gaseous injection in a nonreacting supersonic combustor". *J. Propul. Power* 4.6, pp. 591–597.

Melling, A. (1997). "Tracer particles and seeding for particle image velocimetry". *Meas. Sci. Technol.* 8.12, p. 1406.

Mulla, I. A., Chakravarthy, S. R., Swaminathan, N., and Balachandran, R. (2016). "Evolution of flame-kernel in laser-induced spark ignited mixtures: A parametric study". *Combust. Flame* 164, pp. 303–318.

Muppidi, S. and Mahesh, K. (2005). "Study of trajectories of jets in crossflow using direct numerical simulations". *J. Fluid Mech.* 530, pp. 81–100.

Nogueira, J., Lecuona, A., and Rodriguez, P. A. (1997). "Data validation, false vectors correction and derived magnitudes calculation on PIV data". *Meas. Sci. Technol.* 8.12, p. 1493.

O'Brien, J., Urzay, J., Ihme, M., Moin, P., and Saghafian, A. (2014). "Subgrid-scale backscatter in reacting and inert supersonic hydrogen–air turbulent mixing layers". *J. Fluid Mech.* 743, pp. 554–584.

Ochs, B. A. and Menon, S. (2020). "Laser ignition in supersonic channel flow". *Combust. Flame* 214, pp. 90–102.

Ombrello, T. M., Carter, C. D., Tam, C.-J., and Hsu, K.-Y. (2015). "Cavity ignition in supersonic flow by spark discharge and pulse detonation". *P. Combust. Inst.* 35.2, pp. 2101–2108.

Papamoschou, D. (1992). "Effect of three-dimensionality on compressible mixing". *J. Propul. Power* 8.1, pp. 247–249.

Papamoschou, D. and Hubbard, D. G. (1993). "Visual observations of supersonic transverse jets". *Exp. Fluids* 14.6, pp. 468–476.

Papamoschou, D. and Roshko, A. (1988). "The compressible turbulent shear layer: an experimental study". *J. Fluid Mech.* 197, pp. 453–477.

Pernpeintner, M., Lauer, M., Hirsch, C., and Sattelmayer, T. (2011). "A method to obtain planar mixture fraction statistics in turbulent flows seeded with tracer particles". *ASME 2011 Turbo Expo: Turbine Technical Conference*, pp. 1341–1350.

Phuoc, T. X. (2000). "Laser spark ignition: experimental determination of laser-induced breakdown thresholds of combustion gases". *Opt. Commun.* 175.4-6, pp. 419–423.

Pizzaia, A. and Rossmann, T. (2018). "Effect of boundary layer thickness on transverse sonic jet mixing in a supersonic turbulent crossflow". *Phys. Fluids* 30.11, p. 115104.

Pope, S. B. (2000). *Turbulent flows*. Cambridge University Press.

Portz, R. and Segal, C. (2006). "Penetration of gaseous jets in supersonic flows". *AIAA J.* 44.10, pp. 2426–2429.

Povinelli, F. P., Povinelli, L. A., and Hersch, M. (1970). "Supersonic jet penetration/up to Mach 4/into a Mach 2 airstream". *J. Spacecraft Rockets* 7.8, pp. 988–992.

Ragni, D., Schrijer, F., Van Oudheusden, B. W., and Scarano, F. (2011). "Particle tracer response across shocks measured by PIV". *Exp. Fluids* 50.1, pp. 53–64.

Rhodes, M. J. (2008). *Introduction to particle technology*. John Wiley and Sons, Hoboken NJ.

Rhodes Jr., R. P., Rubins, P. M., and Chriss, D. E. (1974). *Effect of Heat Release on Flow Parameters in Shock Induced Combustion*. Tech. rep. Rep. AEDC-TDR-62-7S. Arnold Airf. Base, TN.

Rogers, E. W. E. and Davis, B. M. (1957). *A note on turbulent boundary-layer allowances in supersonic nozzle design*. HM Stationery Office.

Rogers, R. C. (1971). *Mixing of Hydrogen Injected from Multiple Injectors Normal to a Supersonic Airstream*. Tech. rep. NASA-TND-6476. Washington (DC): NTRS, NASA Langley Research Center (US).

Rothstein, A. and Wantuck, P. (1992). "A study of the normal injection of hydrogen into a heated supersonicflow using planar laser-induced fluorescence". *28th AIAA Joint Propulsion Conference*, p. 3423.

Saghafian, A., Terrapon, V. E., and Pitsch, H. (2015). "An efficient flamelet-based combustion model for compressible flows". *Combust. Flame* 162.3, pp. 652–667.

Santiago, J. G. and Dutton, J. C. (1997). "Velocity measurements of a jet injected into a supersonic crossflow". *J. Propul. Power* 13.2, pp. 264–273.

Sarnacki, B. G., Esposito, G., Krauss, R. H., and Chelliah, H. K. (2012). "Extinction limits and associated uncertainties of nonpremixed counterflow flames of methane, ethylene, propylene and n-butane in air". *Combust. Flame* 159.3, pp. 1026–1043.

Sautet, J. C. and Stepowski, D. (1994). "Single-shot laser Mie scattering measurements of the scalar profiles in the near field of turbulent jets with variable densities". *Exp. Fluids* 16.6, pp. 353–367.

Schetz, J. A. and Billig, F. S. (1966). "Penetration of gaseous jets injected into a supersonic stream." *J. Spacecraft Rockets* 3.11, pp. 1658–1665.

Sciacchitano, A. and Wieneke, B. (2016). "PIV uncertainty propagation". *Meas. Sci. Technol.* 27.8, p. 084006.

Settles, G. S. (2001). *Schlieren and shadowgraph techniques: Visualizing phenomena in transport media*. Springer.

Sforzo B.and Kim, J., Jagoda, J., and Seitzman, J. (2015). "Ignition probability in a stratified turbulent flow with a sunken fire igniter". *J. Eng. Gas Turb. Power* 137.1.

Shan, J. W. and Dimotakis, P. E. (2006). "Reynolds-number effects and anisotropy in transverse-jet mixing". *J. Fluid Mech.* 566, pp. 47–96.

Shao, J., Davidson, D. F., and Hanson, R. K. (2018). "A shock tube study of ignition delay times in diluted methane, ethylene, propene and their blends at elevated pressures". *Fuel* 225, pp. 370–380.

Sibulkin, M. (1957). "Boundary-Layer Measurements at Supersonic Nozzle Throats". *J. Aeronaut. Sci.* 24.4, pp. 249–252.

Smart, M. (2007). "Scramjets". *Aeronaut J.* 111.1124, pp. 605–619.

Smart, M. K., Hass, N. E., and Paull, A. (2006). "Flight data analysis of the HyShot 2 scramjet flight experiment". *AIAA J.* 44.10, pp. 2366–2375.

Smith, G. P., Golden, D. M., *et al.* (July 2020). *GRI-MECH 3.0*. http://combustion.berkeley.edu/gri-mech/version30/text30.html.

Smith, S. H. and Mungal, M. G. (1998). “Mixing, structure and scaling of the jet in cross-flow”. *J. Fluid Mech.* 357, pp. 83–122.

Smith, S. M. and Brady, J. M. (1997). “SUSAN—a new approach to low level image processing”. *Int. J. Comput. Vision* 23.1, pp. 45–78.

Soria, J. (1996). “An investigation of the near wake of a circular cylinder using a video-based digital cross-correlation particle image velocimetry technique”. *Exp. Therm. Fluid Sci.* 12.2, pp. 221–233.

Spaid, F. W. and Zukoski, E. E. (1968). “A study of the interaction of gaseous jets from transverse slots with supersonic external flows”. *AIAA J.* 6.2, pp. 205–212.

Sun, M. and Hu, Z. (2018a). “Formation of surface trailing counter-rotating vortex pairs downstream of a sonic jet in a supersonic cross-flow”. *J. Fluid Mech.* 850, pp. 551–583.

Sun, M. and Hu, Z. (2018b). “Mixing in nearwall regions downstream of a sonic jet in a supersonic crossflow at Mach 2.7”. *Phys. Fluids* 30.10, p. 106102.

Sykes, R. I., Lewellen, W. S., and Parker, S. F. (1986). “On the vorticity dynamics of a turbulent jet in a crossflow”. *J. Fluid Mech.* 168, pp. 393–413.

Takahashi, H., Masuya, G., and Hirota, M. (2010). “Effects of injection and main flow conditions on supersonic turbulent mixing structure”. *AIAA J.* 48.8, pp. 1748–1756.

Urzay, J. (2018). “Supersonic combustion in air-breathing propulsion systems for hypersonic flight”. *Annu. Rev. Fluid Mech.* 50, pp. 593–627.

VanLerberghe, W. M., Santiago, J. G., Dutton, J. C., and Lucht, R. P. (2000). “Mixing of a sonic transverse jet injected into a supersonic flow”. *AIAA J.* 38.3, pp. 470–479.

Velikorodny, A. and Kudriakov, S. (2012). “Numerical study of the near-field of highly underexpanded turbulent gas jets”. *Int. J. Hydrogen Energ.* 37.22, pp. 17390–17399.

Wang, G. H. and Clemens, N. T. (2004). “Effects of imaging system blur on measurements of flow scalars and scalar gradients”. *Exp. Fluids* 37.2, pp. 194–205.

Wantuck, P. and Watanabe, H. (1990). “Radio frequency (RF) heated supersonic flow laboratory”. *26th AIAA Joint Propulsion Conference*, p. 2469.

Watanabe, J., Kouchi, T., Takita, K., and Masuya, G. (2012). “Large-eddy simulation of jet in supersonic crossflow with different injectant species”. *AIAA J.* 50.12, pp. 2765–2778.

White, F. M. and Corfield, I. (2006). *Viscous fluid flow*. Vol. 3. McGraw-Hill New York.

Wieneke, B. (2015). “PIV uncertainty quantification from correlation statistics”. *Meas. Sci. Technol.* 26.7, p. 074002.

Willert, C. E. and Gharib, M. (1991). “Digital particle image velocimetry”. *Exp. Fluids* 10.4, pp. 181–193.

Xu, C. and Konnov, A. A. (2012). “Validation and analysis of detailed kinetic models for ethylene combustion”. *Energy* 43.1, pp. 19–29.

Yoshida, A. and Tsuji, H. (1977). “Supersonic combustion of hydrogen in a vitiated airstream using transverse injection”. *AIAA J.* 15.4, pp. 463–464.

Zhang, Y., Liu, W., Wang, B., Zhao, Y., and Zhang, D. (2015). “Investigation of injectant molecular weight effect on the transverse jet characteristics in supersonic crossflow”. *Acta Astronautica* 114, pp. 101–111.

Zukoski, E. E. and Spaid, F. W. (1964). “Secondary injection of gases into a supersonic flow”. *AIAA J.* 2.10, pp. 1689–1696.